Functionalization and microfluidic integration of silicon nanowire biologically gated field effect transistors

Pfreundt, Andrea; Svendsen, Winnie Edith; Dimaki, Maria; Andresen, Lars

Publication date:
2016

Document Version
Publisher's PDF, also known as Version of record

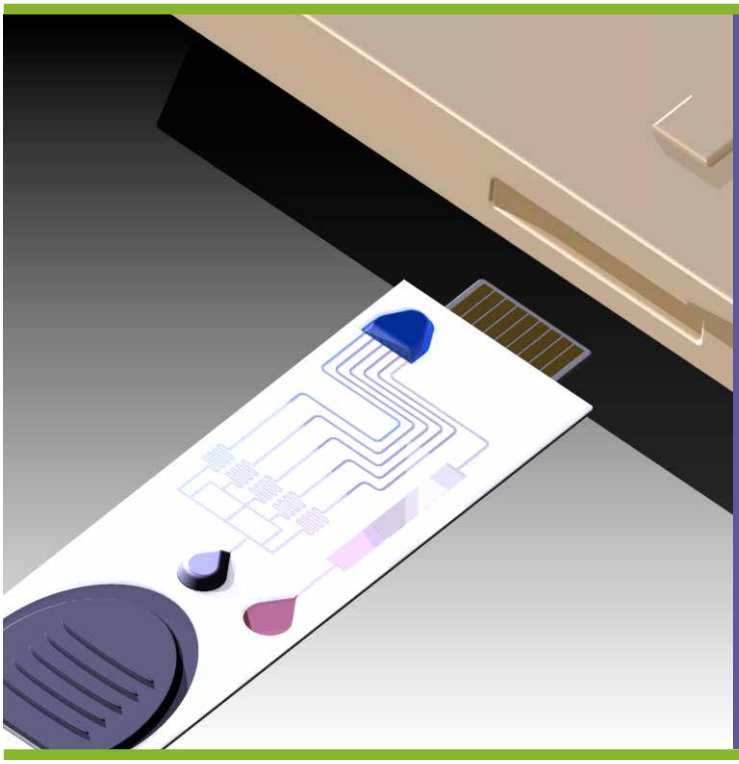

Functionalization and microfluidic integration of silicon nanowire biologically gated field effect transistors

Andrea Pfreundt
PhD Thesis February 2016

DTU Nanotech
Department of Micro- and Nanotechnology

PhD Thesis

Functionalization and microfluidic integration of silicon nanowire biologically gated field effect transistors

Andrea Pfreundt

March 1, 2016
Technical University of Denmark

Supervisors:
Winnie Edith Svendsen
Maria Dimaki
Lars Andresen

Preface

This thesis is submitted as part of work done to obtain the PhD degree at the Technical University of Denmark. The project is part of the EU Initial Traning Network (ITN) EngCaBra, a European collaboration for the development of novel diagnostic and therapeutic tools for cancer and brain diseases, and funded as a Marie-Curie Actions fellowship.

The research was conducted in the group Nano-Bio Integrated Systems lead by Winnie E. Svendsen at the Department of Micro- and Nanotechnology. The full project at DTU consists of three PhD students, Azeem Zulfiqar, who is primarily responsible for the development and fabrication of the sensor hardware, Francois Patou, who is responsible for the development and implementation of a mobile sensing platform as a readout system, and myself, responsible for surface functionalization, protein work and microfluidic integration of the sensor. Both have contributed in many ways to this thesis.

All research, graphics and text is my original work to the best of my knowledge unless other authors and contributors are mentioned.

A version of chapter 5.5 will be resubmitted for publication (omitted in published version of this thesis).

A version of chapter 10 has been published with open access in the Journal of Micromechanics and Microengineering, 25 (11) 115010, on September 28th 2015.

Kongens Lyngby, December 2015

Abstract

This thesis deals with the development of a novel biosensor for the detection of biomolecules based on a silicon nanowire biologically gated field-effect transistor and its integration into a point-of-care device. The sensor and electrical on-chip integration was developed in a different project. The presented research is based on this sensor structure and investigates its potential as a versatile biomarker detection platform by evaluating different functionalization approaches. The functionalization of the silicon sensor surface with organic molecules was investigated in detail to determine the suitability of different methods for the preparation of organic interfaces for protein attachment. Oxide-free silicon surfaces offer unique possibilities to create highly sensitive sensor surfaces for charge detection due to the lack of an insulating oxide layer, but the highly reactive surface presents a challenge for modification under ambient conditions. Self-assembled monolayer formation by hydrosilylation with alkenes and alkynes was thus investigated under different conditions, both ambient and controlled, and quantified using x-ray photoelectron spectroscopy. With the aim to create a platform for subsequent immobilization of receptor molecules, amine- and carboxylic acid- as well as alkyne-terminated surfaces were prepared that allow for the conjugation of biomolecules using established cross-linking schemes. Using a receptor-ligand model system protein detection experiments were performed with nanowire sensors functionalized using different modification schemes. To facilitate functionalization and measurement and as a first step towards integration into a point-of-care device, several microfluidic tools were developed for sample delivery to the sensor surface and as a modular platform for the further development of automated functionalization and sample preparation schemes.

Acknowledgement

A PhD thesis has just one author. There is one name, one person, who supposedly did it all. But the work that went into the last 3 and a half years, every day of experiments, of data analysis, of meetings and of discussions; none of that could have been done, not even a single day, without the combined effort of many people. Teaching practical and theoretical knowledge, guiding thoughts in the right direction and directly being part of much of the work is just one side of it. Emotional support, kind words and a smile every once in a while are just as important.

In this spirit:

I would like to thank my supervisors Winnie Svendsen, who always had an open door and open ear, Lars Andresen who was still supporting me even after he left the department and of course Maria Dimaki, without whom this thesis would not have been possible at all and who has found time to help me finish despite many other responsibilities. Thank you! They have been there with me through all the ups and downs, providing encouragement and support when I most needed it.

Thanks to everyone in the NaBIS group (and some outside of it) I have felt welcome and in the right place very quickly after I joined! Thanks Azeem, Dorota, Karsten, Luigi, Romen and Jaime, who were there from the start and helped me find my way around Lab and the department as part of the NaBIS family. You taught me so much, it would be impossible to name even half of it. Be it critical milling parameters, the way to prototype even faster, how to keep things structured, fabricate devices in the cleanroom or giving me in introduction to electrochemistry. Julie, Tanya, Sune and Fatima, you were Master students at some point when I started and now you're all doing PhD's as well. It's been such a pleasure getting to know you, working with you and exchanging ideas over coffee. I can't believe how fast time has passed, thank you for still being there.

I also want to thank my students Zarmeena, Esben, Steen and Elisa for their good work and their trust in me as (co-)supervisor. I really enjoyed being part of your education; I think learned as much from you as you did from me.

Also a big thanks to my parents and my sisters Ulrike and Claudia, and to Ufuk, Aghiad

and Carlotta, for their patience and support and their relentless reassuring words. I couldn't have done it without you and almost didn't, you turned me around, over and over. Thank you. Thank you so much.

This project is funded as part of the EU Marie Curie Initial Training Networks (ITN) Biomedical engineering for cancer and brain disease diagnosis and therapy development (EngCaBra). Project no. PITN-GA-2010-264417.

I want to thank the European Union for making this project possible and for similar networks that enable researchers and students like myself to experience a very international and interdisciplinary environment. I am grateful for such a great opportunity and hope that initiatives like this will continue to inspire future researchers. In this spirit I want to mention my fellow EngCaBra fellows, who I am so glad to have gotten to know and to work with: Azeem Zulfiqar, Francois Patou, Franziska Uhlenbrock, Joanna Obacz, Rene Splinter, Wei Gong, Daniela Pucciarelli, Ben van Lier, Amir Shadmani, Valeria Fioravanti, Sona Kontsekova, Reza Ebrahimifard, Joao Pimentel and Filippo Cipriani.

Contents

List of Figures

List of Tables

1 | Introduction

With the advent of integrated circuits, the personal computer and the use of smart miniaturized devices have rapidly become an integral part of almost every aspect of our lives. Currently, a similar trend is underway with the development of lab-on-a-chip technology. Miniaturization of sensors, the capabilities of integrated microfluidics and advancements in wireless technology and processing power enable the development of new classes of medical devices. Analyses that previously required a fully equipped laboratory and specialized personnel become possible at the press of a button; diagnostics and health monitoring become cheaper, faster and more diverse. This is leading to a paradigm shift in global healthcare towards more personalized, de-centralized medical care at the hands of the patient or local medical professional. Technological developments promise more efficient screening for early detection and prevention of disease, monitoring of disease development and treatment efficacy on an individual level and ease of data collection for an in-depth understanding of epidemiological developments and prediction of global and local medical trends.

Point of care devices and lab-on-a-chip systems

Point-of-care (PoC) medical devices or rapid tests are devices that enable the determination of a specific disease or health state in a short time and independent of a laboratory.[2, 3, 4] Their purpose is generally to provide a quick answer about the health state of an individual with regard to a specific condition either, in order to diagnose a disease, to monitor the development or to determine factors that can impact disease outcome. Some well known examples that have been on the market for decades are the pregnancy test that provides a simple yes/no answer and glucose monitors, that empower diabetics to measure their blood glucose levels. More recently, tests kits have become available for HIV rapid testing, providing an alternative to a doctors or health center visit that may be an obstacle for the patient for many different reasons. This can lead to a faster response and commencement of treatment and mitigation of further infections, but further developments are needed for disease management and transfer to developing countries.[5]

On the other hand, numerous home testing kits for a diverse range of molecules (such as vitamins and hormones) as well as mobile phone apps for logging and monitoring of different health parameters have come to market in the recent years, showing the increasing demand for self testing and preventive medical initiatives. While testing at home can often only provide guidelines

and lifestyle recommendations if no medical professional is involved in the decision process, there is a demand for rapid testing for use by trained medical personnel at a clinic or in the hospital. Point-of-care devices in hospital settings provide an alternative to sending clinical samples to a central laboratory where they are processed and the results returned to the doctor. The spatial separation of sample collection and analysis adds logistical challenges to the diagnostic process that can be avoided using point-of-care devices and instruments. It reduces the time to result significantly, lowers the risk of wrong diagnoses due to human error such as incorrect labeling or swapped samples and requires less resources due to a higher degree of automation. While the impact of replacing standard tests with faster bedside alternatives on clinical outcome in high-resource settings may not be significant, the impact on patient well-being during treatment has recently been investigated[6].

The real opportunity for point-of-care devices to have tremendous impact on treatment outcome and disease prevention is in low- and middle-income countries where resources are scarce and central laboratories, if available, are accessible only by a few.[7] However, the requirements for rapid tests, often consisting of instrumentation and disposables or all in one, differ considerably depending on the target application area. For example in low-resource settings or for disaster response instrumentation needs to be rugged and portable and disposables need to be extremely cheap.[8] These variable and challenging operating conditions, political and socio-economic instability in many of the target areas as well as perceived or factual poor economic incentives are yet limiting the development and deployment of game-changing initiatives.[9] Whereas devices for the high end market where tests are performed in a hospital can be more expensive and complex and drive the implementation of novel technologies. This provides opportunities to go beyond the capabilities of current methods, such as advanced and adaptable multiplexing and ulta-high sensitivity.

Requirements and advantages of Point-of-Care devices

In addition to the benefits of a faster time-to-result integrated diagnostic devices usually use only a very small amount of patient sample. Especially for blood tests this can be a huge benefit, for example in intensive care where a large number of tests are required or in neonatal care, where the blood loss is a high burden[10]. Many point-of-care devices therefore focus on the use of blood from a fingerprick as a minimally invasive procedure.[3] The smaller sample volume makes it necessary to develop sensors that are capable of detecting very low amounts of the target molecule. Nanomaterials such as nanowires, carbon nanotubes or similar structures are promising candidates to achieve this very high sensitivity. Due to a high surface to volume ratio, surface-based sensors can benefit from the use of nanomaterials to enhance their efficiency. Examples of this are field effect transistors made from nanowires[11], SERS substrates to enhance spectroscopic signals or the use of nanograss in combination with electrochemical readout to increase the surface area used for detection.

In order for this to be feasible, the integration often requires the storage of biological material

such as labels and antibodies on the chip and care needs to be taken to make sure that the material is functional when the device is used. This poses specific requirements on the storage and transport conditions such as a cold chain or alternatively advanced methods for stabilization that can tolerate more varied conditions. Sample collection and disposal need to be safe for both patient and doctor and can for example be integrated into the disposable part of the device, so that there is no risk of contamination.

Molecular diagnostics: The present and the future

Standard molecular diagnostic methods include Enzyme-linked Immunosorbent Assay (ELISA), polymerase chain reaction (PCR), flow cytometry and mass spectrometry (MS). Most of these require extensive equipment in a laboratory setting but for all of them there are developments in different stages to adapt the technologies for the adoption into point-of-care-devices. The earliest rapid tests were used on some type of immunoassay such as ELISA, a labeled technique with a colorimetric or fluorescent optical readout. Receptors (typically antibodies or aptamers) are immobilized onto a surface such as a standard well-plate or glass slide, the sample containing the analyte is introduced and followed by a blocking step to avoid unspecific binding. In a second step, an Enzyme-labeled secondary antibody that binds a different part of the analyte is introduced, which binds to the now surface bound analyte. In the detection step, a substrate is introduced that is converted by the enzyme and produces a strong color change, the intensity of which is proportional to the amount of analyte detected. The planar platform of the immunoassay had been supplemented with the use of suspension arrays, in which microbeads are used as a support and fluorescent molecules rather than enzymes are used as labels. Analysis is in this case done using flow cytometry described below. The detection limit of ELISA has been pushed down into the fM or even aM regime using beads and microfluidic confinement[12] or nanoparticle generation for calorimetric readout[13], which can compete with some of the more advanced methods based on nanostructures. ELISA is the standard method that is used in many current point-of-care devices due to the flexibility in choices of substrate, markers and detection system that make it a versatile platform. Established calibration routines for individual assays make the readout quantitative, enabling automation in microfluidic devices[14] or larger instruments with passive disposables that can be used without extensive training. A challenge that is partly addressed by suspension arrays is large scale multiplexing. The simultaneous analysis of a large number of markers provides a huge potential for higher accuracy and more specific diagnostic predictions. However, the necessity of preventing cross-reactions between a large number of protein labels is one of the major reasons that these are not yet routinely implemented in addition to more fundamental issues with biomarker identification and clinical validation.

Flow cytometry on the other hand, still requires large expensive equipment and sample preparation methods and needs to be performed by trained personnel, even though development of microfluidic devices for automation of all or part of the process is well under way[15]. The technology uses a small capillary to pass cells or microbeads in a liquid sample individually across a laser beam that then classifies each detection event according to wavelength and intensity. De-

pending on the system up to several different colors (corresponding to fluorescent molecules that are used as labels) can be distinguished simultaneously. This powerful technique can be used in two ways, either as Fluorescence-activated cell sorting (FACS), where cells are counted according to labeled surface markers or in bead based immunoassays. Commonly a panel of several surface markers is used to diagnose or monitor a specific disease state. Statistical data analysis software is used to classify the detection events into categories or clusters (gating), generating a characteristic profile of the panel outcome. The analysis and diagnostic decision needs to be done by trained and experienced personnel.

In addition to these labeled techniques that are the cornerstones of current molecular diagnostics, label-free techniques are still mostly confined to analysis in research laboratories. The challenge with label-free techniques is that the direct detection of analytes relies on their inherent physical properties such as mass, charge or binding energies. Without amplification that can be provided by an (enzymatic) label, label-free sensors need to be highly sensitive in order to detect small amounts of molecules. Except in the case of spectroscopic methods, where binding energies are investigated, the bio-recognition layer is solely responsible for ensuring specificity of the sensor. The advantage is a lack of often expensive labels and the requirement of the labeling step in the sample preparation protocol, promising a faster and cheaper path to detection. To illustrate some of the underlying principles, three relevant methods will be introduced in the following.

Surface plasmon resonance is a well established technique used to quantitatively analyze protein binding. Surface plasmons are collective oscillations of the electrons in a metal surface or interface that are highly sensitive to their environment. A gold film evaporated onto a prism acts as the sensing surface, where resonance energies of the plasmons can be probed with visible light. Upon changes in refractive index at the interface due to density changes as well as electronic contributions, events close to the surface can be monitored in real time. As the recognition layer, a receptor protein is immobilized in a flowcell on the gold surface (other surfaces are also available and used for specific cases). The ligand (protein to bind to the receptor) is then introduced and the time constants of the protein-protein binding kinetics can be studied. This is the standard method to determine association and dissociation constants between proteins on surfaces.

Quartz crystal microbalance is another surface technique in which small changes in mass are measured by the resonance shift in a vibrating membrane. The membrane with the sensing surface (metal or semiconductor) is piezo-electrically actuated while protein is introduced into the fluid chamber. The attachment of proteins to the surface adds mass as well as changes the dissipation behavior by impacting the surface tension depending of the stiffness of the molecules. This method is generally less sensitive than SPR and more often used to analyze polymerization processes and thicker surface films.

As a third example, the charge of molecules attaching to a surface can be used as a means of detection. Changes in the electric field in the vicinity of a semiconducting channel, changes the number of electrons contributing to the current, which can be measured as a change in conductance. These sensors have been around for a while as field effect transistors, used both in

integrated circuits but also as ion-sensitive sensors for chemical measurements. By modifying the surface with receptor proteins, the induced change in conductance can also be used to detect protein binding.

The three discussed label-free sensing technologies benefit from miniaturization and the use of nanostructures. The plasmonic properties of nanoparticles have been extensively used for sensing applications. This then becomes technically a labeled technique, but the principle of operation is similar to that of SPR. Miniaturized devices have been developed for both mass and charge sensing, pushing the sensitivity limit down considerably and opening up new applications for diagnostic methods and integration into PoC devices. The sensor that will be used and discussed in this thesis is a silicon nanowire or nanoribbon based biological field effect transistor.

Biomarkers and multiplexing

In the current era, the systematic understanding of cellular biology and pathway regulation both in healthy and diseased cells is increasing rapidly. The discovery of potential diagnostic markers and drug targets is directly impacted by this. In addition, there are considerable advancements in bottom-up protein design and artificial evolution to generate the complementary targets or receptors. And at the same time, the development of adaptable and highly sensitive sensor systems is laying the basis for quickly implementing new markers into diagnostic devices. These trends, not even mentioning genomic research, are to change the healthcare landscape considerably in the coming decades.

One of the challenges in molecular diagnostics is the identification and verification of molecular biomarkers. Finding proteins, nucleic acids or other molecules that have a predictive function or direct relationship to the state of disease is a very intense field of study.[16, 17] The underlying cellular pathways are extremely complex and we are only just beginning to gain a more systematic insight due to the surge of bio-informatics using super computers and advanced machine learning algorithms. While some diseases are clearly linked with the increase or decrease of certain plasma protein concentrations, others evade detection very efficiently. Classification and identification of tumor types is done by molecular and morphological analysis of tissue samples in order to make prognoses or therapeutic decisions. The knowledge of the underlying molecular mechanisms is undergoing rapid changes.[18] It is the function of the bodies immune system to find and target proteins that indicate the defective state of a cell such as cancer or a viral infection. Many diagnostic methods rely on the detection of antibodies against known disease antigens, especially for viral infections such as HIV. In this way, the amplification of the low detection signal (presence of the antigen on cells) is provided by the immune system through the production of antibodies. Other diseases are more difficult to detect, especially in early stages. Cancers for example, are a class of diseases that are extremely varied in their origin, symptoms and molecular basis. What they have in common is the uncontrolled division of cells causing the growth of a tumor or spreading through the body. While there are numerous cellular mechanisms and functions in our immune system that should identify and repair such damage inside

the cells, or destroy cells that show abnormal behavior, in the case of cancer, these mechanisms fail. In some cases, the cancer cell develops its own mechanism to evade detection, for example by shedding surface markers that would identify the cell as cancerous. While much research is focused on the development of devices that filter and identify cancerous cells from patient blood, these incredibly rare circulating tumor cells (CTCs) are not the only indicator of an early state of the disease. Processes as the one described above lead to increased levels of a specific plasma protein and can have great potential as diagnostic markers.

Understanding the cellular pathways and how they are related to disease states and expression levels of proteins provides us with new biomarkers that can be extracted from a blood sample. These can be both diagnostic or related to the efficiency of a specific type of treatment or related to treatment outcome.[19] The development of highly sensitive protein sensors is therefore a step towards easier and faster diagnostic methods. Due to the complexity of the involved biological processes and their relation to quantitative protein measurements it is imperative to develop sensors with the potential for multiplexing. Being able to measure several markers at once is already the standard for laboratory based diagnostics. Current methods are not only limited by the clinical context; the nature of immunoassays themselves limit the number of proteins that can be contained in an array. This is in part due to cross-reactivity between the reagents that lead to loss of specificity and in part due to limitations in the detection technology and availability of independent labels.[20] By developing label free methods that are based on direct electrical readout, these limitations can be circumvented and the number of proteins can be increased. Transferring this multiplexing potential to the bedside will enable ever more complex diagnostic methods that can provide the relevant information not only for a detailed diagnosis but for personalized therapy development.

This thesis provides a step towards the development of such a technology and investigates the functionalization of field effect transistor based biosensors. The key element that turns a sensor into a biosensor is the bio-recognition element. In a label-free sensor system, this recognition is either achieved using an immobilized probe or receptor that can recognize and bind the target molecule or it is part of the data analysis if the sensor is capable of directly measuring intrinsic molecular properties. Here, we are working with a charge sensor that can detect changes in the surface potential of a semiconducting channel. Since this process is independent of the identity of the attached molecule and averaged across the surface, a specifically tailored bio-recognition layer needs to be established to provide specificity. This layer consists of receptor molecules that can bind the specified target, tethered to the sensor surface by an interface layer. The interface layer serves a very important function, as it is the link between the recognition element and the transducer. It needs to be stable, thin and electrically suitable, so that the surface charge induced potential is transmitted efficiently, without allowing leakage currents. In addition, it can be used to encode multiplexing capabilities if a chemistry is chosen that allows for the selective immobilization using electrically or light activated chemical reactions.

Thesis overview

This thesis is overall structured into introduction, main content and conclusion. The introduction is held rather general giving an overview of the clinical and application context that is the motivation for the research done in this thesis. It introduces the concept of lab-on-a-chip and point-of-care devices and their role in the future of healthcare.

Part one gives an introduction to silicon surfaces and silicon surface chemistry, focusing on different mechanisms for hydrosilylation. This is followed by a chapter on the used experimental methods, explaining X-ray photoelectron spectroscopy and how this is used for surface chemical analysis of organic monolayers. The experimental/results section is subdivided into two parts. The first one covers the initial experiments and findings that were performed on the silicon sensors for the preparation of surfaces for click-chemistry, a method that would enable multiplexing. The second part is an in-depth analysis of organic monolayers on different silicon surfaces to shed light on the mechanisms and reproducibility of the functionalization following the phenomena observed in the first part.

Part two introduces the silicon nanowire field effect transistor as a biosensor and discusses the impact of protein binding using simulations and theoretical analysis. The experimental/results section demonstrates the use of the sensor for protein detection and the role of surface functionalization.

Part three deals with the microfludics and integration aspect of the sensor system. After an introduction of the principle behind microfluidic devices some of the tools are discussed that were used for sample delivery and functionalization. Patient blood sample handling and sensor integration are discussed briefly.

The final chapter provides a synopsis and conclusive discussion of the three separate parts.

I | Functionalization of silicon surfaces for biosensing

2 | Introduction to silicon surface chemistry

The biorecognition element of a biosensor is the vital part that makes a sensor specific and selective. The interface layer, by which the biorecognition event and transducer are in connection is an important factor impacting the quality of the sensor. And while the sensitivity is not solely dependent on the interface layer, it nevertheless plays a very important role to maintain it. This introduction gives an overview of the surface chemistry and analysis methods that were used to investigate this key part of the biosensor system.

2.1 Silicon crystal structure and surfaces

Silicon is the most important material in the semiconductor industry and the primary material used in integrated circuits. The base material for this industry is monocrystalline silicon grown in one of the main crystal directions, so that wafers cut from the crystal typically present the (100) or (111) surface. These highly ordered substrates have very controlled electrical properties that can be tuned by doping with other atoms, which is extensively used in the IC industry to produce different regions for CMOS transistors. However, since monocrystalline silicon cannot readily be grown in additional layers during the fabrication process, polycrystalline and amorphous silicon is used for additional semiconducting or conducting layers where it can be deposited and patterned at will. These materials are especially important for the development of nanoscale biosensors and micro-electro-mechanical systems that are to be integrated with IC circuits in design and fabrication. The crystallinity of semiconductors plays a vital role in determining their electronic properties and is especially important when considering surfaces or interfaces with other materials. While the monocrystalline versions of silicon substrates and features present highly ordered surfaces that may undergo particular reconstruction processes depending on their environment, polycrystalline silicon is naturally less ordered with crystalline grains separated by defect-rich grain boundaries. Polysilicon thus presents different crystal planes in the grains, the size of which depends on growth conditions and other processing parameters, making the surface less uniform on the small scale and electronic properties inhomogeneous.

2.1.1 Oxidation of silicon surfaces

A clean silicon surface exposed to air reacts with oxygen to form silicon oxide or results in the incorporation of carbon contaminants[21, 22]. The oxidation process proceeds readily at room temperature by reaction of surface silicon dangling bonds with dioxygen and subsequent incorporation of oxygen atoms. The structure of surface silicon oxides depends on both the crystallinity of the bulk silicon and the conditions under which it grows. For monocrystalline silicon with (100) or (111) surfaces the native oxide is commonly around 2 nm thick, corresponding to approximately 5-10 monolayers of silicon dioxide. Native oxides are formed in a slow process by spontaneous creation of dangling bonds in air and the quality of such surfaces is rather poor compared to oxides grown under controlled cleanroom conditions due to the incorporation of a large amount of structural defects. Considering the oxidation of polysilicon, structural defects along the grain boundaries that are an inherent part of the inhomogeneous surface, will reflect on the thickness and quality of a natively grown silicon oxide. In some cases, the thickness of surface oxides can exceed that of the monocrystalline counterpart by an order of magnitude[23]. The grown oxide layer naturally leads to surface passivation in terms of electrical conductivity and chemical reactivity. However, defects at the silicon/silicon oxide interface lead to trapped interface charges, i.e. electron energy levels in the band gap of the bulk silicon substrate, resulting in a high surface recombination velocity. The surface recombination velocity is related to the average lifetime of a generated electron-hole pair (or exciton) in the surface and is the usual measure of passivation quality, since defects present scattering centers, where recombination is possible. The longer excited charge carriers are free to move the more they contribute to the conduction of current and the better the passivation. For the sensor surface it is important to reduce the number of traps and the distance to the analyte. One approach is therefore, to remove the oxide completely and rely on a well-ordered organic monolayer for passivation and as the basis for further functionalization. Another approach involves the atomic layer deposition of well-ordered metal oxides to replace the native oxide. In this case, the deposition needs to be followed by the silanization of the surface as in the case of silicon oxide to provide the basis for protein attachment.

2.1.2 Silanization of silicon oxide surfaces

The functionalization of oxide surfaces has many important applications for the immobilization of biomolecules on sensors and other devices since silicon oxide presents a convenient passivation layer for silicon structures that is easily grown or deposited. By oxygen plasma treatment surface hydroxyl groups can be created on the silicon surface, which are unstable in air and react readily with alkoxy-silanes. Since the focus of this study was on oxide-free surfaces, the chemical mechanisms involved in the silanization process have not been studied in detail. Briefly, the alkoxy group is replaced by an hydroxyl group under the generation of ethanol and condenses on the surface, forming Si-O-Si bonds. In presence of an acid (protons) in the functionalization solution, the formation of silane-polymers is facilitated through direct cross-linking. The use of a base, such as Diisopropylethylamine (Hünig's base) can supress this side reaction by binding free protons. Silanes are molecules with a silicon atom in the center and different side groups. Alkoxy-

silanes, which typically contain three methoxy- or ethoxy groups, are available with different functional head groups such as amines or thiols. Different molecules have been used to achieve amino-terminate surfaces (APTES (3-aminopropyl)-triethoxysilane, APDMES (3-aminopropyl)-dimethylethoxysilane or APTMS (3-aminopropyl)-trimethoxysilane are examples).

2.1.3 H-Terminated silicon surfaces

Opposed to oxidized silicon surfaces that form readily under ambient conditions, bare silicon surfaces with free electrons that form dangling surface bonds are highly reactive and unstable. The simplest possible passivation layer for such a surface is a termination with hydrogen atoms, saturating all dangling bonds with hydrogen atoms (H-terminated surface). These can form mono-, di- and trihydrides with surface silicon atoms, depending on the crystal plane and surface reconstruction that may be favored in a particular environment. H-terminated silicon surfaces are reasonably stable in ambient conditions, since the H-Si bond needs to be broken in order to form another bond with oxygen or adventitious carbon from air. Therefore, the H-terminated silicon surface is an ideal platform for subsequent modification with organic molecules due to a vast range of surface modifications routes that are possible from this starting point[24].

2.1.4 Preparation of H-terminated Silicon surfaces and alternatives

Etching of silicon surfaces in aqueous solution containing fluoride ion species readily leads to hydrogen termination after removal of the (native) oxide. Such ion species are hydrofluoric acid (HF) and ammonium hydrofluoride (NH_4F), both of which are highly toxic. Different concentrations of HF or NH_4F in deionized water can be used to etch silicon oxide and create a passivated H-terminated silicon surface. Etching rates as well as the resulting roughness and reconstruction of the surface, especially in the case of Si(100), depend on pH of the solution and the ionic species present in it[25, 26, 27]. Typically, the (111) silicon surface, which presents a uniform spacing of identical silicon atoms in its bare form is etched most efficiently in NH_4F to produce a primarily mono-hydride terminated surface. The (100) silicon surface is constituted of surface silicon atoms in two layers, which leads to primarily di-hydride terminated surfaces when etched in an HF solution. Consequently, etching of polycrystalline silicon surfaces needs to be considered specifically, since different crystal orientations are combined. Generally, the fluoride ion solutions do not attack the underlying pure silicon substrate, even though different doping concentrations and other conditions can lead to pitting and corrosion of the material (see below).

2.2 Grafting of alkenes and alkynes to H-terminated silicon surfaces: Mechanisms

The modification of hydrogen terminated silicon surfaces with organic molecules has been a field of intense research since the early 1990s, when monolayer grafting of alkenes and alkynes assembled on silicon surfaces was first described in analogy to the molecular reaction with silanes.[28] A radical initiator was used to form a dangling bond (silicon radical) on the surface leading to

a radical chain reaction grafting unsaturated hydrocarbons to the silicon surface. Since then a multitude of other methods and further mechanisms have been proposed to describe the covalent grafting of unsaturated hydrocarbons to silicon surfaces, some of which lack an equivalent in the molecular case and are based on bulk properties of the substrate rather than the individual surface molecular structure[29, 30, 31, 32, 33]. The proposed mechanisms involve events such as photoemission and exciton generation, which depend on the semiconductor nature (band structure) of silicon which is a result of the crystallinity rather than the chemical composition of the surface itself. A recent review by Buriak gives a thorough introduction to the involved mechanisms in the case of photoactivation[34].

The following presents an overview of the different mechanisms that have been suggested and demonstrated to be involved in the formation of carbon monolayers on H-terminated silicon surfaces. Depending on the conditions of the functionalization experiment, one or several mechanisms can be involved in the grafting process as will be discussed in the results section.

2.2.1 Radical initiator mediated and radical chain reaction

In their initial work Linford and Chidsey used alkyl radicals produced by thermal decomposition of diacyl peroxides to generate a tightly packed monolayer of covalently bound hydrocarbons on silicon surfaces.[28] They proposed a mechanism proceeding through the formation and reaction of several radicals. The initially produced alkyl radical abstracts (removes) a hydrogen atom from the H-terminated silicon surface leading to the creation of a silyl radical in the surface. Subsequently, this radical can either form a covalent bond with another alkyl radical or break apart another diacyl peroxide and incorporate one of the acyloxy fragments via a carbonyl bond. Later work showed that using a majority of terminal alkenes and alkynes with a small proportion of radical initiators such as diacyl peroxides leads to more stable monolayers due to direct incorporation of the carbon chains via Si-C bonds and fewer, less stable carbonyl bound species. Both reactions described above are performed at elevated temperature (100°C) to decompose the peroxide into its radical fragments. At even higher temperatures, the thermal energy is sufficient to break the strong Si-H bond and create surface dangling bonds without the use of a radical initiator.[30] Hydrosilylation by thermal activation proceeds at temperatures above approximately 150°C. Homolytic cleavage of the Si-H bond in the presence of terminal alkenes or alkynes leads to the incorporation via Si-C bonds. The silyl radical binds to the α-carbon transferring the electron to the β-carbon of the double bond. It could be shown that the initial formation of a dangling bond on the silicon surface is likely to initiate a radical chain reaction: The first created silyl radical leads to the incorporation of an alkene or alkyne containing a secondary carbon radical. This radical can in turn abstract a neighboring hydrogen from the surface leading to another reactive dangling bond for further attachment. The process is schematically shown in Figure 2.1a).[35]

2.2.2 Thermal activation and Lewis acid mediated reaction

Another common method for hydrosilylation in solution that is prevalent in organic chemistry is using Lewis acid mediated reactions and transition metal catalysis as illustrated in Figure

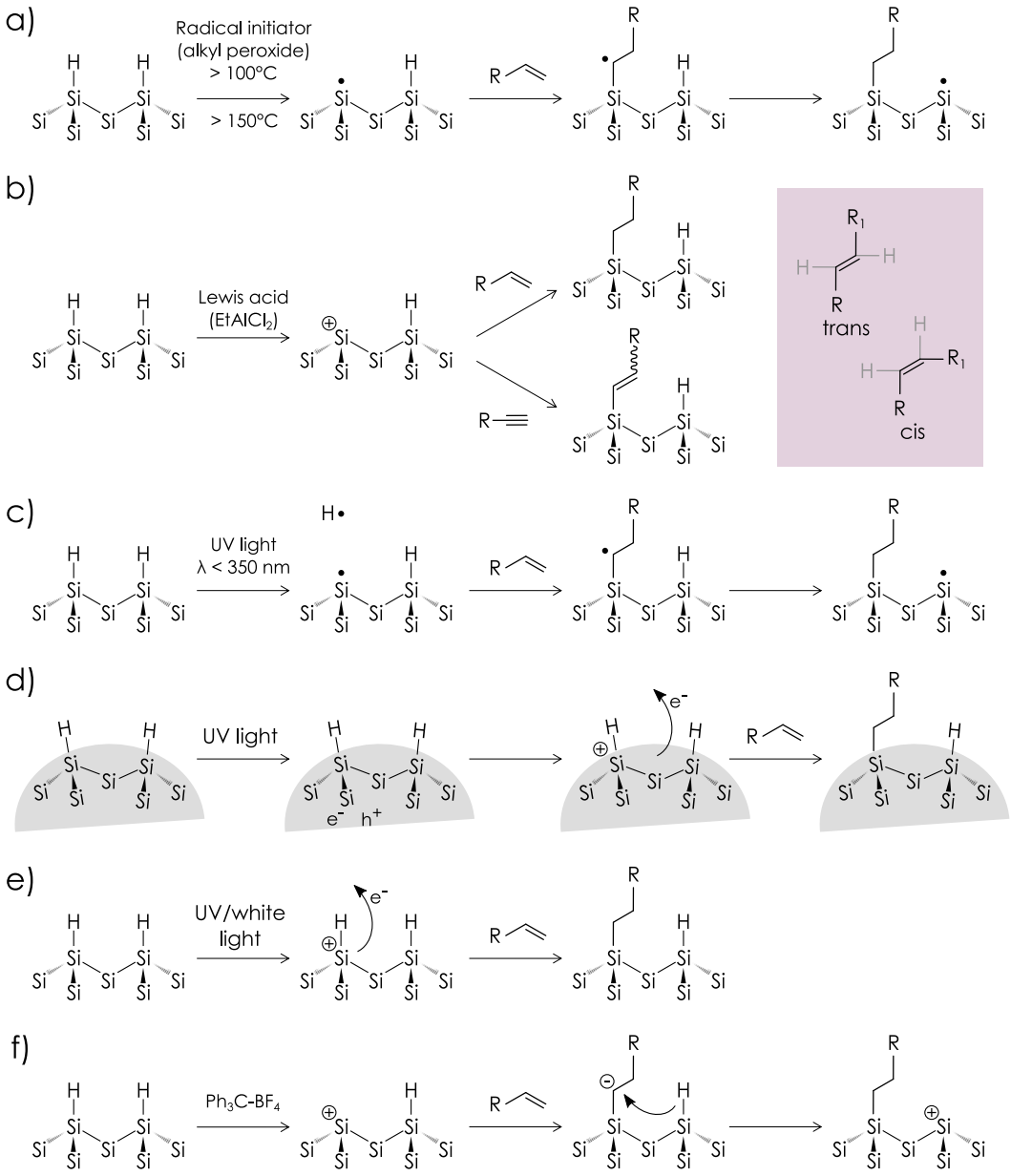

Figure 2.1 Different mechanisms responsible for the attachment of alkenes and alkynes to silicon surfaces. a) Radical chain reaction (w/wo initiator) b) Lewis acid mediated reaction c) Photo-initiated hydrogen desorption d) Exciton initiated mechanism in nanocrystalline silicon (nucleophilic attack) e) Photoemission initiated mechanism f) Grafting by hydride abstraction (radical mechanism)

2.1b). The acidic molecule (such as AlCl3 or EtAlCl2) accepts an electron pair from the alkene or alkyne, binding to one of the carbons while removing a hydride ion from the surface Si-H bond to bind to the second carbon. The resulting silyl ion subsequently replaces the Lewis acid covalently binding the carbon chain to the silicon atom. This reaction with alkenes yields different proportions of cis- and trans- bound compounds. Due to π-orbital in the double bond, the carbon molecule has no rotational symmetry with respect to the two other silicon bonds and each case is specified as either cis- or trans- as shown in the inset in Figure 2.1. In order to produce densely packed monolayers with good passivation properties it is important to consider the orientation of the molecules and location of their attachment since some may lead to steric obstruction of neighboring sites. It has been found that silylation on surfaces primarily results in α-bound carbon chains instead of a β-silylated branched structure.[36] On surfaces, Lewis acid mediated hydrosilylation has been demonstrated to yield stable and uniform monolayers using EtAlCl2 and several different alkenes as well as alkynes.[37]

2.2.3 Photo-initiated radical mechanism

Photoinitiated grafting of alkenes and alkynes to silicon surfaces was first reported by Cicero, Linford and Chidsey in 2000.[32] In this process, the photon delivers the energy to remove a hydrogen atom from the H-terminated silicon surface creating the surface silicon dangling bond shown in Figure 2.1c). This electron can react with either oxygen or unsaturated carbons to form a peroxy radical or a Si-C bond with a secondary carbon radical. The efficiency of the initial removal of hydrogen is wavelength dependent and has been reported for wavelengths below 350 nm. The estimated approximate energy of Si-H bonds on silicon surfaces (in the monohydride terminated Si(111) surface) is 3.4-3.65 eV which roughly corresponds the the energy of photons at a wavelength of 350 nm (3.54 eV). For the Si(100) surface, which presents asymmetric inter atomic distances and two hydrogen atoms per silicon in the saturated surface (di-hydride termination) the energy needed to remove one hydrogen and the activation energies for the attachment of terminal unsaturated carbons is expected to be lower due to the additional hydrogen bound to the surface silicon atoms. In addition to activation by ultra-violet light, white light has also been shown to have an effect that can not be explained by this process (see below).

2.2.4 Exciton initiated mechanism in nanocrystalline (such as porous) silicon

Nanocrystalline materials show some unique electronic properties over their monocrystalline counterparts due to quantum confinement. This can play an important role for the chemical interaction with a nanocrystalline surface, due to the involvement of plasmons or excitons that alter the electronic properties of the interface. Porous silicon is generally considered a nanocrystalline material due to the small pore size of the etched structures and can be characterized by its resulting electronic properties. In some cases the material shows photoluminescence, a process that involves the generation of an exciton, a coupled electron-hole pair, in the surface by an impinging photon and subsequent re-emission of a photon with shorter wavelength after the recombination of the electron-hole pair. Due to quantum confinement in the nanostructured material these excitons have a much higher energy than in bulk silicon, which increases their

lifetime significantly. This exciton generation has been suggested to play an important role in the surface functionalization of porous silicon surfaces by white light irradiation[29]. A long-lived positive charge that is created near the surface makes surface silicon atoms available to nucleophilic attack by the terminal alkene or alkyne[36] as shown in Figure 2.1d). Using oxidizing agents in the functionalization solution that scavenge the generated electron and increase the life time of the generated positive charge have shown to additionally increase the grafting efficiency and overall yield of the reaction and confirm the exciton involvement in the process[38]. This reaction, which seems to be unique to nanocrystalline silicon (both as crystalline particles and on surfaces), illustrates the importance of considering substrate involvement when studying surface chemical reactions.

2.2.5 Exciton or photoemission mediated mechanism on flat silicon surfaces

After hydrosilylation was reported to proceed by white light illumination even on flat silicon surfaces, it was suggested that an exciton or phonon mediated mechanism is at play here as well[39, 40, 41]. Since excitons in monocrystalline silicon have a low binding energy and short life-times compared to those in nanocrystalline silicon it is improbable that the reaction proceeds in the same way. The time needed to obtain a comparable coverage with 1-alkenes is significantly higher, with several hours required for completion rather than minutes in the case of porous silicon. In addition, the doping concentration has an impact on the reaction rate and overall yield of the attachment, whereas in nanocrystalline silicon photoluminescence was the sole requirement without significant dependence on the doping type or level. After experiments performed on iodine terminated surfaces suggested the involvement of photoemission as the driving force behind the positive charge generation in the surface[42] as illustrated in Figure 2.1e). Further experiments on hydrogen terminated surfaces support this proposition of a new mechanism, however performed using shorter wavelengths[43]. The dependence on dopant concentration does suggest the involvement of minority carriers in the surface as the primary source of positive charge, since pinning of the Fermi level at the surface and subsequent band bending would lead to accumulation and depletion of positive charge in n- and p-type sample respectively. Photoemission as a mechanism cannot be ruled out for porous silicon, since long illumination times were not examined and at short times the exciton mediated process seems to clearly dominate the attachment. However, at longer illumination times, dependence on dopant concentration or rather a substantial grafting efficiency might still be observed for non-photoluminescent samples if photoemission plays a role.

2.2.6 Hydride abstraction initiated mechanism

Removal of the hydride termination of a silicon atom in the surface by chemical abstraction, i.e. removal of a hydrogen atom by a radical, will result in a positive charge located at the silicon atom making it available for attachment of unsaturated carbon molecules. Stable carbocations such as Triphenylcarbenium are able to abstract a hydride ion from silyl compounds in molecular form[44, 45, 46] and this mechanism was transferred to silicon surfaces to create hydrocarbon monolayers[33]. The self-assembly of thus initiated layer formation is proposed to propagate via

abstraction of a neighboring hydride by the created β-silyl carbocation. The process is shown in Figure 2.1f). The method was first tested on porous silicon under ambient conditions but was proposed to not be limited to nanocrystalline silicon due to evidence that the reaction does not rely on exciton generation. The use of controls with radical inhibitors further rule out a mechanism based on a radical chain reaction in this case.

2.2.7 Differences in the grafting of alkenes and alkynes

There are important differences in the formation of alkyl and alkenyl monolayers on H-terminated silicon.[47] For one, the maximum obtainable surface coverage using 1-alkenes (50-55%) is lower than the corresponding coverage for 1-alkynes (65%)[48, 49]. For modification using elevated temperatures or UV irradiation, the differences in reactivity of the two groups is not immediately apparent, since an excess of activation energy and commonly long reaction times have been studied. However, an investigation by Scheres et al. showed that under mild conditions, such as in ambient light or in the dark, 1-alkynes are considerably more reactive towards H-terminated silicon than 1-alkenes[50]. This has also been found for the Lewis acid mediated reaction, where dense layers with alkene could only be obtained after reaction times of the order of 12h versus less than 1 h for a similar process using alkynes.[51] In ambient conditions, no completion of the densely packed partial monolayer can be found even for very long reaction times and the resulting surface layer remains unordered. In contrast, the use of UV irradiation leads to completion of the reaction for 1-alkenes after several hours resulting in self assembled layers of similar quality to those obtained with 1-alkynes through white light illumination[41].

2.3 Surface characterization using X-ray photoelectron spectroscopy

For the detailed characterization of the modified surfaces, x-ray photoelectron spectroscopy (XPS) is a common method that is highly surface sensitive. Due to the necessity to average over an area of at least 50 μm, this technique can not be used to characterize the sensor chips directly. We decided to perform detailed studies on larger pieces of the same surface material first and the transfer the protocol to the sensor chip for electrical confirmation.

2.3.1 Operation principle and experimental setup

XPS is a spectroscopic technique that uses electrons emitted from a sample due to irradiation with x-ray photons. The thus emitted electrons are called photoelectrons and their kinetic energy is detected using a monochromator which filters out electrons of a specific energy and a detector which counts the number of electrons. Aluminum or magnesium targets are typically used as x-ray sources to produce photons of sufficient energy to remove electrons bound in the core levels of atoms in the sample surface. The binding energy E_B of these electrons is unique and can be used to identify the element that the electron originates from and can be calculated from the measured kinetic energy E_K as follows:

$$E_B = h\nu - E_K - \phi \tag{2.1}$$

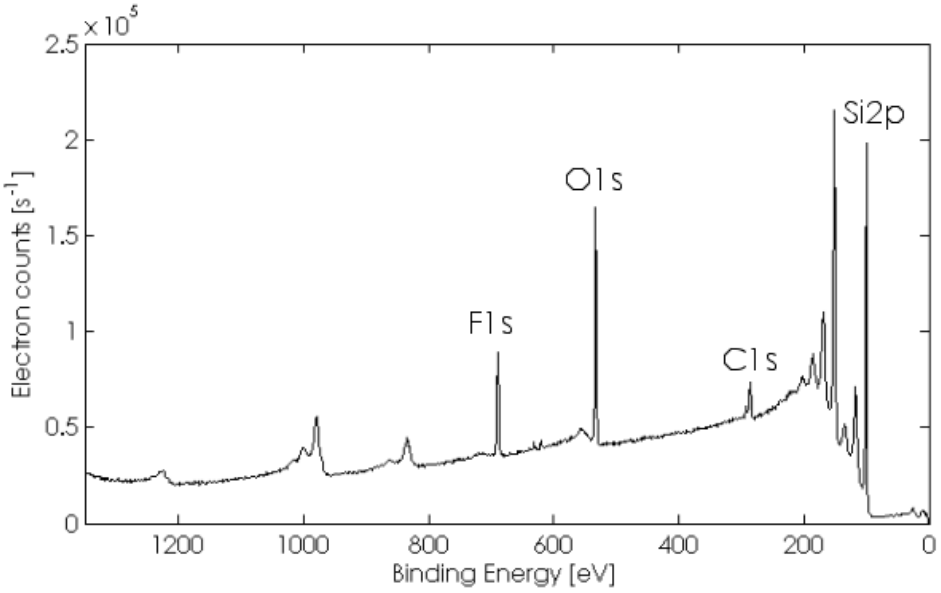

Figure 2.2 Example of an XPS survey spectrum from a silicon surface modified with perfluoro-dec-1-ene. The most prominent peaks to the right, at the low energy end of the spectrum, show the Si2p electrons of the silicon substrate

where $h\nu$ is the x-ray photon energy which depends on the used source and ϕ is the work function, i.e. the energy needed to expel an electron from the solid. An example of a survey spectrum (from a silicon surface functionalized with perfluoro-1-decene) is shown in Figure 2.2, where different peaks can be assigned to different elements present in the sample. The binding energy of each core electron determines the position of the peak in the spectrum, whereas the intensity and width of the peak depends on several factors, which will briefly be discussed here and in more detail later with the quantification of the spectroscopic data. The area under the peak corresponds to the total count of electrons from that particular element and is an indication for its abundance in the samples. However, the scattering cross section, i.e. the probability with which a photon will interact with the electron and eject it from its position influences the relative abundances of electrons across the spectrum. Furthermore, absorption of photoelectrons in the material leads to attenuation of the emerging signal the further away from the surface its origin is located. This effect is additionally energy dependent and characterized by the so-called inelastic mean free path (IMFP). This parameter has been studied intensely both experimentally and theoretically and both empirical formulas and tabulated values can be found to estimate it.[52, 53] Finally, the used sensor system (source, monochromator, detector and angles) result in an instrument specific transfer function that needs to be considered. In carefully considering all the involved parameters it is possible to determine the elemental composition of the sample to within a certain accuracy that also depends on the resolution, size of the sampled area and sample quality. For some elements where the overall sensitivity is high, abundances below 1% can routinely be quantified whereas other elements are more difficult to detect.

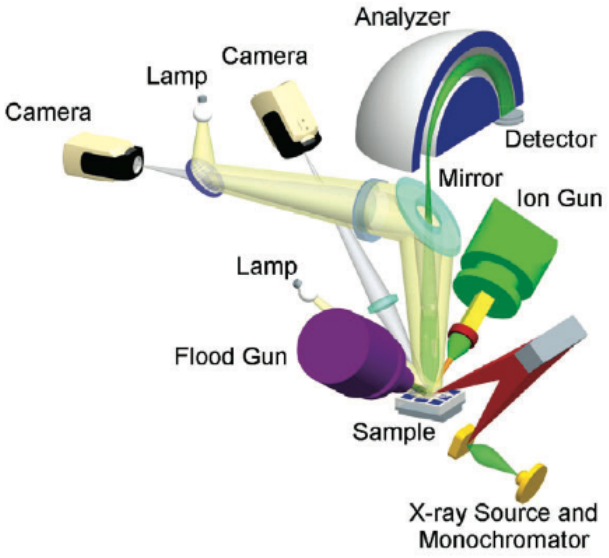

Figure 2.3 Configuration of the detector system of the K-Alpha XPS system. (Image source: Thermo Scientific)

Chemical shift

The binding energy of an electron also depends on the oxidation state of the atom, meaning the chemical environment in which it is bound. This is the reason for a so-called chemical shift, a small shift in binding energy, that allows the assignment of electrons with shifted energies to different chemical bonds. In addition to the survey spectrum discussed above, which is typically recorded using a low energy resolution, high resolution spectra are recorded in specific energy regions of interest. The energy range that corresponds to a specific core level energy and encompasses its possible chemically shifted side peaks are well defined and the HR spectra denoted accordingly as C1s (for Carbon 1s electrons), Si2p (for Silicon 2p electrons) etc. Small shifts of the whole spectrum due to charging effects induced by the constant depletion of the surface of electrons are usually corrected for using a peak common to all samples as a calibration point. For example, the 1s electron of a carbon atom that is bound to another carbon in the backbone of a hydrocarbon chain by a symmetrical non-polar bond will have a binding energy of approximately 285 eV. This form of carbon is typically present as contamination on all surfaces and can thus be used for calibration. If the carbon is bound to oxygen or nitrogen, which are both more electronegative than carbon, the binding energy of the core electron will show a positive shift due to the withdrawal of valence electrons. The more electronegative an atom in the vicinity of the detected element, the larger is the positive chemical shift. This can be understood in terms of the Coulomb interaction between the electron with the positive core and the electron cloud surrounding it. The higher the oxidation state of the atom, the less electrons are screening the positive core, thus the binding energy is higher (in most cases).[54]

The XPS system

For all XPS analysis done in this work the K-Alpha^{TM}X-ray Photoelectron Spectrometer by Thermo Scientific^{TM}was used. The system is equipped with a monochromated Al K-alpha x-ray source that produces x-rays with an energy of 1486.68 eV and a beam spot size that can be set between 30 - 400 μm. The detector is a double focussing hemispherical analyzer with an energy detection range between 100 - 4000 eV. It further provides a flood gun that can be used for charge compensation of the sample, which was always used. The setup is illustrated in Figure 2.3. For all experiments the maximum spot size of 400 μm was used; the spot size refers to the length of the major axis of the elliptical spot. For the survey spectra an energy range from 136.6 eV up to 1496.6 eV with a step size of 1 eV and a dwelling time of 50 ms. The high resolution spectra were recorded with a resolution of 0.1 eV and a dwell time of 50 ms.

3 | Experimental Methods and Analysis

This chapter gives an overview of the methods and analysis techniques used for the functionalization of surfaces and sensor chips. The experimental procedures are described in a general way, the detailed protocols to each experiment discussed in the following two chapters can be found in the Appendix (the references are mentioned in the respective section).

3.1 Grafting of Alkenes and Alkynes to H-Terminated Silicon surfaces 2: Experimental procedures

The grafting mechanisms described in the previous chapter can be used to modify silicon surfaces under specific conditions. The methods described here were chosen due to different criteria. Initially, no appropriate equipment for controlled surface chemical reactions was available to us, and experiments focused on investigating the process under ambient conditions and in UV light.

3.1.1 Materials

Molecules used for hydrosilylation

1. Alkenes:
    - 1-Octene (Sigma-Aldrich)
    - 10-N-Boc-amino-dec-1-ene (abcr)
    - 10-Undecenoic acid (Sigma-Aldrich)
2. Alkynes:
    - 1-Octyne (Sigma-Aldrich)
    - 1,7-Octadiyne (Sigma-Aldrich
    - 10-Undecynoic acid (Sigma-Aldrich)

General equipment

Desiccator A glass vacuum desiccator was used, equipped with a top valve that allowed for the switching between vacuum and nitrogen lines in order to flush and purge the chamber in the fume cupboard.

Light bulb For all experiments involving exposure to white light a 60 W standard light bulb was used, mounted into a desk lamp that could be moved into the fume cupboard.

Photoreactor The commercial photoreactor Stratalinker 2000 was equipped with a 254 nm UV light source and no ventilation for temperature control.

Glove bag To perform experiments in inert atmosphere, a glove bag (AtmosBag - size S from Sigma-Aldrich) was equipped with valves for nitrogen and vacuum lines and used as a test setup.

Glass syringes For the silanization reaction, two dedicated glass syringes were used (50 μL and 200μL) to transfer the reagents.

Hot plate and stirrer An IKAMAG hotplate stirrer was used, equipped with an external temperature sensor to adjust the solution temperature.

Custom equipment

Homebuilt photoreactor The photoreactor was equipped with soft UV light tubes (>350 nm) that illuminate a drawer on which the samples can be placed. A ventilation system enabled a certain degree of temperature control of the environment during operation.

UV sample holder In order to ensure a closed environment (e.g. with exclusion of oxygen) a sealed reaction chamber was build. The bottom part consisted of a support made from Teflon that contained 4 separate chambers for 3 silicon substrates each. The lid was fabricated from COC which has a high transparency in the ultraviolet region compared to glass and other plastics and good chemical resistance. Holes in the lid made it possible to close the chamber with screws, sealing the lid against Teflon flanges around the chambers.

Glove bag environment For functionalization inside the glove bag, a setup was build to facilitate the performance of experimental steps. As the need for gloves makes the handling of small components increasingly difficult, reverse tweezers were used for holding of the surface samples and all smaller equipment was fixed onto a polycarbonate support plate that was placed on the bottom of the bag.

Argon line surface chemical setup For the experiments performed by thermal activation in argon atmosphere, a home built surface chemical setup was used. The setup was built into a fume cupboard and consisted of vacuum and argon lines connected to the tubing network, equipped with a cold trap to filter out any residual water or reagents circulating in the system.

3.1.2 General Procedures

Etching of silicon surfaces to remove surface oxides

To remove the surface native oxides from different silicon samples different aqueous solutions of hydrofluoric acid (HF) or ammonium fluoride (NH_4F) were used. All procedures with these highly toxic chemicals needs to be carried out in a fume cupboard and while using additional chemical gloves. Any spills need to be monitored and removed immediately to avoid accidental exposure. The solutions were stored in and amount of maximally 600 μL in a 1 mL eppendorf tube and re-used. For etching, the tube was opened, the substrate inserted for the specified amount of time and then removed with reverse tweezers. The sample and the part of the tweezer in contact with the solution were immediately thoroughly rinsed with a stream of MilliQ water and dried under a flow of nitrogen.

Thermal activation under argon atmosphere

For hydrosilylation by thermal activation, the alkene or alkyne was placed into a Schlenk tube, degassed using 3 freeze-pump-thaw cycles and stored under argon. The surface samples were etched, to remove the oxide layer and dried under a stream of nitrogen before introducing them into the liquid reagent under argon atmosphere. They were kept there at 150 °C for the specified time. After the functionalization process, surfaces were rinsed in chloroform 3 times and sonicated twice in chloroform to remove physisorbed material. Until samples were transfered into the vacuum in the XPS analysis chamber at the end of the experiment they were placed into sealed tubes filled with nitrogen.

UV and white light irradiation

To carry out hydrosilylation using photoactivation, one of three light sources could be used. Surfaces were exposed to either 254 nm UV light in the commercial photoreactor, soft UV light in the home built photoreactor or white light from the 60 W light bulb. For experiments in ambient light or in the dark samples could additionally be placed under nitrogen atmosphere in the desiccator for the duration of the functionalization procedure, this was not possible in combination with the other light sources. Instead, the home built sample chamber was used to reduce exposure to oxygen during functionalization in this case. Surfaces were placed into the reaction chamber directly after etching, covered with reagent and in some cases a glass coverslip and the chamber sealed by tightening the screws.

Silanization of oxidized silicon surfaces with (3-aminopropyl)triethoxysilane

The silicon oxide surface was first cleaned in ethanol and dried in a stream of nitrogen before being activated by oxygen plasma to obtain an OH-termination. This surface is highly reactive and will quickly degrade in air. Therefore, samples were placed in absolute ethanol immediately after activation. The samples were then placed in a glass vacuum desiccator on a hotplate

at 60 °C with connected vacuum and nitrogen lines. With dedicated glass syringes, 20 μL (3-aminopropyl)triethoxysilane (APTES) and 50 μL N,N-diisopropylethylamine were placed in two small dishes next to the samples inside the desiccator. The desiccator was then evacuated and flushed with nitrogen 3 times and then kept at low nitrogen overpressure continuously for 1 h. At the end of the procedure the temperature was increased to 110 °C for another 10 minutes. The samples were removed from the functionalization desiccator and stored either in an evacuated desiccator or in methanol until characterization or further processing.

3.2 Fabrication of test structures for the characterization of surface modification steps

Characterization of the surface modification steps on the silicon nanowire sensors is not possible using standard surface characterization techniques such as XPS or FTIR due to the small footprint of the active device area. In order to gain insight into the different modification steps it is necessary to test these on larger test structures that can be characterized more easily. However it is important to keep in mind that the test structures need to resemble the materials and dimensions used in the actual device in as far as these might impact the functionalization process. This is necessary to be able to compare the obtained results and be able to transfer the process. The materials that are used and will be exposed to functionalization reagents and conditions in the nanowire sensor chip are polysilicon as active material, thermally grown silicon oxide as substrate as well as the bulk monocrystalline silicon substrate. Test chips were designed in the same size as the sensor chips, containing the three materials, identical to those used on the device, both as extended surfaces for contact angle and XPS measurements and as smaller features that make it possible to investigate the materials in close proximity using microscopic techniques. Gold was not included as a material, since this should be fully covered by the passivation layer in the final device and leads to complications if not. The layout of the test chip is shown in Figure 3.1. A custom fabricated SOI wafer (made by Azeem Zulfiqar according to the process described in [55]) was used as a starting point. It consists of a 4" Si(100) wafer as a substrate with an approximately 200 nm thick thermally grown silicon dioxide layer and a 50 nm thick Boron doped (p-type) layer of polysilicon with an approximate grain size of 50-100 nm. The fabrication process involves 2 photo-lithography steps to define a first etched pattern in the polysilicon layer to expose the silicon oxide surface and a second pattern in the silicon oxide to expose the Si(100) substrate. In this way, the test substrate contains 3 different surfaces that can be functionalized simultaneously and analyzed individually. The layout is shown in the right part of the diagram and modeled after the layout of the silicon nanowire BioFET sensor with electrodes and identification number in the top part.

In addition to the open areas for contact angle and averaged XPS measurements, the test chip contains polysilicon electrodes (surfaces that are connected to contact pads that fit a 10-pin ZIF-socket) for electrochemical experiments. Two electrodes of the same surface area are located at the bottom of the chip for easy immersion into a liquid cell with connected electrodes. The other polysilicon structures are also connected to contact pads to provide a set of electrodes with

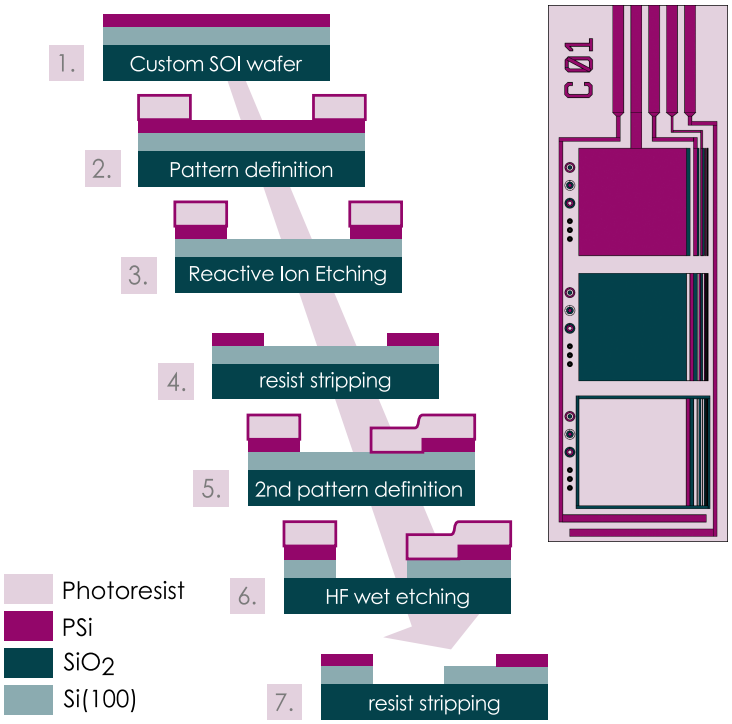

Figure 3.1 Process outline of the cleanroom fabrication process and layout of the test substrate fabricated for characterization of the functionalization process on different materials/surfaces.

different and defined surface areas. Since the monocrystalline silicon surfaces are exposed areas on the bulk substrate, no individual electrodes are defined here. The backside of the chip is composed of the same SOI configuration of polysilicon on a silicon dioxide layer. The details of the fabrication process can be found in the Appendix in C.1.

3.3 Quantitative analysis of XPS data

Obtaining quantitative information about organic monolayers on silicon surfaces is not an easy task and many models and analytical approaches have been developed to quantify spectral data[56]. In addition to the different scattering cross sections and machine parameters that determine the so-called atomic sensitivity factor, the presence of the surface layer itself has an impact on relative electron counts. The attenuation lengths, or inelastic mean free path (IMFP), of different core electrons in the organic layer or other thin surface films need to be estimated in order to quantify the elemental composition of the sample surface accurately. In the following, the methods are presented that have been used in this work to obtain an estimation of the monolayer coverage and oxide thickness for silicon samples with thin carbon films. For the full derivation of the formulas in this section please refer to the Appendix B.1.

3.3.1 Quantification of thin carbon films on silicon surfaces using a surface-overlayer model

The derivations and formulas described in this section are adapted from [57] and [58]. The model assumes an a substrate such crystalline silicon and an overlayer, which is an adsorbed layer on top of the substrate that exhibits a different order and/or composition as the underlying material. The following formula is used to determine the overlayer thickness, in case of a thin film. Here, thin refers to a thickness that falls well within the analysis depth of the method used, for XPS this is typically a few nanometers.

$$d_{ov} = \sin\theta\lambda \ln\left[\left(\frac{I_{ov}}{I_{Si}}\right)\left(\frac{SF_{Si}}{SF_{ov}}\right)\left(\frac{\rho_{Si}}{\rho_{ov}}\right)\right] \tag{3.1}$$

Hereby were are considering the integrated peaks of the substrate (Si) and overlayer (ov) electron energy spectral peaks (I) together with the respective atomic sensitivity factors SF[59] and approximate densities of the two materials. To estimate the number of molecules in the surface the following equation for the number density per surface area was adapted from [43]:

$$N_C L = \frac{\rho_{Si}}{\sigma_S i}\alpha\lambda_{SiSi}\frac{SF_{Si}}{SF_C}\frac{I_C}{I_{Si}}\ln\left(\frac{I^0_{Si}}{I_{Si}}\right)\frac{I_{Si}}{I^0_{Si}}\left(1-\frac{1}{1-\frac{I_{Si^0}}{I^\alpha_{Si}}}\right) \tag{3.2}$$

where ρ_{Si} is the bulk density of monocrystalline silicon, λ_{SiSi} is the attenuation length of Si2p electrons in silicon, SF denotes the atomic (modified Scofield) sensitivity factors[1]. α denotes the ratio between attenuation lengths of Si2p and C1s electrons in the carbon overlayer and was taken from [43] to be estimated as 1.131 with an uncertainty of 0.002 for varies types of carbon layers. $N_C L$ is thus the number of atoms in the surface overlayer N_C times the film thickness L. Since it is not possible to separate the two parameters unless the thickness is well defined and measured separately, the number of molecules per surface silicon can be estimated by division by the surface density of silicon atoms $\sigma_S i$. This is included in Equation 3.3.1. The surface density of the silicon surface for Si(111) is 7.8 nm^{-2} and for Si(100) it is 7.5 nm^{-2} considering all surface atoms. If only the top layer of silicon atoms is considered in Si(100) this value drops to 3.75 nm^{-2}, which might be more suitable in the case of fully reconstructed dihydride terminated Si(100) surfaces. For polysilicon samples the value of 7.8 nm^{-2} was used due to the etching behavior that resembles that of a Si(111) surface rather than Si(100). For better comparison of the results, the higher surface density was used for the Si(100) surface as well.

Using the high resolution spectra of elements other than carbon may be more convenient in the case where these are typically not present in other parts of the sample and provide therefore unique evidence for the presence of a particular molecule. The N1s spectrum has been used in this way to assess the presence and quantity of 10-N-BOC-dec-1-ene and 3-Amino(propyltriethoxysilane), which each contain a single nitrogen atom in their structure.

[1] The factors were obtained from the Thermo Avantage software library supplied with the K_α X-ray photoelectron spectrometer

3.3.2 Quantification of surface oxidation on silicon surfaces

For the quantification of the thickness of silicon oxide in the surface a simple substrate overlayer model similar to the one presented above was used as described for example in [60]. As opposed to the method described for estimation of carbon overlayers, the O1s high resolution scan is not suitable to estimate the silicon oxide thickness, due to the presence of oxygen in other components of the surface such as carbon contaminants and the grafted hydrocarbon layer itself. Therefore, the amount of silicon oxide is estimated from the ratio between the Si2p peak assigned to Si covalently bound to O (generally Si-O_2, but other oxides such as Si_2O_3 and Si_3O that are slightly shifted in energy can also be found in the sample and are included in the silicon oxide count).

$$d_{ox} = \lambda_O \sin\theta \frac{\ln\left(1 + \Gamma^0_{SiO}\frac{I_O}{I_{Si}}\right)}{t_{SiO}} \tag{3.3}$$

where θ is the collection angle as above (0°). $\Gamma^0_{SiOx} = I_{Si-H}/I_{SiO2}$ is a normalization factor that accounts for the difference in sensitivity for electrons obtained from silicon oxide and surface silicon, estimated from the ratio between the signals obtained for fully H-terminated and fully oxidized reference surfaces. This ratio was calculated as approximately 1.2, which deviates from the value obtained by Pomykal *et al.*[60] by 0.1. I_{SiOx} and I_{Si} are the integrated peak areas for the Si2p Si-O peak and the Si2p spin doublet respectively. The monolayer thickness for stoichiometric silicon dioxide t_{SiO} = 3.6 Åwas used to obtain the number of monolayers. It should be noted that XPS is not suitable to detect lateral inhomogeneities in the surface and as such to determine whether or not the detected silicon oxide is actually present in form of a homogeneous layer or in form of islands.

3.4 Other methods for surface characterization

3.4.1 Contact angle measurements

Surface characterization by measurement of contact angles can be a complex task. The contact angle between a liquid droplet on top of a solid surface in a solid-liquid-vapor system is determined by a number of factors, in the simplest case the surface free energies of the interfaces. Governed by the Young-Dupre equation

$$\cos\theta = \frac{\gamma_{lv}}{\gamma_{sv} - \gamma_{ls}} \tag{3.4}$$

Contact angle measurements were done using a drop shape analyzer and drop shape analysis software. Typically 2μL droplets of MilliQ water were dispensed on a surface and the left and right angles were determined continuously using the sessile drop method and a Tangent model for fitting of the angles.

3.4.2 Fluorescence microscopy

An Olympus fluorescence microscope equipped with a Xenon broad spectrum light source and a cellSense black and white camera was used to take all fluorescent images. Beside brightfield and differential interference contrast, filters were available for Texas Red (ex. 596 nm, em. 620 nm), FITC (green) (ex. 490 nm, em. 520 nm) and DAPI (blue) (ex. 372 nm, em. 456 nm). Image processing such as extraction of area histograms or line profiles was done using ImageJ v1.46r.

3.4.3 Atomic force microscopy (AFM)

AFM images were taken with a XE150 (Park Systems, Korea) using XEP Version 1.7.70 for operation of the microscope. An Al coated tip with a force constant of 40 $^{\mathrm{N}}/_{\mathrm{m}}$ and a nominal resonance frequency of 300 kHz (Budget Sensor, Bulgaria) was used in non-contact tapping mode with a scanning frequency of 0.5 or 1 Hz. Scanned areas range from 0.5 x 0.5 μm^2 to 5 x 5 μm^2 with resolutions between 128 and 512 pixels. For image processing and statistical analysis XEI version 1.8.0 software and the open source software Gwyddion were used. Images were corrected for tilt using a linear fit along the X and a 3rd order polynomial in the Y direction using the whole image for most images. For some images a line-wise fit along the X direction resulted in better results images, which was then used instead. Statistical analysis to obtain root mean square surface roughness and peak-to-valley distance as well as other feature information was obtained for each image as a whole and on individually selected regions to exclude nanoparticles. Line profiles were taken in X or Y direction and statistical analysis was performed automatically.

4 | Surface preparation for Click-chemistry

Copper assisted Alkyne-Azide cycloaddition (CuAAC) as a method for protein immobilization on biosensors is a promising method to implement a flexible sensor platform. This chapter explores the possibility of implementing a functionalization scheme to modify oxide-free silicon nanowire surfaces to create an alkyne terminated surface, the starting point for the CuAAC reaction. Such a platform would enable further investigation of the click reaction itself to investigate electrical means of activation for targeted, localized immobilization for multiplexing and other means of creating an adaptable platform that can readily be prepared with proteins before use. The initial experiments and results presented in this chapter lead to the conclusion that further detailed investigation of the intermediate layer is required and does not include discussions of the sensor functionality. While this chapter already deals with the silicon nanowire sensor as a substrate for functionalization, the following chapter returns to the investigation of unstructured surfaces. This follows the chronological progression and is necessary to understand the motivation behind some of the decisions that follow. The second part of the thesis will return to the sensor system and introduce the functionality of the biosensor and discusses protein sensing.

4.1 Surface functionalization with 1,7-octadiyne

A promising molecule to use for the direct modification of oxide-free silicon sensor surfaces is the symmetric 1,7-octadiyne, with two terminal alkynes on an 8-carbon chain. The length of this molecules was chosen for two reasons: it is short enough to prevent the occurrence of loops, where both ends attach to the surface while providing a sufficient spacing between surface and head group. A shorter molecule could potentially reduce the binding efficiency of immobilized proteins due to the difficulty of a large molecule to specifically bind to a rigid group close to the surface. It is common practice to use longer linker molecules when interacting with biological material to increase flexibility. In initial experiments 1,7-octadiyne was grafted onto mono-crystalline silicon surfaces using activation by light and hydride abstraction and subsequently labeled with an azide-conjugated fluorophore to image the result using fluorescence microscopy. This method was used in direct analogy to the characterization that can be done on structured polysilicon that does not allow for surface characterization techniques that require averaging over a larger surface area (such as XPS or contact angle measurements). In further experiments, the same protocol was used on polysilicon nanoribbons and characterized both by fluorescence microscopy and electrical measurements of the impedance change induced by the functionalization steps.

4.1.1 Monocrystalline silicon surfaces labeled with Alexa 594-azide

Protocols: see Appendix C.3.1 and C.3.2

Figure 4.1 shows the fluorescent images taken with a Texas Red filter after functionalization of the surfaces with 1,7-octadiyne and labeling with Alexa Fluor 594-azide. An increase in fluorescence intensity is apparent with increasing concentrations of 1,7-octadiyne in the grafting solution (mixed with ethanol). Assuming the fluorescence intensity is directly proportional to the amount of immobilized fluorophore, this result confirms the successful labeling of surface bound alkyne by the click-reaction and a clear increase in grafting yield with reagent concentration. It should be noted that there was considerable evaporation of solution from the samples during the incubation time due to insufficient sealing of the reaction vessel. This inevitably leads to an inaccuracy of the nominal octadiyne concentration on the samples. We can assume that the actual concentration was higher due to the higher volatility of ethanol over octadiyne.

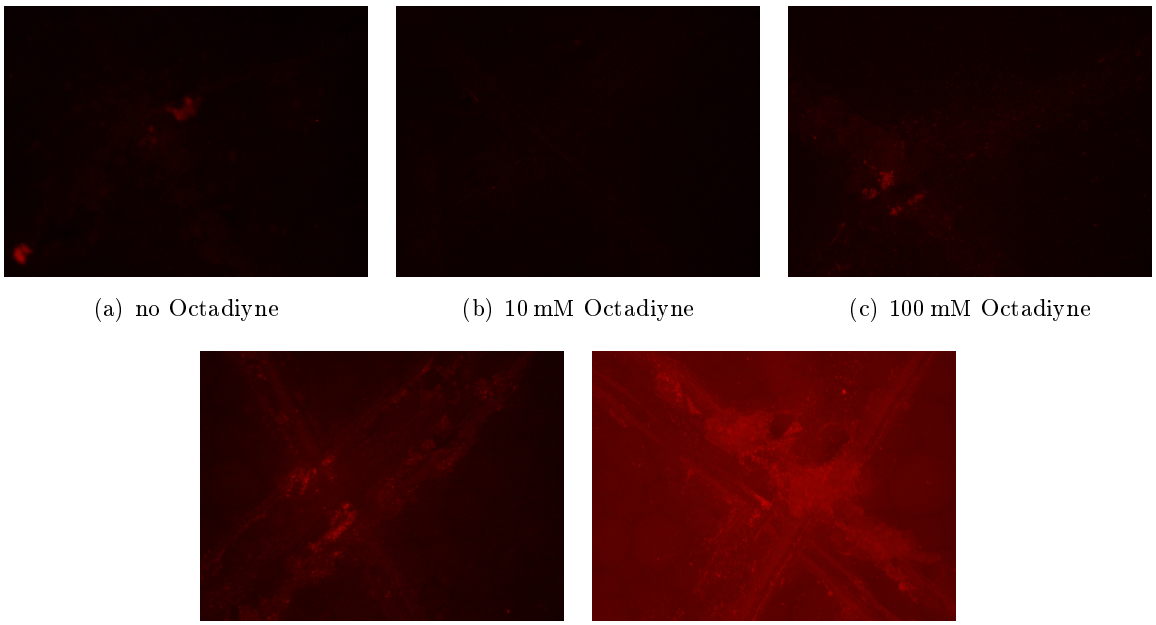

(a) no Octadiyne (b) 10 mM Octadiyne (c) 100 mM Octadiyne

(d) 1 M Octadiyne (e) 3 M Octadiyne

Figure 4.1 Octadiyne titration on scratched monocrystalline silicon surfaces (the scratch removes the surface oxide and introduces random surface orientations as well as it provides a focus point for fluorescent imaging). Verification by labeling with Alexa Fluor 594-azide using Copper-catalyzed Alkyne-Azide coycoaddition (CuAAC).

4.1.2 Polysilicon nanoribbons labeled with Alexa Fluor 594-azide

In an attempt to selectively functionalize polysilicon nanoribbons for biosensing an initial passivating layer of 1,7-octadiyne can provide the basis for further modification with biomolecules using the CuAAC click-reaction described above. To confirm the presence of the octadiyne layer

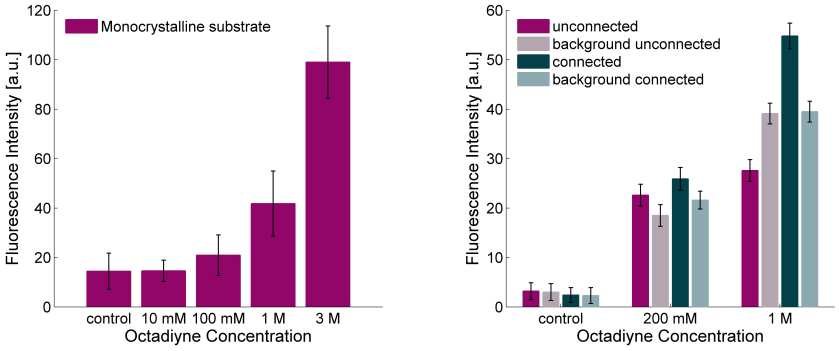

(a) (b)

Figure 4.2 Average fluorescence intensity of Alexa Fluor 594-azide labeled surfaces and nanoribbons functionalized with different concentrations of octadiyne. **(a)** Scratched monocrystalline silicon surfaces: The sample numbers correspond to increasing concentrations of octadiyne as follows: 1) negative control, 2) 10 mM, 3) 100 mM, 4) 1 M, 5) 3 M. **(b)** Polysilicon nanoribbon sensor chips, the fluorescence intensity was averages on background and ribbon surfaces respectively. for the two different locations (see text). Octadiyne concentrations as follows: 1) negative control (no octadiyne), 2) 200 mM, 3) 1 M

and visualize unspecific binding the surface was labeled with Alexa Fluor 594-azide as in the above experiment on monocrystalline silicon surfaces.

The fluorescent images of several nanoribbons after functionalization with different concentrations of 1,7-octadiyne and labeling with Alexa Fluor 594-azide are shown in Figure 4.3. The bright fluorescence seen on both sides of each image show the auto-fluorescent polyimide deposited to form both electrical passivation layer and microfluidic channel on the nanoribbon chip. Underneath the polymer the ends of the ribbon can be seen in the top row of images; these are un-connected ribbons used as control structures during fabrication. In the lower row of images the gold contact pads and connection to the gold side gate electrode can be seen. The central part of each image shows the microfluidic channel with a bottom layer of thermally grown silicon dioxide and polysilicon nanoribbons across it. The values in Figure 4.2 are normalized fluorescence intensity values from extracted histograms in two different areas of each image (channel background and nanoribbon surface). For the control chips, shown in (a) and (d), background and nanoribbon could not be distinguished.

Comparing the intensity values for background and ribbons we can see that there is no consistent trend of a higher value for the ribbons. Secondly, there is a large difference in fluorescence intensity between ribbon and background for the highest concentration of octadiyne. While for the image of the un-connected nanoribbon the background intensity is considerably higher than the fluorescence measured on the ribbon surface, the reverse is true for the connected ribbon. Since the control chip does not show any background fluorescence of the channel or on the ribbon, we can conclude that there is no considerable amount of non-specific adherence of the fluorophore to either oxide or polysilicon. Furthermore, the background intensity increases with increasing

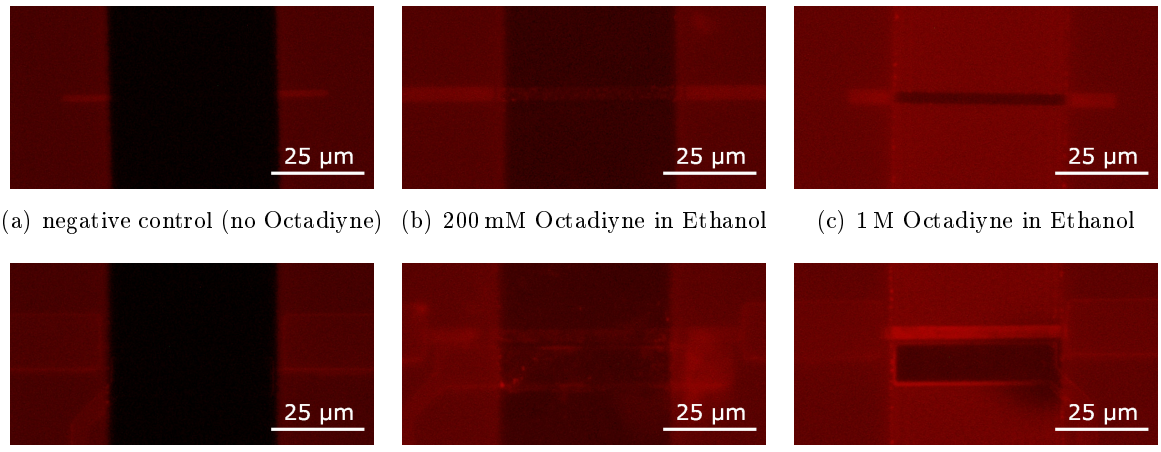

(a) negative control (no Octadiyne) (b) 200 mM Octadiyne in Ethanol (c) 1 M Octadiyne in Ethanol

(d) negative control (no Octadiyne) (e) 200 mM Octadiyne in Ethanol (f) 1 M Octadiyne in Ethanol

Figure 4.3 Octadiyne titration on PSi nanoribbon samples. **(a)-(c)** show an individual ribbon in the microfluidic channel without electrical connection (no patterned Cr/Au contact pads), **(d)-(f)** show the nanoribbon in the FET configuration with Cr/Au contact pads and a PSi/Cr/Au side gate.

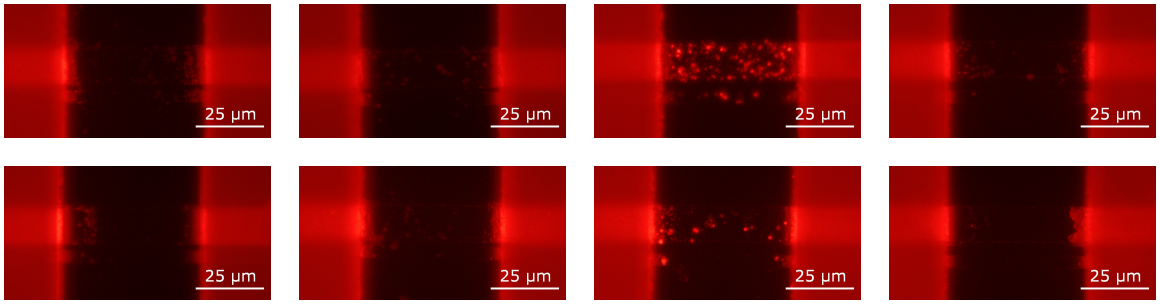

(e) no Octadiyne (f) 200 mM Octadiyne (g) 500 mM Octadiyne (h) 1 M Octadiyne

Figure 4.4 a-h) Octadiyne titration on silicon nanoribbons. Modified surfaces were labeled with Alexa Fluor 594-azide by CuAAC.

octadiyne concentration.

4.1.3 Electrical measurements of the functionalization process using polysilicon nanoribbons

To further investigate the functionalization process with octadiyne on polysilicon nanoribbons, the electrical impedance of each ribbon was measured before and after octadiyne attachment and after labeling with Alexa Fluor 594-azide. The chips that were used were sensors from W11 (see C.2). The results are shown in Figure 4.5, where 4.5(a) shows the averaged differential conductance from 4 ribbons on each functionalized chip after the different steps. A decrease in conductance of the nanoribbons can be seen for all concentrations of octadiyne. While the trend is not consistent for the lower concentrations, it shows a significant change when considering the 2 samples treated with neat octadiyne (corresponding to a concentration of 7.6 M). However, the

fluorescent images in a) through h) show no significant labeling of the surfaces as seen above. Instead a precipitation of aggregates can be seen, especially in the 200 mM sample, which is also the outlier in the impedance data. The graph in Figure 4.5(b) shows a real-time measurement of the labeling process with Alexa Fluor 594-azide. The click-reaction requires the addition of $CuSO_4$, which acts as a catalyst and sodium ascorbate (NaAsc), which acts as a reducing agent. The reduction of Cu from its Cu^{3+} configuration in solution to its reactive Cu^{2+} state and lower ionization states initiates the coupling reaction. We can see a change in conductance upon the addition of NaAsc that seems to saturate after approximately 500 s (8 minutes).

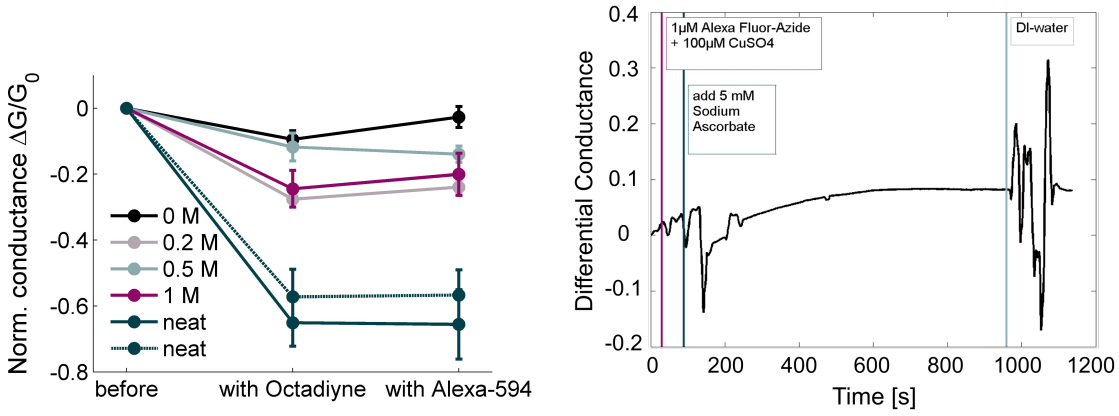

(a) (b)

Figure 4.5 a) Conductance measurements before and after surface modification and after labeling. Given are the concentrations of Octadiyne in the functionalization solution. The Alexa Fluor-Azide concentration was held constant. Two neat samles were prepared to monitor the spread. The errorbars correspond to measurements from 4 nanoribbons on the same sensor chip (recorded in steady state for 20 s). **b)** Conductance measurement during CuAAC attachment of Alexa Fluor-Azide to a silicon nanoribbon sensor.

4.1.4 Discussion

The fluorescence intensity variation between the samples labeled with fluorophore reveal that this type of characterization entails some difficulties. The trend of an increasing fluorescence signal with increasing concentration of octadiyne can be observed clearly for the monocystalline silicon surfaces and indicates an increased amount of immobilized organic molecules and successful coupling using the CuAAC click reaction. On the heterogeneous sensor chips the situation is different and we observe a more complex dependency of the fluorescent signal on both concentration and material. Fluorescence intensity is not a direct measure of grafting efficiency and cannot be used directly for fluorophore quantification. In addition to effects such as self-quenching by high concentrations of molecules, investigation of plausible further effects impacting the fluorescence intensity specifically on silicon surfaces in the literature reveals additional issues. Thin transparent (in the observed wavelength range) films such as silicon oxide atop reflective surfaces create multiple reflections and refractions of incident light causing interference phenomena observed in the returned signal. This phenomenon termed fluorescence interference contrast (FLIC) can lead

to attenuation or even complete quenching of the fluorescent signal from its surface.[61, 62, 63] Destructive interference is also the reason why the thickness of thin silicon oxide films can be characterized by their color. This is also true for very thin polysilicon films that are thin enough to be transparent in the visible spectrum. This effect would explain the high background fluorescence on the 3rd sample (on the thick oxide layer), while leaving the nanoribbon (no oxide layer) comparatively dark.

To explain the discrepancy in intensity between the two different wires (connected versus un-connected) we need to consider another effect that can lead to significant changes in the material. In the first step of the functionaliation procedure, the polysilicon ribbon is etched in fluoride solution to create a H-terminated surface for hydrosilylation. While this is a standard process for silicon surfaces, it becomes a more intricate matter in the presence of additional materials such as noble metals; a difficulty that is given surprisingly little attention in the processing literature. Investigation of this process for our purpose is the topic of the following section (4.2). In brief, electrochemical corrosion is most likely responsible for creation of a high surface roughness and unordered structure of the silicon ribbon and the creation of a type of porous silicon can not be ruled out. This would lead to both an higher amount of fluorophore due to the increased surface area and an elimination of the quenching effect due to the lack of a reflective surface.

As for the presence of fluorophore and consequently the prior attachment of octadiyne to silicon oxide surface constituting the background of the channel, the images clearly indicate the presence of a considerable amount of terminal alkynes. Since the control surfaces rule out unspecific adhesion of the fluorophore we need to consider that hydrosilylation can occur on silicon oxide surfaces. Detailed infrared reflectance spectroscopy studies of the silicon dioxide dissolution mechanism in hydrofluoric acid solutions have demonstrated the presence of silicon hydrides, both dihydrides and backbond-oxidized monohydrides.[64] It has previously been demonstrated that UV light promoted hydrosilylation does not proceed on H-terminated silicon oxide surfaces (prepared by treatment with triethoxysilanes)[65] while hydrosilylation promoted using a catalyst (Karstedts catalyst) can even occur more rapidly on twice backbond-oxidized silicon hydrides[66]. Our observation indicates that hydride abstraction by the carbocation triphenylcarbenium leads to hydrosilylation of hydrogen terminated silicon species on the etched oxide surfaces where the involvement of electronic effects in the substrate (such as photoemission or generation of excitons) are hindered by the insulating oxide layer. The problem of selectivity of the hydrosilylation reaction will be further investigated in later chapters.

4.2 Silicon oxide removal from polysilicon nanostructures

Surface functionalization of the silicon surface by hydrosilylation requires the creation of a H-terminated silicon surface. The commonly employed method is etching in hydrofluoric acid or ammonium hydrofluoride, depending on the crystal structure of the substrate. This section investigates the etching process using both etchants for the preparation of hydrogen terminated polysilicon nanoribbons embedded in a sensor chip.

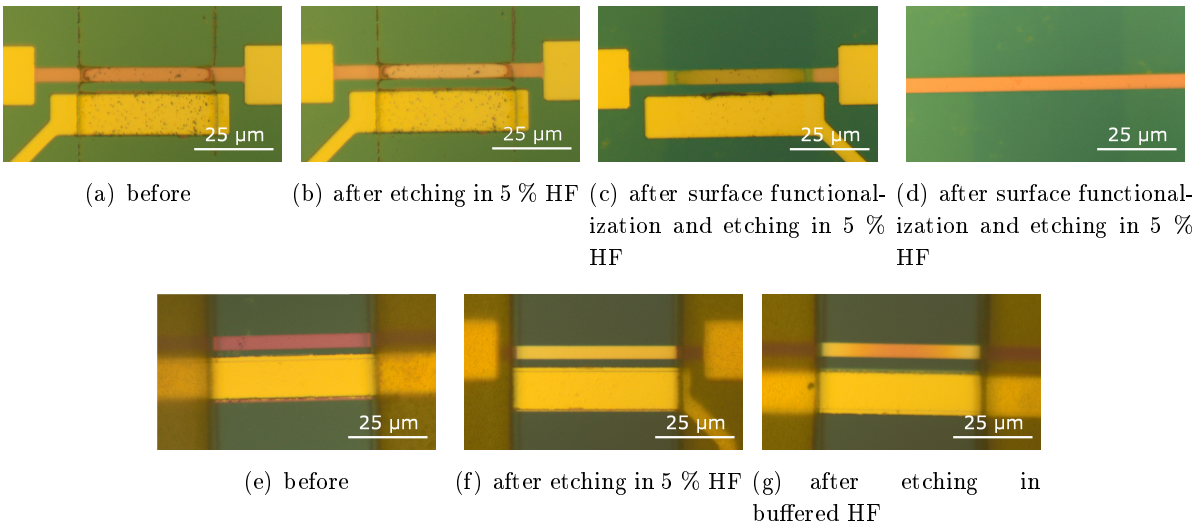

(a) before (b) after etching in 5 % HF (c) after surface functionalization and etching in 5 % HF (d) after surface functionalization and etching in 5 % HF

(e) before (f) after etching in 5 % HF (g) after etching in buffered HF

Figure 4.6 Optical microscopy images of silicon nanoribbons before and after etching in aqueous hydrofluoric acid solution.

4.2.1 Brightfield microscopy and conductance measurements

Sensor chips with polysilicon nanoribbons were etched in 5 % HF and subsequently modified with octadiyne using the identical protocol that produced promising results on the monocrystalline silicon surface. In the previous experiment we could observe a significant amount of fluorophore attachment when labeling the alkyne terminated surface using CuAAC on the ribbons and silicon oxide surfaces. While initial experiments on the then current generation of sensor chips resulted in measurable changes in ribbon-conductance, later repetition of the same process lead to irreproducible results.

The electrical conductance through the nanoribbons was measured before and after etching and after the functionalization process. Current measurements through the untreated nanoribbons showed reproducible values across the ribbons on individual chips and conductivity was reasonably uniform across the wafer (variation up to 30 %). After etching in 5 % HF current levels dropped below the noise threshold for around 63 % of the tested ribbons, around 33 % showed a significant decrease in current to about 50 % of the previously measured values and only 1 out of 12 chips retained similar conductivity before and after treatment on all 4 ribbons. Brightfield microscopy further reveals color changes in the nanoribbons as shown in Figure 4.6. Color changes in thin films such as the nanoribbon and underlying silicon oxide originate from light interference effects that depend on film thickness, as was mentioned with respect to the observed fluorescence intensity above. The color change that is observed here shows an irregular patterning of the ribbon, especially the area around the channel walls. Removal of the native oxide alone should result in a small but uniform color change across the nanoribbons, since the 50 nm ribbon is thinned by the thickness of the native oxide in this process. The variation in color between different ribbons and across the ribbons are an indication of a poorly controlled etching process that results in a number of different morphologies, suggests a highly irreproducible

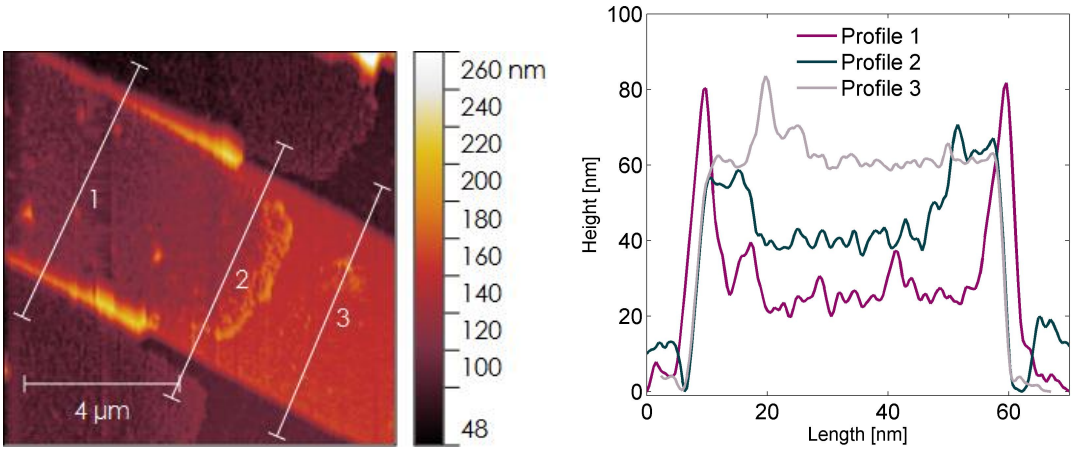

Figure 4.7 AFM images of a polysilicon nanoribbon etched in 5 % aqueous HF solution in the presence of a gold electrode without applied potential. Shown is the edge of the SU-8 microfludic channel that was removed prior to imaging.

process. The conductance measurements show that is also causes considerable damage to the sensor structure, which we would not expect if only the surface oxide were removed. Further investigations were undertaken in order to gain insight into the dynamics of this process and understand how we can achieve more control over the surface modification process.

4.2.2 Atomic force microscopy

Atomic force microscopic images from etched nanoribbons are shown in Figures 4.7 and 4.8; the passivation layer that formed the microfluidic channel was removed prior to imaging. Figure 4.7 shows the polysilicon nanoribbon close to the gold contact region after etching in 5 % HF for 15 s and subsequent storage in ethanol over night. Figures 4.8 shows a nanoribbon on an identical sensor chip after 15 s etching in 5 % HF solution and subsequent incubation with 1,7-Octadiyne over night in light. The latter sample has been additionally etched for 1 minute in 5 % HF after the surface modification and after removal of the microfluidic channel in order to investigate the stability of the functionalization layer under etching conditions and to evaluate the amount of etching on the silicon oxide surface. Height profiles in three different positions were taken across the nanoribbons as indicated by the labeled lines in the images. The height profiles are shown after baseline correction.

The profiles in Figure 4.7(b) reveal a significant gradual reduction in ribbon thickness from approximately 60 to 20 mn when we move from the location of profile 3, where the material that was protected by the channel walls, into the center of the former microfluidic channel (to the left). Profile 1 shows a buildup of material on the (transverse) ribbon edges, which flattens out toward the center of the ribbon, where we can see an increase in surface roughness.

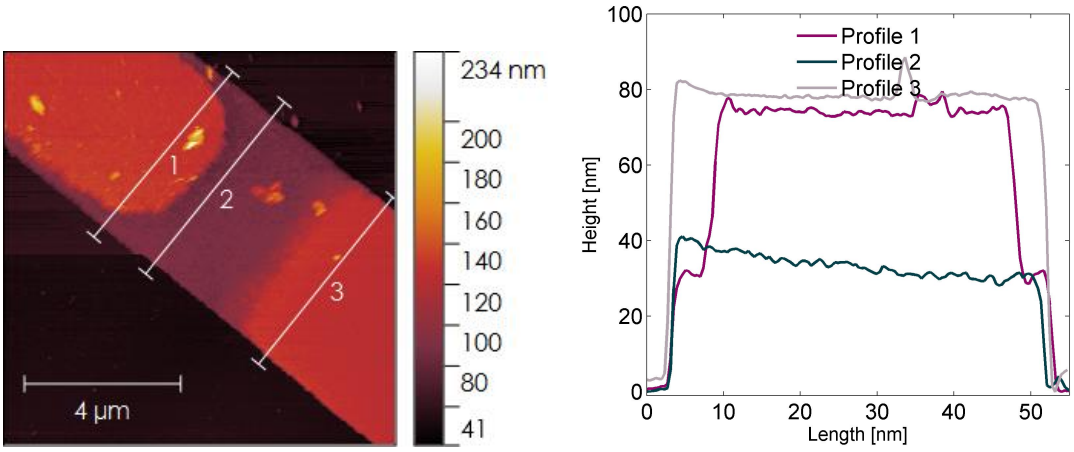

Figure 4.8 AFM images of a polysilicon nanoribbon etched in 5 % aqueous HF solution for 15 minutes in the presence of a gold electrode without applied potential, functionalized with neat octadiyne and etched again in the same etching solution for 1 minute. Shown is the edge of the SU-8 microfludic channel that was removed prior to imaging.

The profiles in Figure 4.8(b) show an effect that seems opposite to the one observed on the first sample. The central part of the ribbon shown in profile 1 is thicker than the area where the edge of the microfluidic channel walls was located, measured in profile 2, reaching the same level as the protected sides of the ribbon shown in profile 3. Measured from the underlying susbtrate, this maximal ribbon thickness reaches 80 nm and exceeds thereby that of the first sample by 20 nm. Whereas the minimal thickness in profile 2 is still 40 nm as compared to 20 nm in the first sample.

4.2.3 Real-time conductance measurement in a flow cell

Protocol: see Appendix C.3.4 Using a microfluidic flow cell it was possible to measure the current through the nanoribbon during etching in real-time, thus monitoring the change in conductance. Measurements were done using the measurement setup described in 8.1.2 by applying a slow alternating voltage of 1 Hz between -50 mV and 50 mV. The results of some of these measurements are shown in Figure 4.9. Measurements are shown for two chips each from two different wafers. Since oxide removal can be a very rapid process, as seen by the amount of damage previously caused to the polysilicon structures, the concentration of the etchant was reduced and an additional oxide was deposited onto the native oxides. All the investigated nanoribbons have the same lateral dimension of 2 μm in width and an exposed area of 50 μm in the microfluidic channel. The length (distance between the deposited gold contacts differs in between the two ribbons in each of the two graphs, with 100 μm for one and 150 μm for the other ribbon. This results in the differences in initial resistance shown in the legend. The devices in Figure 4.9 a) have an additional 10 nm thick silicon oxide layer deposited by PECVD, the devices in b) a 30 nm thermally grown oxide. While the deposited PECVD oxide does not consume the underlying ribbon, keeping its thickness unchanged, the thermal process involves conversion of part of the

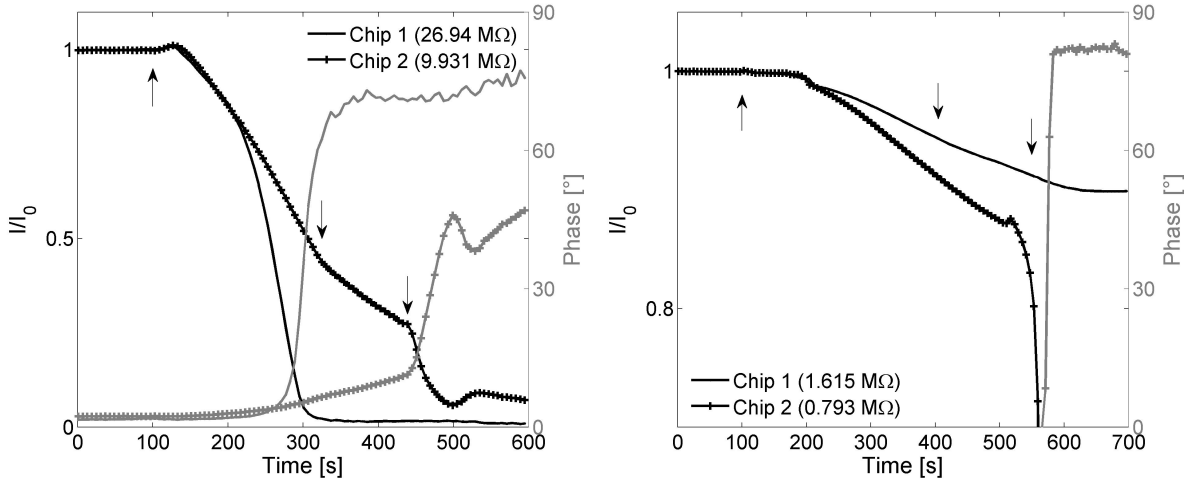

Figure 4.9 Real-time recording of electrical current in silicon nanoribbons during etching in aqueous hydrofluoric acid solution

ribbon into oxide, thus reducing the overall polysilicon thickness by half the resulting oxide layer thickness. The effective thickness of the polysilicon nanoribbon is therefore in this case reduced by at least 15 nm, resulting in a thinner conductive cross-section. This is not immediately reflected in the resistance values that we observe and we need to consider other effects, i.e. an change in grain size and electronic properties by the thermal treatment. We therefore expect different behavior in the two cases. The arrows indicate, from left to right, the injection of 1 % HF aqueous solution, injection of a separating air bubble and injection of deionized water for rinsing respectively.

The current plot in a) shows a brief increase at the onset of etching followed by a nearly linear decrease and ending in an exponential breakdown of the current after an extended time in etching solution. chip 1 shows a more rapid decrease in current whereas chip 2 is still conducting current when the air bubble is injected and the current continues to decrease during the period in air. When deionized water is injected into the channel the current drops more rapidly. The current plots in b) show a similar behavior with some important differences. While the initial increase in current can be observed as well, the time until a reduction in current is observed is significantly longer. For both chips, the current starts to decrease approximately 90 s into the etching process. The the end of the steady reduction in conductance, chip 2 shows the same exponential current drop at the injection of water, whereas chip 1 is still functional after etching in 1 % HF solution. We need to assume that etching continues after the bubble has been introduced, due to wetting of the channel walls and the sensor structure. Comparing both figures we can see how the difference in oxide thickness shifts the onset of the linear current decrease, which occurs approximately 30 s and 90 s after introduction of the HF solution for 10 nm and 30 nm oxide respectively. Secondly, we can observe a degradation of the conductive properties to a varying degree in all cases.

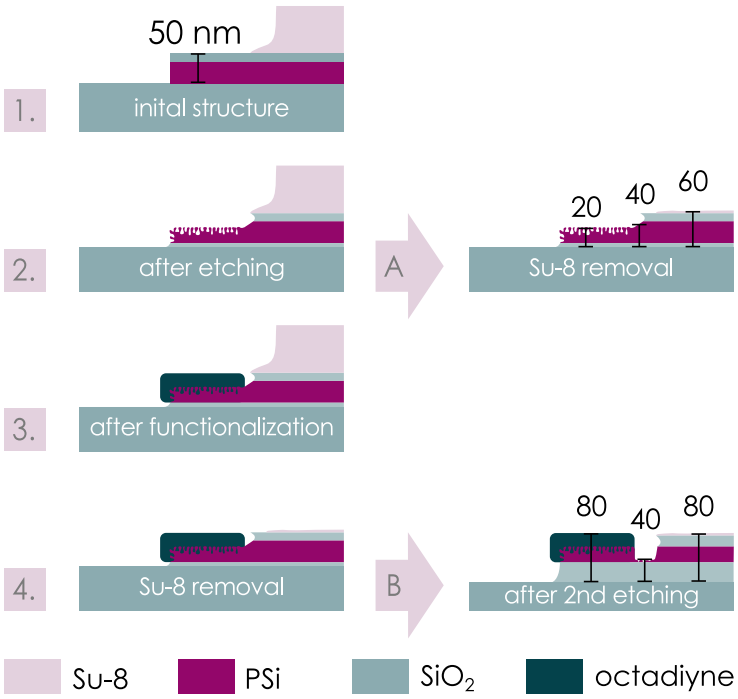

Figure 4.10 Proposed scenario explaining the etching process: 1. In the initial structure the thickness of the nanoribbon with native oxide is approximately 50 nm. 2. After the initial etching process, the native oxide is removed and the surface of the polysilicon is roughened due to proximity of the gold electrode. This results in the profiles show in A as observed in the AFM image. 3. After functionalization of the surface with Octadiyne, the roughened polysilicon is covered in a SAM of organic molecules protecting it against further etching. 4. After removal of the SU-8 microfluidic channel a residual layer of polymer protects the underlying polysilicon against the second etching step while the exposed silicon areas are etched further, resulting in the profiles shown in B.

4.2.4 Discussion

The presented data and investigations reveal severe problems with the etching process of polysilicon nanoribbons on the sensor chips in hydrofluoric acid. It is clear that the etchant not only removes the oxide layer on top of the polysilicon, but that the silicon underneath is also affected, as the decrease in conductance indicates. The color changes observed previously indicate either an inhomogeneous thickness of the ribbon after etching or a change in composition. The AFM images confirm that etching occurs in a non-uniform manner and leads to a high surface roughness on the ribbons. Furthermore, the progression between the two AFM images, though they are not showing the identical chip but two similar ones, gives more insight into the process and Figure 4.10 suggests a scenario to explain the observations. The initial etching step (2.) removes the native silicon oxide from the surface and the underlying polysilicon is pitted and roughened, possibly along defects in the grain boundaries facilitated by electrochemical corrosion (see below). The curved edges are likely a result of residual polymer (Su-8) left over after development

of the photoresist in the lithographic process. The first AFM image shows this state, as illustrated by the scenario A. Then the resulting H-terminated surface is modified by hydrosilylation with octadiyne, which leads to formation of a dense SAM on the roughened polysilicon surface (3.). After removal of the Su-8 (4.) the subsequent immersion in HF for another 60 s leads to the scenario given in B. Assuming further etching of all susceptible surfaces shows that the octadiyne SAM prevents attack by the etchant as well as possibly residual polymer where the channel structure has been removed, while the surrounding area is etched.

Investigation of the etching process in a flow cell, using a more dilute solution of HF to slow down the process and make it easier to observe, lets us estimate both the etch rate and influence on the polysilicon layer in a different way. Since the nanoribbons are conductive (an essential property for their use as field effect sensors), monitoring the current during etching is a direct method to observe potential degradation of the material. The measurements show a decrease in current preceded by a delay that corresponds proportionally to the oxide thickness. The estimated etch rate is approximately 20 nm per minute or $0.34\,^{\mathrm{nm}}/_{\mathrm{s}}$, which corresponds to roughly one monolayer of oxide per second for both types of oxide. The measurements indicate that in this initial etching time of the oxide itself, the conductivity of the nanoribbon is not considerably affected. The following decrease in the current on the other hand shows, that after a certain amount of oxide (possibly all of it) is removed, the polysilicon itself is attacked by the etchant. The slope of the declining curve differs from one ribbon to another and it is reasonable to assume a non-uniform process associated with the irregular structure of the material itself. It is interesting to note that the process does not self-terminate before the conductance is lost completely, so there is no doubt that the conductive properties of the polysilicon is destroyed. Possible mechanisms for this are the formation of surface oxides that are subsequently removed by the etchant. Under normal conditions and on monocrystalline surfaces this process is orders of magnitude slower than the removal of already present oxide species that it can be neglected. Firstly, we should consider, that in our case an alternating voltage is applied to the material, creating conditions similar to those used for electro-polishing[67]. It is therefore not surprising to observe a degradation of silicon. What is striking however, is that we observe the same destructive effect after etching without applied potential, as numerous previous test have shown. Considering once more the microscopic bright field images of different etched ribbons we observe another peculiarity. The ribbons that are acting as test structures for the fabrication, i.e. that are not connected to gold leads do not show the characteristic discoloration associated with attack of the material. We conclude that either the gold leads or (more likely) the gold electrode in the vicinity of the nanoribbons is responsible. Study of the literature regarding the fabrication of integrated circuits confirms the impact of noble metals in close proximity to silicon during the etching process and can explain the observed effects. Differences in surface chemical potential, for example in the presence of noble metals such as the gold side gate electrode or through application of a voltage in an electrochemical cell can lead to dissolution of silicon in a corrosion reaction, when in contact with certain ionic species[68, 69]. This mechanism has actually been used for electro-polishing of silicon surfaces and to create porous silicon[27, 70, 71], explaining what we see in the AFM images.

Conclusion and further work

The above results have demonstrated some of the difficulties that arise when working with surface functionalization of biosensors and outlines some of the parameters that play a paramount role in successful surface modification. The influence of the immediate environment as well as the details of both bulk and surface structural and electronic properties of the area under investigation can not be underestimated. Furthermore, the choice of characterization methods and knowledge of possible artifacts such as FLIC need to be well-understood to be able to truly monitor each step of the process.

Due to time constraints and unavailability of further nanoribbon devices with the same characteristics this investigation could not be continued further and priority was given to study of the formation of organic SAMs on silicon and polysilicon surfaces. A systematic and thorough study of the impact of the etching and functionalization process on the morphology and electrical properties of the ribbons is however of interest for different reasons. The differences in surface potential, which have a detrimental effect on the polysilicon in our case could potentially be utilized positively for selective functionalization by the reduction of metals at the surface. Or by creation of tailored porous silicon, which is of course a large field of study in itself, as a higher surface area could benefit sensitivity of the resulting sensor. Instead, due to the highly irreproducible nature of the experimental conditions, including the substrate to be functionalized, dedicated test-structures were fabricated. These were used in the study and optimization of the functionalization procedure and the investigation of different etching and grafting schemes using x-ray photoelectron spectroscopy. This will be the topic of the following sections.

4.3 Etching of silicon and polysilicon surface in aqueous HF and NH_4F

Test chips were fabricated as described in 3.2. Each chip contains polysilicon, Si(100) and thermally grown silicon oxide surfaces that were used to investigate etching rates and resulting silicon surfaces under different conditions in order to obtain a protocol for the selective H-termination of polysilicon sensor structures. Aqueous 2.5 % and 5 % HF as well as 40 % NH_4F were used since they are the most commonly reported etchants in the literature. The graphs in Figure 4.11 and Table 4.1 summarize the results of two experiments. They show the silicon oxide thickness as determined from the Si2p high resolution spectra using the method described in 3.3.

In the first experiment, different etching conditions were tested on the fabricated test surfaces to evaluate the impact on polysilicon and monocrystalline surfaces respectively under identical etching conditions. We observe that the monocrystalline silicon surface is much less affected than the polysilicon surface for all etching conditions with an apparent etch stop around 1.5 nm oxide thickness. These findings stand in contrast to the second experiment, where pristine n and p-type silicon wafers were diced, cleaned and etched without further processing. The two measurements also show that oxide thickness differs between the two surfaces of the same material. A possible reason for the discrepancies between pristine and processed chips might be introduced by the

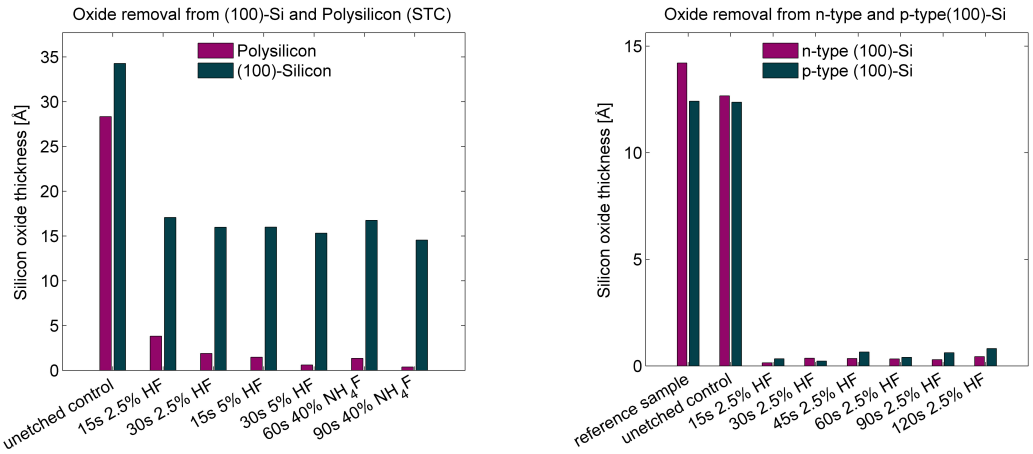

(a) (b)

Figure 4.11 Silicon oxide thickness on different silicon surfaces as obtained by quantification from the XPS Si2p scan.

additional cleaning in Piranha solution which oxidizes the surface additionally leading to thicker surface oxides. However, this does not explain why etching does not seem to continue beyond 1.5 nm equivalent oxide thickness; this corresponds roughly to the native oxide thickness of the unaltered silicon wafer. During the final fabrication steps of the test chips, the buried oxide layer that serves as a substrate for the polysilicon is removed in a dry etch, followed by a wet etch to remove any residual oxides.

The bare wafer dices are easily etched in 2.5 % HF already after 15 seconds, with only minor variations in between the samples that are most likely a result of exposure to air after etching until the samples were placed into vacuum. This also explains a slight increase in oxidation towards longer etching times, since the surfaces were prepared in the order of decreasing etching time to limit exposure to air. For further functionalization, care was taken to cover the etched surfaces immediately with the respective functionalization solutions to prevent re-oxidation.

Etching time	2.5 % HF	5 % HF	40 % NH_4F
15s	60	76	-
30s	73	79	10
60s	75	79	41
90s	72	74	80

Table 4.1 Water contact angle measurements on polysilicon and Si(100) surfaces etched in aqueous HF and NH_4F. The values present the measured average contact angles of at least two surfaces, with an accuracy of $\pm 2°$.

The native oxide on the polysilicon surface is etched most efficiently in NH_4F, which is a slower etchant than HF and most commonly used for (111)-Silicon surfaces. However, for these surfaces, reported etching times are usually of the order of several minutes, which proved damaging to the

polysilicon layer, resulting in irregular discoloring of the surface. A short etching time of 90 to 100 seconds (a dependence on the temperature of the etching solution was observed) resulted in complete removal of the oxide layer according to the XPS measurement without visible damage to the surface. Since we do not have the possibility to perform FT-IR measurements on silicon surfaces, the H-termination can not be confirmed at this point and needs to be assumed. This is reasonable since the literature confirms the creation of H-terminated surfaces under similar or identical conditions.

5 | Self-assembled monolayers (SAM) on oxide-free silicon surfaces

As the previous chapter illustrates, interfacing biological material with inorganic surfaces that are not well defined comprises a number of challenges already in the first steps of the surface modification. In order to apply appropriate characterization methods, this chapter focuses on the functionalization of larger surfaces. The polysilicon layer that constitutes the sensing element in the silicon nanowire BioFET will be studied in specifically fabricated devices that allow for a thorough investigation of self-assembled monolayers (SAMs) on their surface. This chapter will approach some of the mentioned challenges in a systematic way, investigating different mechanisms and molecules for construction of the interface layer in a quantitative manner. Initially focusing on polysilicon and silicon oxide, grafting efficiency, re-oxidation and material selectivity will be discussed for different functionalization conditions. Comparisons will be made with silanization of the native oxide and hydrosilylation on two different monocrystalline silicon substrates that provide a reference for the achieved results. In addition, thermal hydrosilylation of polysilicon, Si(100) and Si(111) is investigated and discussed in the following chapter (to be published).

5.1 SAM formation of alkenes and alkynes by hydrosilylation on polycrystalline silicon in ambient conditions

Testchips with different surfaces, fabricated as described in 3.2, were used to investigate the formation of self-assembled monolayers by hydrosilylation on oxide-free, H-terminated silicon surfaces. The formation of SAMs of 1,7-octadiyne (octadiyne) and 10-N-BOC-amino-dec-1-ene (Boc-alkene) were studied as two possible passivation layers for polysilicon biosensors and to present platforms for further conjugation of proteins by different methods. To utilize different grafting mechanisms for the covalent attachment of the SAMs to silicon, specific experimental conditions were investigated. Illumination by light of different wavelengths as well as the use of the carbocation triphenylcarbenium (salt in complex with tetrafluoroborate was dissolved in ethanol) were studied. The surfaces were investigated by XPS to estimate the amount of carbon chains bound to the substrate and concurrent formation of silicon oxide.

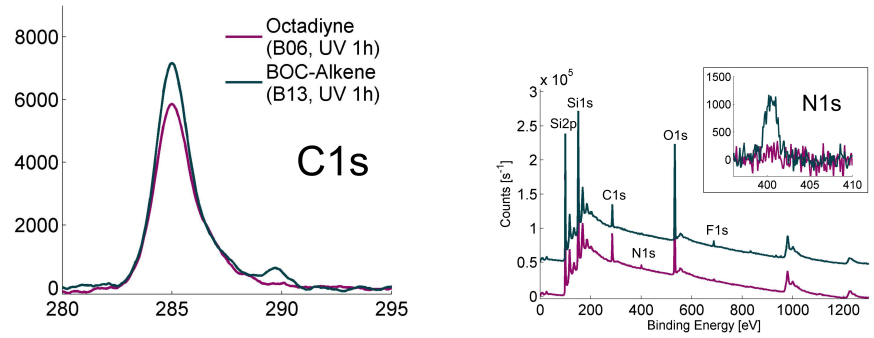

(a) (b)

Figure 5.1 Example of XPS spectra of polysilicon surfaces modified with octadiyne and Boc-alkene for 1h in neat reagent with illumination by soft UV. **a)** High resolution XPS C1s spectrum. The main peak at 285 eV is attributed to carbon in the chain of the molecules and was used to correct for charging effects. The spectra differ in intensity and position of theirs side peaks due to contributions from the different head groups. The small peak at 289.5 eV evidences the C=O bond in the BOC group of the alkene which is not present in octadiyne. **b)** Survey spectrum. The survey spectrum differs very little between the two samples, most of the signal originating from the substrate and only a small fraction of the electrons account for the surface monolayer. The inset shows the high resolution N1s spectrum that confirms the presence of nitrogen in the Boc-alkene sample, and no nitrogen (contamination) on the octadiyne sample.

5.1.1 XPS spectral analysis of 1,7-Octadiyne and 10-*N*-BOC-amino-dec-1-ene SAMs

The XPS spectra in Figure 5.1 show examples of the spectral data obtained from the polysilicon surfaces modified with neat octadiyne and Boc-alkene under identical conditions for 1h under irradiation with soft UV. Figure 5.1(b) shows the survey spectra recorded. The repeated features on the low energy end of the spectrum between 90 and 200 eV stem from the 1s and 2p (Si2p) core electrons of the silicon substrate. The series of smaller peaks is a result of electron energy losses to excitation of phonons (lattice vibrations) and other scattering effects. At 285 eV the carbon 1s (C1s) electron peak is visible in both spectra, which evidences the presence of carbon species on the silicon surface. The detailed structure of this peak, given in Figure 5.1(a) provides further insight into the composition of this carbon layer as discussed below. The small feature around 400 eV derives from nitrogen 1s (N1s) and is therefore only present in the Boc-alkene spectrum. The inset shows the corresponding high resolution spectrum of the nitrogen energy range, which clearly shows the lack of nitrogen containing species in the octadiyne spectrum, making it a suitable marker to confirm the presence of Boc-alkene in the surface layer. However, the low sensitivity of the N1s peak, due to a low scattering cross section, results in a peak with low signal-to-noise ratio. This leads to a large error when estimating the number of molecules solely based on the area of this peak. Therefore, we are using both the C1s and the N1s spectrum for quantification of the SAM surface coverage for this molecule. The intense peak at 480 eV shows the presence of oxygen (O1s) in the sample. Oxygen stems from the oxidized silicon substrate and in the case of the Boc-alkene includes a contribution from the BOC-group, which

contains 2 oxygen atoms. The relative intensity of the oxygen and carbon peaks do not reflect the respective abundances directly due to different sensitivity factors (1 for C1s and 2.9 for O1s). Finally, the peak at 550 eV shows a small amount of fluor present on the surfaces, which could be seen in some of the samples and results from residual fluor species created during the etching process. The presence of fluor in the samples and possible implications will not be investigated in this thesis.

The C1s spectrum in Figure 5.1(a) gives structural information about the SAM forming molecules due to the chemically shifted electron energies of the different bonds between carbon atoms in the surface layer. The main carbon peak at 285 eV, deriving from the hydrocarbon backbone in both molecules was defined to lie at 285 eV to correct for charging effects that lead to energy shifts in the data[72]. Each C1s spectrum is fitted with Gaussian/Lorentzian peaks and the number of molecules in the SAM quantified accordingly (the chosen constraints for fitting can be found in the Appendix B.2.2, the quantification method has been described in the Methods section).

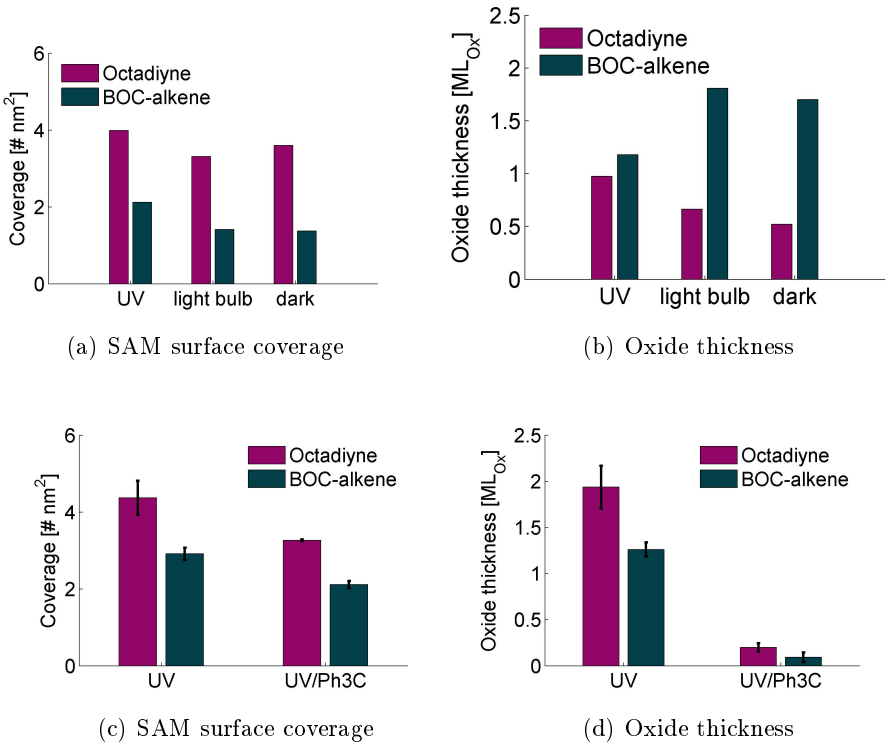

(a) SAM surface coverage

(b) Oxide thickness

(c) SAM surface coverage

(d) Oxide thickness

Figure 5.2 SAM surface coverage and oxide thickness of octadiyne and Boc-alkene on polysilicon surfaces obtained from quantified XPS data. (a) + (b) Different light conditions during functionalization for 1h in neat reagent. (c) + (d) Exposure to UV light for 3h in either neat reagent or a 1:1 mixture of the reagent and 10mM $Ph_3C\text{-}BF_4$ in EtOH.

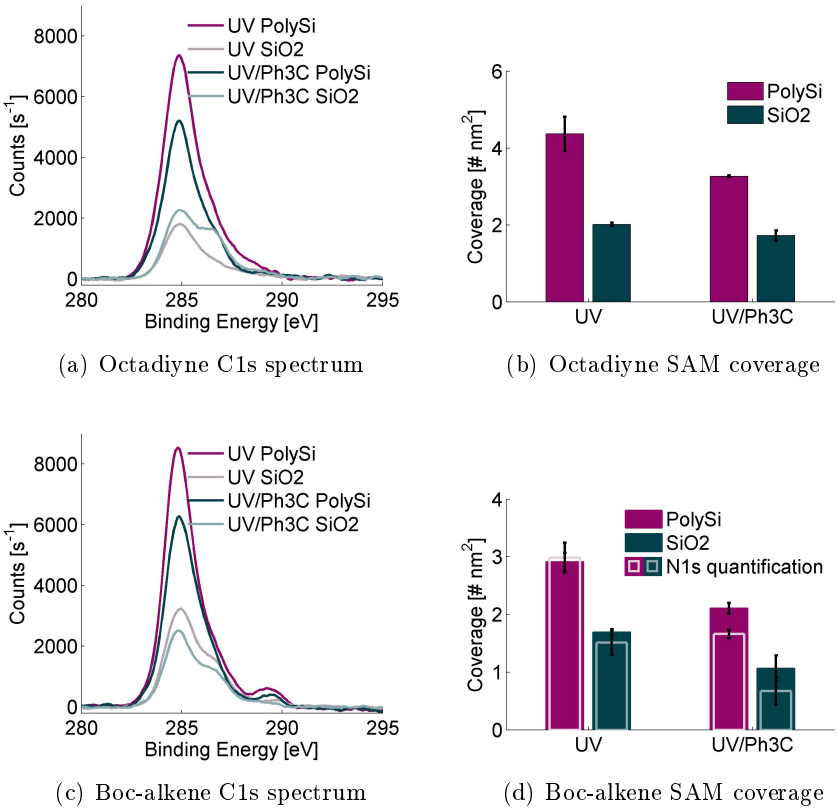

(a) Octadiyne C1s spectrum (b) Octadiyne SAM coverage

(c) Boc-alkene C1s spectrum (d) Boc-alkene SAM coverage

Figure 5.3 Comparison of octadiyne and Boc-alkene SAMs on polysilicon and SiO_2 surfaces. The C1s spectra show differences both in signal strength and peak shape for the different surfaces for both molecules.

5.1.2 Surface coverage of 1,7-Octadiyne and 10-*N*-BOC-amino-dec-1-ene SAMs and substrate oxidation

The bar graphs in Figure 5.2 (a) and (b) show SAM surface coverage and oxidation, determined from XPS spectra. The surfaces were modified with neat octadiyne and Boc-alkene respectively for 1h while being illuminated with different light sources. The coverage obtained for octadiyne is close to 4 molecules per nm^2 and approximately doubled compared to Boc-alkene for all light conditions while there seems to be only a minor influence of the illumination on the grafting efficiency. For the Boc-alkene UV light irradiation results in a higher coverage of about 35% compared to both illumination with white light and in the dark. The impact of illumination conditions is more apparent in the competing oxidation process during functionalization. Since all experiments in this section were performed in ambient conditions, both oxygen and water are present to react with the surface to form surface oxides. It is very interesting to note that while oxidation proceeds faster in UV light in the presence of octadiyne the effect seems to be opposite for Boc-alkene.

Both parameters were further investigated for longer modification times with UV irradiation

and with the addition of triphenylcarbenium tetrafluoroborate (Ph_3C). The data shown in Figure 5.2 (c) and (d) shows surfaces that were irradiated with UV light for 3h while immersed in neat reagent or reagent solution. For both molecules, the addition of Ph_3C reduces SAM coverage by 25% while it simultaneously reduces oxidation by at least 90%. Further comparing the coverage obtained after 3h in UV light with that after 1h shows no significant difference for octadiyne and an increase of 35% for Boc-alkene, while oxidation increases twofold for octadiyne and does not vary for Boc-alkene.

5.1.3 Selectivity: Hydrosilylation on etched *silicon oxide* surfaces

As seen previously for the fluorescently labeled octadiyne surfaces, a considerable amount of fluorophore was present on the silicon oxide surface (see 4.1) that was most likely attributed to octadiyne attachment and not to unspecifically bound fluorophore. To further investigate the selectivity of hydrosilylation in different conditions we are comparing the polysilicon surface (PolySi) that we are aiming to functionalize to thermally grown silicon dioxide surfaces (SiO2).

The C1s spectra shown in Figures 5.3(a) and 5.3(c) display the differences between the PolySi and the SiO_2 surfaces of samples functionalized under UV irradiation and in the presence of Ph_3C. Generally, the amount of carbon on the samples is significantly reduced on the SiO_2 surface compared to the PolySi. Additionally, we can see an increase in one of the chemically shifted peaks at 286.8 eV in all but one of the spectra. Comparing the spectra to a control surface that was cleaned and etched using the same procedure, we can see that the shape of the C1s spectrum is very similar to those obtained for the functionalized surfaces (The data can be found in the Appendix A.1). This is to be expected, as a certain amount of adventitious carbon immediately forms on the etched surface when exposed to air due to its hydrophobic character. However, the intensity should be significantly lower due to an abundance of smaller molecules and low surface coverage. At the same time, the peak at 286.8 eV that is present on the functionalized SiO_2 surfaces seems to be especially pronounced here and does not contribute considerably to the contamination spectrum otherwise present.

The graphs in Figure 5.3 show the quantified SAM surface coverage for PolySi and SiO_2 surfaces for octadiyne and Boc-alkene respectively. Each data point presents the average from two different samples. The reduction in intensity from PolySi to SiO_2 across all the samples for both molecules is on average 50% $\pm$ 10%. In addition to the SAM coverage quantified using the C1s spectrum Figure 5.3(d) shows the same data calculated using an analog method for the N1s spectral data. In the samples functionalized with the addition of Ph_3C we can see a consistent underestimation of the coverage with the same magnitude when using the N1s spectra. The same underestimation can be seen in one of the SiO_2 spectra of the Boc-alkene functionalized surface without addition of Ph_3C. This is the same spectrum that is displayed in the C1s spectrum in Figure 5.3(c) and we can see the appearance of the same additional peak.

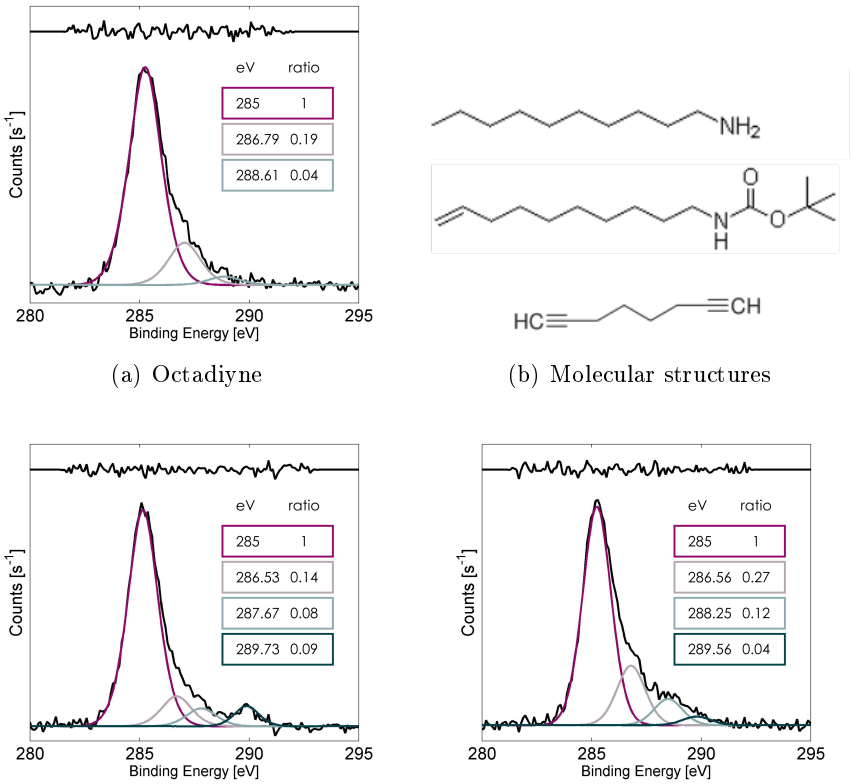

(a) Octadiyne

(b) Molecular structures

(c) Boc-alkene

(d) Amino-alkene after de-protection by boiling

Figure 5.4 C1s high resolution spectra of octadiyne and BOc-alkene SAMs on polysilicon surfaces fitted with Gaussian/Lorentzian peaks. Peak position and area reveal structural information about the two molecules.

5.1.4 Structure and composition of octadiyne and Boc-alkene SAMs

Figure 5.4 shows fitted C1s spectra for octadiyne and Boc-alkene SAMs on polysilicon surfaces. Peak positions and relative peak area are listed in the table insets. The octadiyne spectrum shows two major features, the main carbon peak attributed to C-C bonded carbon and an additional peak at 286.8 eV. This additional peak accounts for the two carbon molecules in the head group that is not bound to the silicon substrate (C-**C**≡**C**H). The full width at half maximum (FWHM) of the fitted peaks is comparatively large in this spectrum (1.75 eV) and if the upper limit for this parameter is reduced (to 1.55 eV) an additional peak can be fitted in the low energy end of the main carbon peak. The Boc-alkene spectrum shows a more isolated characteristic peak at 289.7 eV, which is attributed to the C=O bond in the BOC group. The peaks fitted at 286.5 eV and 287.7 eV are likely to correspond to the C-**C**-N and O-**C**-3CH3C carbons in the Boc-alkene molecule. The three C-**C**H3 carbons in the BOC group do not appear to be significantly shifted to be distinguished from the main peak. Attempted removal of the Boc-group leads to a clearly visible reduction of the peak at 289.7 eV and an increase in the peak at 286.5 eV. The first evidences the reduction of the number of carboxyl carbons while the latter is probably an

indication of increased surface contamination. A significant energy shift is observed in the third side peak from 287.7 to 288.3 eV, which indicates the appearance of terminal amines.

5.1.5 Amino-termination of the silicon surface by de-protection of 10-N-Boc-amino-dec-1-ene in boiling water

Illumination	Boc-alkene	de-protected (-NH_2)
UV	71°	63°
white light	73°	66°
dark	72°	63°
no etching	40°	23°
etched PolySi	80°	-

Table 5.1 Water contact angle measurements on surfaces functionalized with Boc-alkene, for 1h and 2h illumination/incubation times before and after removal of the tBoc group by boiling in water. All angles are averages of a continuous measurement for a single droplet with an estimated error of approximately 1°.

Table 5.1 summarizes the results of contact angle measurements on polysilicon surfaces with Boc-alkene SAMs, before and after de-protection of terminal amine. The de-protection was performed by boiling the functionalized chips in deionized water for 15 minutes followed by a rinse in water and drying in nitrogen. The removal of the *tert*-butyloxycarbonyl (Boc) group has been demonstrated for a number of different molecules in this way as a mild alternative to the common procedure of de-protection by TFA[73]. The average contact angle of surfaces treated with Boc-alkene under different conditions is 72°. There is no significant difference between the different conditions under which the surfaces were functionalized (Data shown in A.1 in A.2.1). Comparison with a native oxide covered and a freshly etched polysilicon surface shows contact angles of 40° and of 80° respectively. The boiling procedure leads to a decrease in contact angle in all cases by 12 ± 2%.

5.1.6 Discussion

Fitting of the C1s spectra for the investigated molecules showed features that could be closely matched to the respective chemical structures. For octadiyne specifically, the data fitting is not unambiguous and the choice of constraints such as the FWHM highly impact data interpretation. In the particular case of this molecule, with no marking features or additional atoms that can be used as a label, fitting results are of comparable quality for FWHMs of 1.75 and 1.55 eV with different numbers of fitted peaks; both values for FWHM are reasonable. Compared with other molecules investigated in this study, the lower FWHM is more commonly found to fit the spectra on silicon surfaces, whereas a higher FWHM is typically found for silicon oxide substrates. The use of side peaks that are not clearly resolved is therefore not suitable for quantification, meaning that carbon contamination, which falls within the same range, cannot be excluded from the data. Since the contamination spectrum observed on etched substrates however is comparatively low and care was taken to immediately process the samples after etching, this contribution is expected

to be small. The smaller size of the octadiyne molecule (8 C) compared to Boc-alkene (15 C) will however lead to an amplification of a potential overestimation of the coverage. Nevertheless, the data shows the successful grafting of fractional monolayers in both cases. The coverage of 4.5 molecules per nm^2, which was obtained for the surfaces functionalized in UV light for 3h, corresponds very well with the maximal coverage of 1-alkynes obtained on monocrystalline silicon surfaces which is up to 65% of converted Si-H groups. Since there are 7.8 Si atoms per nm^2 in the Si(111) surface, 4.5 grafted molecules correspond to 58% coverage. The generation of a significant amount of oxide at the same time suggests that the photoactivated process by UV irradiation does not preferentially lead to the formation of Si-C bonds over Si-O bonds in the presence of oxygen. For Boc-alkene the obtained coverage is lower amounting to less than 50% in all cases. This is in line with the reported lower efficiency of hydrosilylation of alkenes over alkynes and the larger size of the head group.

The difference in grafting efficiency for the surfaces modified with and without Ph_3C under UV irradiation remains the same, indicating that the efficiency scales for both molecules. As described in section 2.2 hydrosilylation by light irradiation can proceed via different routes, depending on wavelength and crystallinity of the substrate. It has been reported, for a process proceeding via photoemission, that the electron acceptor level of the distal head group plays a role in the grafting process. The BOC-group has been shown to act as electron acceptor in this way and may be an additional factor for the difference in grafting efficiencies. Oxidation is greatly reduced in the reaction using Ph_3C, leading to minimal inclusion of oxide in the surface, even in the here tested ambient conditions. The carbocation Ph_3C has previously been used to promote hydrosilylation on porous silicon by hydride abstraction from the H-terminated surface. The effect on oxidation under ambient functionalization conditions has not been studied in that case and our results clearly show the suppression of oxidation in presence of the molecule.

The differences in calculated coverages using the C1s and N1s spectra for Boc-alkene modified surfaces reveal an interesting trend under functionalization conditions with Ph_3C, showing that part of the carbon signal does not originate from Boc-alkene molecules. The presence of ethanol as a solvent in the functionalization reaction may have led to the incorporation of ethanol into the surface. Preferential incorporation of the solvent has been found for 2-propanol on both Si and SiO_2 surfaces for metal catalyzed hydrosilylation, though no incorporation occurred in the case of UV grafting[65]. The peak at 286.8 eV that has become more pronounced in the SiO_2 spectra agrees well with the energy shift associated with the methylene carbon in ethanol.[72] Our findings show that ethanol incorporation is also likely the case of a reaction mediated by hydride abstraction with Ph_3C. This will be discussed further in the next section.

While hydrosilylation results in a denser SAM on H-terminated PolySi some degree of attachment of the molecules to etched SiO_2 surfaces occurs as well. Oxygen back-bonded silicon hydrides, i.e. $O_2SiSi\text{-}H_2$ and $O_3Si\text{-}H$, are present in the SiO_2 surface[66] and can additionally be created as an intermediate in the etching process. While the number of silicon atoms in the SiO_2 surface that can be H-terminated is half as much as on the silicon surface a hydrosilylation yield of less than 50% compared to PolySi would be expected. Since this agrees with our findings we can conclude that the reaction proceeds with an at least comparable efficiency on OSi-H as on Si-H under the tested reaction conditions both with and without the addition of Ph_3C and may

Sample ID	Boc-alkene	ethanol	Ph_3C-BF_4	Etching procedure
A	neat	-	-	90 s in 40% NH_4F
B	90%	10%	5 mM	90 s in 40% NH_4F
C	50%	50%	5 mM	90 s in 40% NH_4F
D	50%	50%	-	90 s in 40% NH_4F
E1	-	-	-	90 s in 40% NH_4F
E2	-	-	-	-

Table 5.2 Sample overview of testchips functionalized in UV light (soft UV photoreactor) for 3h.

only be limited by the availability of OSi-H groups in the surface.

While de-protection of the amino-group in the Boc-alkene surfaces has been demonstrated, the result has not been reproducible. The preliminary XPS data presented here show a shift associated with the de-protection that suggests a successful reaction is a significant fraction of the head groups. The contact angle measurements are in line with values reported in the literature on surfaces terminated with tBoc protected amino groups and after de-protection[74, 75]. The common procedure for de-protection of the amino groups consists of rather harsh chemical treatment of the samples with TFA which results in a surface with of mixed protonation states of the terminal amines as shown by XPS and resulting in a lowering of the contact angle after treatment. Re-establishment of the neutral head groups results in an increase in contact angle[74] and agrees with the values we measured.

5.2 Hydrosilylation by hydride abstraction: 10-*N*-BOC-amino-dec-1-ene

10-*N*-BOC-amino-dec-1-ene was used as a model system to study the attachment to silicon surfaces under different conditions using XPS. The protected amino-group provides both a label for detection in the XPS as well as a potential platform for the subsequent attachment of biomolecules via different conjugation methods.

As discussed above, the addition of Ph_3C dissolved in ethanol lead incorporation of ethanol into the surface layer while efficiently suppressing oxidation during the hydrosilylation reaction in UV light. To further investigate these two phenomenon and to better determine the origin of both effects, different mixtures of Boc-alkene, ethanol and Ph_3C-BF_4 dissolved in ethanol were prepared to functionalize testchips under UV irradiation and investigated with XPS. All sample chips were cleaned in Piranha acid and rinsed with MilliQ water before etching and washed in ethanol and dichloromethane after functionalization and before the measurement. Samples were characterized immediately after modification. The specifications of the prepared samples are

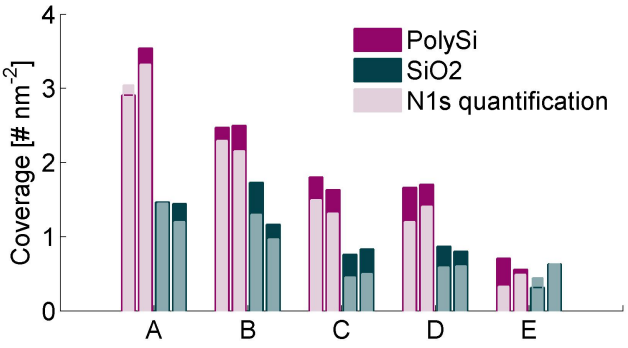

(a) SAM surface coverage

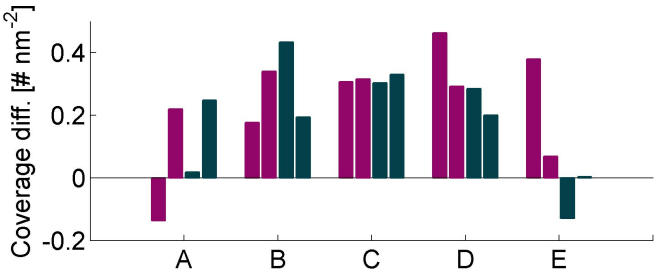

(b) Difference between coverages quantified by C1s and N1s spectral data

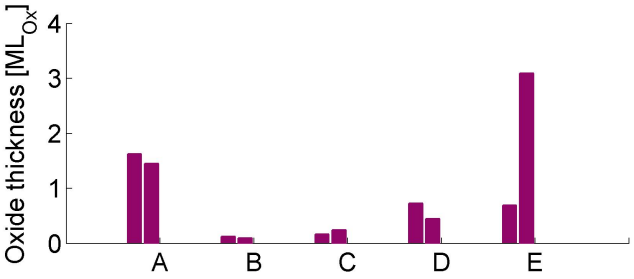

(c) Oxide thickness

Figure 5.5 SAM surface coverage and oxidation for Boc-alkene functionalized polysilicon surfaces. The graphs show different functionalization conditions with and without the addition of $Ph_3C\text{-}BF_4$ and ethanol. SAM coverage has been quantified using C1s and N1s spectra respectively to illuminate the influence of signal-to-noise of and surface contamination.

summarized in Table 5.2.

5.2.1 Ethanol incorporation and suppression of substrate oxidation

The data in Figure 5.5(a) shows the SAM surface coverage for the PolySi and SiO_2 surfaces for the conditions according to Table 5.2. Shown are two individual samples for each of the conditions. The first column of the reference samples E shows an etched surface that has been exposed to UV light without the addition of any solution, the second sample is an untreated reference surface with native oxide. Considering the coverages only, the neat reagent produces the highest surfaces coverage as observed before, with a maximum of 3.5 molecules/nm^2 while the coverage on SiO_2 is below 2 molecules/nm^2 for all samples. The reference samples show a similar amount of carbon contamination, on average corresponding to 0.5 $\pm$ 0.1 Boc-alkene molecules or 8 $\pm$ 2 carbon atoms per nm^2 across both surfaces. It should be noted that the N1s signal generally has a very poor signal-to-noise ratio with an estimated accuracy on the value corresponding to a coverage of 0.5 molecules/nm^2. Comparing samples C and D, which contain the same fraction of ethanol with and without addition of Ph_3C, we observe no difference in grafting efficiency. Samples B show a higher coverage for the same amount of Ph_3C and a ten times lower fraction of ethanol. Taking a look at the amount of oxide formed during functionalization, shown in Figure 5.5(c), we observe a decrease in oxide thickness for samples with Ph_3C irrespective of ethanol content, whereas the sample with added ethanol shows an oxide thickness comparable to that re-grown on the etched control surface, about 0.8 of a monolayer. Sample A functionalized with neat Boc-alkene shows a, compared to this, accelerated oxidation that reaches half the level of the native oxide thickness within 3 hours. Finally, considering the differences between the two quantification methods, shown in Figure 5.5(b), there is an increased discrepancy in samples with added ethanol, even though no clear trend can be seen as to the influence of the proportion of the solvent in the mixture.

We further investigated the role of UV irradiation on the grafting yield. Since no significant difference in terms of coverage was observed for the ethanol mixed samples with and without Ph_3C, its role in mediating hydrosilylation is unclear. Surfaces were prepared with alkene and Ph_3C/EtOH in a 90%:10% ratio, identical to sample B above, but with and without UV irradiation. The results are shown in Figure 5.6, clearly demonstrating that UV irradiation is responsible for a great proportion of the grafting of the Boc-alkene to the silicon surface.

5.2.2 SAM formation on Si(100) in air and in nitrogen atmosphere

Due to issues with reproducibility of some of the presented results on polysilicon, the following section focuses on the study of monocrystalline (100) silicon surfaces to further investigate grafting mechanisms in a more controlled manner. Since polysilicon contains a number of different crystal orientations, defect-rich grain boundaries and a variation of grain sizes, the hydrosilylation with alkenes and alkynes on its surface is necessarily more complex and inhomogeneous than on well defined monocrystalline substrates. To gain further insight into the mechanism by which the alkene is bound to the surface and especially to understand the suppression of

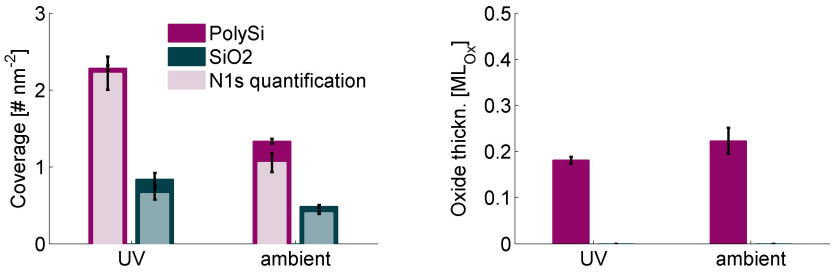

(a) SAM surface coverage (b) Oxide thickness

Figure 5.6 SAM formation in UV light and under ambient conditions by hydride abstraction using $Ph_3C\text{-}BF_4$.

oxidation, modification was carried out in the presence of $Ph_3C\text{-}BF_4$ under ambient conditions for an extended period of time. We want to investigate SAM formation and oxidation by hydride abstraction without activation by light. The experiment was carried out in air and in a nitrogen flushed desiccator to reduce the oxygen and water content in the environment (labeled: air and N_2 respectively). We have previously observed a suppression in oxidation and it has been reported that the process performed in air can actually lead to an increase in alkene attachment due to the spontaneous generation of silicon radicals by reactive oxygen species.

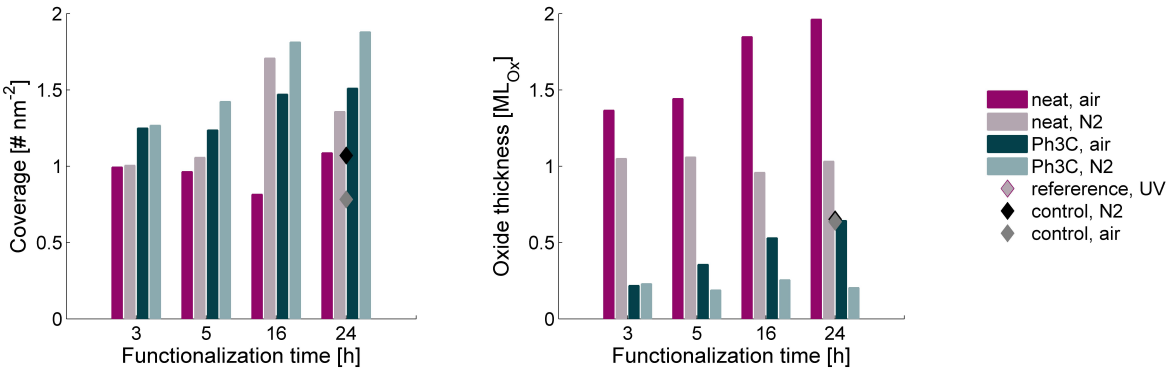

(a) (b)

Figure 5.7 SAM surface coverage and substrate oxidation on Si(100) surfaces for samples functionalized with neat Boc-alkene and with the addition of $Ph_3C\ BF_4$ in air and in a nitrogen flushed desiccator (N2). Etched references and the average of samples functionalized by UV grafting are shown as diamonds. Solid lines and symbols represent the C1s, dashed lines and empty symbols the N1s quantification values.

The progression of SAM formation in terms of yield is summarized in Figure 5.7(a). The highest yield is achieved in the presence of Ph_3C and with reduced oxygen (N2) and after 24h it is comparable to the yield achieved by UV grafting after 3h. The sample functionalized in neat reagent in air shows no significant progression and the yield falls within the lower limit of the signal-to-noise ratio, suggesting no grafting in this case (compare etched references). Figure

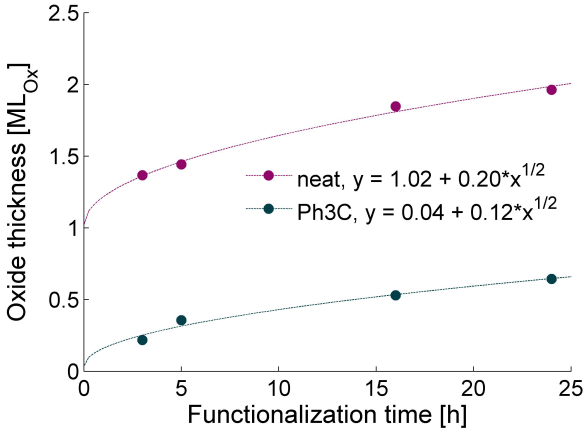

Figure 5.8 Oxidation of the Si(100) substrate during hydrosilylation in air, with and without the addition of Ph_3C. The curves are fitted to the square root of the incubatio time, with the equations given in the graph.

5.7(b) summarizes the oxidation on all samples. The controls included in the figures are etched surfaces that were exposed to the same conditions without the addition of a reagent for 24 h. Interestingly, there is no difference in the thickness of the oxide layer grown in air and the nitrogen chamber under these conditions. The oxidation in oxygen depleted atmosphere seems to be limited to a quarter of a monolayer in the presence of Ph_3C and 1 monolayer in the presence of the alkene alone without further oxidation over extended exposure to the same conditions. In the case of exposure to air, oxidation progresses throughout the full incubation time.

Figure 5.8 shows the oxidation curves for the functionalization performed in air. The curves are fitted to the square root of the incubation time, with resulted in the best fit. This behavior is typical for silicon oxide growth that is limited by diffusion of the oxygen through the oxide layer rather than a surface reaction, which results in a linear growth curve.

5.2.3 Discussion

The initial experiments on polysilicon surfaces with Ph_3C and ethanol confirm that Ph_3C efficiently suppresses oxidation during the functionalization of oxide-free silicon surfaces with Boc-alkene in ambient conditions. Neat alkene on the other hand increases the oxidation rate. Functionalization using the neat alkene results in the highest surface coverage compared to the mixture with ethanol. Comparison of the influence of UV irradiation in this process, confirms that not the addition of Ph_3C, but activation by UV light is primarily responsible for the grafting mechanism. Since alkene and oxygen are competing for incorporation into the surface, the light induced generation of holes and/or silicon radicals due to Si-H bond breaking influences both efficiencies similarly increasing both the yield and the amount of oxidation while the presence of Ph_3C leads to preferential incorporation of the alkene. Consistent differences in estimated surface coverage using the C1s and N1s spectra, respectively, can be observed for samples functionalized with solutions containing ethanol. This suggest a contribution from other carbon molecules to the

composition of the surface layer in this case. The high resolution C1s spectra from SiO_2 surfaces present the characteristic methylene peak associated with ethanol. Incorporation of ethanol into the surface layer is therefore likely and a reduced fraction of ethanol in the functionalization solution or use of a different solvent is recommended. We propose therefore that the sample preparation according to B yields the best results under the ambient conditions investigated here.

Considering the results on monocrystalline silicon under ambient conditions we note a few additional things. Firstly, the oxygen depleted atmosphere is not enough to prevent oxidation on the etched control sample, the level after 24h is exactly the same as for the sample exposed to air. Secondly, the addition of the functionalization solution in air does not decrease oxidation rates. On the contrary, while the addition of Ph_3C has no impact on the oxidation in this case, the lack thereof increases the amount of oxide approximately 3-fold. In nitrogen atmosphere on the other hand, addition of the functionalization solution seems to limit the oxidation after a specific level is reached. Here again, this level is about 4-fold higher for the neat reagent that with the addition of Ph_3C and in both cases is reached already after 3h.

This indicates that the amount of oxygen that is still present in the nitrogen chamber is not alone limiting oxide growth; rather the growth rate is limited by the interface reaction. In turn, the addition of Ph_3C does not seem to reduce oxide growth rate, but quenches an accelerating effect introduced by the presence of the alkene itself. Considering the amount of present oxygen directly, as observed in the high resolution O1s spectra shows the expected increased amount of oxygen on the samples with higher silicon oxide estimates (data not shown). This confirms that it is indeed silicon oxide that forms the observed Si-O bonds, and not a secondary chemical reaction that involves the Boc-headgroup of the molecule. In nitrogen atmosphere oxide formation does not proceed past the equivalent thickness of a single monolayer, whereas under the same conditions in air oxidation continues to proceed. The fact that an oxide is formed in the oxygen depleted chamber is clearly a sign for the presence of oxygen and insufficient exclusion. If the majority of the oxygen stems from dissolved oxygen and water in the alkene solution, this would explain why oxidation does not proceed past a certain point, when this source has been depleted. However, the equal oxide thickness in the two control samples contradicts this finding unless oxidation occurred mainly during sample handling outside of the chamber. Another possibility explaining the oxide formation on the control samples is the brief exposure to air during opening of the chamber to remove samples. This would provide direct access of oxygen to the surface in the case of the dry etched sample, while samples covered in alkene solution would be protected by the liquid. Oxygen would need to diffuse into the alkene solution first, a process that may not be sufficiently fast to enable considerable amounts of oxygen to remain before their removal by the next pump cycle.

The silicon oxide growth curves for samples functionalized in air displayed in Figure 5.8 show similar growth behavior for both cases. The mechanism of oxide growth in parallel to the hydrosilylation reaction is not straight forward and there are several possibilities. Firstly, oxide can grow in a layer-by-layer manner or in islands, where more that one monolayer exists in one place

and no oxide in another simultaneously. Furthermore, the oxides can form at the oxide/silicon interface, which requires the oxygen atoms to diffuse through the already formed oxide layers. Or it can form at the surface while unoxidized silicon atoms are available there.[76] The growth rate can be limited by the reactions at the silicon/silicon oxide and silicon oxide/alkene interface or by diffusion through the silicon oxide. Additionally the further oxidation of sub-oxides and presence of silicon clusters in the oxide film can play a role in oxide growth and these might be impacted by reactions taking place at the surface. However, since in both cases oxidation proceeds with the square-root of functionalization time we propose that surface reactions have no further effect on oxide growth at the investigated time scale. The absolute difference in oxide thickness at the first measurement point after 3 hours on the other hand indicates different reaction speeds in the initial phase of oxide formation. Assuming that Ph_3C does not diffuse though the oxide due to its size, it can only impact oxide formation at the silicon oxide/alkene interface and will only impact oxide growth in the initial phase where it can directly access the interface. This further indicates that the oxide grows in a layer-by-layer process rather than in islands, even in the presence of the competing alkene grafting. If this were not the case, we would expect to see an effect of Ph_3C on the the remaining silicon islands during further growth.

In line with the proposed mechanism in which a hydride ion is abstracted from the H-terminated silicon surface[33], the oxidation rate seems to be impacted in the initial time period before completion of the first monolayer, where the surface still presents accessible Si-H bonds. Considering a complete conversion of all Si-H bonds at that point, we would not expect significant incorporation of hydrocarbons and thus an increase in bound alkene. However, even though the estimated molecule coverage shows some outliers (16h, N_2, neat) there is a clear increase over time for all of the surfaces, which stands in contrast to that assumption.

Taking the estimated molecular coverage into consideration as well, the maximum surface coverage (shown to correspond to approximately 55% of a monolayer due to steric reasons[49]) is not seen in either of the samples. Oxidation competes with the formation of Si-C bonds that link the alkene to the silicon surface and an increased oxidation rate would be accompanied by a lower level of molecular coverage. This is clearly the case for the shown data of experiments performed under ambient light conditions. Irradiation with UV light changes this relationship. In either case, with and without Ph_3C, UV irradiation accelerates oxide formation resulting in thicker oxides after 3h of functionalization (triangles, error bars for 2 and 4 surfaces for functionalization with added Ph_3C and neat alkene, respectively).

The time series shows a slow progression of the hydrosilylation reaction after an initial quick onset, speaking for a mechanism with fast kinetics that is suppressed after an initial incorporation of a certain amount of material. There could be two reasons for the reduced incorporation rate after this first onset. One is steric hindrance after a certain density is reached, that makes subsequent attachment more difficult. Another interpretation is that the initial reaction is incorporating both alkene and oxygen into the surface layer until a mixed monolayer of full coverage is created. Subsequent attachment of the alkene would thus occur on the oxidized part of silicon

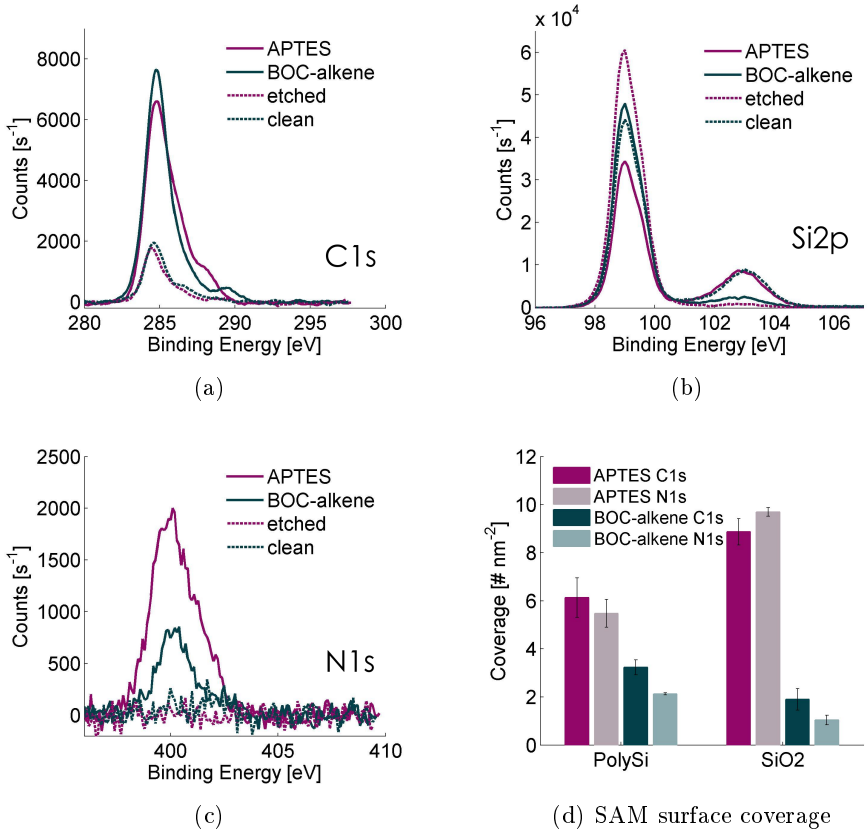

(a) (b)

(c) (d) SAM surface coverage

Figure 5.9 Comparison of surfaces functionalized with APTES and Boc-alkene. **a)-c)** High resolution XPS spectra. **d)** SAM surface coverage for APTES and Boc-alkene on PolySi and Silicon oxide surfaces.

and with a slower secondary mechanism or reduced efficiency.

5.3 Silicon oxide surface functionalization with APTES

One of the most common methods to attach proteins to silicon (oxide) surfaces is through silanization as described in 3.1.2. We adopted an optimized protocol for gas-phase silanization with (3-aminopropyl)triethoxysilane (APTES) from Karen Martinez group at Copenhagen University. Surface test chips were functionalized and characterized by XPS for comparison with Boc-alkene.

The high resolution XPS spectra shown in Figure 5.9 display a characteristic carbon spectrum on the functionalized surfaces, for both molecules, APTES and Boc-alkene. The amount of carbon is significantly increased compared to the control surfaces (etched and cleaned surfaces). The fitted C1s spectrum for APTES shown in Figure 5.10(a) shows differences in the fitted peaks compared to the Boc-alkene spectrum encountered previously in Figure 5.4(c). The peak position reflects the different chemical environments of the carbon molecules while the ratios between the different peaks provides insight into the structure of the monolayer. For an unbound APTES molecule we expect to see 3 different chemical environments as depicted in Figure 5.10(b). Elec-

trons originating from the carbon atoms at a (C-**C**H2-C), a' (C-**C**H2-Si) and a" (C-**C**H3) will have a very similar energy and they will all be included in the major C1s peak at 285 eV. Carbon atoms bound to more electronegative atoms such as oxygen or nitrogen will experience a larger (positive) chemical shift due to the depletion of electrons in the outer shells, leading to a higher binding energy. The value of the chemical shift can vary depending on the exact environment and we expect two resolved peaks for the C-**C**H2-NH2 and the C-**C**H2-O carbon atoms. However, if APTES is completely bound to the surface, the second peak should disappear, since the molecule is bound via a Si-O-Si bond eliminating the oxygen bound carbon. The agreement between the molecular coverages obtained from carbon versus nitrogen counts suggests a higher contribution from adventitious carbon in case of the Boc-alkene. The nitrogen count should directly reflect the number of molecules in both cases, since each contains exactly one nitrogen atom. We can see a coverage of 6 respectively 10 molecules of APTES per square nanometer for the PolySi and SiO_2 surfaces. Compared to 2 respectively 1 for the Boc-alkene. A coverage of 1 molecule per nm^2 falls below the noise threshold and can be disregarded as physisorption. As discussed previously, the hydrosilylation on silicon oxide surfaces is not expected to be very efficient and we would expect no attachment of alkene on this surface.

5.3.1 Discussion

Comparing the resulting coverages of APTES and Boc-alkene on the two different surfaces, we can clearly see an larger amount of APTES in both cases. Firstly, we note that the Boc-alkene coverage here does not correspond to the maximal values that were previously found in other experiments. This reflects the low reproducibility of the used functionalization process and shows that while it may be possible to achieve a higher coverage, our control of the experimental conditions is not sufficient to achieve this every time. Secondly, the coverage with APTES on PolySi corresponds to close to one APTES molecule per surface silicon, which exceeds the coverage expected for a well-ordered monolayer (4.3 in analogy to hydrocarbons on gold, which is often used as a reference). The coverage on the silicon oxide surface is even higher and indicates the formation of a double- or multi-layered structures in both cases. This is in line with the implications from the observed chemically shifted peaks in the carbon spectrum that indicate an incomplete crosslinking between the molecules.

5.4 Controlled hydrosilylation: Thermal grafting of 10-*N*-Boc-amino-dec-1-ene and 10-Undecenoic acid in argon atmosphere

After studying the grafting of organic molecules to different silicon surfaces in ambient conditions, the next important step is to compare the results with what is achievable using more controlled experimental conditions, such as exclusion of oxygen and elevated temperatures. These conditions significantly increase complexity of the experimental procedure and were therefore not investigated previously. The choice of molecules for this experiment is based on two considerations. Boc-alkene was used for comparability with the previously obtained coverages and

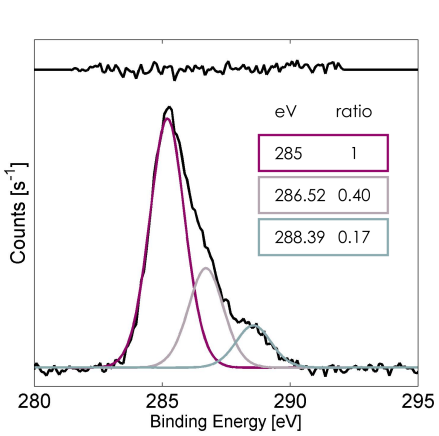

(a) C1s spectrum

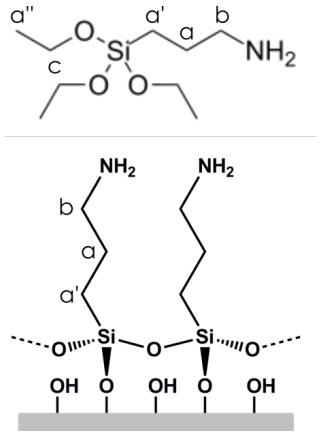

(b) APTES molecule: Unbound and bound to the surface

Figure 5.10 a) C1s spectrum of APTES bound to the silicon oxide surface. Peak energies are for different chemical environments as indicated. **b)** Molecular structure of the free APTES molecule and bound to the surface in a monolayer configuration.

to be able to use nitrogen as XPS marker and undecenoic acid was chosen due to the ease of protein conjugation to carboxylic acid-terminated surfaces that poses some advantages over amino-terminated surfaces. Octadiyne has not been studied further due to the added complexity and necessity of protocol optimization for subsequent protein conjugation via click-chemistry.

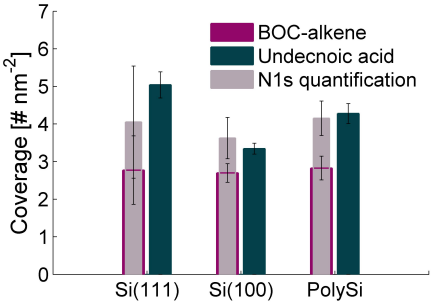

(a) SAM surface coverage

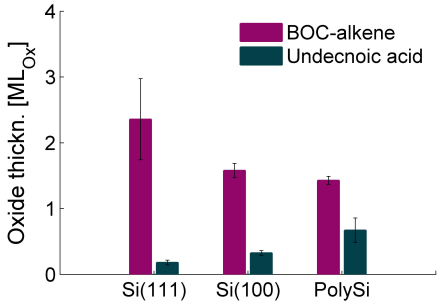

(b) Oxide thickness

Figure 5.11 SAM surface coverage and oxide thickness of undecenoic acid and Boc-alkene on different silicon surfaces functionalized in argon atmosphere at 150°C for 90 minutes

Figure 5.11 shows the SAM surface coverage and oxidation data for thermally functionalized surfaces. Coverages are generally higher than what was previously achieved in ambient conditions. There are small variations in the yield, with Si(111) showing the highest coverage for undecenoic acid and Si(100) the lowest. The values for Boc-alkene show a larger spread and are similar within the accuracy, but there are larger differences in the C1s and N1s quantified samples than previously observed. Looking at the oxidation we can see a significant increase

in the amount of oxide on the Boc-alkene functionalized surface over the functionalization in ambient conditions. The Si(111) surface presents hereby an equivalent thickness of 2.3 ML_{Ox} while Si(100) and PolySi surface lie below that with approximately 1.6 and 1.4 ML_{Ox} respectively. The oxidation for the undecenoic acid functionalized surface is considerably lower for all surfaces, showing opposite behavior. The largest amount of oxide is found on the PolySi surface with 0.7 ML_{Ox}, the least on the Si(111) surface with 0.2 ML_{Ox}.

5.4.1 Discussion

The large amount of surface oxide for the Boc-alkene surface is very surprising, since the experiment was performed in argon atmosphere and the presence of oxygen should be limited to leftover traces in the reagent. Additionally, the underestimation of the coverage from the C1S spectrum compared to the N1s counts indicates a loss of carbon from the attached molecules. These two findings indicate that de-protection of the amino group occurred under these thermal conditions. This would lead to an overestimation for the attached alkene and can produce release additional oxygen containing groups into the solution which are responsible for the observed Si-O bonds. The method is therefor not suitable for grafting of Boc-protected amino groups to silicon surfaces. The investigation of undecenoic acid surfaces can be found in the following chapter, pending publication.

5.5 Surface functionalization of oxide-free silicon for biosensing applications

Andrea Pfreundt, Sergey Chernyy, Dorota Kwasny, Karsten B. Andersen, Kristoffer Almdal, Maria Dimaki, and Winnie E. Svendsen

Unpublished manuscript has been removed for publication of the thesis.

6 | Summary and Conclusion

6.1 Note on the accuracy of the quantification data and possible data correction methods

Due to the assumptions made for some of the scenarios and the approximations that are used, there is an inherent inaccuracy when quantifying XPS data. Some of the weaknesses of the model will be outlined here briefly. The used model assumes complete monolayers that are uniform across the measured area and will not account for inhomogeneities. It will therefore average out accumulations of material such as aggregates of polymerized reagents and report a higher surface coverage in that case. Samples were inspected with an optical microscope to ensure that there are no visible traces of precipitated material. If this was the case, for example if the reagent was too old, the sample was discarded. Inhomogeneities on a smaller scale, such as island formation, will not be detected with either of the used methods. The model further does not include contributions of the partially oxidized silicon on surfaces with SAMs. A thin oxide film would lead to an additional attenuation of electrons originating from the underlying substrate. A correction for this additional film could easily be included in the model, but it is unwise to do so on the grounds that these oxide layers often show sub-monolayer coverage. It is unclear if oxidation occurs preferably in areas with less carbon (which would be a reasonable assumption) or if and to what extent it can grow underneath such layers. Attempts have been made to distinguish the two cases from the data and adapt the model to include the appropriate correction terms. But due to the low signal-to-noise ratio and the high sample-to-sample variation this did not yield meaningful results.

6.2 Functionalization of oxide-free silicon surfaces

As demonstrated in this chapter, we have successfully modified oxide-free silicon surfaces with organic molecules. Near maximal coverage could be achieved for both 10-N-Boc-amino-dec-1-ene and 1,7-Octadiyne, even under ambient conditions. For 10-N-Boc-amino-dec-1-ene a considerable amount of oxide formation was observed under all conditions. This could to some extent be suppressed by the addition of triphenylcarbenium tetrafluoroborate dissolved in ethanol. The carbocation addition resulted in the efficient suppression of up to 90% of the oxidation under ambient and conditions and under UV irradiation. From experiments with the exclusion of oxygen it is further likely that triphenylcarbenium acts in the initial phase of the reaction, limiting the

competition of oxidation with the hydrosilylation process. At the same time, the incorporation of ethanol into the surface could be observed when used as a solvent and a reduction in the amount of this solvent improved the result. For further investigation of this process it would be advised to test different solvents such as toluene or directly dissovle the salt in neat alkene or alkyne to prevent solvent contamination of the surface.

The thermal hydrosilylation process performed under argon atmosphere resulted in the best yield and was investigated for undecenoic acid and 10-N-BOC-amino-dec-1-ene. The BOC protective group is likely removed in the thermal process and considerable amounts of oxide formation could be observed. This makes this process unsuitable for the molecule. For undecenoic acid very good coverages with low amounts of surface oxidation could be achieved, already after a hydrosilylation time of 90 minutes. The process was performed on three different silicon substrates to investigate the influence of the underlying crystal structure and the presented surface on the functionalization process. In addition to the SAM coverages investigated with XPS measurements, the resulting COOH-terminated surfaces were further used for the immobilization of protein decorated gold nanoparticles. This demonstrate the ability to used these platforms as a substrate for bio-functionalization in a biosensor and enabled us to further investigate the effect of surface coverage on particle density. Our preliminary results show a particle density that is correlated with the surface coverage.

The next step to further optimize the attachment of biomolecules on the sensor surface would be the investigation of mixtures of alkenes and alkynes with and without functional head groups. This should make it possible to tune the number of head groups in the surface layer and thus impact the efficiency of protein attachment. Initial experiments using these mixtures were unsuccessful, due to unequal evaporation in the reaction vessels. Better control of the atmosphere and choice of reaction vessels should make it possible to perform hydrosilylation reactions in well defined mixtures of alkenes and alkynes.

II | Label-free detection of biomolecules

7 | Introduction to biosensors and label-free sensing

The essence of any biosensor is to convert an event involving biological material into an electronic or otherwise interpretable signal. This is a very broad definition since the biological material can be protein, DNA or other macromolecules but also whole cells, tissues or microorganisms and the sensing element or transducer can take many different forms. For the purpose of this thesis the following chapter will focus on impedance or resistance based biosensors for the detection of biological binding events and will introduce alternative concepts for comparison that detect similar events or used comparable methods.

7.1 Biological assays

The detection of specific biological target molecules from complex mixtures is often a routine task in biological research, diagnostics or forensic science. Many different forms of assays are readily available that use bioconjugates, linked complexes of proteins, chemically active compounds and nucleic acids that provide several functionalities. Often, several antibodies are used as targeting molecules in combination with detection labels such as enzymes or fluorescent dyes. Such assays commonly involve a purification or extraction step which enriches the target and removes most of the other material. This step can be done by a targeting molecules linked to a solid support such as a gel-matrix, membrane, beads or nanoparticles that allow for binding, washing steps and subsequent extraction of the purified component. The detection can be done by optical means, using fluorescent or luminescent probes or enzymes that produce a detectable signal in the presence of the relevant substrate. The number of available assays is probably as plentiful and diverse as are their biological targets and their role in almost every aspect of medical testing is paramount. What is common among the established methods is the use of labels for detection. While labeled techniques have undergone tremendous advances in terms of detection limits and sensitivity, they require the use of specifically designed and produced labels and amplification techniques. As an alternative label-free techniques offer the possibility to reduce the amount of expensive reagents needed and simplify assay protocols.

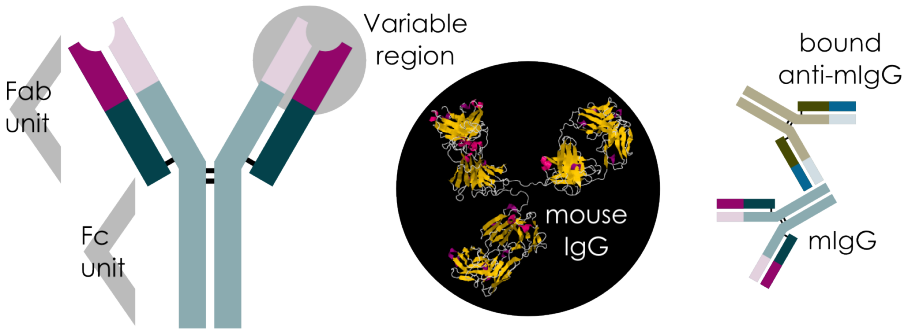

Figure 7.1 Left: Illustration of the general antibody structure. Center: protein structure of mouse Immunoglobulin G. Right: anti-mouse IgG can bind to the Fc unit of mouse IgG.

7.1.1 Antibodies

Antibodies or immunoglobulins (Ig) are proteins produced by the immune system to identify and fight foreign substances. Their structure can differ between different organisms and there are several types, but most commonly and antibody is thought of as Y shaped protein with a stem and two arms as shown in Figure 7.1. The stem consists of two so called Fc units and a top part of two Fab units with variable identification centers. These identification centers are generated randomly by the body to create a vast amount of different proteins that can identify potential threats. The ones that encounter a complementary structure they can bind to are incorporated into immune cells that circulate in the body. Due to the invariable part of each category of immunoglobulin, these can be used to extract all the proteins of this type from an organism. Since antibodies are made to bind to many different kinds of structures, they are commonly in conjugation with labels (fluorescent, radioactive, enzymatic) to identify structures in tissues or on cells for diagnostic purposes.

7.1.2 Protein-protein interaction

Binding between macromolecules at the scale of proteins is complex and governed by thermodynamic principles, meaning that it is not a straightforward process but a matter of statistical probabilities. The binding kinetics of two interacting proteins are characterized by their affinity constant, or the more commonly used inverse, the dissociation constant. These experimentally determined values[102] are defined by the number of unbound proteins, the ligand and receptor (without ligand), and the number of bound complexes (receptors with a ligand).

$$k_D = \frac{[Ligand][Receptor]}{[Complex]} \tag{7.1}$$

The unit of the dissociation constant is concentrations (mol/L or M) and the value represents that concentration of ligand at which exactly half the receptors will be occupied (since this leads to [Receptor] = [Complex]). Therefore, the smaller the dissociation constant, the stronger is the binding. It can range down to 1 fM in the case of Biotin-(Strept)avidin, which is a rare case of extremely strong binding between proteins. Typical values for good binding between two

proteins are in the nM range, but there is often a high level of uncertainty and disagreements in the literature due to several reasons. Firstly, the conditions to study binding kinetics and in which the k_D is determined needs to be identical to those in which the binding is performed, since parameters such as pH, salt concentration, temperature, and interference of other molecules play an important role and can impact the binding constants considerably. Secondly, one of the most common methods used for determination of binding constants is surface plasmon resonance (SPR). This technique requires a deep understanding of the involved processes and models. Much of the published literature lacks this necessary standard as judged by leaders in the field.[103] It is therefore essential to carefully consider the parameters that will influence the dynamics of protein-protein binding for each particular case and optimize protocols accordingly. Additionally, if one of the proteins is immobilized on a substrate there are further factors that need to be considered such as orientation of the tethered protein and surface topology of the substrate. Especially for the development of novel sensing schemes using affinity based biosensors, such as the silicon nanowire BioFET discussed below the appropriate choice of immobilization and characterization methods is imperative.

7.1.3 Protein Immobilization on Organic surfaces

Conjugating proteins with different functional elements or other proteins is routinely done in solutions for various kinds of biological applications. Conjugation refers to the process of chemically coupling two functional groups to permanently or reversibly create a link between the two. Proteins are made up of amino acids which provide a multitude of different functional residues that are suitable for coupling reactions. The methods employed in this work rely on the coupling via amino (-NH_2) or carboxylate (-COOH) groups which are present as residues on lysine (Lys) and glutamic acid (Glu) as well as the N and C terminus of each protein respectively. Figure 7.2 gives an overview over the surfaces and conjugation methods that were used in this thesis.

Copper catalyzed Azide-Alkyne cyclo-addition (CuAAC) for protein immobilization

Immobilizing proteins using functional groups, that are not natively found in the molecules can provide an additional means of control over the binding location and open new opportunities for selective immobilization.

The Azide-Alkyne Huisgen Cycloaddition is one of the corner stones of a group of chemical reactions referred to as click chemistry, as first introduced by Sharpless[104]. The 1,3-dipolar azide reacts with the dipolarophile alkyne to form a triazole as illustrated as process A in Figure 7.2. This reaction is usually performed under elevated temperatures and requires several hours to obtain a considerable yield. The use of Cu(I), provided by $CuSO_4$ with the addition of a reducing agent such as ascorbic acid as a catalyst increases the reaction speed immensely and is widely used for bioconjugation.[105] This is often enhanced by the addition of appropriate copper ligands that provide better stability or catalytic activity of the reduced copper. Copper free click chemistry[106] is used where the cytotoxic effects of copper forbid its use, as for the direct labeling of living cells. For biosensors, this functionalization scheme provides the means to create a clickable platform, which can be used for quick and specific attachment of biomolecules to the

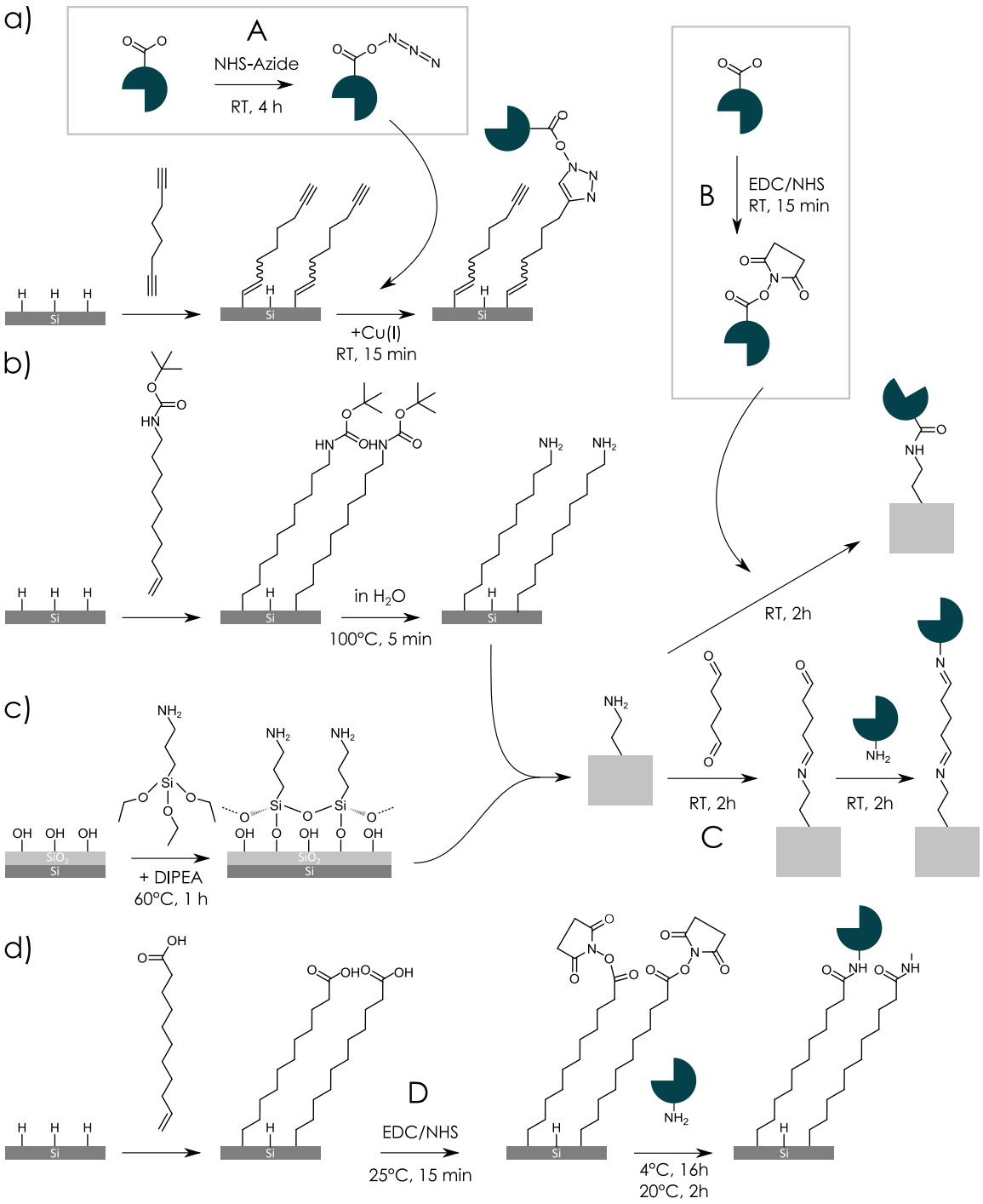

Figure 7.2 Protein immobilization on different surfaces. a) Alkyne-terminated surface by Octadiyne modification. Protein immobilization using Azide-conjugated Protein via Copper assisted cycloaddition (A). Amine-terminated surface by b) Boc-alkene functionalization and subsequent removal of the Boc-group or by c) APTES functionalization of silicon oxide. Protein immobilization using EDC/NHS-activated protein (B) or glutaraldehyde as a linker (C). d) Carboxyl-terminated surface by functionalization with undecenoic acid. Protein immobilization after surface activation with EDC/NHS (E).

sensor surface. By grafting of an α,ω-diyne to the silicon surface, an alkyne-terminated tightly packed monolayer can be obtained that is highly stable and inert under a range of conditions[107] making it an ideal precursor for further functionalization. To achieve this, the protein needs to be previously conjugated with the azide group, which is not natively found in amino acids. This provides an additional level of control over the location of this additional group on one hand but adds an extra step to the conjugation protocol that needs to be optimized for high yield of usable product.

Conjugation of primary amines and carboxylate groups by aminocoupling (EDC/NHS)

Amide bonds are the bonds that connect the individual amino acids in the protein chain. They are formed in a reaction between a primary amine and a carboxylate group, which are therefore present on each amino acid molecule. Aminocoupling can be done in several ways, one of which is using N-hydroxysuccinimide (NHS) and 1-Ethyl-3-[3-dimethylaminopropyl]carbodiimide (EDC) and is therefore often referred to as the EDC/NHS conjugation methods. As Figure 7.2 shows, EDC reacts with a carboxylate group present in the protein (B) or on the surface (D) to form an amine-reactive O-acylisourea intermediate. This intermediate hydrolyzes quickly in aqueous solutions and regenerates the carboyl, but forms a more stable amino-reactive ester in the presence of NHS or Sulfo-NHS. Thus, in the presence of accessible primary amines, a stable amide-bond can be formed formed.[108] This is typically done in a two step reaction, since the conditions required for the efficient progression of each reaction are different. The first step is performed in MES buffer at low pH (pH 6) to create the esters, which should then be stable for several hours. The second step, the aminocoupling, is more efficient at higher pH and is performed at pH 7 or pH 10 in PBS.

Conjugation of amino groups by reductive amination using glutaraldehyde

Another way to immobilize proteins via amino groups is by a process called reductive amination which forms an amide bond with an aldehyde group. Using the symmetric, bi-functional liker molecule glutaraldehyde two amino groups can be coupled, one on the surface and one on the protein to be immobilized as shown in Figure 7.2, process C. Aldehyde groups readily form so-called Schiff bases with terminal amines in a slightly to strongly basic pH between 7 and 10. However, this bond easily hydrolyzes in aqueous conditions and needs to be reduced to make it stable. A reducing agent, sodium cyanoborohydride, is used to provide an additional electron and results in formation of a stable amide bond. The immobilization needs to be done in two steps, first linking glutaraldehyde to the surface bound amino groups resulting in an aldehyde terminated surface and them immobilizing the protein on this surface. This ensures that no crosslinking and aggregation of the protein can occur in solution.

7.2 Label-free sensing

As the name implies label-free sensing differs from labeled sensing in the choice of transduction methods. While labels can be used to generate, enhance or transform the signal that we want

to detect, label-free methods need to make use of properties that are inherent to the molecules studied and directly induce a measurable signal in the transducer element. The differentiation between the two is, however, fluent. Consider the example of gold nanoparticles used as a label in solution compared to a gold surface in a label-free setup. Both measurement signals could be based generated in the same way, relying on the same properties of the analyte, such as surface plasmon resonance or Raman spectroscopy. Especially the latter could benefit from roughened surface (Surface Enhanced Raman Spectroscopy) on the nanoscale, which would employ the same amplifying effect that the nanoparticles make use of. Now, binding the nanoparticles to the surface first would then technically be label-free, even though it differs neither in the use of reagent or involved components. A clear definition of label-free is therefore not trivial and I will refrain from giving one since this inevitably leads to some ambiguous cases. General statements about one or the other are most often not meaningful due to the vast variety of technologies in both and there is no need for strict classification.

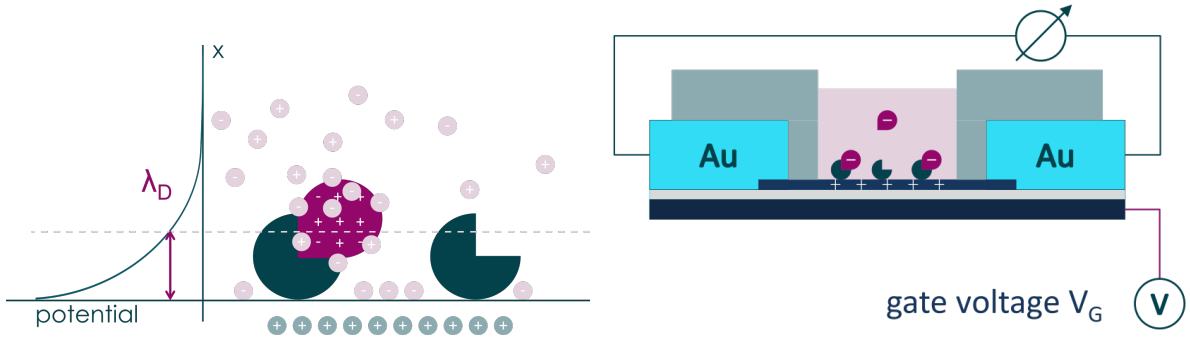

(a) (b)

Figure 7.3 a) Illustration of screening in electrolyte solution and the Debye length. **b)** Operation principle of the SiNW BioFET: The silicon nanowire is separated from the substrate by a silicon dioxide layer and on top enclosed in a microfluidic channel that passivates the surface contacts.

7.2.1 Charge sensing: The field effect transistor (FET)

A field effect transistor is a semiconducting channel, the conductance of which can be influenced by electric fields in its vicinity. This is the basic principle of transistor technology used in integrated circuits, in which this field is generated by a gate electrode and provides a way to turn the current flow on and off. This is the digital version, where the most important characteristic is the dynamic of the on/off switching which determines speed and energy consumption of the logic circuits. The other way around, and now considering the analog behavior of the transistor, by measuring the current flow through the channel, it is possible to gain information about the applied field at the gate. Since an electric field is generated by an applied voltage or any other change in potential, this setup can be used to measure changes in the charge distribution close to the conducting channel. Numerous different versions of sensors employ this principle, possibly the oldest being the ion-sensitive field effect transistor (ISFET)[109] which detects the presence of ionic species on the surface of the gate by appropriate surface modifications responsible for

selectivity. Charged small molecules such as ions are an obvious target for this type of sensor system and pH sensing has become a routine application for ISFETs[110]. From there, several groups have focused on transforming the technology for biosensing[111, 112], a task that adds the complexity of biological molecules into the equation. While the charge of a small ion is well-defined and localized, a macromolecule such as a protein is typically composed of hundreds of amino-acids with various ionizable residues. The advent of nanomaterials for sensor systems has given rise to a modified version of the thin-film ISFET, in which a wire or tube of different geometries and materials is used as the channel to increase sensitivity and enable novel fields of application.[113, 75, 83]

7.2.2 Pushing the sensitivity limit: Silicon nanowire BioFET

By confining the electrons in the FET channel to a nanometer sized wire, the flow of electrons can be controlled by very small changes in surface properties. The sensitivity of such a semiconductor charge sensor is to a large degree characterized by two screening lengths, the Debye-Hückel length λ_D and the Thomas-Fermi length λ_{TF}. A screening length describes how much a potential is weakened in a given environment, and is defined as the length at which a given potential is reduced to 1/e of it's initial value. The two lengths characterize hereby the two environments outside and inside of the nanowire material.

The Debye-Hückel length describes the screening of surface charges by ions in an electrolyte solution. Any charged surface that is immersed in an electrolyte solution will attract ions of the opposite charge towards it. These charges screen the potential that is created by the surface charge, leading to an exponential decrease of electrical potential with distance from the surface. The approximation for dilute ions that follow the Boltzmann-distribution gives us the Debyle-Hückel length (or just Debye length)

$$\lambda_D = \sqrt{\frac{\epsilon\epsilon_0 k_B T}{2N_A e^2 I}} \tag{7.2}$$

Where k_B is the Boltzmann constant, T is the temperature, N_A is the Avogadro constant, e is the elementary charge and I is the ionic strength of the solution, which depends on the concentration c of the ions and their charge number: $I = 1/2 \sum c_i Z_i^2$.

This length can be thought of as the distance within which a charge will have an effect and it applies just as well to particles or molecules in an electrolyte solution as to a flat surface. The potential that is created by any charge distribution will be diminished by the ionic strength of the solution as long as the ions have access to it. For a charge based sensor this means, that any analyte residing on the sensor surface will be subject to screening as long as ions can access the space around the analyte. Typical screening lengths are of the order of a few nanometers, which corresponds to the size of most proteins and is therefore an important factor to consider. Table 7.1 gives the Debye lengths for some buffer solutions that are typically used in sensing experiments and protein conjugation.

The Thomas-Fermi length describes the screening inside the nanowire material that is medi-

Buffer	Ionic Strength [mM]	Debye length [nm]
1x PBS	162.7	0.76
0.1x PBS	16.2	2.41
0.01x PBS	1.6	7.61

Table 7.1 Ionic strength and Debye length of different concentrations of PBS at room temperature ($T = 300K$) at pH 7.4.

ated not by mobile ions, but by freely moving charge carries (electrons and holes). This length is derived from the Thomas Fermi model for the description of the charge carried distribution inside a semiconductor. The model assumes a uniform distribution of charge carriers and a constant chemical potential. Furthermore it only considers the local potential and charge carrier concentration in each point, which practically means that the model is only valid for small perturbations on a given applied potential (where the change can be assumed to be linear). The resulting length reads as follows for an n-type semiconductor (for p-type, the hole concentration p is used in analogy)

$$\lambda_{TF} = \sqrt{\frac{\hbar\epsilon\epsilon_0\pi^{3/4}}{me^2 3n^{1/3}}} \tag{7.3}$$

where m is the mass of the electron.

7.2.3 BioFET-SIM: A tool for the simulation of BioFET responses[1]

BioFET-SIM is a program and web application for the simulation of some aspects of charge based biosensing with silicon nanowire bioFETs. Based on a theoretical model developed by de Vico *et al.*[91], parameters such as dimensions, doping concentration and other properties of the device as well as detailed computational models of the biomolecules in question are taken into account to predict changes in conductance or measurement signals.

The model assumes a perfectly rod-shaped semiconductor nanowire of a uniform internal structure. The wire dimensions are characterized by length, radius and oxide thickness, the material properties by charge carrier concentration, mobility and the internal screening length λ_{TF} (Thomas-Fermi length). The outside of the wire, which contains the biofunctional layer and the electrolyte solution, is characterized by the Debye screening length λ_D and the chosen protein, which is modeled to great detail. The conductance sensitivity, or differential conductance, that is used to fully describe this system, reads as follows:

$$S = \frac{\Delta G}{G_0} = -\frac{2}{Rep_0}\Gamma\sum_i(\Gamma_{l,i}\sigma_{b,i}) \tag{7.4}$$

The parameters Γ and Γ_l are the defining functions that result from the specific solution of the differential equations used to describe the system. Their derivation and exact definition can be found elsewhere[1, 114]. Γ takes on a value between 0 and 1 and describes the overall sensitivity of the nanowire to external charges. Γ_l is a term that includes the location of the charges,

characterized by their distance from the nanowire surface. The last parameter in the equation σ_b finally characterizes the protein or molecule that is being investigated, by its charged groups. σ is calculated based on a model of the protein, which can be obtained from large databases such as the protein data bank[115], using the PROPKA algorithm[116]. The algorithm determines the pK_a values for all ionizable groups in the protein in an iterative fashion that takes into account the interaction between different groups in the closely packed 3D structure of the macromolecule. Considering all influencing factors is of course not feasible and the obtained values are naturally an approximation that does not include the influence of interfering ionic species in solution and the presence of water molecules. Nevertheless, close agreement with experimental values has been reported and with regard to the complexity of the system this is a considerable achievement. Using these pK_a values and a given pH of the solution, charges are assigned to the ionizable groups in their appropriate location. A 3D model of the result of this modeling is then shown in the software and it is possible to manually adjust the orientation of the whole complex with respect to the surface. By changing different simulation variables it is then possible to calculate and plot sensitivity curves with respect to changes in pH, ionic strength of the solution (these are treated as independent parameters, which they are not, so they need to be adjusted accordingly).

8 | Materials and Methods

This chapter introduces the silicon nanowire field effect transistor (SiNW BioFET) that was fabricated in-house and functionalized for to be used as a biosensor. Different measurement setups are described that were used at different stages of the project. The simulation tool BioFETsim was used for simulation of protein binding in different conditions it investigate the impact of orientation and binding kinetics with the help of a simple model. Since the tool only generates data for limited configurations, the relevant formulas to gain further knowledge from the simulated dataset are derived in this chapter.

8.1 SiNW Sensor setups and measurement system

8.1.1 SiNW BioFET sensor chip

The silicon nanowire sensor chips used in this work were fabricated by my colleague Azeem Zulfiqar as part of his PhD research.[55] For the full fabrication process and specifications please refer to the thesis given in the reference above.

The layout of the sensor chip is a die of 17.5 by 5.5 mm as displayed in Figure 8.1, consisting of a connector pad with electrodes, and a sensing area that is passivated with an opening in form of a microfluidic channel to allow access to the sensors. Each die or chip includes 4 nanoribbons individually connected to electrode pads in the connector area of the chip. In addition, there are two so-called side-gates (one for two wires each), additional electrodes in close proximity to the wires, that are connected to an additional electrode pad. As test structures during fabrication two more ribbons are patterned onto the chip, but are not connected in the conducting layer.

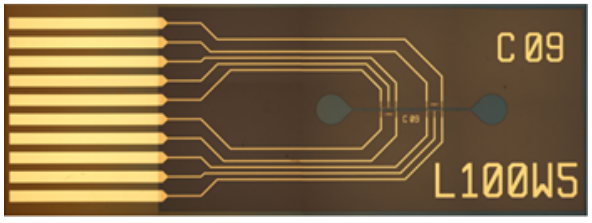

Figure 8.1 Photo of the SiNW chip after fabrication and dicing. To the left we can see the contact pads with leads to the sensing area. Four wires are connected in the microfluidic channel in the center. The number on the top right identifies the die, the lower number indicates the nominal length and width of the individual wires on this chip in μm.

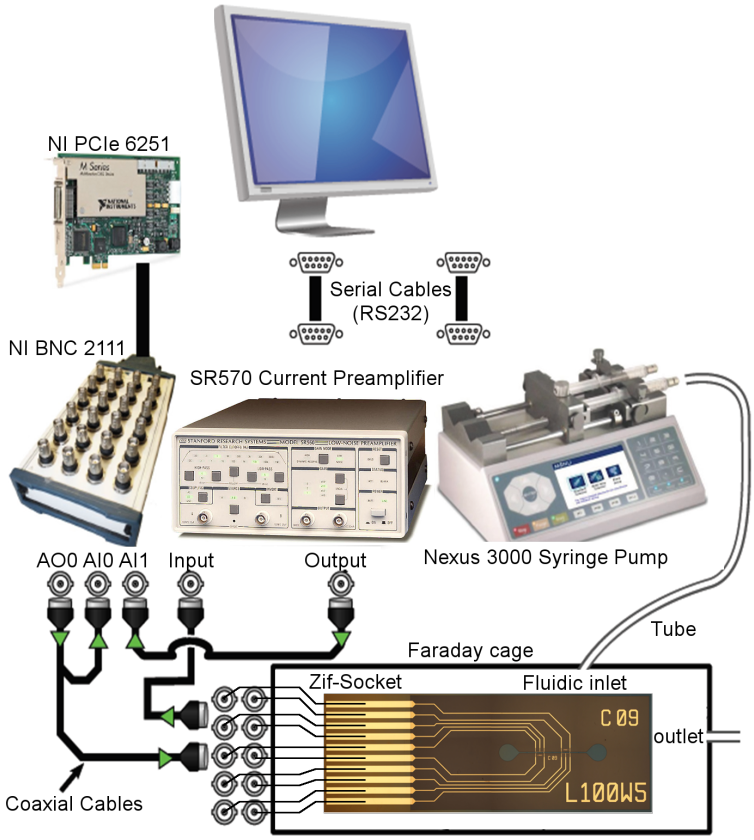

Figure 8.2 The image shows a schematic of the original measurement setup.

8.1.2 SiNW BioFET instrumented measurement setup

The measurement setup that was used initially, was designed and built by Michael Jørgensen and is depicted in Figure 8.2. The basic idea is to apply a voltage between source and drain of the nanoribbon sensor and continuously measure the current. This makes it possible to detect changes in the nanoribbon conductance that may be induced by molecules at the sensor surface. The setup consists of a current pre-amplifier, a multichannel digital-to-analog converter that is connected to the PC via a PCI card (DAC card) and the sensor chip contained in a Faraday cage to reduce electrical noise. The Faraday cage contains switches to establish electrical connections between two coaxial cables and each of two terminals of a nanoribbon sensor on the chip. Outside the cage, one of the wires is connected to a terminal on the DAC card through which the voltage is applied. The other cable is connected to the current pre-amplifier, which reads the current and converts it to a voltage signal that is passed on to the DAC card. The whole system is operated using LabVIEW software, in which the applied voltage can be specified as a sinusoidal signal. The current is recorded simultaneously as a continuous signal so that the complex impedance can be calculated for each period. This makes it possible to determined both the conductance of the semiconducting channel and the phase shift between the two which is indicative of trapped

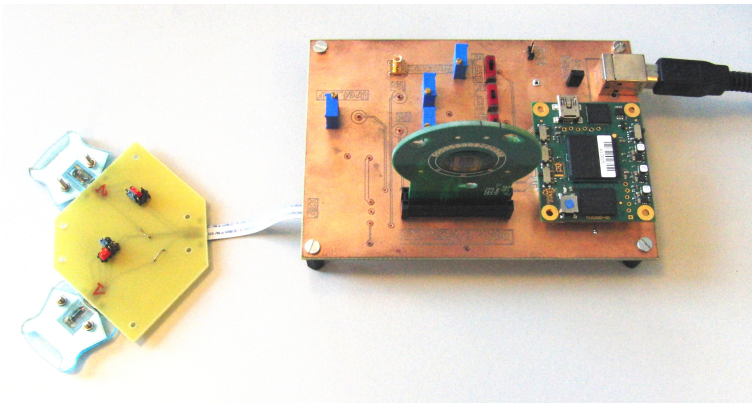

Figure 8.3 Schematic of the CMOS measurement setup. Adapted graphic from [117].

charges at the contact surfaces or interfaces.

Details on the software parameters and instrumental settings are omitted here since they are not relevant to the discussion of the results and can be found elsewhere.[117]

8.1.3 SiNW BioFET CMOS measurement setup

As an alternative to the previous setup and as a step towards systems integration a second measurement setup was used. This setup, shown in Figure 8.3 has been developed at the group of Andreas Hierlemann for use with different types of nanowire sensors.[118] It consists of a PCB board which serves as the basis to hold the separate components. The central part is a CMOS integrated circuit chip which encompasses all the amplification and conversion functionality for several separate channels. The SiNW sensor chips are plugged into the board directly, or via an additional adapter device that allows for more flexibility. The adapter board shown in the image is used to connect two chips to the same input port. This is necessary for this particular demonstrator setup, since each of the ports uses a different conversion method. To keep the data from two chips identical (for comparative measurements with a control) it became necessary to split the 4 channels contained in the plug-in port into two for each chip. 4 separate channels (nanoribbons) can be recorded simultaneously where the applied voltage is the same on all and the current readout is independent, i.e. no phase information is contained in the data.

Data analysis of the recorded data was done using specifically developed MATLAB scripts for each of the measurement setups. Some of the scripts can be found in the Appendix B.3.

8.2 Simulation of sensor responses to protein binding using BioFET-sim

The tool that has been introduced in the introduction to this part was used to generate a number of basic datasets using 2 different proteins. To analyse mixtures of different protein orientations

and discuss the impact of binding kinetic, we are deriving the relevant relationships based on the charge model used in BioFETsim in the following section.

8.2.1 Impact of receptor orientation on initial sensor response

We are interested in how the response of the nanowire sensor can be influenced by immobilizing the protein with different orientations. Since the used immobilization technique will potentially influence the orientation of the protein, different techniques can lead to different results.

We can imagine that the functionalization of the sensor surface results in a mixture of different orientations. Both due to unspecific binding and because, depending on the method, the targeted functional groups are often present in multiple locations on the protein. Considering such a mixture can easily be implemented in the model, by extracting the raw data of the sensitivity versus Debye length for each orientation and combining them. Since the model relies on a linear relationship between charges, number of molecules and sensor response as shown in Equation 7.4, we can use a linear combination of the different datasets to represent the mixtures.

$$S_R = S_{total} = \Delta G/G_0 = \sum_{i=0}^{3} f_i S_i \tag{8.1}$$

The fractions f_i represent the fraction of the total number of molecules on the wire, that are immobilized in orientation i.

8.2.2 Impact of ligand binding on the sensor response (Sensing signal)

Protein detection or quantification with a silicon nanowire BioFET relies on the transduction of a binding event into a measurable electrical signal. The detected analyte is the ligand that binds to the immobilized receptor and in the following we will evaluate some possible scenarios and their implications on sensor response.

The conductance sensitivity scales linearly with the charge term, which considers the number of charges i and their distances l from the surface. This particular charge term describes the effect of the receptor, which is calculated by the applet when loading and orienting the protein:

$$\sigma_R = \sum_i (\Gamma_{l,i}\sigma_{R,i}) \tag{8.2}$$

A similar expression exists for the receptor plus ligand:

$$\sigma_{R+L} = \sum_i (\Gamma_{l,i}\sigma_{R+L,i}) \tag{8.3}$$

The contribution from the ligand only can thus be extracted as simply the difference between the two terms.

$$\sigma_L = \sum_i (\Gamma_{l,i}\sigma_{R+L,i}) - \sum_i (\Gamma_{l,i}\sigma_{R,i}) \tag{8.4}$$

Since the sensor response S is proportional to the charge term, we can simply calculate S_L from S_R and $S_{(R+L)}$ by linear combination of the two datasets.

In a real measurement, it is likely that we are operating the sensor below the saturation limit, i.e. that only a fraction of the receptor molecules are bound to a ligand. Firstly we will consider the simple case, in which the sensors surface is covered with receptor molecules in a single orientation and calculate the response for different surface concentrations. As metric we will use the percentage of occupied receptors on the surface s. The resulting sensor response scales linearly (in this model) and can be calculated as the differential signal from the total binding response

$$S_{Binding}(s) = [(1-s)\, S_R + s S_{R+L}] \tag{8.5}$$

and the initial receptor only response S_R as

$$S_L(s) = S_B(c) - S_R = s\,(S_{R+L} - S_R) \tag{8.6}$$

For a mixture of different orientations we can use the same formula as derived previously, now for the differential signal of the ligand binding.

$$S_{total}(s) = s \sum_{i=0}^{3} f_i S_i \tag{8.7}$$

The above expression assumes that the same fraction of receptors in each orientation are occupied for a given surface concentration, i.e. that the ligands are evenly distributed across the orientations. It also does not yet tell us anything about the relationship between the number or percentage of surface bound ligands and the actual concentration of this analyte in our sample solution. The relationship between the two will be considered next.

8.2.3 Impact of the binding efficiency on the detection signal

The affinity of the ligand for the receptor is concentration dependent and characterized by the dissociation constant k_D. To illustrate the difficulties and the complexity of simulating quantitative measurements using an affinity based sensor from first principles we are in the following deriving an expression for the sensor response depending on the analyte concentration in solution. The relationship between surface concentration of bound ligand s_L (which is what the sensor can measure) and the analyte concentration in solution c_L (which is what we want to determine) can be defined through the dissociation constant. If we assume to total number of available receptors on the surface to be 1 and the concentration of occupied receptors at equilibrium is s_L, then the number of free receptors is consequently $1 - s_L$. If we insert this into the definition of the dissociation constant and reorder, we obtain the following expression (at equibilbrium):

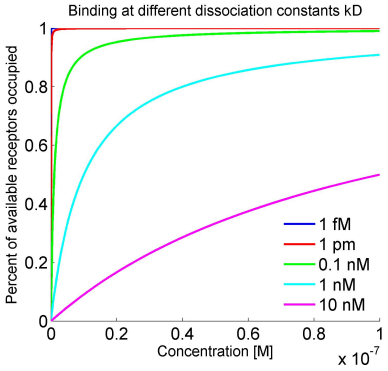

Figure 8.4 Relationship between surface coverage and concentration of the analyte in solution for different values of the dissociation constant k_D

$$s_L = \frac{c_L}{k_D + c_L} \tag{8.8}$$

The curves in Figure 8.4 show the concentration behavior for different values of k_D.

In addition, receptor orientation will impact the accessibility of the binding site and influences the efficiency with which a ligand is likely to bind, resulting in different dissociation constants for different orientations. To take this into consideration we need to extend the formula above. Assuming again different fractions of the receptor that are oriented in specific ways f_i of which $f_{RL,i}$ are receptor-ligand complexes or binding events we arrive at the following expression for the complete sensor response in the presence of the analyte.

$$S(c_L) = S_R + \sum_i f_{RL,i}(S_{RL,i} - S_{R,i}) = S_R + \sum_i f_i \frac{c_L}{k_D + c_L}(S_{RL,i} - S_{R,i}) \tag{8.9}$$

8.3 Cancer biomarkers

The aim for the biosensor system investigated here is the detection of cancer biomarkers. The proteins ULBP2 and MICA, ligands to the immune cell receptor NKG2D are being investigated as potential biomarkers by the group of Søren Skov at the University of Copenhagen. In collaboration with Franziska Uhlenbrock, the immobilization of the purified receptor protein was investigated on silicon surfaces as a first step towards a biomarker detection system. Since proteins are complex macro-molecules, the immobilization and subsequent activity as a receptor needs to be tested for each candidate. Unfortunately, the detection experiments with the SiNW sensor using the NKG2D system were unsuccessful due to failure of the sensor devices and are therefore not included in the results section.

As a model system we were using mouse Immunoglobulin G (mIgG), a protein mixture of antibodies of type G, extracted from mouse plasma, as a receptor. As ligand or analyte, either

goat or rabbit derived anti-mouse IgG antibodies were used (a-mIgG). These antibodies bind to the Fc unit of the mIgG and were obtained with and without fluorescent labels for microscopic verification of the detection process.

9 | Experiments and Results

9.1 Simulation of BioFET sensing: The impact of protein orientation

The simulation tool BioFET-SIM was used to study the impact of protein orientation on the measurement signal in order to get a qualitative idea of the nanowire response. We acknowledge that the model is not necessarily appropriate for our system, due to the dimensions of the wire and because the simplification of the sensing layer does not include the effect of interface charges or any structural or electrical impact of the intermediate functionalization layer. The purpose of this study is to illustrate and evaluate the impact that the biomolecular aspect of the sensing system has, regardless of any other parameters.

The proteins used for this evaluation are NKG2D (natural killer group 2, member D) an immune cell receptor that is important for the identification of infected cells in the body and one of its ligands. Ligands of this receptor have the potential to be used as a cancer biomarkers since their modified regulation in certain stressed cells could make it possible to detect elevated levels of it in the blood plasma.[119, 120, 121] Of course the protein data bank does not provide structural models for all known proteins and our choice of a model system is limited by availability. A receptor ligand complex model was only available for the ULBP3 ligand, so we chose this ligand for our detection. There was a problem in obtaining the model data for the free binding domain of the human NKG2D receptor (the native protein is membrane bound and contains a transmembrane domain that is not part of the model and a receptor used for detection is manufactured with an Fc domain instead). Instead, the structurally similar murine NKG2D (from a mouse) model was used to evaluate the receptor response. Since we are not interested in absolute values to predict the actual response for our system, this model system is still suitable and closely related to a real system that may be relevant to our sensor. It provides us with a general insight into the possible scenarios and pitfalls that are associated with the detection of charge based affinity sensing using silicon nanowire BioFETs.

9.1.1 Receptor orientation

The receptor protein is chosen from the protein data bank (1HQ8)[122] and loaded into the program. Firstly, we want to obtain the variation of the protein charge with pH and the resulting

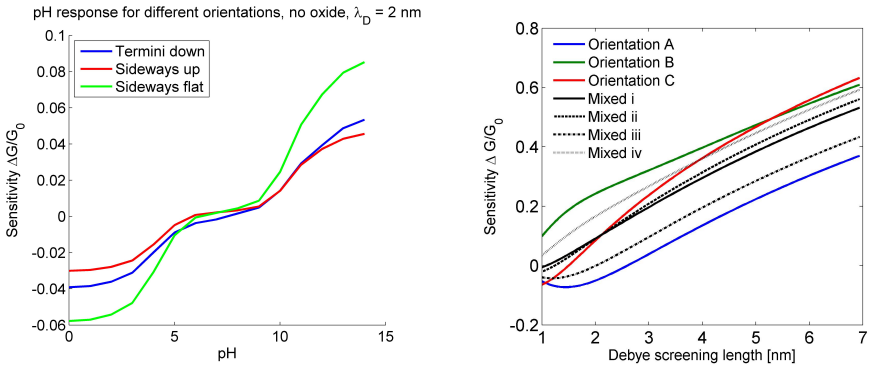

(a) (b)

Figure 9.1 Simulation results: *a)* Silicon nanowire sensor response to changes in pH when covered with the model protein in 3 different orientations. *b)* Differential conductance for three chosen orientations and different mixtures of orientations: i. 0.33 A/0.33 B/0.33 C, ii. 0.25 A/0.25 B/0.5 C, iii. 0.75 A/0.1 B/0.15 C, iv. 0.1 A/0.6 B/0.3 C

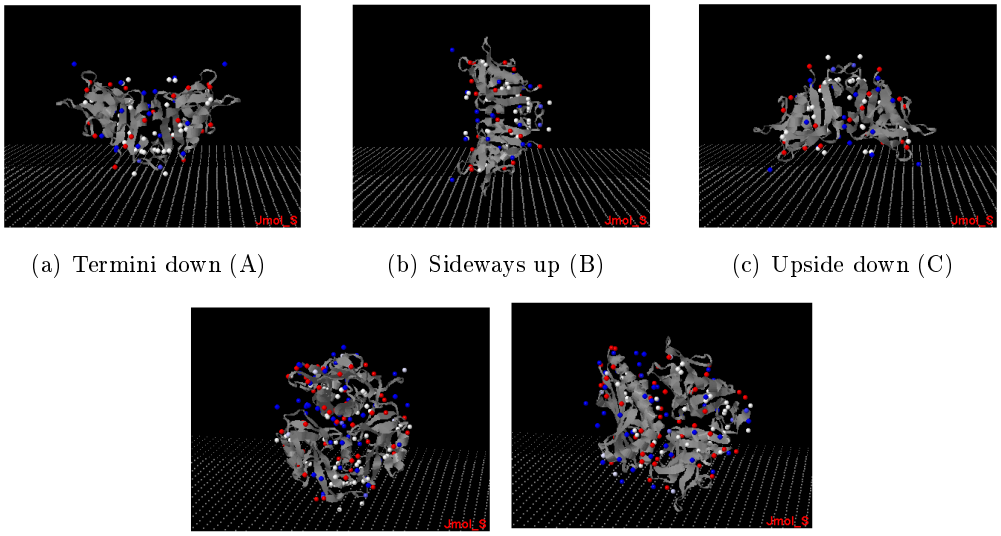

(a) Termini down (A) (b) Sideways up (B) (c) Upside down (C)

(d) Termini down (A) + Ligand (e) Sideways up (B) + Ligand

Figure 9.2 Orientation of the immobilized receptor (a)-(c) and with a bound ligand where the binding site is accessible (d),(e).

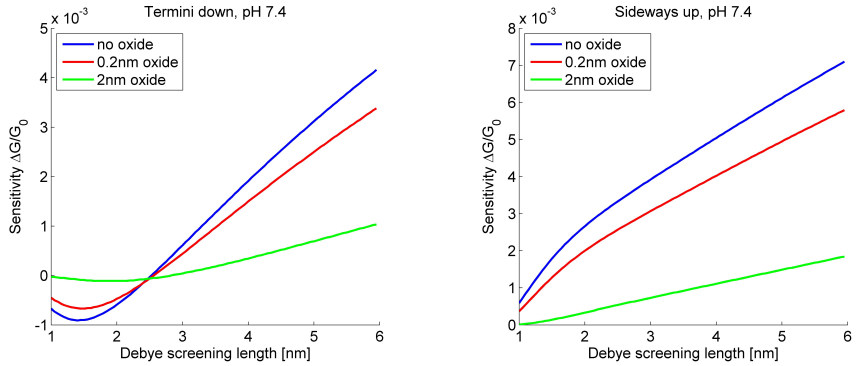

Figure 9.3 Differential conductance of the silicon nanowire sensor covered with protein in 3 different orientations in electrolytes with different ionic strengths (variation in Debye length). The response if plotted with and without taking into account an oxide layer of 2 different thicknesses.

impact on the nanowire response. The curve shown in Figure 9.1(a) shows the pH dependence of the differential conductance (compared to the blank wire without any functionalization layer) for a wire densely covered with protein in three different orientations. The orientations are shown in Figure 9.2. For the chosen Debye length of 2 nm we can see only small changes within the pH range around neutral pH and a rapid change towards low and higher pH values. All orientations show the same trend but vary in absolute values by up to 100% for the highest and lowest values. Since the pH influences the ionization of the charged groups and leads to more positively charged groups in one and more negatively charged groups in the other end of the spectrum, we expect this behavior. It should be noted, that a change in pH of an actual sensing buffer will impact its ionic strength and thus the length of the Debye length, i.e. screening. This interdependence is not considered here and the Debye length is held constant.

The sensor response for each of the orientations versus Debye length are shown in Figure 9.1(b), where each point on the x-axis corresponds to a specific ionic strength of the sensing buffer. We can see significant differences in the sensor response for the different orientations. The black lines show the simulated responses for different mixtures of the three orientation examples, demonstrating how this will create responses that can take a variety of values and if this is an unknown factor, will be very difficult to predict.

9.1.2 Oxide and interface layer

The Debye length, determined by the ionic strength of the electrolyte surrounding the protein, represents the distance from the surface at which changes in the charged groups will still have an impact on the charge distribution inside the nanowire. Therefore, the longer the Debye length, the larger the portion of the protein that can be detected. The graphs in Figure 9.3 are plotted as differential conductance versus the Debye length to include the impact of the sensing solution in each case. The interface layer, that constitutes the electrical passivation as well as the linking layer to attach the protein affects the sensitivity considerably. In this simplified model, the oxide layer is modeled as a uniform silicon dioxide film and the functionalization interface can

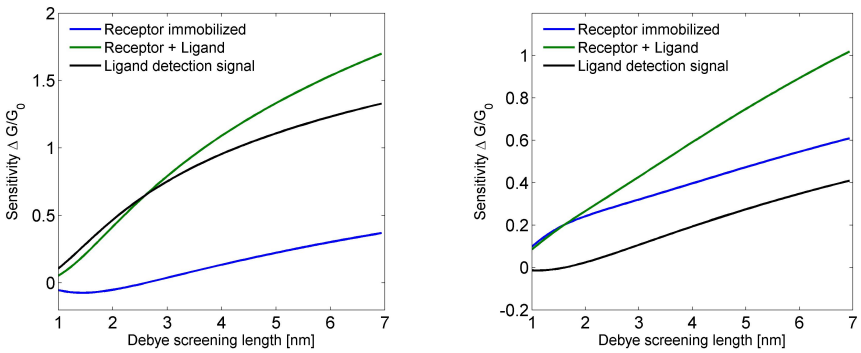

Figure 9.4 Response of the silicon nanowire sensor covered with a receptor protein for 2 different orientations in which the binding site is accessible. The curves show the differential conductance for different Debye lengths after immobilization of the receptor and after binding of the ligand as well as their difference, which is the response that would correspond to the detection of the bound ligand (analyte).

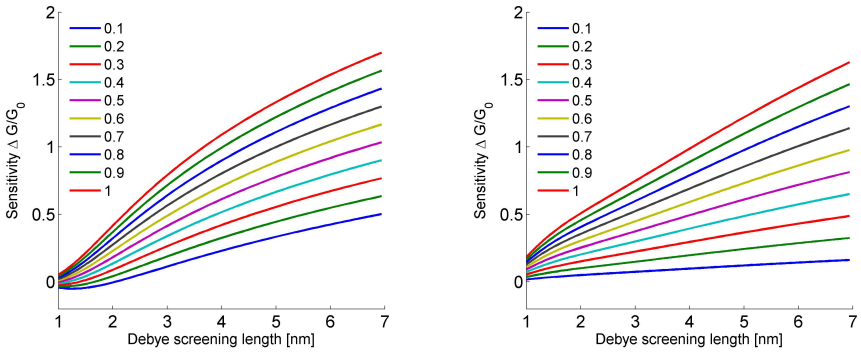

Figure 9.5 Titration curves for the sensor response assuming purely orientation A and orientation B respectively. We can see from their differences that combinations of both orientations by an unknown ratio can lead to arbitrary values for individual responses even without yet taking into account the relationship between surface and solution concentrations.

be included as a distance parameter. In this simulation we have varied the oxide thickness only. The plots show the impact of a 2 nm oxide layer compared to no oxide or a very thin film of 0.2 nm. It is clear that the closer a protein binds to the surface of the semiconductor, the higher the impact on the charge distribution and thus on the conductivity. It is very important to consider configurations such as the first orientation, in which a crossover occurs in the differential conductance. This means, that there is a point (for a specific ionic strength) where binding of the receptor to the surface will theoretically have no impact on the conductance. In this case charges neutralize each other and only a change in Debye screening length (practically, an exchange of the sensing buffer) would reveal this. Overall, the impact of the immobilization layer on the conductance is of no direct consequence for the detection signal, since this once again is a differential signal detected as a conductance change upon introduction of the analyte.

9.1.3 Detection of ligand binding events

Binding was evaluated by simulating the nanowire response for the 2 orientations where the binding site is accessible using the protein model for the combined receptor-ligand system of NKG2D and ULBP3 (1KCG)[123]. The resulting differential conductance is plotted in Figure 9.4 alongside the response of the receptor alone. The difference of the two curves (in black) is the expected sensing signal that would thus result from binding of the ligand. Both the added charge of the ligand and conformational changes in the receptor contribute to the signal, which is taken into account in this way, at the level of accuracy that the model allows. For the two presented orientations there are striking qualitative and quantitative differences in the sensor response. While for orientation A the signal from the immobilized receptor and for the bound receptor-ligand complex differ considerable, orientation B differs very little for low Debye lengths and only shows a variation when more of the molecule is 'visible', i.e. for longer screening lengths. Surprisingly, the orientation where the receptor is bound with the termini down, presenting the binding site on top is the one with the largest difference, especially for low screening lengths. We would expect the opposite, since the ligand binds at a certain distance from the wire and should be visible only at longer Debye lengths. The reason for this unexpected result is probably due to the choice of model proteins rather than an actual conformational change upon binding, since the receptor in both cases is actually not the same protein. The free version is the human and the bound version is the murine variant of the NKG2D receptor and they do differ to a larger extent than initially expected (when the simulation was set up). Therefore, a major part of the discrepancy may derive from these differences. But there is no doubt that the signal from the bound ligand will differ considerably depending on the orientations nevertheless and we included the data here for demonstration purposes on how such an evaluation could be done.

All of the simulations so far assume a full coverage of the wire with protein and a saturation of receptors in the analyte detection. Cases with less that full occupation of binding sites (receptors) are easily calculated, as discussed in the Methods section of this chapter. However, this is likely to be very far from any real observed signal due to the uncertainty of the receptor orientation and unknown dissociation constants. To obtain quantitative information about the detected binding events from a sensor it is imperative to determine a titration curve for calibration. We have simulated such curves as examples, shown in Figure 9.5, where the concentration is given as percent of the surface coverage. A real titration curve would be performed based on solution concentration of the analyte and would thus include the dissociation constant for the complete system the theoretical relationship of which has been described above.

9.1.4 Discussion

The simulated sensor responses have demonstrated some of the dependencies of the measurement signal on different aspects of the biofunctional layer. While the model that is considered here is rather simple in its consideration of the silicon-protein interface, it is clear that the thickness of the oxide layer already has a considerable impact on the strength of the signal and a thin oxide, or no oxide would be preferred, which justifies the investigation of alternative immobilization

schemes that involve direct coupling of the organic interface layer to the underlying semiconductor rather than the native or deposited oxide.

Investigation of the orientation dependence of the charge distribution and their impact on the nanowire response have demonstrated a variety of possible behaviors. This leads to an unpredictability in the measurement response if orientation and binding efficiency are not known. It is clear from this, that any attempt at obtaining quantitative measurements with such a system needs to involve a calibration step after the affinity layer has been established. And unless a high degree of control, i.e. reproducibility in the composition of the layer, can be guaranteed, this calibration step would have to be performed on the identical device which is to be used as sensor.

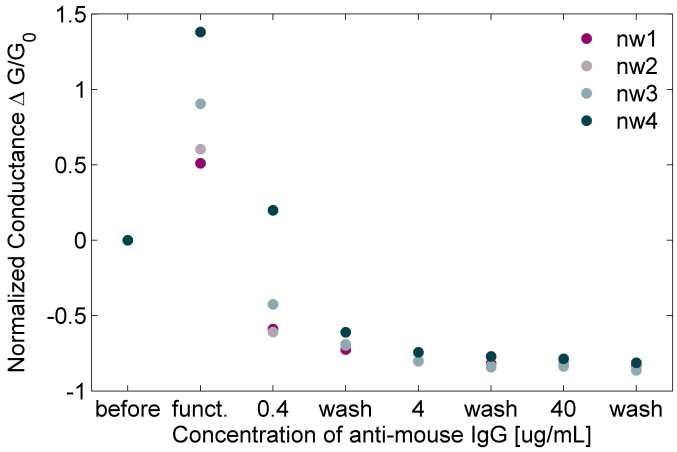

Figure 9.6 Detection of the binding of anti-mouse IgG to immobilized mouse IgG on a SiNW BioFET functionalized with 1,7-octadiyne. The initial two measurements were made before and after the functionalization process. Plotted is the average of 15 to 30 consecutively recorded data points of the differential conductance (G_0 is the initial value for each wire)

9.2 Detection of anti-mouse IgG with silicon nanowire BioFETs

This section gives an overview of the measurements that were performed with different silicon nanowire BioFETs using several functionalization schemes. The quality and specifications of the sensor chips differ considerably from batch to batch. This is one of the reasons why a systematic investigation of the functionalization procedure and protein immobilization could not be performed on the nanowires using electrical measurements. The experiments that are discussed in this section were performed at different stages of both sensor and chemistry development and therefore both the experimental procedures and results differ considerably. Reproducibility of the results has been an issue, both due to the low yield of functional sensor chips (especially after functionalization, see 4.2) and due to low sensitivity of the initial sensors. Even though some of the results look promising and show the expected trends the data is not reproducible and evidence is sparse to draw conclusions about the sensitivity or functionality of the sensor.

9.2.1 Click-chemistry immobilization on BioFETs

Silicon Nanowire devices (specs: C.2 W11) were functionalized with 1,7-Octadiyne to create an alkyne-terminated surface for protein conjugation (Protocol: C.3.9). As a model system, mouse immunoglobulin (mIgG) was conjugated with azide groups (Protocol: C.3.8) and immobilized on the sensor surface using the copper assisted azide-alkyne cycloaddition (CuAAC or click-chemistry reaction, Protocol: C.3.11). In brief, the chips were etched in 1% hydrofluoric acid to remove the native oxide layer, grafted with 1,7-octadiyne to obtain an alkyne terminated surface. Using the CuAAC, mouse IgG was immobilized on the sensor surface. Since no characterization method was available to confirm the success of the immobilization, the measurement of the conductance change itself needs to be taken as an indication of a change in the sensor surface.

Each chip contains 4 nanowires with individual electrical connections. The experiment was performed as part of the PhD summer school on label-free sensing. Unfortunately, the control chip was not usable in this experiment, which needs to be considered for any conclusions drawn from the measurements. It is included here for the purpose of illustration of the measurement principle.

The measurement was performed using the original BioFET measurement setup described in 8.1.2, which records impedance measurements from one wire at a time for a set number of points. Each point was recorded as the average over a sinusoidal voltage sweep with a period of 1 second and an amplitude of 100 mV for a total number of 15 to 30 seconds. The initial measurements were performed before the functionalization process and again after immobilization of the primary antibody. For the detection, we used goat anti-mouse IgG (a variety of secondary antibodies that bind to mouse IgG that were obtained from a goat, in the following: a-mIgG), which should bind to the immobilized protein and induce a change in conductance. For each step, 5 μL protein solution of the respective concentration of a-mIgG in 1xPBS was introduced into a reaction chamber on top of the sensing area of the nanowire sensor chip and the measurements were performed immediately. After rinsing the chamber with PBS another measurement was performed.

As the graph in Figure 9.6 shows, the conductance of all nanowires changed upon introduction of the complementary antibody. The normalized differential conductance shows a saturation behavior towards higher concentrations of the antibody as expected. The conductance is reduced upon introduction of the sample, which indicates a depletion of electrons in the nanowire and therefore a negative net surface charge in the protein layer. Considering the size of the nanowire, especially the thickness of approximately 50 nm, the magnitude of the conductance change is unlikely to be induced solely by attachment of the protein layer. The lack of a control doesn't allow us to investigate the possibility of drift being responsible for the observed result. We have often observed a continuous increase or decrease in conductance with this setup which might stem from a buildup of charge or temperature changes or other external factors that are not considered.

9.3 Boc-alkene immobilization on BioFETs

Silicon Nanowire devices (specs: C.2 W09) were functionalized with 10-N-amino-Boc-dec-1-ene and de-protected to create an amino-terminated surface for protein conjugation. As a receptor protein, mouse IgG was immobilized on the sensor surface using the EDC/NHS aminocoupling reaction (Protocols: C.3.10 and C.3.13). As a control, one chip was left blank, i.e. the surface is terminated with the de-protected Boc-alkene, resulting in an amino-terminated surface. The measurement was performed using the CMOS BioFET measurement setup, which is capable of recording measurements from several nanowires at once on the same sensor chip in a continuous manner. In the first experiment two chips (a control and a sample) were connected to the measurement setup, recording the response from 2 wires each. The chips were individually enclosed in a frame that forms a cavity on top of the sensing area, so that the different sensing solutions could be introduced. For the second experiment, a single chip was enclosed in a microfluidic

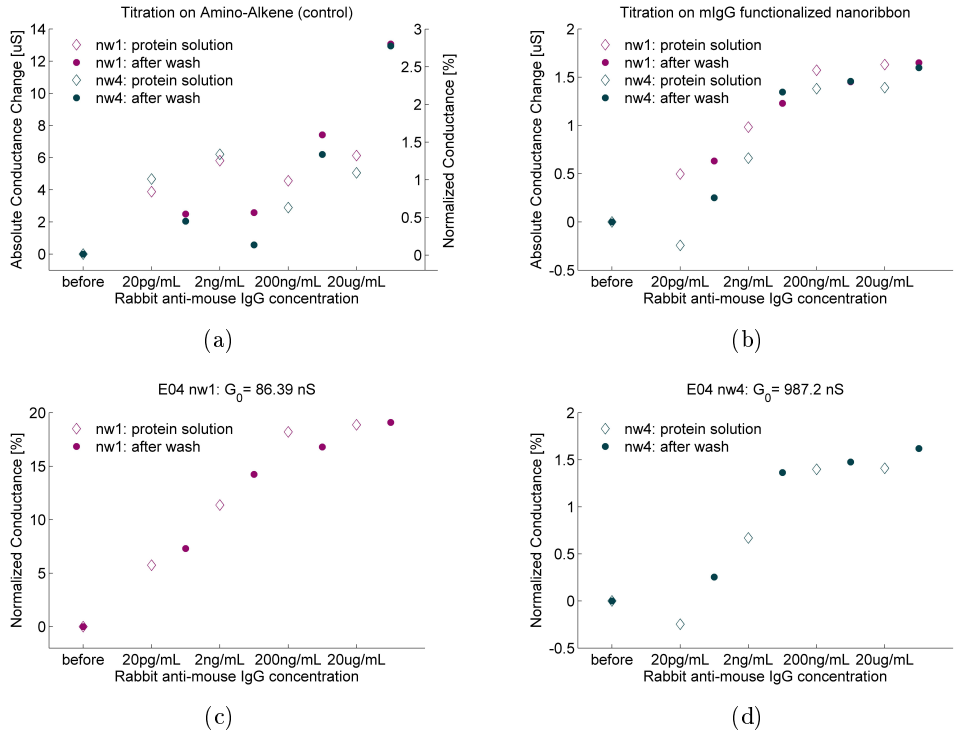

Figure 9.7 Detection of the binding of anti-mouse IgG to immobilized mouse IgG on a SiNW BioFET functionalized with Boc-alkene. Plotted is the differential conductance (G_0 is the averaged initial value for each wire) of the average of a 50 second measurement at the end of each incubation cycle. a) Control (no immobilized antibody): Absolute and normalized differential conductance. b) Sample (with immobilized primary antibody): Absolute differential conductance and c)-d) Normalized differential conductance

flowcell connected to an opening for pipetting on one end and a syringe filled with clean sensing buffer on the other end of the channel. For each step, 10 μL protein solution was introduced via a pipetting tip either into the open cavity or at one end of the channel and transfered to the sensing area by withdrawal from the syringe. The tip was left at the inlet for subsequent removal of the protein solution. After the appropriate incubation time of a minimum of 5 minutes, the sensing area was flushed with buffer solution injected from the syringe and removed with the pipetting tip. This was followed by a washing step which consisted of introducing more sensing buffer into the sensing area several times for another 5 minutes.

Figure 9.7 summarizes the results from the first experiment. Since considerable differences were seen in the responses of the two wires on the actual sensor (sample), both the absolute and normalized values are plotted. Regarding the resulting shape of the titration curves, it is easy to see that the sample shows the S-curve behavior that is expected for a protein binding reaction, whereas the control shows more random increases in conductance. The absolute values differ hereby considerably, and the control shows a response that is an order of magnitude higher. Comparing the base conductance values it should be noted that the control has a one resp. two orders of magnitude higher intrinsic conductance. The difference between the two wires on the

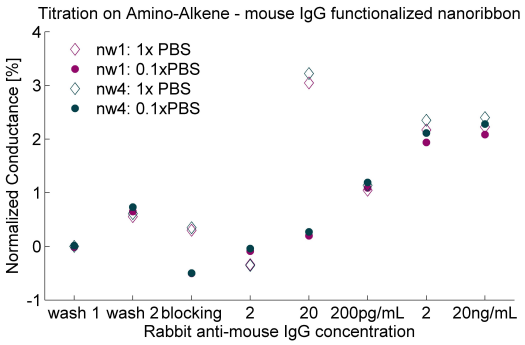

Figure 9.8 Detection of the binding of anti-mouse IgG to immobilized mouse IgG on a SiNW BioFET functionalized with Boc-alkene. Initially 2 wash cycles were performed, exchanging the buffer between 1xPBS and 0.1xPBS, followed by a blocking step with human serum albumin (HSA). Protein binding was performed in 1xPBS, at the end of which the first measurement was taken and subsequently washed in 0.1xPBS where the second measurement was taken in each cycle.

sample in terms of base conductance (86 and 987 nS respectively) is unfortunate and a result of the low reproducibility of the functionalization process, most likely caused by the etching step. However, comparing the absolute responses it is interesting to see that the signal is comparable, indicating that the offset in base conductance does not impact the changes induced by protein binding.

The graph in Figure 9.8 shows the result of the second experiment, where protein detection was performed in a closed microfluidic channel on top of the sensor area. A blocking step was added to reduce the influence of unspecific binding, and several smaller concentrations were investigated as well. After each incubation step a measurement was made in a buffer with reduced salt concentration in order to increase the Debye length and increase the sensitivity. Considering those measurement steps in reduced salt buffer only, we can see a similar curve to the ones above, showing the S-shaped character associated with protein binding kinetics. Since the experiment could not be repeated in this way, a discussion of sensitivity limit or a quantitative evaluation of the results are not adequate at this point. The results presented here are however a promising first step in the development of a silicon nanowire BioFET for protein detection.

III | Microfluidic integration

10 | Introduction

The field of microfluidics has taken its place as one of the major disciplines bringing personalized, patient-centered healthcare to the next level. Driven by the need to process small amounts of fluids and biological material therein, down to the controlled manipulation of individual molecules, microfluidic technology is rapidly developing. The unique properties of confined liquids on the small scale enable new functionalities that have not previously been possible. Especially in medical applications the advantage to extract material and thus information from very small amounts of sample combined with ever more sensitive sensors leads to powerful new technologies for diagnostics, drug discovery as well as personalized treatment and therapy development. Detecting small concentrations of different biomarkers in the amount of blood that can be obtained from a finger prick or continuous monitoring of bodily fluids using implanted devices are just two examples where microfluidic sample handling is required. Replacing laboratory procedures that commonly involve several discrete steps for sample extraction, purification, labeling and other possible treatments, miniaturized lab-on-a-chip device can integrate many of these steps into a continuous, automated process flow that does not require trained personnel and a fully equipped laboratory.

10.1 The physics of fluid behavior in microfluidic systems

Fluid flow in microscopic channels is governed by principles that differ from our intuitive understanding of its macroscopic counterpart due to non-linear scaling of physical laws. Interfacial and surface forces play a paramount role in the behavior of liquids due to the high surface-to-volume ratio in microfluidic systems. Viscous forces typically dominate over inertial forces, as characterized by the Reynolds number of a system, leading to laminar flow that does not show turbulence or chaotic behavior. This combination enables utilization of the now dominating phenomena such as diffusion and interfacial tensions that are often mere perturbations on the macroscale.

10.1.1 Reynolds number, pressure and fluid flow

The Reynolds number of a microfluidic channel or around a body in a fluid, a dimensionless number, is defined as the ratio of inertial to viscous forces:

$$Re = \frac{\rho v L}{\eta} \tag{10.1}$$

Where ρ is the density of the fluid, v is the flow velocity and η is the viscosity of the fluid. The characteristic length L is typically the width of height of the channel, whichever is smallest, or a dimension of the body that is being described. If the Reynolds number exceeds a critical value, typically between 1000-3000, the laminar flow transitions into turbulent flow, which means that small disturbances lead to large effects on fluid behavior and low predictability. Microfluidic systems are generally designed with low Reynolds numbers and rely on the predictability and high degree of control of fluid flow.

Determination of the flow rates in a microfluidic network can be done in close analogy to Kirchhoff's laws for electrical circuits. The resistance is replaced by the hydraulic resistance, which depends on the length L of the channel and additionally on the shape of the cross section due to the complex behavior of fluids along interfaces. Approximations are given below for a circular, square and rectangular cross section. The rectangular approximation includes a correction on the square case that is more accurate for ratios of $w/h >> 1$.

$$\text{circular, radius r:} \quad R_{Hyd} = \frac{8\eta L}{\pi r^4} \tag{10.2}$$

$$\text{square, width = height = a:} \quad R_{Hyd} = \frac{12\eta L}{a^4} \tag{10.3}$$

$$\text{rectangular, width w, height h:} \quad R_{Hyd} = \frac{12\eta L}{wh^3(1-0.630h/w)} \tag{10.4}$$

The flow rate is then determined by the pressure difference between the ends of the channel Δp in analogy to Ohm's law:

$$Q = \frac{\Delta p}{R_{Hyd}} \tag{10.5}$$

These laws can directly be used for the design of simple pressure driven devices that are actuated either by an active pump at the inlet(s) or through underpressure at the outlet(s). For microfluidic devices with complex geometries and multiple interconnected channels, finite element simulation tools such as COMSOL are used to accurately determine the flow velocities and fluid behavior in the system.

10.1.2 Diffusion and mixing in microchannels

On the microscale and in laminar flow, the dynamics of mixing are dominated by diffusion due to the lack of turbulence. The diffusion of molecules and small particles such as cells is characterized by the diffusion constant D as defined by the Stokes–Einstein–Sutherland equation

$$D = \frac{k_B T}{6\pi\eta r} \tag{10.6}$$

This equation is valid in laminar flow and involves the viscosity of the fluid, temperature T and the radius/diameter of the particle. The relationship between diffusion length and diffusion

constant is $l^2 = 2Dt$, which indicates that the distance a given particle will travel by Brownian motion increases with increasing diffusion constant. As we can see this will lead to different particle movement depending on size, which is important for intermixing of species in the fluid. On the small scale of microfluidic systems, diffusion can be used as a tool for sorting of particles by size and it has implications on mixing behavior of different liquids. This is of great interest for the treatment of biological samples that can include cells, proteins, DNA and other particles and molecules of a variety of sizes and morphologies. The equation stated above is a simplification for a rigid, spherical particle and as such care needs to be taken when applying it to soft material with complex geometries, surfaces and internal structure. As an approximation it is useful to employ simple relations, but more detailed modelling and experimental data are required for the design of real systems for treatment of biological samples.

Since diffusion is the dominant force driving intermixing in laminar flow, the intentional homogenization of two merging fluid streams needs to be given sufficient time or facilitated by active mixing. There are several concepts that can be implemented, two of which will be discussed here. In a straight channel, molecules at the interface need to have enough time to diffuse across the complete fluid stream (for example half of the channel width) in order to create a homogeneous solution, which takes a considerable distance/time. Meandering channels are often used to compress a longer channel into a smaller footprint and improve mixing additionally due to the shearing forces created by differences in the flow velocity within the sharp bends of the turning channel. For larger particles and accordingly designed channel geometries, meanders have also been used for particle focusing, it is therefore important to consider that different forces that may act on different components in the fluid. Generally, meanders are often used for mixing by diffusion of small particles (such as molecules). This passive method however requires long channels and thus increases the size of the overall device. An alternative is active mixing using for example so called herringbone mixers. These are channels with structured channel walls that generate turbulent flows into the system. The geometry of the herringbone features, an example of which is shown in Figure 13.3(d), determines the efficiency with which mixing can occur. Due to the resulting folding of the laminar interface, the diffusion distance is greatly reduced and mixing can take place in a much shorter time.

10.2 Chip-to-world interfaces

Interfacing electronics, such as impedance based biosensors, with wet biological or chemical materials is a challenge on several levels. As discussed in the previous chapters, the immediate interface between sensor surface and analyte presents one of the most crucial elements in a sensing system. In the following the next higher level of interfacing and integration will be discussed. Providing an interface for the controlled and automated delivery of fluids from the external environment to a sensor on a silicon chip can be as straight forward as immersing the chip in a liquid, but in many cases a more sophisticated system is required or enables novel functionalities that are not possible otherwise.

Different mechanisms have been developed to deliver samples to microfluidic devices, depending on the many different requirement of where they are used. In a laboratory setting, where

functionality of a specific microfluidic module is to be tested, or where a microfluidic device is used as an analytical tool in biological or chemical research the requirements for a chip-to-world interface are vastly different from those required in a clinical setting, where ease-of-use and simplicity are the foremost driving forces.

10.2.1 Fully integrated concepts

To used microfluidic devices for applications in the field outside the laboratory, the requirements for liquid handling can be very different. Typically, all needed reagents apart from the sample need to enclosed within the device or provided as a separate device that is easily stored and interfaced. One of the concepts to store multi-step biological protocols on a microfluidic chip employs a length of tubing or extended channel in which the reagents are stored in sequence, separated by air bubbles. To activate the process, the reagents are pushed or sucked out of the channel and thus delivered to a reaction chamber.[7] Even though this concept has shown very promising results in field tests, there are concerns related to intermixing of the stored reagents along wetted channels, especially during transport. Furthermore, the lifetime of biomaterials stored in liquid depends critically on conditions such as temperature and requires a cold-chain for storage and transport. Another approach uses sealed reservoirs or blisters that contain reagents in liquid form and can be opened on demand, which avoids the problem of potential intermixing and may be especially useful for cartridge based systems used in the industrialized world where adequate storage conditions are not a problem. This concept is already being used in some commercial devices for clinical settings. A third and very common way to store reagents in microfluidic systems is the use of freeze dried or matrix immobilized materials. While some biomolecules such as DNA are extremely stable under various conditions, others such as proteins and enzymes are very sensitive, especially in liquid. Many lateral flow tests, such as the pregnancy test, already employ dried reagents that remain functional after storage in ambient conditions. In this case, the test is based on a simple binding process that only requires the structural preservation of a single functional unit. Recently, much more complex biological systems including translation of genetic code into functional proteins, a process that requires advanced enzymatic activity, have been successfully immobilized, stored in dry, ambient conditions and reactivated. This offers promising new opportunities for medical devices in developing countries and under less controlled conditions.

10.2.2 Continuous flow interfaces

To provide continuous access to a microfluidic device is commonly achieved by the attachment of lengths of tubing that deliver reagents as active materials or air to provide actuation functionality. In a laboratory setting, fluid actuation is often achieved externally by using syringe, peristaltic or gravity pumps and thus advanced reagent storage and preservation is a secondary concern. The primary functionality of such systems is often the delivery of fluid to biosensor surfaces or provision of medium to cell cultures which requires a continuous flow. This can be combined with pre-loaded cartridges as described above to deliver a predefined protocol in an automated manner without the need to switch tubing or fluids in between steps.

11 | Journal publication: An easy-to-use microfluidic interconnection system to create quick and reversibly interfaced simple microfluidic devices

In the progress of this work, an interface was developed that enables the quick and reversible attachment of tubing to microfluidic devices, making it easy to set up flowcells for delivery of functionalization protocols with continuous electrical or optical monitoring. The interconnection system is composed of a *socket*, a modification of the microfluidic device that replaces simple holes for inlet and a plug that is pushed into the socket to hold down attached tubing by an interference fit mechanism. The design of the components allows for complete reversibility of the connector, no glue is used to hold it in place. In this way the parts can easily be cleaned and reused. Devices with such connectors can be set up very quickly simplifying prototyping and testing. Robustness testing shows high pressure tolerance of the connectors of more than 17 bar and a dislocation force when pulling along the direction of the tubing of 12.5 N. The interconnection system was routinely used in the flowcells and continuous flow devices described in this chapter and by colleagues for several other projects.

Journal of Micromechanics and Microengineering - accepted 2015

An easy-to-use microfluidic interconnection system to create quick and reversibly interfaced simple microfluidic devices

Andrea Pfreundt, Karsten Brandt Andersen, Maria Dimaki and Winnie E. Svendsen

11.1 Abstract

The presented microfluidic interconnection system provides an alternative for individual interfacing of simple microfluidic devices fabricated in polymers such as polymethylmethacrylate (PMMA), polycarbonate (PC) and cyclic olefin polymer (COC). A modification of the device inlet enables the direct attachment of tubing (such as polytetrafluoroethylene (PTFE) tubing) secured and sealed by using a small plug, without the need for additional assembly, glue or o-rings. This provides a very clean connection that does not require additional, potentially incompatible, materials. The tightly sealed connection can withstand pressures above 250 psi and therefore supports applications with high flow rates or highly viscous fluids. The ease of incorporation, configuration, fabrication and use make this interconnection system ideal for rapid prototyping of simple microfluidic devices or other integrated systems that require microfluidic interfaces. It provides a valuable addition to the toolbox of individual and small arrays of connectors suitable for micromachined or template based injection molded devices since it does not require protruding, threaded or glued modifications on the inlet and avoids bulky and expensive fittings.

11.2 Introduction

Interfacing microfluidic devices to external equipment remains a challenge that is yet lacking a widely accepted standard.[124, 125] While the development of applications for microfluidic devices is progressing, microfluidic technology is refined and re-invented alongside. Both the interdisciplinary nature and the vast variability in methodologies create a large amount of individual solutions to similar problems such as the chip-to-world interface.[126] Different requirements and desired levels of flexibility have given rise to numerous specialized interconnection systems used both for complex lab-on-a-chip systems and for simpler microfluidic devices that provide a proof-of-concept for a certain design or constitute the interface to other components such as biosensors. An excellent overview over the current state of the field can be found in a recent review[127].

A few commercially available platforms have emerged providing a standardized solution for operation of devices from specific manufactures or devices that are designed to match a certain layout.[128, 129, 130] Some research groups have also developed interface platforms that can

provide access to a large number of inlets simultaneously, for example in polydimethylsiloxane (PDMS)[131] or using an aluminum clamp and flanged PTFE tubing[132]. These components and platforms are generally rather large compared to the devices and while the standardized layout is suitable for the routine operation of microfluidic devices it lacks the flexibility that is often necessary for early prototyping and the development of modular systems. The individual commercially available connectors such as Luer and Nanoport on the other hand need to be irreversibly glued or bonded to the devices. While there are solutions to overcome some problems associated with epoxy glues[133], the additional material can lead to chemical or thermal incompatibilities. As an alternative, the required protruding structures can be molded as part of the device, which avoids the adhesive but complicates fabrication and bonding procedures[134]. In either case, the added structures are generally large compared to inlet size and, in the case of the Luer connector, associated with large internal and dead volumes. Additionally, a wide variety of other solutions for individual connectors have emerged in recent years. Many are based on a press fit mechanism to interface needles or capillaries directly with PDMS devices[135, 136, 137, 138, 139, 140] or using PDMS as a gasket material[141, 142, 143]. PDMS however is not chemically inert, which prohibits applications that use solvents, and usually these connectors suffer from low leakage pressures unless very thick layers are used. Furthermore, cored holes in PDMS films are difficult to reproduce with good quality and easily damaged[135]. Press fit[134, 137] and interference fit[144, 145] mechanisms have also been presented using other materials such as SU-8, but these show low pressure tolerance and handling robustness[137] or are limited to be used as a chip-to-chip interface[145]. Interconnections that are composed of a number of materials such as metal needles, adhesives and other polymers that are irreversibly attached to devices are often not compatible with common sterilization procedures such as autoclaving due to different thermal expansion coefficients hindering adequate cleaning for biomedical applications. Recently, the advent of additive manufacturing techniques (3D printing) has enabled novel approaches to microfluidic device design. No longer limited to planar designs with unidirectional feature definition, complexity does no longer come at the cost of tedious assembly and alignment. Naturally, this has given rise to additional solutions for interfacing of microfluidic devices[146] and the development of modular systems[147].In this paper we are presenting a novel interconnection system based on an interference fit mechanism that does not require the use of o-rings or the assembly of an external platform, but is integrated into the device fabrication. The connection is chemically robust to the extent of the device material chosen for each application, fully reversible and can withstand pressures above 250psi (1720 kPa), which was the limit of the used pressure test setup. Being composed of only two or three materials, that of the device, that of the plug and that of the tubing, which can be completely separated from each other, make this interconnection especially robust, easy to clean and sterilize and thus compatible with most chemical or biological applications. It is intended for quick, reversible and reliable interfacing of simple microfluidic devices providing high flexibility and ease-of-use. External tubing can be connected individually or in small arrays, with a small footprint and low dead volumes. We are demonstrating its use in the attachment of standard PTFE tubing to devices fabricated in a variety of polymers. Different parts of the interconnection can be fabricated in the same or a combination of different materials to meet the requirements of the application, without compro-

mising functionality. The connectors have been incorporated in continuous flow systems as well as to connect different modules into a combined microfluidic system.

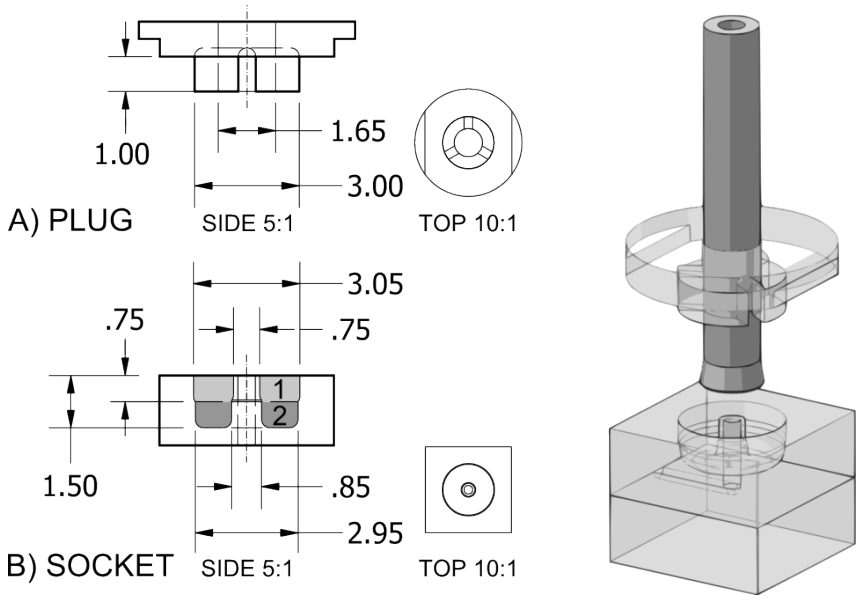

Figure 11.1 Technical drawings of the plug (a) and socket/inlet (b) and 3D model of the connector. The shaded areas labeled 1 and 2 in b) mark the two step pocket that creates the depression around the inlet hole. The drawing describes the standard connector used to interface standard PTFE tubing (ID 0.8/OD 1.6). All dimensions are in mm.

11.3 Materials and Methods

11.3.1 Design and Function

The interconnection system was designed to directly interface PTFE tubing (Bola, Germany) with microfluidic devices fabricated in hard polymers, as opposed to rubber-like polymers such as silicones that readily form a seal, without using o-rings or glue. Each connector consists of three components: a socket, which is a modified fluid inlet on the device, the tubing itself and a small separate plug as shown in the technical drawing in Figure 1. Figure 2a shows how devices are interfaced with the tubing by inserting the plug while the sequence 1-4 in Figure 2 illustrates how the different parts of the interconnection interact and how the seal is formed. The function of the socket is to receive the tubing and to create the sealing interface between the inside of the tubing and the microfluidic channel. It is composed of a pin surrounding the inlet hole that matches the inner diameter of the tube and a surrounding trench, which receives the plug and fastens the tubing by an interference fit mechanism. The plug is a separate part that slides onto the tubing before attachment. To connect, the cleanly cut edge of the tube is first pushed onto the pin and then compressed into a tight seal when the plug is pushed into the socket. To release the tubing, the plug is simply lifted from the device by one of its edges. In this way tubing can

easily be removed or exchanged. Figure 2b shows the tubing/socket interface and illustrates the fluid path. The red marked area outlines the area in which recirculation can occur. Of course the size of this area depends on the used flowrate and the inner diameter of the inlet hole. For the size of interconnection presented here the volume is estimated to lie between 25 and 50 nL.

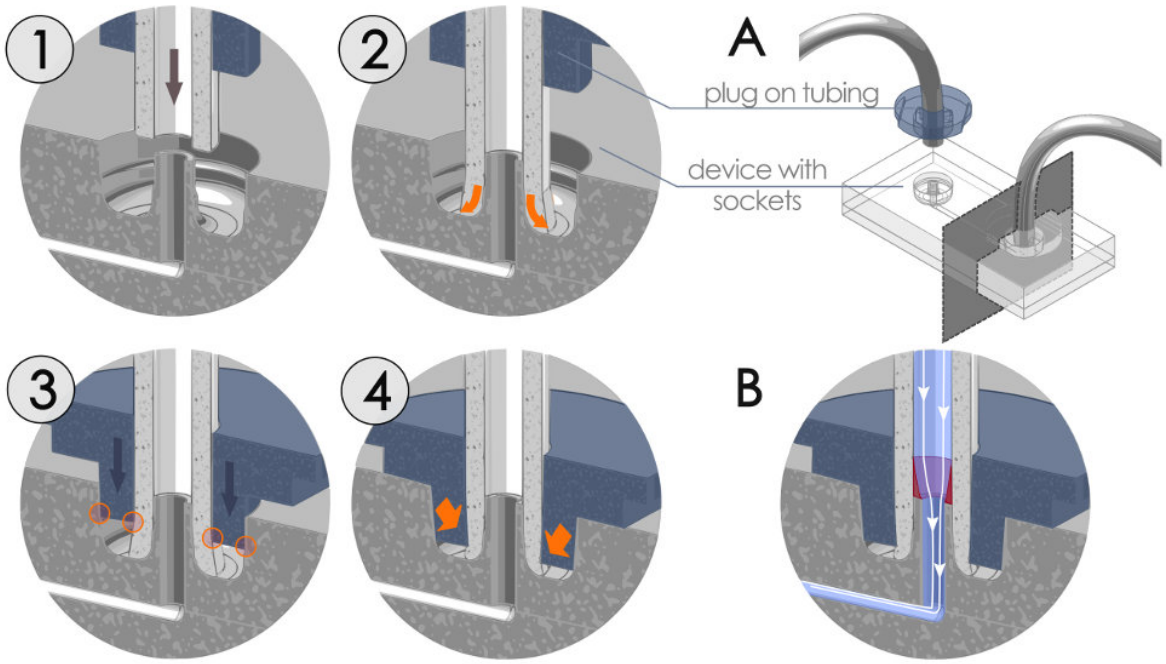

Figure 11.2 1-4) Schematic illustration of the interference fit mechanism. First the tubing is inserted into the socket (1). It is pushed onto the pin surrounding the inlet where the edges deform outwards guided by the curved surface (2). Then the plug (blue) is pushed down, sliding along the tubing (3); the circles indicate where force is exerted. This force leads to an inward deflection of the interfering part of the plug exerting force on the tubing to form a tight seal and an outward force to fasten the connector in the socket (4). The connector can be removed by lifting the plug by its edge. a) Schematic of a device with 2 sockets; the grey area illustrates the cut plane across the interconnection that is shown in the other images. b) Flow path at the interface and recirculation area (red).

11.3.2 Fabrication

All parts and devices were designed using Autodesk AutoCAD 2012 and fabricated by CNC milling using EZ-CAM Express 15.0 to generate the instructions. For demonstration, three different materials were used, poly(methyl methacrylate) (PMMA), cyclic olefin co-polymer (COC, grade: Topas 5013-S-04) and polycarbonate (PC).

Fabrication of microfluidic devices A typical microfluidic device of the type that we are considering here consists of a minimum of two layers of polymer: one layer that contains the channels system (bottom plate) and one layer that contains the inlets (top plate). The plates are

bonded together using thermal bonding for 15 to 20 minutes at 87°C (PMMA), 120°C (COC) and 105°C (PC) for the three materials respectively and a pressure of approximately 500 N/cm2 for all of them. Devices were left to cool down to below 50°C before releasing the bonding pressure. Bonding has not been found to have a negative effect on the function of the interconnection.

Fabrication of the socket Each inlet hole in the top plate is surrounded by a socket. This ring shaped depression is formed in a two-step pocketing process as denoted in Figure 1b. The first step creates a ring with an outer diameter (OD) slightly larger than that of the plug and an inner diameter (ID) slightly smaller than the ID of the tubing. In a second step a narrower ring is pocketed inside the first, with an OD slightly smaller than that of the plug and an ID slightly larger than that of the tubing. The edge that is formed in this way is enabling the transition from easy insertion of tubing and plug to a tight fitting connection.

Fabrication of the plugs The plugs are fabricated by micro-milling from a 2 mm polymer plate. Figure 1a shows a technical drawing of the plug, which consists of a central hole that has an ID slightly larger than the OD of the tubing (1.65 mm for 1.6 mm tubing) which will receive the tubing. The hole is surrounded by a segmented ring (3 segments) on a circular base plate of 6 mm diameter with two edges that facilitate lifting of the plug off the device. The segmentation enables the individual segments to deflect inwards when the plug is pushed into the socket, in this way holding the tubing in place and securing the seal.

11.3.3 Pressure and Strain Testing

To test the maximal operation pressure of the interconnection pressure tests were performed using uncompensated (no internal correction for temperature changes, this was done by monitoring the excitation voltage) gauge pressure sensors (Honeywell, 24PCGFH1G) which have a pressure limit of 250 psi or 17.2 bar. The sensors were operated by application of a constant current of 2 mA and recording of the output voltage using 2 Keithley 2400 sourcemeters. Sensor calibration was validated for up to 8 bar prior to testing using a compressed air source with calibrated pressure gauge. Linearity was assumed to hold up to the maximal given pressure range, and even though higher pressures could be obtained, 17.2 bar is given as maximal value throughout this article. Two types of pressure tests were performed with a setup that is illustrated in Figure 3a.

(A) Leakage pressure The flow path for this test is denoted as (A) in Figure 3b. Two pressure sensors are used to monitor the pressure drop across the test device as well as determine the maximal operation pressure. The first sensor is flush mounted using a T-junction (Upchurch scientific flangeless fittings) between a syringe pump and the device. The second one is mounted in the same way at the outlet with one terminal of the T-junction sealed. The device contains several channels in order to be able to test multiple connections at the same time (as in- and outlets respectively). The upper part contains a distribution channel, which splits the flow into 5 separate outlets (2-6). The lower part contains 5 closed channels with only one inlet each (7-11). By connecting every two out- and inlets via tubing, two connectors can be tested while the closed

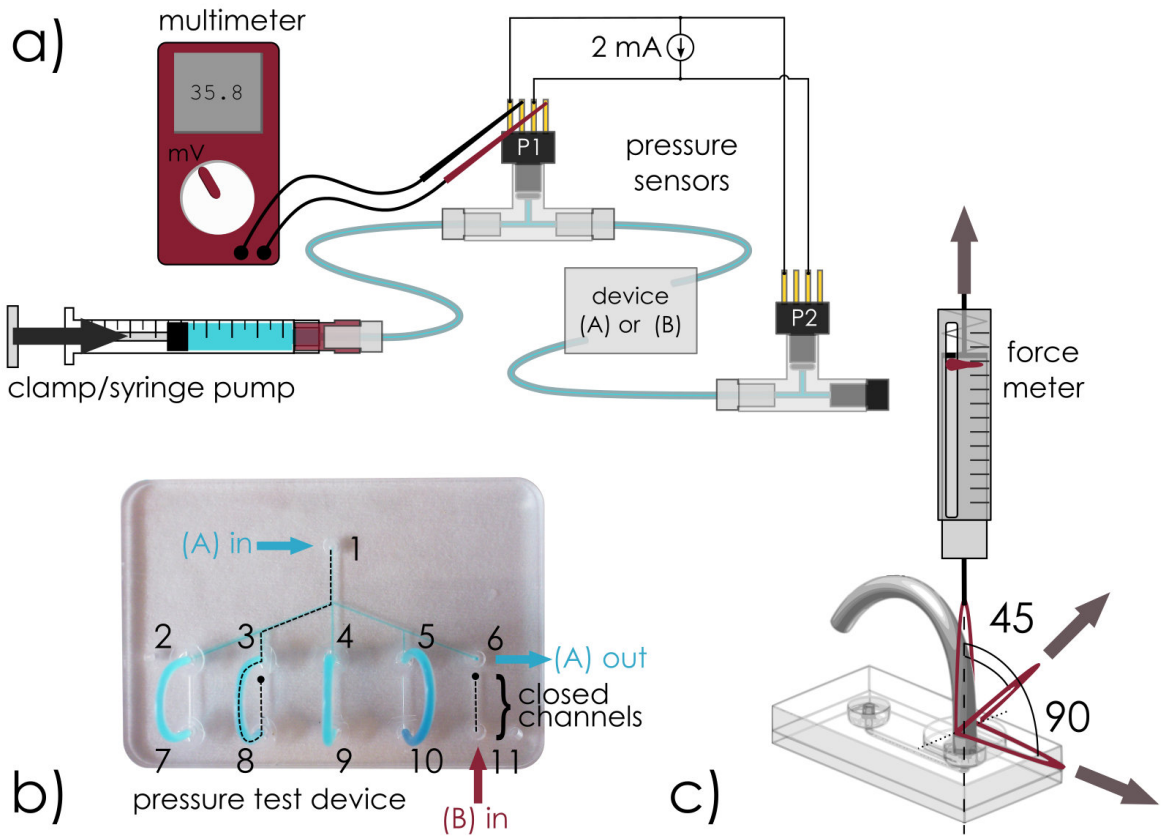

Figure 11.3 a) Pressure tests were performed by applying pressure to a syringe, either by clamping or using a syringe pump, connected to a closed system. One (only P1) or two (P1 and P2) pressure sensors with a linear range up to 250 psi were flush mounted using T-junctions and excited by a constant current of 2 mA. Pressure was indicated as a voltage between the output terminals of the pressure sensor and read out using a voltmeter. b) The device shows 2 possible configurations: (A) the pressure source is connected to a channel system with 5 outlets, one of which leads to P2 while the 4 others are connected to closed channels (indicating pressure by air-compression) or (B) the pressure source is connected to a single inlet ending in a closed channel. c) For estimation of the force needed to dislocate the plug, a small hole is drilled into a piece of tubing to which a force meter is attached. When force is exerted on the force meter the force indicator is moved and retains its maximal value after release. The force was measured for three different angles with the surface normal as indicated: 0°, 45° and 90°.

channel is filled with air and acts as a visual pressure indicator (an example of the flow path is shown as dotted line). In this way, ten connectors are tested at the same time. Tubing and channels are filled with colored water up to the inlets of the dead-end channels to visualize any leakage.

(B) Leakage pressure after re-plugging In a second pressure test the leakage pressure and the failure rate for connections that have been re-plugged multiple times without cutting a fresh edge of the tubing was investigated. For this, a number of individual inlets ending in dead end channels are fabricated in PMMA, COC and PC. A pressure sensor is mounted as described above between syringe pump and inlet. The syringe pump is used to gradually increase the pressure on the inlet, while monitoring the bottom of the inlet for any signs of leakage. A constant flowrate is used to increase the pressure up to the limit of the linear range of the pressure sensor (250 psi or 17.2 bar). In different tests the pressure was either increased stepwise (4 bar per step and kept for 5 minutes at each step or 1 bar steps and kept for 1 min at each step) or increased continuously (slowly: 5 μL/min or quickly: 100 μL/min) until the maximal value is reached. It was then kept at this maximal value for several minutes before decreasing the pressure again. Testing the connectors by slowly ramping the pressure ensured that failure could be identified in cases where a certain time is required for it to be visible. If no failure occurs during a cycle, the tested connector is un-plugged and re-plugged immediately. The test is then repeated in the same way until leakage occurs either during ramping of the pressure or during the time at maximal pressure. In case no failure occurs after 8 cycle repetitions, the connector is unplugged and re-plugged 5 times before running the next pressure test. If failure occurs, a fresh edge is cut off the tubing and it is re-inserted into either the same or a different inlet for the next test.

Dislocation forces Forces needed to dislocate plug and tubing from an interconnection were assessed to measure the robustness of the interference fit mechanism. To evaluate the strength of this interference fit plugs were fabricated within a small range of sizes (outer diameter of the rim: 2.99, 3.0, 3.01, 3.02, 3.03 mm) and the force needed to dislocate the connector or tubing was measured. For each size, 4 plugs were measured 8 times each, cutting an edge off the used tubing for each test and using different sockets of the same size. The size of the socket has a nominal diameter of the outer edge of 3.05 mm decreasing to 2.95 mm in one step at the edge (see technical drawing in Figure 1B). A force meter equipped with a movable marker that shows the maximal applied force value after release is mounted between the devices and a handle to exert force as illustrated in Figure 3c. Devices are fixed in a clamp and the force on the tubing of the tested interconnection is exerted parallel to the direction of the tubing. The force is gradually increased until dislocation occurs. The force was measured for three different angles with respect to the surface normal: 0°, 45° and 90°.

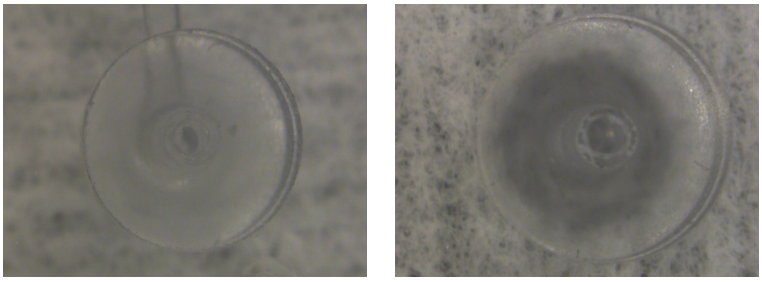

Figure 11.4 Inlet fabricated in Topas. The closeup images taken before and after bonding show no deformation.

11.4 Results

11.4.1 Fabrication

The three materials have been chosen for their use in different types of applications. While PMMA, being cheap and easy to machine using micro milling, is often the material of choice to test new concepts and make quick prototypes, other materials are likely required for specialized devices. PC is widely used in biomedical applications, where it is important to be able to sterilize devices according to standard protocols such as autoclaving. As a third material, COC was chosen due to its high chemical compatibility and excellent optical properties, which makes it suitable for analytical chemistry and optofluidic devices.[148]

The socket was optimized for easy fabrication using a two-step pocketing process that results in an inner and an outer edge within the fastening depression. The size of these two edges was optimized to yield the best sealing behavior by interaction with the inner diameter of the tubing on one hand and to create a strong interference fit with the plug on the other hand. The width of the edge is 100 μm in both cases. The upper part of the central pin has a diameter that is 80 μm smaller than the ID of the tubing while the lower part is 120 μm larger. This transition facilitates placement of the tubing and leads to the sealing deformation when the tubing is pushed down past the edge. On the outer part of the socket, the edge guides the plug and leads to an inward deflection of the segmented flange which fastens plug and tubing holding the interconnection in place. Using a 1 mm ball mill for fabrication of these features additionally creates a rounded bottom at the base of the socket, providing a large sealing surface with the tubing. Furthermore, all the edges are curved, generating a smooth transition between guiding and sealing/fastening surfaces.

Micro-milling parameters were individually adjusted according to the material and resulted in devices of comparable feature quality with PMMA showing the smoothest surface, while PC and COC are more prone to burring. Even though the shape of the connectors defines the sealing surfaces, we found that the different material properties do impact interconnection robustness in terms of reusability as discussed below.

The inlet structure is fully contained within the device without protrusions out of the sur-

face. This planar design offers the possibility to fabricate standard devices from templates that contain only the sockets and can readily be bonded to complementary parts with customized channel structures. In the same way, templates can be fabricated using injection molding with an invariable arrangement of inlets on one side combined with a variable channel system on the other side of the polymer plate. Such an approach is commonly used with Luer connections[149, 150, 151, 152]. Using thermal bonding, ready-to-use prototypes can be produced in a quick manner. Since the tip of the inlet pin ends in the same plane as the surface of the device, pressure is applied evenly around underlying channel structures to ensure sealing in the bonding process (Images of the socket before and after bonding are shown in Figure 11.4). In addition, devices can be sealed with adhesive tape for storage or incubation, where the shape of the socket helps to prevent spillage of liquid.

It was possible to directly reproduce the features for socket and plug by stereolithographic 3D printing. The inlet to the microfluidic channel and the pin structure could be printed without collapsing, but structural quality is lacking. We believe that the correct sizes for a tight fitting interference fit can be achieved by optimization of exposure times and printing material which has not been done at this time.

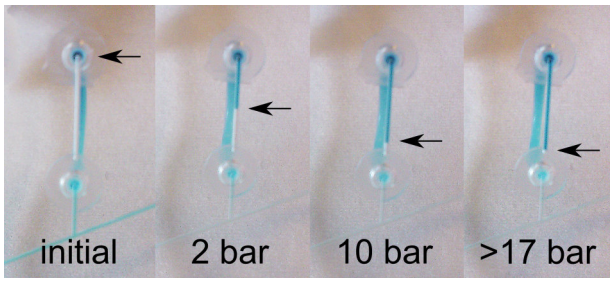

Figure 11.5 Close-up of one of the dead-end channels on the pressure test device. The compression of air in the channel indicates the applied pressure in the system. From this perspective (below the device) leakage can easily be spotted when inspecting the interconnection.

11.4.2 Pressure drop and pressure limit

In the first pressure test two pressure sensors, p1 and p2, were used to monitor the pressure drop Δp across the test device in order to ensure that the measured pressure values were valid. Δp was found to be 9% $\pm$ 1% of p1 across the whole range up to 17 bar with a 2% decrease between lowest and highest pressure (data not shown). The decrease indicates added pressure loss in the system at higher pressure, most likely due to deformation of the PTFE tubing along its length. The hydraulic resistance of the device and of the complete length of tubing between device and the two sensors are of the same order of magnitude. We can therefore conclude that pressure p1 measured at the first sensor will correspond to the pressure at the first inlet to within a few percent. The closed channels were used as additional visual pressure indicators, to directly monitor that the pressure was the same in each branch (one channel at three different pressures

is shown in Figure 5).

The device was further used to test exposure to high pressure for an extended time. No leakage occurred after 12 hours at 17 bar on any of the 11 newly connected interconnections in PMMA. Repeated tests of increasing the pressure to the maximal value and decreasing it again after 5 minutes showed no leakage.

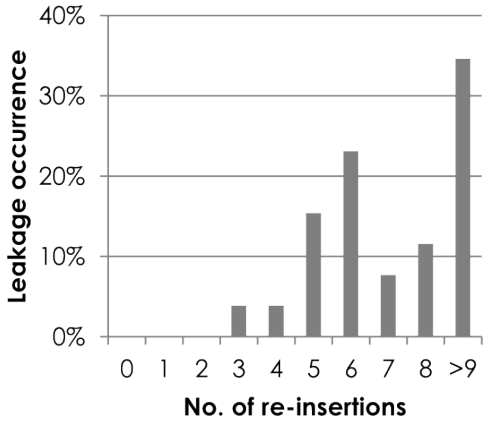

Figure 11.6 The bar graph shows the number of connections (in percent of total tested) that failed after a particular number of re-insertions. Every re-insertion cycle consists of un-plugging the connection and immediately replacing it by pushing first the tubing onto the inlet pin and then the plug into the socket followed by increasing the pressure in the system to maximum, keeping it for at least 1 minute and decreasing it back to atmospheric pressure.

Pressure testing of individual re-plugged interconnections To determine the leakage pressure of the interconnection in different materials, individual or small sets of connectors were tested in the stepwise manner described above. The results are summarized in Table 1. Since for most connectors, except 2 in case of COC, no leakage occurred up to the limit of the testing system, the table further shows the average number of re-insertions after which leakage occurred (at any pressure) and the average pressure at which it occurred. The pressure here does not represent an actual pressure limit of the connector as it depends highly on the number of re-insertions, i.e. the amount of damage inflicted on the tubing. It is to be expected that the robustness decreases for re-plugged tubing (with a necessarily deformed tip), but there are considerable differences for the 3 tested materials. For PMMA, a total of 36 connections were tested in this way until they failed after re-plugging (the details of this test are shown in Figure 11.6). These connectors stay highly pressure tolerant for up to 3 re-insertions, where some of them start to fail at high pressures (between 14 and 17 bar). 36% of the connections could be re-plugged more than 8 times without showing any sign of leakage even at maximal pressures. For COC about half of the connectors start to show a measureable leakage pressure (typically at 6 bar) after the first re-insertion, while this pressure drops further for failure at a later re-insertion. The performance

of PC connectors lies in between that of PMMA and COC, where failure occurs typically within the first 5 re-insertions (except for some outliers that did not fail at all) at high pressures above 14 bar.

The data suggests that the quality of the micro milled inlet structure plays a major role in the reliability of the interconnection, as milling in PMMA produces the smoothest surface and least amount of burrs or cracking compared to PC and COC. Since the surface roughness affects the sealing behavior, we propose that injection molded devices would improve the pressure tolerance of these materials even further and should be the fabrication method of choice if high pressures are expected in a system.

The spread of the data points for the PMMA connectors suggests that the damage induced by re-inserting the tubing is not systematically affecting the connection and other factors such as the evenness of the cut and size of the plug will most likely have a larger impact on the proneness to failure than the deformation of the tubing itself. Since leakage generally did not occur suddenly and with a large spillage, but after several seconds at maximal pressure, we suggest that small scratches on the tubing that are created by removing and re-inserting the tubing several times provide fluid paths for leakage. Since these scratches are induced by the inlet, burrs and a high surface roughness of the material has a large impact. Our tests show that while the freshly connected interconnection does not fail at extended times at high pressures, reliability is compromised if the deformed tubing is re-inserted several times.

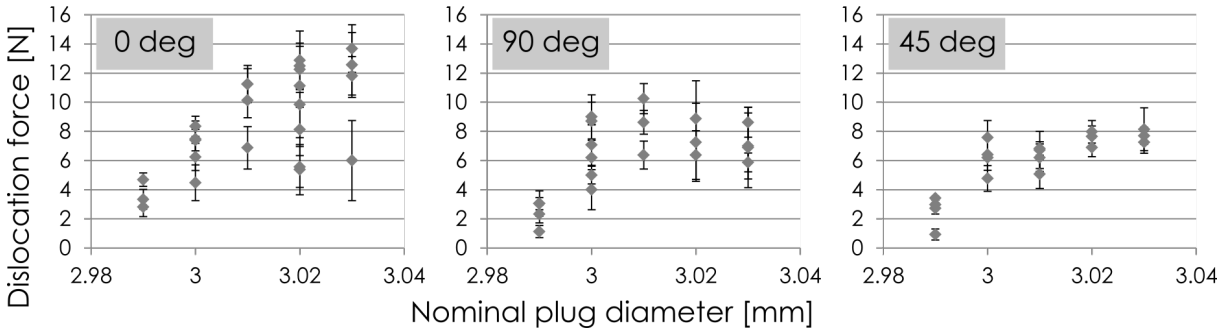

Figure 11.7 Dislocation force normal to the device surface for interconnections fastened with plugs of different sizes. Each point represents the average of 8 (0 deg) or 4 (90 deg and 45 deg) dislocation force measurements for a single plug and a minimum of 4 plugs were tested for each nominal size. The strength of the the interference fit increases with increasing plug size.

Interference fit and dislocation force The interconnection is secured by an interference fit between the plug and the outer edge of the socket. The data in Figure 11.7 summarizes the dislocation force measurements for 3 angles with respect to the surface normal (0, 45 and 90°). For a force parallel to the surface normal, the dislocation force increases with increasing plug diameter. Some outliers can be seen, which presumably represent plugs with fabrication defects. With decreasing size, the interference fit is not strong enough to hold the plug and tubing in

	(A) First connection (no. leakage/no. total tests)		(B) Re-inserted connection		
Material	slow pressure increase	quick pressure increase	average no. re-insertions until leakage	average pressure [bar]	total tests
PMMA	0/10	0/26	7.5 (2.8)	14.9 (4.8)	24
COC	2/15 (12.5 bar)	0/13	1.4 (0.7)	5.5 (2.8)	12
PC	0/15	0/15	3.2 (1.7)	17.2*	14

Table 11.1 Summary of the pressure test. The pressure limit of the test system was 17.4 bar. The left column (A) shows that out of all tested connections only 2 fabricated in COC showed leakage (at 12 and 13 bar), while the rest did not leak even at an extended time at maximal pressure. The right column (B) shows the average number of times that a connector can be re-inserted without cutting a new edge off the tubing until leakage occurs and the average leakage pressure of this re-inserted connector. The numbers in brackets show the standard deviation of each average. There are major differences in the number of times a connector can be re-inserted without compromising pressure tolerance depending on the material. *For PC leakage was only observed at maximal pressure.

place and the dislocation force drops. If force is exerted on the tubing at an angle of 45 or 90° by bending the tubing, the dislocation force levels off between 6 and 8 N, and does not increase above a plug size of 3.01 mm. Lower values are only found for the smallest plug. While the strength along the surface normal increases, bending of the tubing destabilizes the connector and leads to easier dislocation. At even larger sizes above 3.03 mm, the plug can no longer be pressed all the way into the socket and dislocates easily (data not shown). As long as the plug can be fastened in the socket without dislocating when bending the tube (which is the case for too small or too large plugs) the strength of the interference fit does not impact the pressure tolerance of the interconnection. Tests performed with plugs of different outer diameters showed unchanged sealing behavior. Overall, the data shows that in the optimized case a dislocation force of 12.5 N on average can be achieved for a force normal to the surface. The data shows that the optimal plug diameter is between 3.01 and 3.03 mm. It should be noted that no damage to the central part of the socket was observed after the experiments.

11.4.3 Application Examples

Sensor integration and surface functionalization in a flow cell The interconnection system enables the fabrication of ready-to-use devices, which is especially useful for the integration and testing of silicon sensor devices that need to be reversibly interfaced with microfluidic flowcells for functionalization and characterization. Different flowcells have been developed to interface a silicon nanowire biosensor for the detection of proteins. A 4-chip flow cell, shown in Figure 11.8(a) was used to functionalize silicon surfaces using a pre-loaded protocol driven by a syringe pump. The reagents were loaded into a length of tubing separated by air bubbles which is a common way to automate the execution of biological assay protocols for microfluidic systems.[7] The tubing could then be easily attached via the socket on the flow cell device to start the process. After execution the silicon chips were removed from the device for characterization by atomic

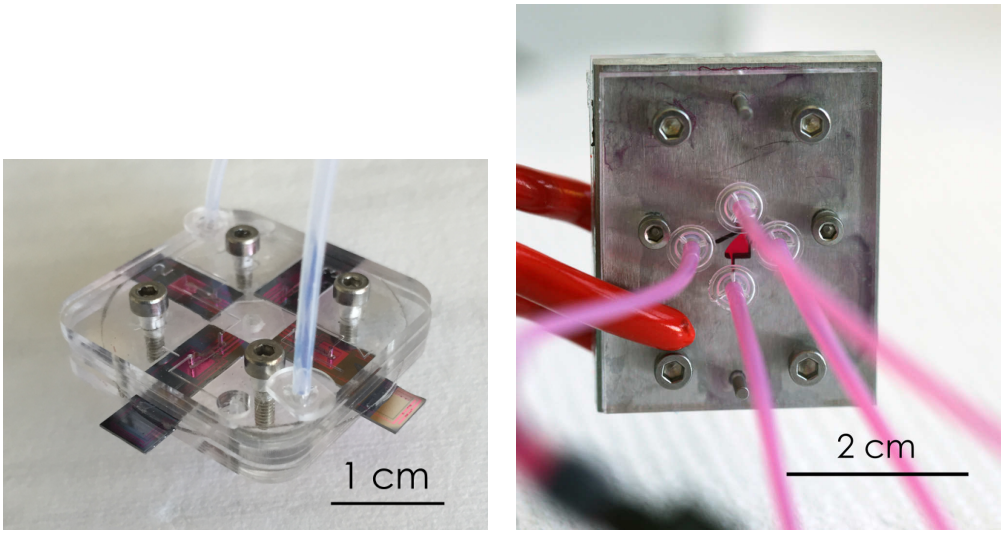

(a) (b)

Figure 11.8 Application examples: a)Flow cell to interface 4 silicon sensor chips in two separate flow streams, two sockets for in- / outlet can be seen in the front and back corner of the device. A PDMS sheet with channels in between the PMMA layers forms the sealing interface with the devices. b) The working model of the RheoStream^{TM}, a microfluidic flow cell for complex rheology measurements has been interfaced using the the interconnection system.

force microscopy, which would not be possible if they had been integrated into a permanent microfluidic chip. This application is an example of quick prototyping and testing of devices.

Brain Slice Culturing For biomedical applications devices need to be sterilized before use which is often done by autoclaving. Therefore, all components must be able to tolerate a temperature of 120°C for at least 15 minutes without deformation or delamination making composite interconnections (employing glues) less suitable. The interconnection system was used in the development of a microfluidic brain slice culturing device fabricated in PC where they proved to be superior to glued connectors and made it possible for the device to be operated without failure in a continuous flow driven by underpressure. The devices used perfusion of culture medium at a membrane interface to culture and monitor brain slices in a continuous flow system.[153]

Complex rheology measurements In addition to many biomedical applications, microfluidic tools are being developed for the on-line determination of fluid properties. Studying the rheology of complex fluids (such as non-Newtonian fluids that show shear-thinning or thixotropy characteristics) can be achieved by precise measurement of small pressure differences in a specially designed flow cell[154]. It is especially important to keep the system free of any pressure leakage and have the possibility to operate with fluids of high viscosity. The interconnection system was used in the working model of the RheoStream^{TM}measurement cell (shown in Figure 11.8(b)) and proved to be an easy to use and reliable interface for continuous measurements of complex fluids.

11.5 Discussion

The interconnection is designed without a gasket or glue, which avoids introducing any additional material into the system. This increases the flexibility in terms of chemical compatibility, since the device material needs to be chosen according to the application, and chemically inert tubing such as PTFE is readily available. No further fabrication steps or additional assembly of the connector parts are necessary in addition to device manufacturing, which reduces time and complexity of device preparation before use; tubing can be plugged in directly in a few seconds. Different materials can be used both for the device and for the plug in the interconnection, three examples of which have been presented. While we focused on micro-milling as fabrication method, the design can be reproduced by additive manufacturing and could be adapted for injection molding. Although the work in this paper has been done exclusively with PTFE tubing, other polymers with similar properties could be used.

No special care needs to be taken for cleaning and sterilization procedures, making the system especially suitable for biological applications. The internal volume of the interconnection is small, considering typical injection flow rates which can range from a few up to a few hundred μL/min for these types of devices. For example in chemical microreactors for synthesis typical injection volumes can be 200 μL[155] with flow rates of several μL per minute or down to 0.1 μl/min[156], and are generally run for several minutes. For microfluidic cell culturing, sorting or filtering systems flow rates span a range from 0.2 μL/min up to 450 μL/min and systems are commonly operated for several minutes up to hours[157, 158].

A high pressure tolerance of at least 17.2 bar for three tested materials (PMMA, COC and PC) makes the interconnection system suitable for applications that require high flowrates or very viscous fluids. Connectors can be un-plugged easily and can be re-plugged after a fresh edge has been cut off the tubing to ensure the highest possible reliability. Depending on the material, the re-plugged connection without a fresh edge can still withstand the same high pressures but may fail after several re-insertions. Compared to screwed connectors, that can typically withstand equally or even higher pressures, the presented structures have the advantage of a smaller size of the complete connector and especially of the socket compared to the threaded female part. In addition to the integrated socket it is also possible to fabricate the inlet separately and glue it using double sided tape to devices where structuring of the inlet feature is not possible or not desirable, such as devices made of glass or thin sheets of polymer. Of course this simplified method is only applicable in a very limited number of cases, where the requirements to material and performance are accordingly low, but it can offer an alternative to expensive and bulky commercial connectors. The dislocation test shows that interconnected devices are tolerant to device handling, which is important when devices are to be operated by people that are less familiar with microfluidics; this facilitates interdisciplinary research. It is common that especially in the prototyping stage microfluidic devices need to be tested and used by researchers other than the developers and simple operation is an important factor for the success of an experiment.

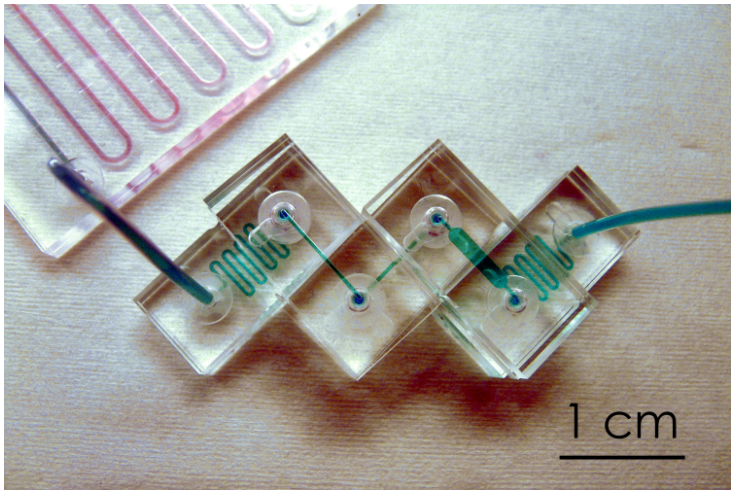

Figure 11.9 An example of individual interconnected modules

To obtain higher port densities, sockets can be spaced at a distance of the tubing diameter plus the diameter of the smallest milling tool use for fabrication of the plugs, typically this would be 500 μm. Multiple plugs can then be included in a small plug array which has been tested and proved to work well for up to 4 plugs. Higher port densities are more strenuous for the plug material and make attachment of the tubing inconvenient. For devices with a large number of inlets, other interconnection options are available that provide better usability. Furthermore, the presented device allows for the direct interconnection of microfluidic modules either via lengths of tubing on a breadboard-like system or using a double sided plug that enables stacking of several devices with minimal flow volume in between modules (an example is shown in Figure 11.9).

11.6 Conclusions

We have developed a microfluidic interconnection system with a high pressure tolerance that is easily integrated with manufacturing of planar polymer devices. The size can be matched to integrate different sizes of tubing and fabricated in different materials, making it easy to tailor properties such as chemical resistance or temperature tolerance. It is very easy to use and offers high robustness. Since no irreversible assembly is required, interconnection parts can be cleaned and sterilized separately, making the system suitable for biomedical applications in particular.

12 | Methods - design and fabrication of microfluidic devices

12.1 Simulation of microfluidic systems

COMSOL is a numerical modeling and simulation tool comprising modules for several types of physical systems. In the investigations performed in this thesis, only the Microfluidics Module in COMSOL Multiphysics 4.2 was used. First, the device layout was prepared in 2D using Autodesk AutoCAD or 3D using Autodesk Inventor and imported as geometrical model into COMSOL using the import function. To generate the mesh for numerical calculations the model was then checked for integrity and adjustments made as needed. The boundary conditions were defined according to the desired device geometry. Typically, the no-slip boundary condition was used for internal walls, inlets were defined using laminar inflow for cases where a syringe pumps was used or constant pressure for passive devices where e.g. gravity was used to drive the fluid. The outlets were defined with a constant atmospheric pressure.

For the device simulations shown in this chapter the process was as follows. In the first step the flow profile was determined for the entire system using a single phase flow for a Newtonian, incompressible fluid with the boundary conditions given by the geometry. In a second step mass transport of particle tracing was calculated to determine the distribution of diluted species through the system or follow the flow path of individual particles depending on their size and location. The first is important to investigate the distribution of reagents or proteins in a system that creates dilutions and performs mixing operations. The second in important for sorting systems and filters that handle different sized particles or cells.

12.2 Fabrication: micro machining and soft lithography

Microfluidic devices can be fabricated in different ways depending on size requirements and material. Many advanced microfluidic systems are fabricated in the clean room using high resolution methods such as photolithography and subsequent etching to define structures. Other devices do not require this precision and it is sufficient to define channel geometries using micromilling. Both approaches can be used to create devices directly or to create molds that are then used to cast devices in a soft material (commonly in PDMS).

12.2.1 CNC Micromilling and device design in EZ-CAM

Computer numerical control (CNC) milling machines, are tools used to create structures from a solid substrate by precise removal of material. The machine consists of a support stage on which the substrate is mounted and a tool head. The stage can be moved in x- and y- direction independently using stepper motors while the tool head can be moved vertically, providing the z-adjustment. The milling tools, that can take different forms, are mounted on the tool head and rotated with a given speed. In our case, no cooling system was integrated in the machine, so that cooling fluid needs to be applied externally during machine operation, depending on the material used.

The definition of the design is done using EZ-CAM15 Express, a software tool that allows for the determination of each machining step in a graphical environment and translates these into coded instructions for the milling machine. The sketches of microfluidic devices and mechanical components were designed in AutoCAD and imported into EZ-CAM as .dxf files. This imports the geometry of the device layout that can then be used to define the path for the milling tools. For each path, the milling tool size and geometry (flat endmill, round ballmill or drill bits are typically used), the feed rate in lateral direction, the step size in z-direction as well as the rotational speed of the tool are defined. The minimal tool size (diameter) that was used in the course of this work was 100 μm, the largest tool size was 3 mm. The feed rate and spin speed are highly material dependent, brittle materials with a high glass transition temperature are the easiest to mill and can be machined with hight feed rates and high spin speeds. Whereas softer materials provide more friction with the tool and parameters need to be adjusted to prevent the generation of heat that leads to melting of the material. Milling parameters were optimized for each material and tool size to achieve the best results.

For the fabrication of each device, the material was chosen according to the requirements of the application. For chemical robustness and solvent compatibility, different grades of COC (Topas) were used. For proof-of-principle applications and those for use with water based solutions only, PMMA was used due to its availability and ease of use. For biomedical applications that required sterilization, PC was used. The materials were obtained from in 10x10 cmsheets of 0.5, 1, 1.5, 2, 3 or 5 mm thickness for PMMA, 0.5 or 1.5 mm thickness for PC purchased from NordiskPlast (Randers, Denmark) and several different sizes for COC grade 5013 (injection molded in-house or obtained directly obtained from TOPAS Advanced Polymers GmbH, Frankfurt, Germany). The device material was mounted on a substrate sheet (to protect the milling stage from accidental tool damage) on top of the x-y-stage using double sided tape. The coordinate system origin (x, y, z) was defined manually, readjusting the location of z = 0 for each tool to match the tip of the tool head. Tool changes were also done manually.

Two-sided milling

For some device designs it is an advantage to be able to create structures on two sides of a piece of substrate. To achieve precise alignment of the designs, alignment marks are provided and

mirrored on the two designs. These are dilled as through holes on the first side of the device. At the end of the patterning, the device is removed and and at the first step for the second side is started before remounting the substrate. This step consists of creating the mirrored alignment marks that are drilled into an underlying substrate. These provide a fixture for 2 mm steel bolts or 2.6 mm steel balls that are used to align the device when it is fixed to the substrate with the second side upwards. In this way it was possible to create inlet structures on the top surface and microfluidic channels on the bottom surface of the same piece of material.

12.2.2 Device bonding

To create closed microfluidic channels in plastic devices, two sheets of material were first structured as explained above and subsequently bonded together. There are several ways to achieve closed devices. The most commonly used method is thermal bonding, in which the two pieces are joined together using elevated temperatures and pressure. Depending on the material, the surface of each of the parts is chemically activated to enable a covalent bond between the polymers. Together with the elevated temperature just below the glass transition temperature and a high pressure, surface roughness is overcome and ideally the bonded surface is as strong as the material itself.

A very simple method that is mostly suitable for proof-of-concept devices is to join two parts of a device using double sided tape. Different types of tape are available that differ in thickness and chemical composition. It was not relevant for the investigations in this thesis to investigate this further and the method was only used for demonstrator devices operated with colored water.

12.2.3 Soft lithography

Soft lithography describes the pattern transfer by bringing a (solid) mold master into contact with an initially soft material that then hardens to create permanent structures. The mold master can be created by clean room processing in silicon or glass, or by micromachining such as CNC milling in plastic or aluminum. PDMS is currently still the most common material to create molded devices, due to its high biocompatibility, low autofluorescence and ease of handling. Some drawbacks, such as poor chemical resistance to solvents and high gas permeability as well as its hydrophobicity have recently given rise to the development of alternatives such as thiol-ene(-expoy) based polymer blends. In this thesis, only PDMS has been used.

PDMS is combined in a 10:1 ratio with a cross-linking agent and the well-blended mixture is degassed in a vacuum desiccator for up to 2 hours to remove air bubbles. The highly viscous liquid polymer is then either directly poured into an open mold master or injected into a closed structure using a blunt syringe with a short tip. The material is then ideally cured overnight at room temperature followed by a short bake at 60 °C. Alternatively, the device can be baked directly at 60 °C for 2 h. The second method is more prone to formation of bubbles due to the quick onset of cross-linking, whereas if the device is left over night, contained gas has more

time to leave the material during the curing process. To create thin sheets of PDMS, the liquid polymer with curing agent was spin coated directly onto PMMA plates. The spin speed was set to 200 rpm for 10 s followed by a 30 s spin at 500 or 800 rpm, depending on the desired thickness. The polymer was cured overnight in the laminar flow bench. The sheets could then be patterned directly on the substrate using laser ablation or cut into larger pieces using a scalpel.

12.2.4 Laser ablation

Another method to rapidly prototype microfluidic devices is by laser ablation. In this process, a CO2-laser (infrared) is focused onto the substrate to burn the material in a predefined pattern. The device design is provided as vector graphic or rastered image, which is translated into the movement of the focusing head. Speed of the movement and power of the laser can be set as parameters. This method is primarily used to cut thin sheets of material such as tape for bonding, but also to create large microfluidic channels in plastic (with a V-shaped profile) or to cut sheets of PDMS.

12.3 Setup and operation of microfluidic devices

Devices containing a PDMS gasket or interface channel that is in contact with a silicon sensor chip (such as flowcells) were assembled under the laminar flow hood to prevent contamination of the PDMS sheet with dust. The sensor chip was placed on a support, the PDMS part first aligned on the plastic device and then attached to the substrate via screws, sealing the PDMS part to the chip by compression. By loosening the screws it was possible to remove and replace sensor chips without the disassembly of the whole structure. In this way, electrical connections could be attached to the chip first (via a ZIF socket) before it was inserted into the microfluidic device.

Most microfluidic devices described in the following chapter were equipped with the interconnection system described above. In this way, PTFE tubing (a 1 mm outer diameter (OD), 0.5 mm inner diamter (ID)) could directly be interfaced with the device using a plug and connected to a syringe (BD, plastic 1, 5, 10, 20 mL) using a blunted syringe needle (21-22 gauge, 0.6-0.8 mm OD). Depending on the application, the syringe was operated manually or using a syringe pump (Chemyx Inc. N3000).

12.4 Image analysis

ImageJ was used for quantitative analysis of fluorescent images and color microscopic images (dilution series). For fluorescent images, the intensity was extracted using line profiles or histograms (for area evaluations). The data was imported into MATLAB and further processed for plotting. If color enhancement was used for better visibility, the same parameters were applied to all images in the series for comparability.

13 | Microfluidic Devices and Concepts

This chapter provides and overview of the microfluidic devices that were developed in the course of the research for this thesis. These include both proof-of-concept devices to test different aspects of the sensor integration as well as tools that were used for some of the experiments discussed in the previous chapters.

13.1 Sensor interfaces: Microfluidic flowcells

To provide a simple and direct means of fluid delivery to silicon nanowire BioFETs and related biosensors, different types of flowcells were developed. One of the requirements was the capability to access the sensors surface in a continuous flow while being able to monitor the electrical sensor response in real time. In addition, the system needed to be temporary, i.e. it was necessary to be able to fully remove the flowcell after a measurement for additional characterization by microscopy.

13.1.1 Design and fabrication

The overall design of the flowcell consists of two different parts: the interfacing channel, the external interface with a support as schematically shown in Figure 13.1. The interfacing channel is the part in contact with the silicon chip and needs to be made from a compressible material that can form a temporary seal between the device and the chip. The external interface provides a means of connecting tubes, i.e. the inlet part of the developed interconnection system, with is connected internally to the inlet of the flowcell. One of the advantages of the interconnection system in this case is the seamless transition between the inner tubing diameter to the microfluidic channel. The channel dimension is of the order of ten of micrometers while the standard tubing has an internal diameter of 0.5 mm. By providing an inlet that is inserted into the center of the tubing, no dead volume or obstruction is created that hinders the precise metering of injected fluid.

The flowcells were designed in AutoCAD and/or Autodesk Inventor and the models translated into instructions for CNC milling using EZ-CAM15 Express. The external part of the flowcell typically consisted of two separate pieces fabricated in PMMA or Topas (depending on the intended application). Each piece was milled from one side; the top part contained only the inlet structures and through holes to connect to the internal channels, the bottom part contained the

channels and through holes that would connect to the underlying PDMS interfacing channel. The two parts were thermally bonded to each other as described in 12.2.2.

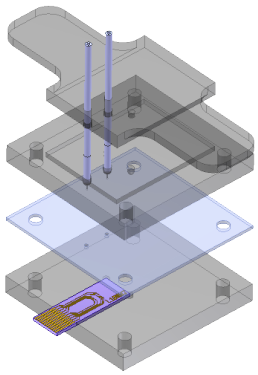

Figure 13.1 Concept of a flowcell to integrate the silicon nanowire sensor chip. The cell consists of a frame made of PMMA, a thin sheet of PDMS that seals the on-chip channel and the interface for the connection of external tubing.

13.1.2 Flowcell implementations

The initial flowcell design consisted of either a single channel in a sheet of PDMS or simply two through holes that interface to an open microfluidic channel directly fabricated onto the device structures. In- and outlet to the channel consist of interconnections in a micromachined PMMA piece without any channel system as shown in Figure 13.2(b)

Extending on this very simple concept, several other designs were developed, including two channels on the same device, electrodes for electrochemical experiments and the integration of several sensor chips within the same flow system (13.2(c)). All these flowcells could be interfaced with tubing to be actuated by syringe pumps or underpressure and enable access to the electrical connections of the sensors chips. As an example of a passively driven device, a flowcell driven by gravity was developed, a proof of concept is shown in Figure 13.2(d). The two reservoirs can be filled with washing buffer and reagent respectively and will initially be applied to the reaction chamber in a mixture until the reagent reservoir empties (bottom at higher level) so that only buffer is left for the washing step.

13.1.3 Experiments and Results

Experiments for the functionalization of silicon nanoribbon chips and the detection of proteins on the functionalized layer were performed with and without the flowcell to compare the impact of the flowcell on the process. Unfortunately, none of the data obtained in these comparison experiments showed promising results. The flowcells were used as tools to perform some of the experiments discussed above. One of the sensing experiments that was performed individually in a flowcell is described above in the biosensing chapter. Other attempts at performing mea-

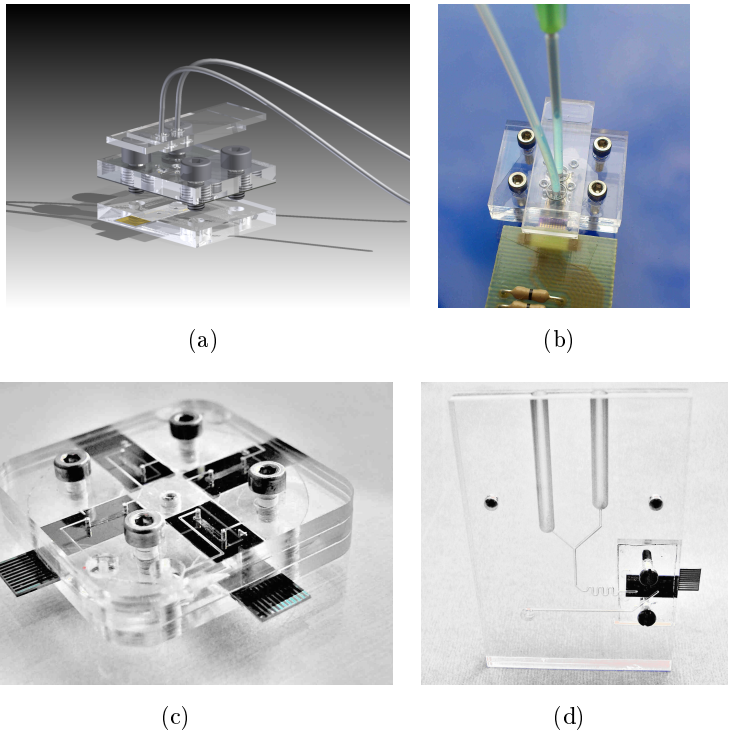

(a) (b)

(c) (d)

Figure 13.2 The figures show different flowcwell devices to integrate one or several silicon nanowire sensor chips (or test chips of the same size). *a)* 3D CAD drawing of the simple flowcell parts and their assembly. *b)* Simple single channel flowcell. *c)* Flowcell to perform experiments on 4 chips at the same time, 2 separate flow paths can be used to access two chips each (sample and control experiment). *d)* Flowcell with gravity driven reservoirs for a two step process.

surements in a flowcell failed due to failure of the sensor chips. The flowcell was further used to monitor the etching of silicon nanoribbons in hydrofluoric acid as described above in the surface chemistry chapter.

13.2 Calibration cartridge and titration tool

Providing quantitative measurements of biological material with miniaturized biosensors requires a means of calibration. In some cases it may be sufficient to perform a calibration procedure per batch of produced sensors and provide the relevant information with the final device. In other cases it may be required to perform calibrations before every measurement, due to environmental influences on the sensor or deterioration and changes over time. In the second case, it is important to be able to supply a simple and robust method for calibration that can be performed by the end user in the field before the actual measurement is taken. Especially in case of one-time-use sensors such as the SiNW BioFET calibration poses a challenge that needs to be addressed carefully.

13.2.1 Calibration curve and dilution series

Calibration of an affinity based sensor is usually done by establishing a titration curve using several concentrations of the analyte in question. For this, a set of predefined concentrations is measured and the resulting measurement points are fitted to a curve that can then be used to determine the unknown concentration of sample. The shape of the curve, and with this the number of required measurement points depend on the different phenomena that govern the affinity parameters. Protein-protein binding on surfaces in itself follows a statistical process that depends on concentration of the protein in solution and surface coverage and orientation of the counterpart immobilized on the sensor. But in addition to that it also depends on temperature, pH and ionic strength, other interfering proteins or molecules and potentially further factors that can affect the charge, structure or immediate environment of the binding macromolecules. In brief, the more closely matched calibration and measurement conditions are to one another, the more reliable will be the quantification. Generating a set of predefined analyte concentrations from a known reference sample can be done in several ways. We have developed a microfluidic dilution system that can generate 5 different concentrations by mixing two input concentrations. Beside its use for calibration, the device can be used to deliver different concentrations of reagents to several separate reaction chambers to achieve a titration series for protocol optimization.

13.2.2 Device design

To achieve a robust way of mixing two samples in a microfluidic device of a small footprint, two things are most important: Accurate metering of the ratio of input solutions and efficient mixing. The common way to generate dilutions, for example to establish a gradient across a channel, is the mixing of fluids in a 1:1 ratio over several stages with intermediate mixing channels such as meanders or chaotic mixers. However, for calibration or protocol optimization involving biological materials it is often required to span several orders of magnitude of concentrations, which would require a very large number of stages or mixing ratios that differ from 1:1. A large number of stages results in an increased footprint of the device due to the required mixing step after each stage to obtain a uniform concentration across the channel at the next bifurcation. To address this, we have developed a dilution scheme that does not require mixing after each stage. As shown in Figure 13.3 the two fluids are combined alternately in vertical and horizontal directions, giving each partial dilution more time/lengths for mixing. This eliminates the need to already reach a uniform distribution after each combination step, since the next split occurs perpendicular to the diffusion direction. Mixing is only required after the second merging stage making it possible to portion the fluid in the first part of the device and move the mixing stage to the second part. By tuning the hydraulic resistance of each channel accordingly, it is possible to obtain mixtures of different ratios.

To create the channel system, each section of the system was created with to obtain the same flow rate in each channel by adjusting the hydraulic resistance (width or height and lengths of the channel) within the limits given my fabrication constraints (tool size and cutting direction). To determine the channel dimensions and device layout in an easy way, the device was divided into segments and designed step by setp. The first segment is the part between the inlet and

the first merging stage, the second segment is between the first and the second merging stage and the third segment is defined as the rest, where mixing occurs and the liquid is guided to the outlet. The last segment was designed with to be identical for each channel, symmetrically merging them into the outlet, so that the pressure is equal in all channels at the end of segment 2. Segment 1 and 2 were designed so that the combined cross section of is equal across the channels along the whole segment, to enable splitting and merging of fluids without a change in channel diameter. This makes the design process more straight forward, removing the need to consider each parameter of the channel dimension. What this means in practice is that if a channel is split into two by a defined ratio (of the cross section), the length of the channel segment can be adjusted to tune the hydraulic resistance to match this ratio, compensating for the power of 4 dependency on the cross section (see 10.1.1). An excel table was generated to chose suitable ratios and channel lengths and the device layout was then designed symmetrically with respect to the two inlets to achieve a symmetrical dilution series.

The system was designed based on simple requirements; each combined channel segment for each stage needed to have the same hydraulic resistance to achieve the same output pressure and flow rate at each of the output channels. The concentrations at the outlets were 0, 0.175, 0.5, 0.825 and 1 of the initial concentration in one of the inlets. These concentrations were chosen due to suitable channel dimensions for proof-of-principle of the device given the fabrication constraints. In the testing device, these channels were combined into a single outlet channel after mixing to simplify the operation and to evaluate the concentration distribution at the outlet (gradient).

13.2.3 COMSOL Simulation

The device was simulated using COMSOL Multiphysics 4.2. The results are shown in Figure 13.3, where the image shows the horizontally and vertically combined fluid flows at each intersection and the final concentration distributions. The integrated areas over each cross section are shown in Figure 13.3c) below the images. The mixing stage has been simulated separately, in the master thesis work of Elisa Popescu[159], and it was shown that sufficient mixing can be achieved with a chaotic herringbone mixer over the small distance of 1 mm as shown in Figure 13.3(d).

13.2.4 Testing

To test the concept, a test device was fabricated in PMMA by micromilling as shown in Figure 13.4. It is composed of the segmentation and merging network described in the simulation above followed by a mixing stage that consists of a meander in each output channel. All the channels are then merged in a stepped manner to achieve a consistent pressure drop and crate a gradient across the output channel. The device was tested by injecting water containing different food dyes into the two inlets and taking bright field images of the channels after the meander and at the outlet channel. The images were then decomposed into R, G and B channels to obtain a color profile. This does not exactly represent the dye concentration, but it gives an impression of the distribution.

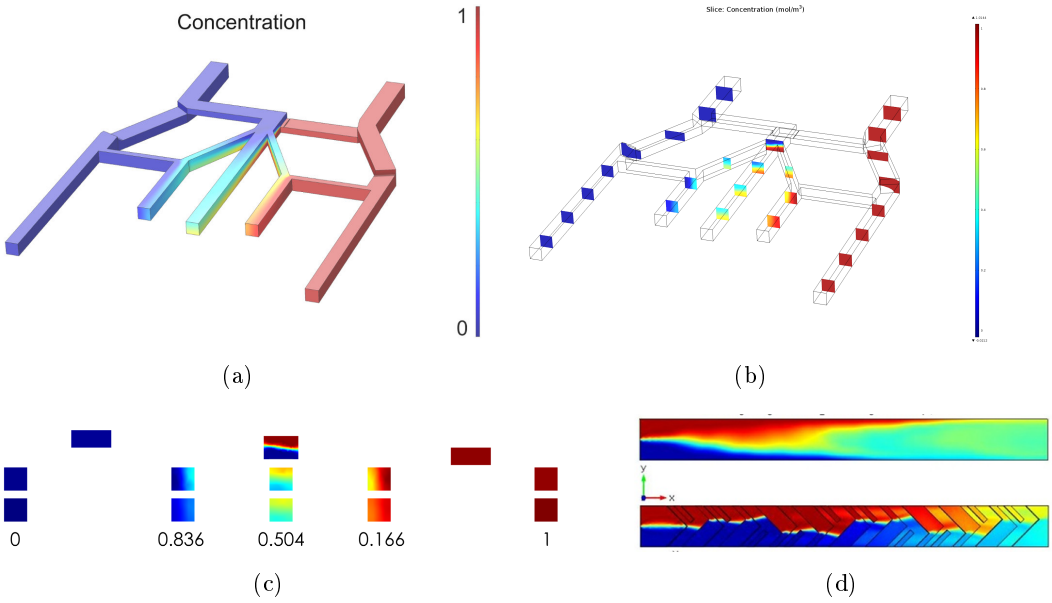

Figure 13.3 3D model with COMSOL simulation of the concentration distribution through the dilution network. a) The surface of the channels, where the left inlet contains a simulated concentration of 0 and the right inlet a concentration of 1. b) Slices through the device show the development of the concentration in the different branches. c) Enlarged images of the slices in 3 stages: after the first branch, after the second branch and close to the end of the outlet. d) Simulation of a Herringbone mixer, illustrating what can be achieved over the short length of 1 mm (channel with 100 μm, height 25 μm, depth of Herringbone features 25 μm.)[159]

13.2.5 Results

The bright field images shown in Figure 13.4(a) are a composition of images taken at each of the outlet channel after the meander. The graph shows the color intensities measured across the central region of each channel. While the color intensity is close to linear for green and blue it differs systematically from a linear curve for the red channel.

At the combined outlet channel, a gradient is generated by merging the different solutions. Analysis of the color image taken just before the device outlet shows this (13.4(d)). The graph shows the profiles of the three separate color channels, displaying a linear distribution of concentrations across the channel for blue and green and an S-curve for the red channel. Comparison with the values (black dots) obtained from the COMSOL model, we can see an agreement with the red curve. This method is not suitable to evaluate the actual concentrations in the channels due to interference of the different colors. A test with fluorescent dyes would be better suited, but has not been performed at this point.

13.3 Functionalization cartridges

The ability to functionalize the surface of a biosensor just before a measurement is performed has several advantages as discussed in the introduction. In order to make this feasible in a clinical

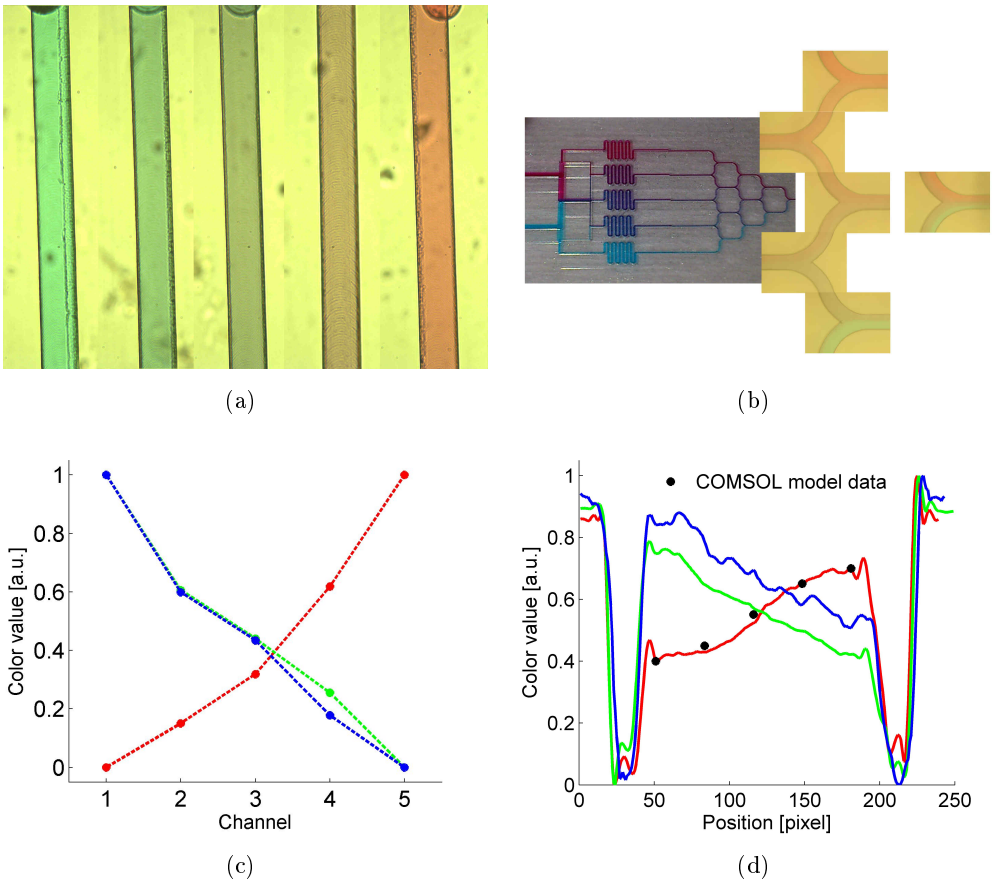

Figure 13.4 Proof of concept for the dilution network. a-b) Testing device and bright field microscope images of the channels after mixing and of the merging network during operation, filled with colored water. c-d) Graph showing the color intensity of the channels (area averages, split into color channels) and a profile across the outlet (split into color channels).

environment, the process needs to be straight forward and robust. Containing the reagents needed for the final immobilization of biomolecules that will act as receptors within the device addresses the stability concerns associated with some biofunctionalized surfaces. Separating the two, sensor and functionalization reagents, by providing a separate cartridge that can be attached to the device prior to the measurement adds additional functionality and opportunities for customization. A modular system could be envisioned that can combine a number of different sensors with several types of analytes, allow for multiplexing and thus the composition of tailor-made panels suiting the diagnostic purpose. In a step towards this modular approach 3 types of cartridges have been devised and tested for functionality.

13.3.1 Air separated reagent storage

One of the straight forward ways to store the reagents for a functionalization protocol is to load them into a length of tubing separated by air bubbles. This if of course only possible if all the steps in the protocol can be carried out in liquid by means of injecting different reagent and washing solutions sequentially. This principle has already been used for diagnostic testing in low-resource settings even though it requires a cold-chain for transport and storage of the tubular cartridge or complete chip as mentioned above. However, it provides a means to test the principle of flowcell functionalization in order to establish a base line of the measurement for comparison with other concepts that may overcome some of the drawbacks associated with this way of storage.

For the experiment, the different reagents are prepared in eppendorf tubes and lined up in sequence of their intended delivery to the sensor. Two separate cartridges were prepared, one as a control without the linker Glutaraldehyde to investigate the amount of unspecific binding. A syringe pump is used to draw the liquids into a clean tube that will act as cartridge. A syringe filled with buffer or deionized water is used as the base medium; the tubing connected to the tip of the syringe. First, the whole length of tubing is filled with this medium by pumping with the syringe pump. Then the pump is switched to the withdraw direction and starting with an air bubble the reagents are loaded into the cartridge, with the amount of reagent determined by the time the tube is inserted into the respective container. The table listing the reagents for sample and control with times and volumes can be found in the Appendix C.3.6.

13.3.2 Compressible reservoirs

For devices that need to handle clinical samples and other biological material, prevention of contact with the contained reagents and samples needs to be ensured to provide safety in operation and disposal. Design concepts that allow for completely closed devices that only allow very limited access to introduce the sample are therefore and advantage. To develop the system for automated functionalization in this direction, a concept was developed that relies on the on-chip storage of all reagents in flexible reservoirs that can be externally actuated for loading and emptying.

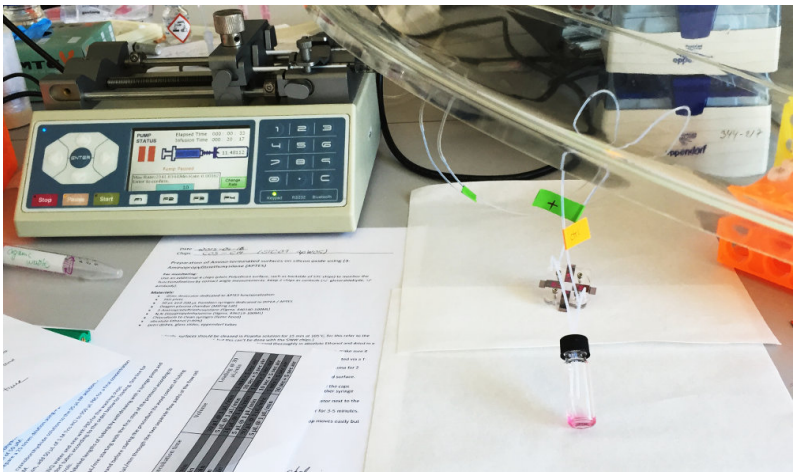

(a)

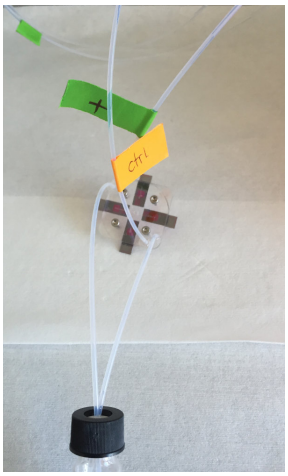

(b)

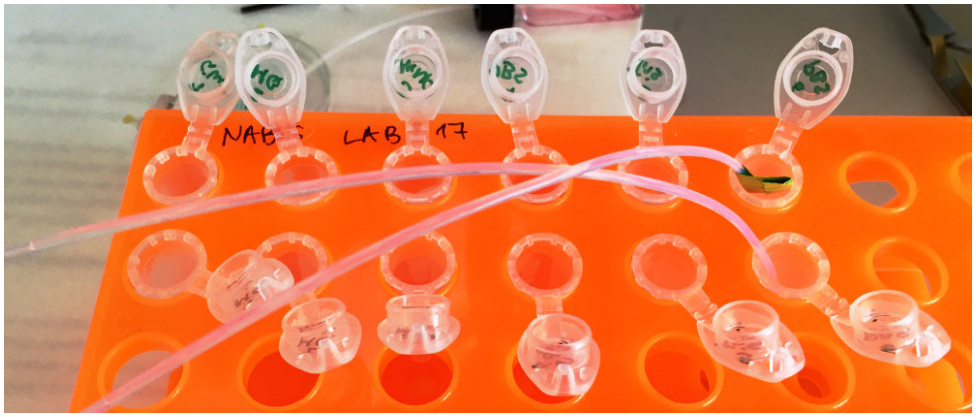

(c)

Figure 13.5 Setup for functionalization in a flowcell. a) The syringe pump (left) drives the individual liquid droplets in the tubing forward towards the device which is located under the fume hood in case of spillage. b) The flowcell consists of separate flow paths with in- and outlet, each of which is in contact with two sensor chips. The liquid at the outlet is collected in a vial for later disposal. c) Filling of the cartridge tubes is done by lining up the reagents and dipping the end of the tubing into the corresponding reagent for a specified amount of time while the syringe pump is withdrawing the liquid. This is done in the 'forward' order, starting with the first reagent that is to be delivered to the chip and then reversing the tubing after filling.

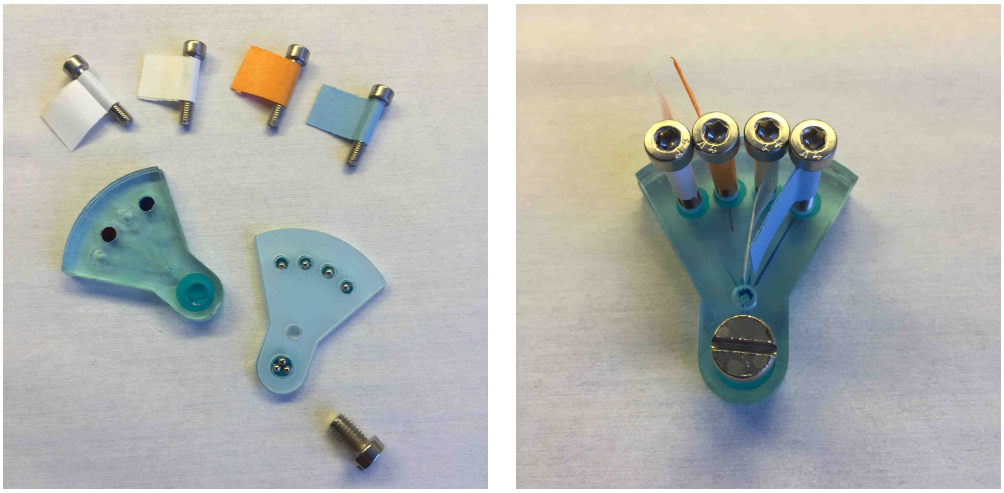

(a) (b)

Figure 13.6 Proof of principle for the operation of a functionalization cartridge with compressible reservoirs. Each of the 4 reservoirs is connected to the functionalization chamber via a channel. The reservoirs are filled with different solutions while the channels are filled with air when the devices is closed. Each reservoir is closed with a flexible membrane on top, that can be compressed by turning the screw, which releases the solution into the chamber. On the opposite side of the chamber, a waste reservoir is the operated in the opposite way, sucking the solution out of the chamber. This way, each of the reservoirs can emptied individually, filling the chamber for a specified amount of time.

Device design and fabrication

The device is made by laser machining using PMMA substrates and further assembly by thermal bonding to close the channel structure and sealing with a flexible, chemically inert nitrile membrane as intermediate layer using medical grade double sided adhesive tape. The minimal number of steps in functionalization protocols to immobilize proteins on prepared sensor surfaces is 4 (activation, washing, protein, washing), so 4 compartments were included in the first prototype as shown in Figure 13.6. From each reservoir a channel leads to a collection chamber which in turn connects to the reaction chamber or sensing area on the chip. In the prototype a dummy chamber on-chip was used for this to avoid connection to the sensor in this initial proof-of-concept. A large (at least 4 times the size of each reservoir to collect all the reagents after use) waste chamber on the opposite end of the reaction chamber is equally equipped with a flexible membrane for external actuation.

Device operation

Two ways were tested to fill the reservoirs, either by filling before sealing with the membrane or loaded into the assembled device through an access hole in the collection chamber. The latter was done by compressing the membrane to remove air and introducing the required amount of reagent (to fill the reaction chamber) with a pipette while gradually releasing the pressure on the membrane. The waste chamber was emptied of air, by putting permanent external pressure on

the membrane and the device sealed. Each reagent is then directed to the reaction chamber by simultaneously releasing some of the pressure on the waste chamber and actuating the according reservoir until the reagent chamber is flushed. The reagent can then gradually be moved through the reagent chamber by continuing this process (which was not tested) if a flow is required. The chamber is emptied in the same way, clearing out the previous reagent with the next or replacing it with air from the back of the reservoir before introduction of the next step. In this way, one reagent after the other can be introduced into the reaction/sensing chamber without the need for external liquid access during the procedure.

Figure 13.7 The blister pack prototype shown here contains 3 reservoirs that are filled and sealed. Upon pressing onto each of the blisters in turn, a pin insider the microfluidic network breaks the seal and releases the stored solution into the channel. Here, a suction pad is used as waste reservoir and pump.

13.3.3 Blister packs

As an alternative to the above solution that does not require the continuous operation of several reservoirs, another concept was developed based on the use of a blister pack for reagent storage. By using blisters, the flexible membrane is replaced by a stiff material that keeps its form after deformation. In this way, when a blister is emptied, no force needs to be exerted in order to prevent liquid back-flow or creation of an underpressure in the system (which can introduce leaks or diffusion of air through porous materials).

Device design and fabrication

The device layout was changed to a linear format with a single channel along which the reagents are stored. Each reservoir is sealed off towards the connecting channels using a thin foil that is also used to form the blisters. A makeshift blister pack is made by pressing aluminum foil into a series of depressions to form small wells, which are then filled with reagents and sealed using a layer of aluminum foil with double sided adhesive tape. The device is fabricated separately by

micromilling and bonded by adhesive tape. Underneath each of the reservoirs a small pin is used to break the foil when the blister is pressurized and release the reagent into the channel. Both parts are combined by another layer of adhesive, the different parts and final device is shown in Figure 13.7. For the shown prototype, the device was not yet sealed completely, but equipped with an open outlet containing a paper strip as capillary pump.

Device operation

After assembly of the device, each reservoir is compressed until the pin breaks the membrane and the liquid is released, starting with the blister the furthest away from the outlet. The liquid moves along the channel towards the outlet where the reagent chamber would be placed. The channel will still be filled with the reagent after the first step. By breaking the second blister and releasing the contents, backflow is not possible and access of the previous reagent into the reagent chamber is prevented while the channel is flushed with the next one.

13.4 Plasma Extraction

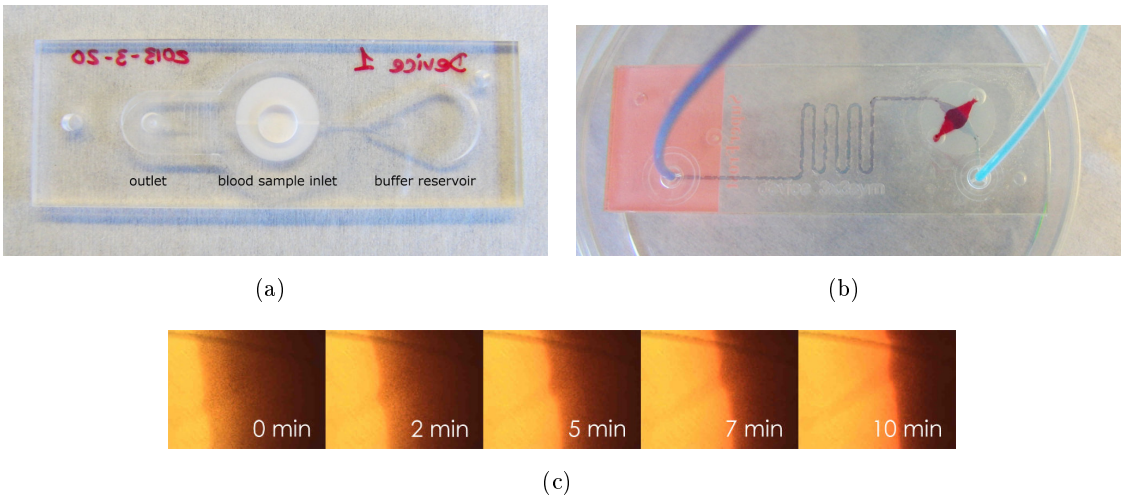

Figure 13.8 Two versions of the membrane based plasma extraction device. a) Membrane filter in an open inlet. b) closed channel on top of a membrane into which the blood can be introduced and then sealed. c) Whole blood sample in device a), the plasma is drawn down into the device while the blood cells remain on top of the membrane.

Extracting different components from whole blood is an important step for patient sample preparation on a chip. The blood plasma is the liquid part of the blood with soluble proteins and coagulation factors. By extracting the red and white blood cells this protein content can be analyzed without the interference from blood cells during the measurement process. Whole blood is a very complex fluid that shows non-Newtonian behavior, meaning that the viscosity is non-linear. Since this behavior differs considerably from other liquids or even suspensions with rigid particles such as beads, the translation of applications from the testing stage into

real devices is a critical point. Our primary focus is on analysis of free protein, therefore, the interference from blood cells should be limited as much as possible.

13.4.1 Membrane based plasma extraction

A membrane based microfluidic inlet was previously developed by Karsten B. Andersen and was adapted to filter out blood cells at the point of entry into the device. The device, shown in Figure 13.8a) was fabricated in PC by micromilling. The bottom substrate was cut into the size of a microscope slide, facilitating imaging using and inverted microscope. It contains a single channel that connects an open (for testing) buffer reservoir with an outlet. In between the channel contains a widened area below the membrane and a meander for mixing between membrane area and outlet. The top part contains a circular opening on top of the membrane and a socket for tubing at the outlet connected to the underlying channel. The device was thermally bonded, enclosing a circular membrane (0.22 μm pore size, polycarbonate, Milipore) in its center.

The device was designed as a proof-of-principle to show how the blood cells can be filtered out of whole blood using a simple setup. The device is first connected to a syringe and filled with PBS via the outlet using a syringe pump until the reservoir is full. The the syringe is the reversed and set to a flow rate of 5 $\mu\mathrm{L}/\mathrm{min}$. Whole blood (Bovine blood obtained from Statens Serum Institute (SSI, Copenhagen, Denmark)) is introduced into the inlet on top of the membrane. The time lapse in 13.8c) shows how the liquid (plasma) on top of the membrane disappears, while the cells remain, demonstrating the the device is capable of retaining the cells while the plasma is drawn into the buffer solution. The quality of the resulting diluted plasma and overall efficiency of the device were not investigated further. Due to the availability of several commercial solutions, such as specialized blood filter membranes and pads that extract the plasma at the point of collection, further investigations of the plasma extraction process were postponed until the requirements of the sensor system could be more clearly defined.

14 | Summary and Outlook

The three different parts presented in this thesis addresses different aspects in the development of affinity biosensors for protein detection.

The first part discussed the topic of surface functionalization. The biosensor surface provides the interface between the biological binding event and the transducer. As such, the mechanisms by which the signal is converted and the properties of the interface are very important for sensor operation. We have investigated the functionalization of oxide-free silicon surfaces for application on silicon nanowire biologically gated field effect transistors. These sensors are sensitive to changes in surface charge, e.g. associated with the attachment of proteins. For this reason they are prone to interference from trapped charges at the interface. By removing the impact of the oxide layer, trapped charges in the oxide are removed and the biomolecule is brought into closer contact with the semiconductor. Different organic molecules were investigated as candidates for surface passivation and as a platform for the attachment of receptor proteins. Initially 1,7-Octadiyne a bi-functional alkyne was investigated as substrate for a subsequent 'click' reaction to attach biomolecules via azide groups. Preliminary results showed a high coverage with octadiyne even though the labeling process with fluorescent molecules was inconclusive on polysilicon surfaces. We further investigated 10-N-Boc-amino-dec-1-ene, an alkene with a protected amino group as functional head group, which can be easily identified using XPS measurements. Quantification of the surface coverage showed a high coverage in a few cases, the functionalization process in the presence of air did not result in reproducibly stable monolayers. We observed a significant suppression of concurrent surface oxidation with the addition of triphenylcarbenium tetrafluoroborate to the functionalization solution, which is an interesting finding that may enable the functionalization of oxide-free surfaces under less stringent atmospheric conditions. The best surface coverage was obtained using thermal functionalization with undecenoic acid. The molecule, terminated by a carboxylic acid group, was chosen due to previous difficulties removing the BOC group to activate the amino-terminated surface for conjugation without damaging the monolayer. COOH also presents a more suitable substrate for the conjugation of protein via aminocoupling, which was demonstrated by the immobilization of antibody conjugated nanoparticles. The next step towards implementing oxide-free surface functionalization methods on silicon sensors it an investigation of mixtures with and without functional head groups to investigate the impact of head group density on protein conjugation efficiency. Octadiyne remains an interesting candidate to investigate as a platform for rapid protein conju-

gation via click chemistry and with the use of more suitable characterization methods such as Fourier-transform infrared spectroscopy the surface grafting under different conditions could be optimized further.

The second part discussed experiments and simulation performed using the SiNW BioFET. Different functionalization protocols were used to modify the silicon nanoribbon sensor at the present state of development and the resulting sensor was characterized for electrical functionality. Protein receptors (primarily mouse immuniglobulin) were immobilized using reductive amination with via Glutaraldehyde, aminocoupling or copper assisted cycloaddition. The electrical response of the nanoribbon was analyzed in order to determine the sensitivity of the sensor. Measurements have demonstrated the ability of the sensor to detect binding events on their surface. The sensitivity varies hereby depending on the fabrication parameters of the sensor and post-treatments, so that a reproducible and quantitative estimation of the sensitivity and detection limit can not be made with confidence. At the conclusion of the experiments included in this thesis, the sensor development had not been at a stage where the sensitivity was suitable for the detection of biomolecules due to issues with material compatibilities and the fabrication process. However, at this time the development has progressed further, and the latest characterization results show promising values for the sensitivity in response to surface charges. The results will shortly be submitted for publication.

In the third part the development of microfluidic tools was addressed. These were used in order to facilitate the handling of the biosensor chip and to target different aspects of the device integration. An interconnection system to interface different microfluidic modules via standard tubing was developed and used for many of the devices. This made it possible to create flexible systems that are rapidly prototyped and set up. Simple flowcells were used to interface with the sensor surface to enable real-time measurements of different surface modification and detection steps. The automation of the functionalization process was attempted by developing cartridge systems that can store the required reagents and deliver them in an automated and timely manner to a sensing area. The presented results demonstrate a proof-of-principle and did not reach the stage in which one of the approaches was implemented with the sensor for further testing and validation, as the sensor did not enable the quantitative analysis of the outcome. A dilution system to be used for generation of a gradient or a set of dilutions was developed in order to facilitate calibration and testing of concentration dependence on surface modification.

Further concepts for the full integration of the point-of-care sensor system were under development but did not reach the prototyping stage due to other priorities. However, the concepts can be tested and implemented once a reliable sensor system and instrumentation for data readout are developed. As a new design of the sensor chip was in discussion to include better noise compensation and further sensors a duplicates or triplicates of each measurement, no specific solution for the current sensor was designed. A concept for the new sensor chip and enclosing device contains several separate (on-chip) microfluidic channels for functionalization and sample delivery that should enable the preparation of a multiplex biosensor platform. While we are one

step closer to the implementation of a silicon nanowire BioFET as sensor for the detection of proteins, many challenges lie ahead.

Bibliography

[1] M. R. Hediger, J. H. Jensen, L. De Vico et al. [**2011**]. 'Biofet-sim web interface: Implementation and two applications'. *PloS one* **7** (10) e45379–e45379

[2] H. Zhu, S. O. Isikman, O. Mudanyali, A. Greenbaum and A. Ozcan [**2013**]. 'Optical imaging techniques for point-of-care diagnostics'. *Lab on a Chip* **13** (1) 51–67

[3] Y. Song, Y.-Y. Huang, X. Liu, X. Zhang, M. Ferrari and L. Qin [**2014**]. 'Point-of-care technologies for molecular diagnostics using a drop of blood'. *Trends in biotechnology* **32** (3) 132–139

[4] F. B. Myers, R. H. Henrikson, J. Bone and L. P. Lee [**aug 2013**]. 'A handheld point-of-care genomic diagnostic system'. *PLoS ONE* **8** (8) e70266

[5] H. Shafiee, S. Wang, F. Inci, M. Toy, T. J. Henrich, D. R. Kuritzkes and U. Demirci [**2015**]. 'Emerging technologies for point-of-care management of hiv infection'. *Annual review of medicine* **66** 387–405

[6] B. Crocker, E.-L. Lewandrowski, N. Lewandrowski, K. Gregory and K. Lewandrowski [**2013**]. 'Patient satisfaction with point-of-care laboratory testing: report of a quality improvement program in an ambulatory practice of an academic medical center'. *Clinica Chimica Acta* **424** 8–11

[7] C. D. Chin, T. Laksanasopin, Y. K. Cheung, D. Steinmiller, V. Linder, H. Parsa, J. Wang, H. Moore, R. Rouse, G. Umviligihozo, E. Karita, L. Mwambarangwe, S. L. Braunstein, J. v. d. Wijgert, R. Sahabo, J. E. Justman, W. El-Sadr and S. K. Sia [**2011**]. 'Microfluidics-based diagnostics of infectious diseases in the developing world'. *Nature Medicine* **17** (8) 1015–1019. ISSN 1078-8956

[8] R. F. Louie, W. J. Ferguson, C. M. Curtis, J. H. Vy and G. J. Kost [**2014**]. 'Vulnerability of point-of-care test reagents and instruments to environmental stresses: implications for health professionals and developers'. *Clinical Chemistry and Laboratory Medicine* **52** (3) 325–335

[9] C. D. Chin, V. Linder and S. K. Sia [**2012**]. 'Commercialization of microfluidic point-of-care diagnostic devices'. *Lab on a Chip* **12** (12) 2118–2134

[10] L. Mahieu, A. Marien, J. De Dooy, M. Mahieu, H. Mahieu and V. Van Hoof [**2012**]. 'Implementation of a multi-parameter point-of-care-blood test analyzer reduces central laboratory testing and need for blood transfusions in very low birth weight infants'. *Clinica Chimica Acta* **413** (1) 325–330

[11] Y. Cui, X. Duan, J. Hu and C. M. Lieber [**2000**]. 'Doping and electrical transport in silicon nanowires'. *The Journal of Physical Chemistry B* **104** (22) 5213–5216

[12] D. M. Rissin, D. R. Fournier, T. Piech, C. W. Kan, T. G. Campbell, L. Song, L. Chang, A. J. Rivnak, P. P. Patel, G. K. Provuncher et al. [**2011**]. 'Simultaneous detection of single molecules and singulated ensembles of molecules enables immunoassays with broad dynamic range'. *Analytical chemistry* **83** (6) 2279–2285

[13] R. De La Rica and M. M. Stevens [**2012**]. 'Plasmonic elisa for the ultrasensitive detection of disease biomarkers with the naked eye'. *Nature nanotechnology* **7** (12) 821–824

[14] T. Wang, M. Zhang, D. D. Dreher and Y. Zeng [**2013**]. 'Ultrasensitive microfluidic solid-phase elisa using an actuatable microwell-patterned pdms chip'. *Lab on a Chip* **13** (21) 4190–4197

[15] X. Mao, A. A. Nawaz, S.-C. S. Lin, M. I. Lapsley, Y. Zhao, J. P. McCoy, W. S. El-Deiry and T. J. Huang [**2012**]. 'An integrated, multiparametric flow cytometry chip using "microfluidic drifting" based three-dimensional hydrodynamic focusing'. *Biomicrofluidics* **6** (2) 024113

[16] C. L. Sawyers [**2008**]. 'The cancer biomarker problem'. *Nature* **452** (7187) 548–552. ISSN 0028-0836

[17] K. R. Calvo, L. A. Liotta and E. F. Petricoin [**2005**]. 'Clinical proteomics: from biomarker discovery and cell signaling profiles to individualized personal therapy'. *Bioscience reports* **25** (1-2) 107–125

[18] M. Dietel, K. Jöhrens, M. Laffert, M. Hummel, H. Bläker, B. Müller, A. Lehmann, C. Denkert, F. Heppner, A. Koch et al. [**2013**]. 'Predictive molecular pathology and its role in targeted cancer therapy: a review focussing on clinical relevance'. *Cancer gene therapy* **20** (4) 211–221

[19] A. Paschen, A. Sucker, B. Hill, I. Moll, M. Zapatka, X. D. Nguyen, G. C. Sim, I. Gutmann, J. Hassel, J. C. Becker et al. [**2009**]. 'Differential clinical significance of individual nkg2d ligands in melanoma: soluble ulbp2 as an indicator of poor prognosis superior to s100b'. *Clinical cancer research* **15** (16) 5208–5215

[20] P. J. Tighe, R. R. Ryder, I. Todd and L. C. Fairclough [**2015**]. 'Elisa in the multiplex era: Potentials and pitfalls'. *PROTEOMICS-Clinical Applications* **9** (3-4) 406–422

[21] S. Kasi, M. Liehr, P. Thiry, H. Dallaporta and M. Offenberg [**1991**]. 'Hydrocarbon reaction with hf-cleaned si (100) and effects on metal-oxide-semiconductor device quality'. *Applied physics letters* **59** (1) 108–110

[22] S. Ye, T. Ichihara and K. Uosaki [**1999**]. 'Attenuated total reflection fourier transform infrared spectroscopy study of the adsorption of organic contaminants on a hydrogen-terminated si (111) surface in air'. *Applied physics letters* **75** (11) 1562–1564

[23] H. Kahn, C. Deeb, I. Chasiotis and A. H. Heuer [**2005**]. 'Anodic oxidation during mems processing of silicon and polysilicon: Native oxides can be thicker than you think'. *Microelectromechanical Systems, Journal of* **14** (5) 914–923

[24] P. Thissen, O. Seitz and Y. J. Chabal [**2012**]. 'Wet chemical surface functionalization of oxide-free silicon'. *Progress in Surface Science* **87** (9) 272–290

[25] J. S. Judge [**1971**]. 'A study of the dissolution of sio2 in acidic fluoride solutions'. *Journal of the Electrochemical Society* **118** (11) 1772–1775

[26] G. S. Higashi, Y. J. Chabal, G. W. Trucks and K. Raghavachari [**1990**]. 'Ideal hydrogen termination of the si (111) surface'. *Applied Physics Letters* **56** (7) 656–658. ISSN 00036951

[27] P. Dumas and Y. Chabal [**1991**]. 'Electron-energy-loss characterization of the h-terminated si (111) and si (100) surfaces obtained by etching in nh_4f'. *Chemical physics letters* **181** (6) 537–543

[28] M. R. Linford and C. E. Chidsey [**1993**]. 'Alkyl monolayers covalently bonded to silicon surfaces'. *Journal of the American Chemical Society* **115** (26) 12631–12632

[29] M. P. Stewart and J. M. Buriak [**1998**]. 'Photopatterned hydrosilylation on porous silicon'. *Angewandte Chemie International Edition* **37** (23) 3257–3260. ISSN 1521-3773

[30] M. R. Linford, P. Fenter, P. M. Eisenberger and C. E. D. Chidsey [**1995**]. 'Alkyl monolayers on silicon prepared from 1-alkenes and hydrogen-terminated silicon'. *Journal of the American Chemical Society* **117** (11) 3145–3155. ISSN 0002-7863

[31] A. B. Sieval, V. Vleeming, H. Zuilhof and E. J. Sudhölter [**1999**]. 'An improved method for the preparation of organic monolayers of 1-alkenes on hydrogen-terminated silicon surfaces'. *Langmuir* **15** (23) 8288–8291

[32] R. L. Cicero, M. R. Linford and C. E. D. Chidsey [**jun 2000**]. 'Photoreactivity of unsaturated compounds with hydrogen-terminated silicon(111)'. *Langmuir* **16** (13) 5688–5695. ISSN 0743-7463, 1520-5827

[33] J. Schmeltzer, L. A. Porter, M. P. Stewart and J. M. Buriak [**2002**]. 'Hydride abstraction initiated hydrosilylation of terminal alkenes and alkynes on porous silicon'. *Langmuir* **18** (8) 2971–2974

[34] J. M. Buriak [**2013**]. 'Illuminating silicon surface hydrosilylation: An unexpected plurality of mechanisms'. *Chemistry of Materials*

[35] R. L. Cicero, C. E. Chidsey, G. P. Lopinski, D. D. Wayner and R. A. Wolkow [**2002**]. 'Olefin additions on h-si (111): Evidence for a surface chain reaction initiated at isolated dangling bonds'. *Langmuir* **18** (2) 305–307

[36] M. P. Stewart and J. M. Buriak [**2001**]. 'Exciton-mediated hydrosilylation on photoluminescent nanocrystalline silicon'. *Journal of the American Chemical Society* **123** (32) 7821–7830

[37] J. M. Buriak, M. P. Stewart, T. W. Geders, M. J. Allen, H. C. Choi, J. Smith, D. Raftery and L. T. Canham [**1999**]. 'Lewis acid mediated hydrosilylation on porous silicon surfaces'. *Journal of the American Chemical Society* **121** (49) 11491–11502

[38] L. A. Huck and J. M. Buriak. 'Supplementary information: Toward a mechanistic understanding of exciton-mediated hydrosilylation on nanocrystalline silicon'. *Journal of the American Chemical Society*

[39] E. J. Faber, L. C. de Smet, W. Olthuis, H. Zuilhof, E. J. Sudhölter, P. Bergveld and A. van den Berg [**2005**]. 'Si-c linked organic monolayers on crystalline silicon surfaces as alternative gate insulators'. *ChemPhysChem* **6** (10) 2153–2166

[40] L. C. de Smet, A. V. Pukin, Q.-Y. Sun, B. J. Eves, G. P. Lopinski, G. M. Visser, H. Zuilhof and E. J. Sudhölter [**2005**]. 'Visible-light attachment of sic linked functionalized organic monolayers on silicon surfaces'. *Applied Surface Science* **252** (1) 24–30

[41] Q.-Y. Sun, L. C. P. M. de Smet, B. van Lagen, A. Wright, H. Zuilhof and E. J. R. Sudhölter [**2004**]. 'Covalently attached monolayers on hydrogen-terminated si(100): Extremely mild attachment by visible light'. *Angewandte Chemie International Edition* **43** (11) 1352–1355. ISSN 1521-3773

[42] W. Cai, Z. Lin, T. Strother, L. M. Smith and R. J. Hamers [**2002**]. 'Chemical modification and patterning of iodine-terminated silicon surfaces using visible light'. *The Journal of Physical Chemistry B* **106** (10) 2656–2664

[43] X. Wang, R. E. Ruther, J. A. Streifer and R. J. Hamers [**2010**]. 'Supplementary information: Uv-induced grafting of alkenes to silicon surfaces: photoemission versus excitons'. *Journal of the American Chemical Society*

[44] M. Horn [**2011**]. *Structure-Reactivity-Relationships of Substituted Tritylium Ions: A Kinetic Investigation.* Südwestdeutscher Verlag für Hochschulschriften

[45] M. E. Jung, R. Lagoutte and U. Jahn [**2015**]. 'Triphenylcarbenium tetrafluoroborate'. *e-EROS Encyclopedia of Reagents for Organic Synthesis*

[46] A. A. Zavitsas and C. Chatgilialoglu [**1995**]. 'Energies of activation. the paradigm of hydrogen abstractions by radicals'. *Journal of the American Chemical Society* **117** (43) 10645–10654

[47] A. Ng, S. Ciampi, M. James, J. B. Harper and J. J. Gooding [**2009**]. 'Comparing the reactivity of alkynes and alkenes on silicon (100) surfaces†'. *Langmuir* **25** (24) 13934–13941. ISSN 0743-7463

[48] L. Scheres, M. Giesbers and H. Zuilhof [**2010**]. 'Organic monolayers onto oxide-free silicon with improved surface coverage: Alkynes versus alkenes'. *Langmuir* **26** (7) 4790–4795. ISSN 0743-7463

[49] L. Scheres, B. Rijksen, M. Giesbers and H. Zuilhof [**2011**]. 'Molecular modeling of alkyl and alkenyl monolayers on hydrogen-terminated si (111)'. *Langmuir* **27** (3) 972–980

[50] L. Scheres, M. Giesbers and H. Zuilhof [**2010**]. 'Self-assembly of organic monolayers onto hydrogen-terminated silicon: 1-alkynes are better than 1-alkenes'. *Langmuir* **26** (13) 10924–10929

[51] J. M. Buriak and M. J. Allen [**1998**]. 'Lewis acid mediated functionalization of porous silicon with substituted alkenes and alkynes'. *Journal of the American Chemical Society* **120** (6) 1339–1340

[52] M. Seah and W. Dench [**1979**]. 'Quantitative electron spectroscopy of surfaces: a standard data base for electron inelastic mean free paths in solids'. *Surface and interface analysis* **1** (1) 2–11

[53] S. Tanuma, C. J. Powell and D. R. Penn [**1988**]. 'Calculations of electron inelastic mean free paths for 31 materials'. *Surface and Interface Analysis* **11** (11) 577–589

[54] J. F. Moulder, W. F. Stickle, P. E. Sobol and K. D. Bomben [**1992**]. *Handbook of x-ray photoelectron spectroscopy: a reference book of standard spectra for identification and interpretation of*. Perkin-Elmer: Boca Raton, FL

[55] A. Zulfiqar [**2015**]. 'Novel diagnostic method for personalized treatment of cancer'

[56] S. Hofmann [**2012**]. *Auger-and X-ray Photoelectron Spectroscopy in Materials Science: A User-oriented Guide*, volume 49. Springer

[57] L. J. Webb and N. S. Lewis [**2003**]. 'Comparison of the electrical properties and chemical stability of crystalline silicon (111) surfaces alkylated using grignard reagents or olefins with lewis acid catalysts'. *The Journal of Physical Chemistry B* **107** (23) 5404–5412

[58] J. A. Haber and N. S. Lewis [**2002**]. 'Infrared and x-ray photoelectron spectroscopic studies of the reactions of hydrogen-terminated crystalline si (111) and si (100) surfaces with br2, i2, and ferrocenium in alcohol solvents'. *The Journal of Physical Chemistry B* **106** (14) 3639–3656

[59] J. H. Scofield [**1976**]. 'Hartree-slater subshell photoionization cross-sections at 1254 and 1487 ev'. *Journal of Electron Spectroscopy and Related Phenomena* **8** (2) 129–137

[60] K. E. Pomykal, A. M. Fajardo and N. S. Lewis [**1995**]. 'Stability of n-si/ch3oh contacts as a function of the reorganization energy of the electron donor'. *The Journal of Physical Chemistry* **99** (20) 8302–8310

[61] A. Lambacher and P. Fromherz [**1996**]. 'Fluorescence interference-contrast microscopy on oxidized silicon using a monomolecular dye layer'. *Applied Physics A* **63** (3) 207–216

[62] C. M. Ajo-Franklin, C. Yoshina-Ishii and S. G. Boxer [**2005**]. 'Probing the structure of supported membranes and tethered oligonucleotides by fluorescence interference contrast microscopy'. *Langmuir* **21** (11) 4976–4983

[63] O. H. Elibol, B. Reddy Jr, P. R. Nair, B. Dorvel, F. Butler, Z. S. Ahsan, D. E. Bergstrom, M. A. Alam and R. Bashir [**2009**]. 'Localized heating on silicon field effect transistors: Device fabrication and temperature measurements in fluid'. *Lab on a Chip* **9** (19) 2789–2795

[64] S. Watanabe [**1995**]. 'In-situ infrared characterization of a chemically oxidized silicon surface dissolving in aqueous hydrofluoric acid'. *Surface science* **341** (3) 304–310

[65] A. Langner, A. Panarello, S. Rivillon, O. Vassylyev, J. G. Khinast and Y. J. Chabal [**2005**]. 'Controlled silicon surface functionalization by alkene hydrosilylation'. *Journal of the American Chemical Society* **127** (37) 12798–12799

[66] A. Saghatelian, J. Buriak, V. S. Lin and M. Reza Ghadiri [**2001**]. 'Transition metal mediated surface modification of porous silicon'. *Tetrahedron* **57** (24) 5131–5136

[67] E. Foca, J. Carstensen and H. Föll [**2007**]. 'Modelling electrochemical current and potential oscillations at the si electrode'. *Journal of Electroanalytical Chemistry* **603** (2) 175–202

[68] L. Torcheux, A. Mayeux and M. Chemla [**1995**]. 'Electrochemical coupling effects on the corrosion of silicon samples in hf solutions'. *Journal of The Electrochemical Society* **142** (6) 2037–2046

[69] P. Allongue, V. Kieling and H. Gerischer [**1995**]. 'Etching mechanism and atomic structure of h-si (111) surfaces prepared in nh_4f'. *Electrochimica acta* **40** (10) 1353–1360

[70] J. C. Flake, M. M. Rieger, G. M. Schmid and P. A. Kohl [**1999**]. 'Electrochemical etching of silicon in nonaqueous electrolytes containing hydrogen fluoride or fluoroborate'. *Journal of The Electrochemical Society* **146** (5) 1960–1965

[71] Z. Huang, N. Geyer, L. Liu, M. Li and P. Zhong [**2010**]. 'Metal-assisted electrochemical etching of silicon'. *Nanotechnology* **21** (46) 465301

[72] U. Gelius, P. Heden, J. Hedman, B. Lindberg, R. Manne, R. Nordberg, C. Nordling and K. Siegbahn [**1970**]. 'Molecular spectroscopy by means of esca iii. carbon compounds'. *Physica Scripta* **2** (1-2) 70

[73] J. Wang, Y.-L. Liang and J. Qu [**2009**]. 'Boiling water-catalyzed neutral and selective n-boc deprotection'. *Chemical communications* (34) 5144–5146

[74] T. Strother, R. J. Hamers and L. M. Smith [**sep 2000**]. 'Covalent attachment of oligodeoxyribonucleotides to amine-modified si (001) surfaces'. *Nucleic Acids Research* **28** (18) 3535–3541. ISSN 0305-1048, 1362-4962. PMID: 10982873

[75] Y. L. Bunimovich, Y. S. Shin, W.-S. Yeo, M. Amori, G. Kwong and J. R. Heath [**2006**]. 'Quantitative real-time measurements of dna hybridization with alkylated nonoxidized silicon nanowires in electrolyte solution'. *Journal of the American Chemical Society* **128** (50) 16323–16331

[76] E. Gusev, H. Lu, T. Gustafsson and E. Garfunkel [**1995**]. 'Growth mechanism of thin silicon oxide films on si (100) studied by medium-energy ion scattering'. *Physical Review B* **52** (3) 1759

[77] W. Chen, H. Yao, C. H. Tzang, J. Zhu, M. Yang and S.-T. Lee [**2006**]. 'Silicon nanowires for high-sensitivity glucose detection'. *Applied physics letters* **88** (21) 213104

[78] M. Curreli, R. Zhang, F. Ishikawa, H.-K. Chang, R. Cote, C. Zhou and M. Thompson [**2008**]. 'Real-time, label-free detection of biological entities using nanowire-based fets'. *IEEE Transactions on Nanotechnology* **7** (6) 651–667. ISSN 1536-125X, 1941-0085

[79] S. Regonda, R. Tian, J. Gao, S. Greene, J. Ding and W. Hu [**2013**]. 'Silicon multi-nanochannel fets to improve device uniformity/stability and femtomolar detection of insulin in serum'. *Biosensors and Bioelectronics* **45** 245–251

[80] N. Elfström, A. E. Karlström and J. Linnros [**2008**]. 'Silicon nanoribbons for electrical detection of biomolecules'. *Nano letters* **8** (3) 945–949

[81] J. H. Chua, R.-E. Chee, A. Agarwal, S. M. Wong and G.-J. Zhang [**2009**]. 'Label-free electrical detection of cardiac biomarker with complementary metal-oxide semiconductor-compatible silicon nanowire sensor arrays'. *Analytical chemistry* **81** (15) 6266–6271

[82] T. Kong, R. Su, B. Zhang, Q. Zhang and G. Cheng [**2012**]. 'Cmos-compatible, label-free silicon-nanowire biosensors to detect cardiac troponin i for acute myocardial infarction diagnosis'. *Biosensors and Bioelectronics* **34** (1) 267–272

[83] A. Kim, C. S. Ah, H. Y. Yu, J.-H. Yang, I.-B. Baek, C.-G. Ahn, C. W. Park, M. S. Jun and S. Lee [**2007**]. 'Ultrasensitive, label-free, and real-time immunodetection using silicon field-effect transistors'. *Applied Physics Letters* **91** (10) 103901–103901

[84] C.-H. Lin, C.-Y. Hsiao, C.-H. Hung, Y.-R. Lo, C.-C. Lee, C.-J. Su, H.-C. Lin, F.-H. Ko, T.-Y. Huang and Y.-S. Yang [**2008**]. 'Ultrasensitive detection of dopamine using a polysilicon nanowire field-effect transistor'. *Chem. Commun.* (44) 5749–5751

[85] C.-H. Lin, C.-H. Hung, C.-Y. Hsiao, H.-C. Lin, F.-H. Ko and Y.-S. Yang [**2009**]. 'Poly-silicon nanowire field-effect transistor for ultrasensitive and label-free detection of pathogenic avian influenza dna'. *Biosensors and Bioelectronics* **24** (10) 3019–3024. ISSN 09565663

[86] L. T.-H. Kao, L. Shankar, T. G. Kang, G. Zhang, G. K. I. Tay, S. R. M. Rafei and C. W. H. Lee [**2011**]. 'Multiplexed detection and differentiation of the dna strains for influenza a (h1n1 2009) using a silicon-based microfluidic system'. *Biosensors and Bioelectronics* **26** (5) 2006–2011

[87] G.-J. Zhang, J. H. Chua, R.-E. Chee, A. Agarwal and S. M. Wong [**2009**]. 'Label-free direct detection of mirnas with silicon nanowire biosensors'. *Biosensors and Bioelectronics* **24** (8) 2504–2508

[88] H. H. Liu, T. H. Lin and J.-T. Sheu [**2013**]. 'Self-assembled monolayer-based selective modification on polysilicon nanobelt devices'. *ACS applied materials & interfaces* **5** (20) 10048–10053

[89] W. R. McKinnon, D. Landheer and G. Aers [**2008**]. 'Sensitivity of field-effect biosensors to charge, ph, and ion concentration in a membrane model'. *Journal of Applied Physics* **104** (12) 124701. ISSN 00218979

[90] X.-G. Zhang and S. T. Pantelides [**2009**]. 'Screening in nanowires and nanocontacts: Field emission, adhesion force, and contact resistance'. *Nano Letters* **9** (12) 4306–4310. ISSN 1530-6984, 1530-6992

[91] M. H. Sørensen, N. A. Mortensen and M. Brandbyge [**2007**]. 'Screening model for nanowire surface-charge sensors in liquid'. *Applied Physics Letters* **91** (10) 102105–102105

[92] P. R. Nair and M. A. Alam [**2008**]. 'Screening-limited response of nanobiosensors'. *Nano Letters* **8** (5) 1281–1285. ISSN 1530-6984, 1530-6992

[93] P. G. Fernandes, H. J. Stiegler, M. Zhao, K. D. Cantley, B. Obradovic, R. A. Chapman, H.-C. Wen, G. Mahmud and E. M. Vogel [**2012**]. 'Spice macromodel of silicon-on-insulator-field-effect-transistor-based biological sensors'. *Sensors and Actuators B: Chemical* **161** (1) 163–170

[94] D. Aswal, S. Lenfant, D. Guerin, J. Yakhmi and D. Vuillaume [**2006**]. 'Self assembled monolayers on silicon for molecular electronics'. *Analytica chimica acta* **568** (1) 84–108

[95] T. Strother, T. Knickerbocker, J. N. Russell, J. E. Butler, L. M. Smith and R. J. Hamers [**2002**]. 'Photochemical functionalization of diamond films'. *Langmuir* **18** (4) 968–971

[96] S. Tanuma, C. Powell and D. Penn [**2011**]. 'Calculations of electron inelastic mean free paths. ix. data for 41 elemental solids over the 50 ev to 30 kev range'. *Surface and Interface Analysis* **43** (3) 689–713

[97] X. Wallart, C. Henry de Villeneuve and P. Allongue [**2005**]. 'Truly quantitative xps characterization of organic monolayers on silicon: study of alkyl and alkoxy monolayers on h-si (111)'. *Journal of the American Chemical Society* **127** (21) 7871–7878

[98] S. Chernyy, B. E. Jensen, K. Shimizu, M. Ceccato, S. U. Pedersen, A. N. Zelikin, K. Daasbjerg and J. Iruthayaraj [**2013**]. 'Surface grafted glycopolymer brushes to enhance selective adhesion of hepg2 cells'. *Journal of colloid and interface science* **404** 207–214

[99] F. Cattaruzza, A. Cricenti, A. Flamini, M. Girasole, G. Longo, A. Mezzi and T. Prosperi [**2004**]. 'Carboxylic acid terminated monolayer formation on crystalline silicon and silicon nitride surfaces. a surface coverage determination with a fluorescent probe in solution'. *Journal of Materials Chemistry* **14** (9) 1461–1468

[100] M. A. Filler and S. F. Bent [**2003**]. 'The surface as molecular reagent: organic chemistry at the semiconductor interface'. *Progress in surface science* **73** (1) 1–56

[101] G. Lopinski, D. Wayner and R. Wolkow [**2000**]. 'Self-directed growth of molecular nanostructures on silicon'. *Nature* **406** (6791) 48–51

[102] R. L. Rich, M. J. Cannon, J. Jenkins, P. Pandian, S. Sundaram, R. Magyar, J. Brockman, J. Lambert and D. G. Myszka [**2008**]. 'Extracting kinetic rate constants from surface plasmon resonance array systems'. *Analytical biochemistry* **373** (1) 112–120

[103] R. L. Rich and D. G. Myszka [**2006**]. 'Survey of the year 2005 commercial optical biosensor literature'. *Journal of Molecular Recognition* **19** (6) 478–534

[104] K. B. Sharpless, H. C. Kolb and M. G. Finn [**2001**]. 'Click chemistry: Diverse chemical function from a few good reactions'. *Angewandte Chemie International Edition* **40** 2004 – 2021

[105] S. I. Presolski, V. P. Hong and M. Finn [**2011**]. 'Copper-catalyzed azide-alkyne click chemistry for bioconjugation'. In A. P. Arkin, L. Mahal, F. Romesberg, K. Shah, C. Shamu and C. Thomas, editors, 'Current Protocols in Chemical Biology', John Wiley & Sons, Inc., Hoboken, NJ, USA. ISBN 9780470559277

[106] R. K. Manova, S. P. Pujari, C. A. G. M. Weijers, H. Zuilhof and T. A. van Beek [**jun 2012**]. 'Copper-free click biofunctionalization of silicon nitride surfaces via strain-promoted alkyne–azide cycloaddition reactions'. *Langmuir* **28** (23) 8651–8663. ISSN 0743-7463, 1520-5827

[107] Y. Li, S. Calder, O. Yaffe, D. Cahen, H. Haick, L. Kronik and H. Zuilhof [**2012**]. 'Hybrids of organic molecules and flat, oxide-free silicon: High-density monolayers, electronic properties, and functionalization'. *Langmuir* **28** (26) 9920–9929. ISSN 0743-7463, 1520-5827

[108] Z. Grabarek and J. Gergely [**1990**]. 'Zero-length crosslinking procedure with the use of active esters'. *Analytical Biochemistry* **185** (1) 131–135. ISSN 0003-2697

[109] P. Bergveld [**2003**]. 'Thirty years of isfetology: What happened in the past 30 years and what may happen in the next 30 years'. *Sensors and Actuators B: Chemical* **88** (1) 1–20

[110] L. Bousse, N. De Rooij and P. Bergveld [**1983**]. 'Operation of chemically sensitive field-effect sensors as a function of the insulator-electrolyte interface'. *Electron Devices, IEEE Transactions on* **30** (10) 1263–1270

[111] S. V. Dzyadevych, A. P. Soldatkin, V. Anna, C. Martelet and N. Jaffrezic-Renault [**2006**]. 'Enzyme biosensors based on ion-selective field-effect transistors'. *Analytica chimica acta* **568** (1) 248–258

[112] D. Landheer, G. Aers, W. R. McKinnon, M. J. Deen and J. C. Ranuarez [**2005**]. 'Model for the field effect from layers of biological macromolecules on the gates of metal-oxide-semiconductor transistors'. *Journal of Applied Physics* **98** (4) 044701. ISSN 00218979

[113] Y. Cui, Q. Wei, H. Park and C. M. Lieber [**2001**]. 'Nanowire nanosensors for highly sensitive and selective detection of biological and chemical species'. *Science* **293** (5533) 1289–1292

[114] L. De Vico, M. H. Sørensen, L. Iversen, D. M. Rogers, B. S. Sørensen, M. Brandbyge, J. Nygård, K. L. Martinez and J. H. Jensen [**2011**]. 'Quantifying signal changes in nanowire based biosensors'. *Nanoscale* **3** (2) 706–717

[115] H. M. Berman, J. Westbrook, Z. Feng, G. Gilliland, T. Bhat, H. Weissig, I. N. Shindyalov and P. E. Bourne [**2000**]. 'The protein data bank'. *Nucleic acids research* **28** (1) 235–242

[116] H. Li, A. D. Robertson and J. H. Jensen [**2005**]. 'Very fast empirical prediction and rationalization of protein pka values'. *Proteins: Structure, Function, and Bioinformatics* **61** (4) 704–721

[117] M. Jørgensen [**2011**]. *Silicon Nanowire Biosensor System.* Master's thesis, Technical University of Denmark

[118] P. Livi, A. Shadmani, M. Wipf, R. L. Stoop, J. Rothe, Y. Chen, M. Calame, C. Schönenberger and A. Hierlemann [**2014**]. 'Sensor system including silicon nanowire ion sensitive fet arrays and cmos readout'. *Sensors and Actuators B: Chemical* **204** 568–577

[119] M. Champsaur and L. L. Lanier [**2010**]. 'Effect of nkg2d ligand expression on host immune responses'. *Immunological reviews* **235** (1) 267–285

[120] F. Uhlenbrock, E. van Andel, L. Andresen and S. Skov [**2015**]. 'A conserved ww domain-like motif regulates invariant chain-dependent cell-surface transport of the nkg2d ligand ulbp2'. *Molecular immunology* **66** (2) 418–427

[121] F. Uhlenbrock, M. Hagemann-Jensen, S. Kehlet, L. Andresen, S. Pastorekova and S. Skov [**2014**]. 'The nkg2d ligand ulbp2 is specifically regulated through an invariant chain–dependent endosomal pathway'. *The Journal of Immunology* **193** (4) 1654–1665

[122] D. W. Wolan, L. Teyton, M. G. Rudolph, B. Villmow, S. Bauer, D. H. Busch and I. A. Wilson [**2001**]. 'Crystal structure of the murine nk cell–activating receptor nkg2d at 1.95 å'. *Nature immunology* **2** (3) 248–254

[123] A. Brooks [**2001**]. 'Conformational plasticity revealed by the cocrystal structure of nkg2d and its class i mhc-like ligand ulbp3'

[124] H. Becker [**2010**]. 'One size fits all?' *Lab on a Chip* **10** (15) 1894. ISSN 1473-0197, 1473-0189

[125] H. van Heeren [**2012**]. 'Standards for connecting microfluidic devices?' *Lab on a Chip* **12** (6) 1022. ISSN 1473-0197, 1473-0189

[126] C. K. Fredrickson and Z. H. Fan [**2004**]. 'Macro-to-micro interfaces for microfluidic devices'. *Lab on a Chip* **4** (6) 526–533

[127] Y. Temiz, R. D. Lovchik, G. V. Kaigala and E. Delamarche [**2015**]. 'Lab-on-a-chip devices: How to close and plug the lab?' *Microelectronic Engineering* **132** 156–175

[128] [**2015**]. 'Dolomite'. http://www.dolomite-microfluidics.com/en/products/multiflux

[129] [**2014**]. 'Micrux technologies'. http://www.micruxfluidic.com

[130] [**2014**]. 'Micronit microfluidics'. http://www.micronit.com

[131] D. Sabourin, D. Snakenborg and M. Dufva [**2009**]. 'Interconnection blocks with minimal dead volumes permitting planar interconnection to thin microfluidic devices'. *Microfluidics and Nanofluidics* **9** (1) 87–93. ISSN 1613-4982, 1613-4990

[132] E. Wilhelm, C. Neumann, T. Duttenhofer, L. Pires and B. E. Rapp [**2013**]. 'Connecting microfluidic chips using a chemically inert, reversible, multichannel chip-to-world-interface'. *Lab on a Chip* ISSN 1473-0197, 1473-0189

[133] M. T. Koesdjojo, J. Nammoonnoy, Y. Wu, R. T. Frederick and V. T. Remcho [**2012**]. 'Cost-efficient fabrication techniques for microchips and interconnects enabled by polycaprolactone'. *Journal of Micromechanics and Microengineering* **22** (11) 115030

[134] B.-K. Lee and T. H. Kwon [**2010**]. 'A novel monolithic fabrication method for a plastic microfluidic chip with liquid interconnecting ports'. *Journal of Micromechanics and Microengineering* **20** (10) 105004

[135] A. M. Christensen, D. A. Chang-Yen and B. K. Gale [**2005**]. 'Characterization of interconnects used in pdms microfluidic systems'. *Journal of Micromechanics and Microengineering* **15** (5) 928

[136] D. Sabourin, M. Dufva, T. Jensen, J. Kutter and D. Snakenborg [**2010**]. 'One-step fabrication of microfluidic chips with in-plane, adhesive-free interconnections'. *Journal of Micromechanics and Microengineering* **20** (3) 037001. ISSN 0960-1317, 1361-6439

[137] J. N. Patel, B. L. Gray, B. Kaminska, N.-C. Wu and B. D. Gates [**2013**]. 'Su-8-and pdms-based hybrid fabrication technology for combination of permanently bonded flexible and rigid features on a single device'. *Journal of Micromechanics and Microengineering* **23** (6) 065029

[138] A. Chen and T. Pan [**2011**]. 'Fit-to-flow (f2f) interconnects: Universal reversible adhesive-free microfluidic adaptors for lab-on-a-chip systems'. *Lab on a Chip* **11** (4) 727. ISSN 1473-0197, 1473-0189

[139] G. Perozziello, F. Bundgaard and O. Geschke [**2008**]. 'Fluidic interconnections for microfluidic systems: A new integrated fluidic interconnection allowing plug'n'play functionality'. *Sensors and Actuators B: Chemical* **130** (2) 947–953. ISSN 0925-4005

[140] D. Snakenborg, G. Perozziello, O. Geschke and J. P. Kutter [**2007**]. 'A fast and reliable way to establish fluidic connections to planar microchips'. *Journal of Micromechanics and Microengineering* **17** (1) 98–103. ISSN 0960-1317, 1361-6439

[141] C.-H. Chiou and G.-B. Lee [**2004**]. 'Minimal dead-volume connectors for microfluidics using pdms casting techniques'. *Journal of Micromechanics and Microengineering* **14** (11) 1484

[142] R. Lo and E. Meng [**2011**]. 'Reusable, adhesiveless and arrayed in-plane microfluidic interconnects'. *Journal of Micromechanics and Microengineering* **21** (5) 054021

[143] P. Skafte-Pedersen, C. G. Sip, A. Folch and M. Dufva [**2013**]. 'Modular microfluidic systems using reversibly attached pdms fluid control modules'. *Journal of Micromechanics and Microengineering* **23** (5) 055011

[144] B. L. Gray and S. Jaffer [**2005**]. *Mechanical and microfluidic interconnects fabricated in SU-8 photopolymer*. Amer Soc Mechanical Engineers, New York. ISBN 0-7918-4185-5. WOS:000243025800082

[145] S. Jaffer and B. L. Gray [**2007**]. 'Mechanically assembled polymer interconnects with dead volume analysis for microfluidic systems'. In I. Paputsky and W. Wang, editors, 'Microfluidics, Biomems, and Medical Microsystems V', volume 6465. Spie-Int Soc Optical Engineering, Bellingham. ISBN 978-0-8194-6578-8. WOS:000245834700024

[146] O. Paydar, C. Paredes, Y. Hwang, J. Paz, N. Shah and R. Candler [**2014**]. 'Characterization of 3d-printed microfluidic chip interconnects with integrated o-rings'. *Sensors and Actuators A: Physical* **205** 199–203

[147] K. G. Lee, K. J. Park, S. Seok, S. Shin, J. Y. Park, Y. S. Heo, S. J. Lee, T. J. Lee et al. [**2014**]. '3d printed modules for integrated microfluidic devices'. *RSC Advances* **4** (62) 32876–32880

[148] P. S. Nunes, P. D. Ohlsson, O. Ordeig and J. P. Kutter [**2010**]. 'Cyclic olefin polymers: emerging materials for lab-on-a-chip applications'. *Microfluidics and nanofluidics* **9** (2-3) 145–161

[149] M. Matteucci, T. L. Christiansen, S. Tanzi, P. F. Østergaard, S. T. Larsen and R. Taboryski [**2013**]. 'Fabrication and characterization of injection molded multi level nano and microfluidic systems'. *Microelectronic Engineering* **111** 294–298

[150] S. Tanzi, M. Matteucci, T. L. Christiansen, S. Friis, M. T. Christensen, J. Garnaes, S. Wilson, J. Kutchinsky and R. Taboryski [**2013**]. 'Ion channel recordings on an injection-molded polymer chip'. *Lab on a Chip* **13** (24) 4784–4793

[151] M. Matteucci, S. T. Larsen, A. Garau, S. Tanzi and R. Taboryski [**2013**]. 'Polymer multilevel lab-on-chip systems for electrochemical sensing'. *Journal of Vacuum Science & Technology B* **31** (6) 06F904

[152] K. Kistrup, C. E. Poulsen, P. F. Østergaard, K. B. Haugshøj, R. Taboryski, A. Wolff and M. F. Hansen [**2014**]. 'Fabrication and modelling of injection moulded all-polymer capillary microvalves for passive microfluidic control'. *Journal of Micromechanics and Microengineering* **24** (12) 125007

[153] A. R. Sørensen [**2014**]. 'Development of a flow system for culturing of brain slice cultures'

[154] [**2015**]. 'Fluidan rheostream'. www.fluidan.com

[155] J. Mu, M. Wang and X. Yin [**2010**]. 'A simple subatmospheric pressure device to drive reagents through microchannels for solution-phase synthesis in a parallel fashion'. *Sensors and Actuators B: Chemical* **146** (1) 410–413. ISSN 09254005

[156] M. Brivio, W. Verboom and D. N. Reinhoudt [**2006**]. 'Miniaturized continuous flow reaction vessels: influence on chemical reactions'. *Lab on a Chip* **6** (3) 329. ISSN 1473-0197, 1473-0189

[157] D. R. Gossett, W. M. Weaver, A. J. Mach, S. C. Hur, H. T. K. Tse, W. Lee, H. Amini and D. Di Carlo [**2010**]. 'Label-free cell separation and sorting in microfluidic systems'. *Analytical and Bioanalytical Chemistry* **397** (8) 3249–3267. ISSN 1618-2642, 1618-2650

[158] A. J. Mach and D. Di Carlo [**2010**]. 'Continuous scalable blood filtration device using inertial microfluidics'. *Biotechnology and Bioengineering* **107** (2) 302–311. ISSN 00063592

[159] E. Popescu [**2013**]. 'Design of a dilution system for automatic calibration of biosensors'

A | Additional Data

A.1 C1s spectra of adventitious carbon (contamination)

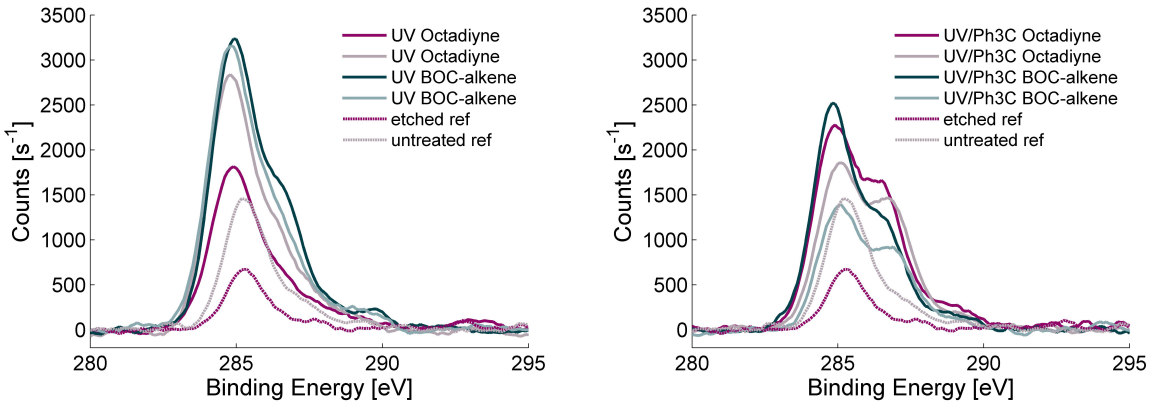

(a) (b)

Figure A.1 XPS high resolution C1s spectra for SiO2 surfaces functionalized with octadiyne and Boc-alkene, comparison with the untreated (Prianha cleaned) surface and a freshly etched surface. The etched surface presents the typical contamination spectrum that is used to determine with shape this spectrum yields. The data is shows for the two cases of illumination with UV light for 3h without (a) and with (b) the addition of triphenylcarbenium.

A.2 Additional data: Surfaces functionalized with 10-N-Boc-amino-dec-1-ene

A.2.1 Contact angle measurements on surface functionalized under different illumination conditions

A.2.2 Time development of SAM formation in UV light with Ph_3C-BF_4

Due to the reduced oxide formation and comparatively high yield of the functionalization with alkene in Ph3C/EtOH in a 90%:10% ratio, further experiments were performed to investigate the time development of SAM formation. The irradiation time with UV light was varied between

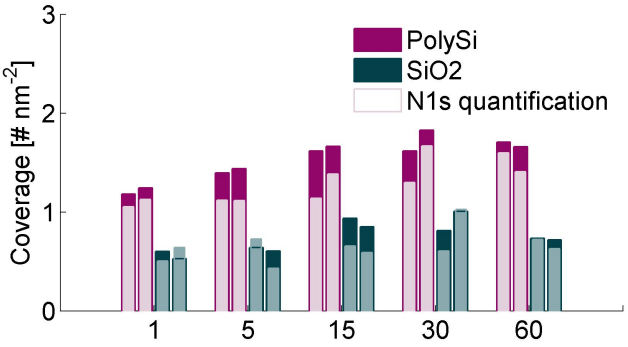

(a) SAM surface coverage

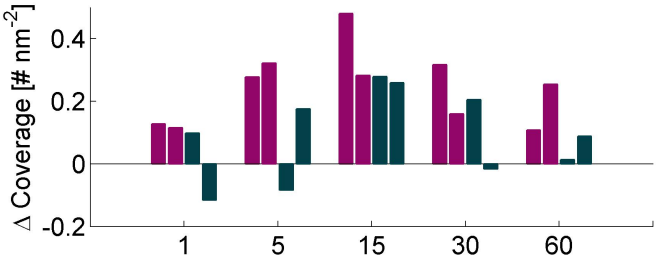

(b) Difference between coverages quantified by C1s and N1s spectral data

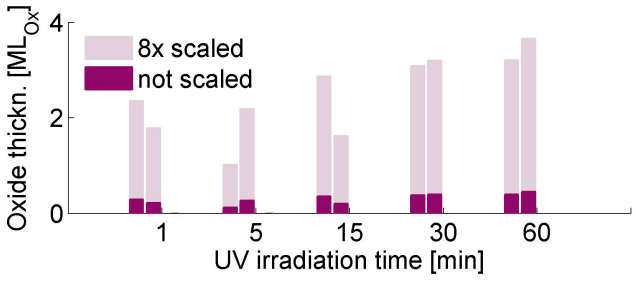

(c) Oxide thickness

Figure A.2 Time development of SAM formation by hydride abstraction using $Ph_3C\text{-}BF_4$ in UV light.

Illumination	254 nm	white light	dark (25°C)	dark (38°C)
1h *t*Boc	63	63	69	69
1h *t*Boc	62	65	76	72
2h *t*Boc	72	72	74	66
2h *t*Boc (-NH_2)	64	63	65	54
2h *t*Boc	72	75	68	66
2h *t*Boc (-NH_2)	62	68	61	61
control (SiO_2)	24	21	30	30

Table A.1 Water contact angle measurements on surfaces functionalized with Boc-alkene, for 1h and 2h illumination/incubation times before and after removal of the tBoc group by boiling in water.

1 minute and 1 h to evaluate the progression of the hydrosilylation reaction. The results are shown in Figure A.2 in analogy to the previously presented data. It should be noted however, that due to the overall lower yield and these shorter incubation times, that signal-to-noise ratios are lower and thus the variation in the data is expected to be higher, especially in case of the N1s quantification; this is visible in the difference plot A.2(b) where especially the SiO2 samples may have to be disregarded. The SAM coverage is increasing over the considered time range and appears to level off starting already at an irradiation time of 15 minutes. Even after only 1 minute a measurable amount of Boc-alkene is present on the surfaces. As for the coverage differences between quantification methods, there seems to be an increase at intermediate irradiation times reaching values comparable to those obtained after 3h. The oxidation progresses slowly over time as shown in the scaled data in Figure A.2(c). A projection of the oxidation curve (not shown) does not meet with the previously observed values for 3h irradiation, which are lower than even the sample irradiated for 1 minute only, suggesting insufficient etching during this experiment.

B | Data analysis

B.1 Theoretical derivation of quantification formulas for SAM surface composition using XPS data

In the following, the different formulas that are used for the quantitative analysis of XPS data will be derived.

B.1.1 Surface-overlayer model to determine carbon film thickness

Starting with the silicon substrate of number density N_{Si} we first want to determine the intensity of outgoing Si2p electrons. Inside the silicon substrate, without any overlayer, the intensity of all Si2p electrons ejected from silicon atoms will be as follows:

$$\begin{aligned} I^0_{Si2p} &\propto N_{Si} SF_{Si2p} \int_0^\infty dz \exp\left(-\frac{z}{\lambda_{Si2pSi}\cos\theta}\right) \\ &= N_{Si} SF_{Si2p} \lambda_{Si2pSi} \cos\theta \end{aligned} \tag{B.1}$$

The proportionality indicates that factors such as incident beam intensity, detector efficiency and other linear parameters of the instrumental setup are excluded. We will in the following only regard ratios of different electron counts or intensities for which these are equal and therefore cancel out. The sensitivity factor here denoted SF is the scattering cross section of the sub-shell ionization process and includes all effects that contribute to the probability of electron emission for a particular element and energy level at the incident x-ray energy. The values that are later used in the final formula are taken from the Scofield standard library supplied with the Avantage analysis software which is based on the original values calculated by Scofield.[59] $\lambda_{Si2pSi}\cos\theta$ is the total electron escape depth, where λ_{Si2pSi} is the inelastic mean free path (IMFP) of Si2p electrons in silicon, for which the calculated values after Tanuma, Powell and Penn[53] were used. The angle θ is the collection angle, the angle between surface normal and detector. For our system this value is 0°.

Under the approximation of a uniform carbon film of thickness $d_C$covering the silicon substrate, the intensity of Si2p electron after passing the carbon layer will experience and additional attenuation:

$$\begin{aligned} I_{Si2p} &\propto I_{Si2p_Si} \exp\left(-\frac{d_C}{\lambda_{Si2pC}\cos\theta}\right) \\ &= N_{Si} SF_{Si2p} \lambda_{Si2pSi} \cos\theta \exp\left(-\frac{d_C}{\lambda_{Si2pC}\cos\theta}\right) \end{aligned} \tag{B.2}$$

The same approach for C1s electrons originating form inside the carbon layer, leads to the following expression for the intensity of collected C1s electrons:

$$\begin{aligned} I_{C1s} &\propto N_C SF_{C1s} \int_0^{d_C} dz \exp\left(-\frac{z}{\lambda_{CC}\cos\theta}\right) \\ &= N_C SF_{C1s} \lambda_{CC} \cos\theta \left[1 - \exp\left(-\frac{d_C}{\lambda_{CC}\cos\theta}\right)\right] \end{aligned} \tag{B.3}$$

The values that we are ultimately interested in are the number density of the carbon layer N_C and the carbon layer thickness d_C since together, those provide us with the amount of material and thereby the surface coverage of the self-assembled monolayers that we are investigating. The XPS measurement provides the electron counts or peak intensities of the Si2p and C1s electrons as experimental input data. To resolve for both the variables and obtain an expression for their product $N_C d_C$ we need to use a second relation, which is given by comparison with a clean reference sample without carbon overlayer I^0_{Si2p}, which can be used according to B.1.

$$\begin{aligned} \Gamma \equiv \frac{I_{Si2p}}{I^0_{Si2p}} &= \frac{N_{Si} SF_{Si2p} \lambda_{Si2pSi} \cos\theta \exp\left(-\frac{d_C}{\lambda_{Si2pC}\cos\theta}\right)}{N_{Si} SF_{Si2p} \lambda_{Si2pSi} \cos\theta} \\ &= \exp\left(-\frac{d_C}{\lambda_{Si2pC}\cos\theta}\right) \end{aligned} \tag{B.4}$$

This leads to an expression for d_C depending only on experimentally measured values or input parameters[1].

$$d_C = -\lambda_{Si2pC} \cos\theta \ln\Gamma \tag{B.5}$$

Now, we will derive an expression for N_C using the ratio of B.3 and B.2 and substituting B.4.

[1] There is an inherent inaccuracy in this method due to the choice of IMFP for the carbon layer, which depends on the density of the layer that is unknown. However, since we can eliminate the use of absolute values for this parameter so we are only interested in the ratio of the attenuation of Si2p over C1s electrons, an empirical expression using an energy scaling factor can be used: $\lambda(KE) = \lambda_0 KE^{0.75}$. Using a predictive formula (TPP-2M)[53] for the molecules we are investigating and a range of possible densities as well as comparison with experimental values for different polymers, we found $\lambda_{Si2pC}/\lambda_{C1sC} = 1.12 \pm 0.01$

$$\frac{I_{C1s}}{I_{Si2p}} = \frac{N_C SF_{C1s}\lambda_{C1sC}}{N_{Si}SF_{Si2p}\lambda_{Si2pSi}} \frac{(1-\exp(d_C/\lambda_{C1sC}\cos\theta))}{(\exp(d_C/\lambda_{Si2pC}\cos\theta))}$$

$$\frac{I_{C1s}}{I_{Si2p}}\exp(d_C/\lambda_{Si2pC}\cos\theta) = N_C\frac{SF_{C1s}}{N_{Si}SF_{Si2p}}\frac{\lambda_{C1sC}}{\lambda_{Si2pSi}}(1-\exp(d_C/\lambda_{C1sC}\cos\theta))$$

$$\frac{I_{C1s}}{I_{Si2p}}\frac{I_{Si2p}}{I^0_{Si2p}} = N_C\frac{SF_{C1s}}{N_{Si}SF_{Si2p}}\frac{\lambda_{C1sC}}{\lambda_{Si2pSi}}\Gamma^{\frac{\lambda_{Si2pC}}{\lambda_{C1sC}}}$$

$$N_C = \frac{I_{C1s}}{I^0_{Si2p}}\frac{N_{Si}SF_{Si2p}}{SF_{C1s}}\frac{\lambda_{Si2pSi}}{\lambda_{C1sC}}\left(1-\Gamma^{\frac{\lambda_{Si2pC}}{\lambda_{C1sC}}}\right)^{-1} \tag{B.6}$$

Combining B.6 and B.5 we get an expression as follows

$$N_C d_C = \frac{I_{C1s}}{I^0_{Si2p}}\frac{N_{Si}SF_{Si2p}}{SF_{C1s}}\frac{\lambda_{Si2pSi}}{\lambda_{C1sC}}\left(1-\Gamma^{\frac{\lambda_{Si2pC}}{\lambda_{C1sC}}}\right)^{-1}(-\lambda_{Si2pC}\cos\theta\ln\Gamma)$$

and defining $\alpha = \frac{\lambda_{Si2pSi}}{\lambda_{C1sC}}$ and thereby eliminating the need to obtain accurate absolute values for the IMFPs in the carbon layer, we obtain a formula for the surface atomic density of the carbon overlayer $\sigma_C \equiv N_C d_C$

$$\sigma_C = \frac{I_{C1s}}{I^0_{Si2p}}N_{Si}\lambda_{Si2pSi}\cos\theta\frac{SF_{Si2p}}{SF_{C1s}}\frac{\alpha\ln\Gamma}{(\Gamma^\alpha-1)} \tag{B.7}$$

To obtain values for the SAM surface coverage for the different molecules under investigation this value can be divided by the according number of carbon atoms per molecules, which gives us the number of molecules per nm^2.

B.1.2 Quantification of the surface coverage using N1s spectra

Under the assumption that the nitrogen atom resides in the topmost part of the SAM, so that electrons originating from it in direction of the detector are not subject to attenuation. Approximating further that the nitrogen atoms reside in a single layer so that they do not influence one another the amount of nitrogen can be quantified directly. We can use the formula for the intensity of the N1s electrons scaled by the sensitivity factor to find an expression for the number density of nitrogen in the sample. Since we need to correct for instrument parameters as mentioned above, we will divide the nitrogen counts by the silicon counts from the reference sample. This will introduce further parameters that are known such as the density of silicon and the IMFP of Si2p electrons in bulk silicon.

$$N_{N1s} = N_{Si}\lambda_{Si2pSi}\frac{SF_{Si2p}}{SF_{N1s}}\frac{I_{N1s}}{I^0_{Si2p}} \tag{B.8}$$

B.1.3 Determination of the thickness of thin silicon oxide layers on silicon substrates

In analogy to the above derivation we are now considering the two separate components of the Si2p high resolution spectrum (background subtracted and fitted with Gaussian/Lorentzian peaks): The doublet arising from the Si-Si in the bulk silicon substrate (I_{Si}) and the chemically shifted silicon oxide peak evidencing the presence of Si-O bonds (I_{SiOx}). The oxide layer will lead to an additional attenuation of electrons ejected from the bulk substrate, which is taken into account. But since the energy of the electrons are only minimally shifted, both intensities are similarly affected by potential carbon or other thin films covering the oxide.

$$I_{Si} = N_{Si} SF_{Si2p} \lambda_{Si2pSi} \cos\theta \exp\left(-\frac{d_{Ox}}{\lambda_{Si2pO}\cos\theta}\right) \exp\left(-\frac{d_C}{\lambda_{Si2pC}\cos\theta}\right) \tag{B.9}$$

$$I_{SiOx} = N_{SiOx} SF_{Si2p} \lambda_{Si2pSiOx} \cos\theta \left[1 - \exp\left(-\frac{d_{Ox}}{\lambda_{Si2pO}\cos\theta}\right)\right] \exp\left(-\frac{d_C}{\lambda_{Si2pC}\cos\theta}\right) \tag{B.10}$$

Considering B.1 and an equivalent expression for a clean bulk silicon oxide substrate

$$I^0_{SiO2} = N_{SiO2} SF_{Si2p} \lambda_{Si2pSiO2} \cos\theta \tag{B.11}$$

and taking the ratio of B.9 and B.10 we can eliminate some of the pre-factors by scaling both counts the according experimental reference values mentioned above (analog to B.4)

$$\begin{aligned}
\frac{I_{Si}}{I^0_{Si}} \frac{I^0_{SiOx}}{I_{SiOx}} &= \frac{\exp\left(-\frac{d_{Ox}}{\lambda_{Si2pO}\cos\theta}\right)}{1 - \exp\left(-\frac{d_{Ox}}{\lambda_{Si2pO}\cos\theta}\right)} \\
\frac{I_{Si}}{I_{SiOx}} \left(1 - \exp\left(-\frac{d_{Ox}}{\lambda_{Si2pO}\cos\theta}\right)\right) &= \frac{I^0_{Si}}{I^0_{SiOx}} \exp\left(-\frac{d_{Ox}}{\lambda_{Si2pO}\cos\theta}\right) \\
\frac{I_{Si}}{I_{SiOx}} &= \left(\frac{I^0_{Si}}{I^0_{SiOx}} + \frac{I_{Si}}{I_{SiOx}}\right) \exp\left(-\frac{d_{Ox}}{\lambda_{Si2pO}\cos\theta}\right) \\
\ln\left(\frac{\frac{I_{Si}}{I_{SiOx}}}{\left(\frac{I^0_{Si}}{I^0_{SiOx}} + \frac{I_{Si}}{I_{SiOx}}\right)}\right) &= -\frac{d_{Ox}}{\lambda_{Si2pO}\cos\theta}
\end{aligned}$$

We end up with an expression for the oxide thickness

$$d_{Ox} = \lambda_{Si2pO} \cos\theta \ln\left(1 + \frac{I_{Si}}{I_{SiOx}} \frac{I^0_{Si}}{I^0_{SiOx}}\right) \tag{B.12}$$

B.2 Data extraction and processing of experimental raw data

B.2.1 Software

Data analysis was performed using Thermo Avantage v4.87 (Thermo Fischer Scientific) software provided with the measurement equipment and MATLAB R2010a (The MathWorks). Hereby peak fitting and identification and quantification of the survey spectra was done using the spectral analysis tools and peak libraries provided in Thermo Avantage. Quantification of molecular coverage and oxide thickness as well as generation of all plotted figures was done using MATLAB after exporting/importing of the spectral data as described below.

B.2.2 Data processing protocol

- **Spectral fitting** Use Avantage Software to load experimental data. In a new processing window, load Si2p, C1s and if applicable N1s or F1s spectra. Fit each spectrum with appropriate conditions as listed in Table B.2. Export the fitted peak data by copying and pasting into a spreadsheet.

- **Charge shift correction** In Excel, each peak table is corrected for energy shift by subtracting the difference between the main C1s peak and 285 eV (typically charging shift values are below 1eV for silicon samples and between 1 and 2eV for silicon oxide samples).

- **Quantification** Each peak table is manually complemented with a column for quantification of SAM coverage and oxide thickness if applicable. Additional columns are used for quantification by N1s or other individual peaks. Since the number of fitted peaks for all elements can vary this step is done manually adjusting the considered ranges for each sample. The formula refers to a list of *Parameters* given in a separate worksheet (copied into each excel file for individual datasets to avoid cross-referencing to data in different files). The parameters are listed in Table B.1.

- **Summary** Each excel file contains a sheet called *Results*, in which the quantified data is summarized in tabular form, referencing the values from the quantification columns. This sheet is accessed by Matlab for plotting and analysis of the data.

- **Plotting** In Matlab, for each Figure, a script extracts the required data from the according excel file and generates a customized bar plot. Averaging of multiple samples is done here as well. The script automatically generates, formats and saves the Figures, so that changes in the data (such as adjustments in the

- *Parameters* propagate automatically and can be replotted directly.

Symbol	Value	Unit	Description
			Material parameters
θ	0	°	Detector angle relative to surface normal
N_Si	49.92	nm^{-3}	Number density of silicon atoms in monocrystalline Si
ρ_{SiO2}	53.06	nm^{-3}	Number density of oxygen in stoichiometric SiO_2
σ_Si	7.8	nm^{-2}	Surface atom density in the Si(111) surface
σ_AuSAM	4.63	nm^{-2}	Molecular density of perfect SAM on Au[]
d_{MLSiOx}	3.6	Å	SiO2 monolayer thickness
d_{BOC}	11.77	Å	calculated layer thickness 10-N-BOC-amino-dec-1-ene
			Sensitivity factors
SF_O	2.93		
SF_{Si}	0.817		
SF_N	1.8		
SF_C	1		
α_2	1.30		Energy scaling factor for IMFP, O1s vs. Si2p
α	1.12		Energy scaling factor for IMFP, C1s vs. Si2p
			Inelastic mean free paths
l_{Si2pSi}	31.36	Å	
$l_{Si2pSiO2}$	37.7	Å	
$l_{O1sSiO2}$	28.2	Å	
l_{l_Si2pC}	40.23	Å	
l_{l_N1sC}	33.06	Å	
l_{l_C1sC}	35.84	Å	
			Experimental/derived values
I_{Si2p_Ox}/I_{Si2p_Si}	1.37		Normalization factor for oxide layer thickness calculation
I^0_{Si}	71708	s^{-1}	Reference Si2p counts for clean silicon surface

Table B.1 Parameter used in the quantitative analysis of XPS data

Table B.2 Parameters used for fitting of high resolution XPS spectra

B.3 MATLAB scripts and functions for analysis of SiNW measurement data

B.3.1 Data structure and analysis of measurements from the original instrumented setup

The LabVIEW software that operates the connected devices allows for the readout of all datapoints of the amplified and converted raw data as well as the calculated and averaged values calculated for the complex impedance after each voltage sweep (period). The raw data consists of pairs of voltage and current values for each time step the averaged data uses the datapoints from each period of the sinusoidal voltage signal and calculates the resistance and phase for that period using the current signal. Most commonly only the averaged impedance values were considered in the analysis and only this case will be discussed here. The data is saved in ASCII format in a simple .csv file that can be imported into MATLAB. The folder structure for each experiment is more important as each detection step is recorded in a separate folder and file for each sensor on each chip (as they are recorded in sequence and not simultaneously).

MATLAB SiNW data plot function

```
%% Plot function: SiNW measurement analysis
% Andrea Pfreundt, DTU Nanotech, 2012-10-26
%
% [data] = SiNWdata_chip_batch(inv,norm,cut_first,cut_last)
%
% Use this function to plot a batch of data of SiNW measurements.
%
% Input data:
% The folder structure required for this script to work is the following:
% > selected_folder
%   > sub_folders containing sets of folders from e.g. wires (arbitrary
%   number)
%     > sub_sub_folders containing the data files (arbitrary number, but
%     the number of sub_sub_folders should be the same in all sub_folders)
%
% Variables:
% INPUT: inv = 1 (default) reverses the order of filenames in the folders,
%        enter 0 to keep the standard (alphabetical) ordering, norm = 1
%        (default) normalizes the impedance data to the first measurement,
%        cut_first and cut_last are the number of characters cut from the
%        folder names of the data to obtain the label for the x-axis of the
%        resulting graphs (the name is everything before IV and the
%        data). (Example: if the folder is named 0BufferIV 2012-01-10,
```

```
%        cut_first = 1 and cut_last = 0, will result in a label "Buffer")
% OUTPUT: data: contains all names (names), Impedance (Mall) and phase data
%         (Pall) for each measurement (wire or chip)
%
% Output graphs:
% Three plots will be produced with the same basic structure: The data from
% one sub_folder is considered as one dataset and plotted in one color,
% containing all measurement points (NOTE: if measurements have different
% numbers of datapoints, the data is cut to the shortest measurement!). The
% sub_sub_folders are considered as experimental steps and plotted along
% the x-axis. The y axis varies to present different aspects of the data:
%
% 1. Phase
% 2. Impedance |Z| (or Delta|Z|/|Z_0|)
% 3. Conductance G (or DeltaG/G_0)
%


function [data] = SiNWdata_chip_batch(inv,norm,cut_first,cut_last)

folder = uigetdir; % opens dialog to select a folder with data
list = dir(folder); % makes a list of all the files and folders in chosen folder

if nargin < 1 % number of input arguments = nargin
    inv = 0;
end
if nargin < 2
    norm = 1;
end

if nargin < 3
    cut_first = 0;
    cut_last = 0;
end

av = 1;

cut_first = cut_first+1;

data = struct(); % creates the empty struct to later hold the data

n = length(list)-2;
```

```
for i=1:n
    [data(i).names,~,~,data(i).Pav,data(i).Pall,~,data(i).Mav,data(i).Mall] = ...
     importSiNWbatch(0,[folder,'\',list(i+2).name],inv,cut_first,cut_last);
    data(i).name = list(i+2).name;
end

color_styles;
color = map3/255;
%['b*';'r*';'g*';'c*';'m*';'y*'];

f1 = figure; % Figure 1: Impedance plot
    for i = 1:n-1
        if norm == 1
            plotdata = (data(i).Mall-data(i).Mav(1))/data(i).Mav(1);
        else
            plotdata = data(i).Mall;
        end
        if av == 1
            plotdata = mean(plotdata);
        end
        plot_SiNWdata(plotdata, folder, data(i).names, '', color(i,:));
        hold on;
    end
        if norm == 1
            plotdata = (data(n).Mall-data(n).Mav(1))/data(n).Mav(1);
            if av == 1
                plotdata = mean(plotdata);
            end
            plot_SiNWdata(plotdata, folder, data(n).names, ...
             'Normalized Impedance |Z|/|Z_0|', color(n,:));
            legend(list(3:end).name,'Location','SouthEast');
        else
            plotdata = data(n).Mall;
            if av == 1
                plotdata = mean(plotdata);
            end
            plot_SiNWdata(plotdata, folder, data(n).names, 'Impedance |Z|', color(n,:));
            legend(list(3:end).name,'Location','SouthEast');
        end

figuresize = [0 0 16 10];
```

```
name = '../Impedance_Plot';
saveimage(name,figuresize);

f2 = figure; % Figure 2: Conductance plot
    for i = 1:n-1
        if norm == 1
            plotdata = (1./data(i).Mall - 1./data(i).Mav(1))*data(i).Mav(1);
        else
            plotdata = 1./data(i).Mall;
        end
        if av == 1
            plotdata = mean(plotdata);
        end
        plot_SiNWdata(plotdata, folder, data(i).names, '', color(i,:));
        hold on;
    end
        if norm == 1
            plotdata = (1./data(n).Mall - 1./data(n).Mav(1))*data(n).Mav(1);
            if av == 1
                plotdata = mean(plotdata);
            end
            plot_SiNWdata(plotdata, folder, data(n).names, ...
            'Normalized Conductance \Delta G/G_0', color(n,:));
        else
            plotdata = 1./data(n).Mall;
            if av == 1
                plotdata = mean(plotdata);
            end
            plot_SiNWdata(plotdata, folder, data(n).names, 'Conductance [S]', color(n,:));
        end
    legend(list(3:end).name,'Location','NorthEast');

% figure; % Figure 3: Phase plot
%     for i = 1:n-1
%         plot_SiNWdata(data(i).Pall, folder, data(i).names, '', color(i,:));
%         hold on;
%     end
%     plot_SiNWdata(data(n).Pall, folder, data(n).names, 'Phase \phi', color(n,:));
%     legend(list(3:end).name);

figuresize = [0 0 16 10];
name = '../Conductance_Plot';
```

```
saveimage(name,figuresize);
end

function plot_SiNWdata(data, folder, names, ylab, color)

    plot(data(:),'Color',color,'Marker','.','MarkerSize',20,'LineStyle','none');
    [l,l2] = size(data);
    xticks = [1:1:l2];
    set(gca,'XTick',xticks);
    set(gca,'XTickLabel',[{'before'},{'0.4'},{'wash'},{'4'},{'wash'},{'40'},{'wash'}]);
    idx = regexpi(folder,'\');
    xlabel('Concentration of anti-mouse IgG [ug/mL]','FontSize',14);
    ylabel(ylab,'FontSize',14);
end
```

MATLAB SiNW data import function

```
%% Import function: SiNW measurement
% Andrea Pfreundt, DTU Nanotech, 2012-08-26
%
% Use this function to import impedance data from all subfolders in a
% folder and extract the resistance values as well as the standard
% deviation of the data.
%
% function [names,Rav,Rall,Pav,Pall,stdev,Mav,Mall] =
% importSiNWbatch(plotON,folder,inv,cut_first,cut_last)
%
% INPUT: turn on plotting of each measurement by setting plotON = 1,
%        default plotON = 0
% OUTPUT: names: Row vector containing file names without timestamp,
%         R: average resistance value from each measurement
%         stdev: Standard deviation of the resistance value.
%
% Plot: The plot displays the resistance data as blue stars, the
%       mean value as red line with the standard deviation indicated by
%       interrupted red lines.
%


function [names,Rav,Rall,Pav,Pall,stdev,Mav,Mall] = ...
importSiNWbatch(plotON,folder,inv,cut_first,cut_last)
```

```
if nargin<1
    plotON = 0;
end
if nargin<2
    folder = uigetdir;
end
if nargin<3
    inv = 0;
end
if nargin<4
    cut_first = 1;
    cut_last = 0;
end

data = struct();
list = dir(folder);
names = [];
Rav = [];
Rall = [];
Iav = [];
Iall = [];
Mav = [];
Mall = [];
Pav = [];
Pall = [];
stdev = [];

for i = 1:length(list)-2
    I = importdata([folder,'\',list(i+2).name,'\Impedance.dat']);
    % Impedance:
    modulus = I(:,1); % first column of the imported data is the
    modulus of the impedance
    phase = I(:,2); % second ... in degrees
    data(i).real = modulus .* cos(phase.*pi/180); %cos(radians)
    data(i).imag = modulus .* sin(phase.*pi/180);
    newR = data(i).real;
    newI = data(i).imag;
    newM = modulus;
    newP = phase;
    s = size(Rall,1);
    l = length(newR);
    if  s == 0 || s >= l % checks for the number of measurements
```

```
and cuts them all to the same size
    if s == 0 || s == l
        if inv == 1 % inv can be used to invert the order in
        which the different measurements appear in the plot
            Rall = [newR,Rall];
            Iall = [newI,Iall];
            Mall = [newM,Mall];
            Pall = [newP,Pall];
        else
            Rall = [Rall,newR];
            Iall = [Iall,newI];
            Mall = [Mall,newM];
            Pall = [Pall,newP];
        end
    else
         if inv == 1
            Rall = [newR,Rall(s-l+1:end)];
            Iall = [newI,Iall(s-l+1:end)];
            Mall = [newM,Mall(s-l+1:end)];
            Pall = [newP,Pall(s-l+1:end)];
        else
            Rall = [Rall(s-l+1:end),newR];
            Iall = [Iall(s-l+1:end),newI];
            Mall = [Mall(s-l+1:end),newM];
            Pall = [Pall(s-l+1:end),newP];
        end

    end
else
    if inv == 1
    Rall = [newR(l-s+1:end),Rall];
    Iall = [newI(l-s+1:end),Iall];
    Mall = [newM(l-s+1:end),Mall];
    Pall = [newP(l-s+1:end),Pall];
    else
    Rall = [Rall,newR(l-s+1:end)];
    Iall = [Iall,newI(l-s+1:end)];
    Mall = [Mall,newM(l-s+1:end)];
    Pall = [Pall,newP(l-s+1:end)];
    end
end
```

```
        % calculates the average values for each measurement

        if inv == 1
            Rav = [mean(data(i).real),Rav];
            Iav = [mean(newI),Iav];
            Mav = [mean(newM),Mav];
            stdev = [std(data(i).real),stdev];
            Pav = [mean(phase),Pav];
        else
            Rav = [Rav,mean(data(i).real)];
            Iav = [Iav,mean(newI)];
            Mav = [Mav,mean(newM)];
            stdev = [stdev,std(data(i).real)];
            Pav = [Pav,mean(phase)];
        end

        % Extract filename without added timestamp
        idx2 = regexpi(list(i+2).name, 'IV');
        if length(idx2) > 1
            idx2 = idx2(end);
        end
        if isempty(idx2)
            idx2 = length(list(i+2).name)+1;
        end
        nwno = list(i+2).name(cut_first:idx2-cut_last-1);
        if inv == 1
            names = [{nwno};names];
        else
            names = [names;{nwno}];
        end

        % Plot data if plotON option chosen
        if plotON == 1
%             figure;
%             plot(data(i).real,'b*');
%             hold on;
%             l2 = length(data(i).real);
%             plot([1,l2],[Rav(i),Rav(i)],'r-');
%             plot([1,l2],[Rav(i)+stdev(i),Rav(i)+stdev(i)],'r--');
%             plot([1,l2],[Rav(i)-stdev(i),Rav(i)-stdev(i)],'r--');
%             title(nwno);
%             xlabel('No. measurement/Time');
```

```
%             ylabel('Resistance [\Omega]');
%             hold off;
        end
    end

  if plotON == 1
    figure;
    plot_SiNWdata(Mall, folder, names,'Impedance |Z|');
    figure;
    plot_SiNWdata(Pall, folder, names,'Phase \phi');
  end

end

function plot_SiNWdata(data, folder, names, ylab)

    plot(data(:),'*');
    [l,l2] = size(data);
    xticks = [l/2:l:l2*l-l/2];
    set(gca,'XTick',xticks);
    set(gca,'XTickLabel',names);
    idx = regexpi(folder,'\');
    title(folder(idx(end)+1:end));
    xlabel('Measurement');
    ylabel(ylab);

end
```

C | Protocols

C.1 Process flow for the fabrication of surface test chips

Table C.1 Processing table for cleanroom fabrication of surface test substrates

Step	Equipment	Procedure	Comments
Preparation			
Wafer selection	Wafer box	Take the wafers from the storage and put them in a wafer box.	Note the wafer IDs in the batch traveler
SiO2 deposition			
SiO2 dry oxidation	Furnace Anneal-Oxide (C1)	Recipe: (from Azeem) Target thickness: 170 ± 10nm	Measure oxide thickness on the filmtech and note the result in the furnace log
Poly-Si deposition			
RCA cleaning	RCA	Perform RCA cleaning process on all wafers to remove organic contaminants, particles and trace metals	
Poly-Si deposition	Furnace: LPCVD Poly-Si (4")	Recipe: POLYBOR, 6 minutes. Target thickness: 50 ± 2 nm. Total process time: 2 h	Include testwafer for Danchip, single side polished (testwafers for furnace -> waferbox)
Thickness measurement	Ellipsometer	Measure the polysilicon thickness	
Thickness measurement	Filmtech	Measure on Danchip testwafer and not in log book	Place wafer into testwafer box and mark with date/thickness/initals
Lithography – 1.5 μm standard			
Surface treatment	HMDS oven	Load all wafers in oven for 30 mins Recipe: program 4	Note time in logbook

Step	Equipment	Procedure	Comments
Clean spinner	SSE spinner	Clean spinner nozzle and run the dummy wafers Recipe: 1.5 4inch 1-3 dummies	Note time in logbook
Coat wafers	SSE spinner	Coat the device wafers 1.5 μm AZ5214e Novolac resist Softbake on hotplate Recipe: 1.5 4 " (Temp: 90°C, time: 60 s)	Resist thickness not checked Note time in logbook
Exposure	KS Aligner	Align transparency mask and fixate using pyrex wafer Recipe: xxxxxx Exposure time: 8 s (consider pyrex+mask absorption) Mask: MASK 1 POLYSI (bright field)	Note time in logbook
Develop	Developer bench	Develop in 351B for 70 ± 10 s	Note time in logbook
Rinse/dry	Wet bench/ Spin dryer	Rinse in DI water for 5 min (300 ± 30 s). Spin dry	
Inspection	Optical microscope	Check pattern and alignment marks	
Poly-Si dry etch			
Cleaning	O2 plasma	Remove residual resist	
Dry etch	Reactive Ion Etching (RIE1)	Use standard/Azeems recipe to etch through the Poly-Si layer.	
Inspection	Optical microscope	Check pattern and alignment	
Strip resist	Acetone	First 2-3 min in rough followed by 5 min in fine strip bath with ultrasound	
Rinse/dry	Wet bench/ Spin dryer	Rinse in DI water for 5 min (300 ± 30 s). Spin dry	
Inspection	Dektak	Measure step height Target: 50 ± 2 nm	
Lithography – 1.5μm standard			
Surface treatment	HMDS oven	Load all wafers in oven for 30 mins. Recipe: program 4	Note time in logbook
Clean spinner	SSE spinner	Clean spinner nozzle and run the dummy wafers. Recipe: 1.5 4 ". 1-3 dummies	Note time in logbook
Coat wafers	SSE spinner	Coat the device wafers 1.5 μm AZ5214e Novolac resist. Softbake on hotplate. Recipe: 1.5 4inch (Temp: 90°C, time:60 s). Resist thickness not checked	Note time in logbook

Step	Equipment	Procedure	Comments
Exposure	KS Aligner	Align transparency mask by eye using the large alignment marks and fixate using pyrex wafer Recipe: xxxxxx Exposure time: 5 s (needs to be determined, consider pyrex+mask absorption) Mask: MASK 2 SIO2 (bright field)	Note time in logbook
Develop	Developer bench	Develop in 351B for 60 ± 10 s	Note time in logbook
Rinse/dry	Wet bench/ Spin dryer	Rinse in DI water for 5 min (300 ± 30 s). Spin dry	
Inspection	Optical microscope	Check pattern and alignment marks	
SiO2 dry etch or wet etch			
A Dry etch	Reactive Ion Etching (RIE1)	Use standard/Azeems recipe to etch through the SiO2 layer.	
B Wet etch	BHF	Etch silicon oxide in BHF (isotropic, will lead to underetching), etch rate 75 $^{nm}/_{min}$ Etching time: 3 min	
Rinse/dry	Wet bench/ Spin dryer	Rinse in DI water for 5 min (300 ± 30 s). Spin dry	
Inspection	Optical microscope	Check pattern and alignment	
Strip resist Rinse/dry	Acetone Wet bench/ Spin dryer	First 2-3 min in rough followed by 5 min in fine strip bath with ultrasound Rinse in DI water for 5 min (300 ± 30 s). Spin dry	
Inspection	Dektak	Measure step height. Target: 170 ± 10 nm	
Dicing			
Dicing	Dicing machine	Cut wafers according to cut lines: steps: 17.2 x 5.5 mm	

C.2 SiNW device specs - wafer table

The table is and excerpt of the full number of batches, based on the specifications given by Azeem Zulfiqar, who fabricated the sensors.

Wafer No.	PSi Thickness	Oxide Thickness	Contact Metal	Passivation
W8	50 nm	420 nm	Cr/Au	SU-8
W9	50 nm	420 nm	Ti/Au	SU-8
W10	50 nm	420 nm	Cr/Au	PI
W11	50 nm	170nm Dry Oxide	Cr/Au	PI- 6.2μm
W12	50 nm	170nm Dry Oxide	Cr/Au	PI- 6.2μm
W13	50 nm	170nm Dry Oxide	Cr/Au	PI-7.5μm

Wafer No.	Back Gate	Evap/Sputter	Mask Type	Dicing Date
W8	Yes: Au		New	
W9	Yes: Au		Old: SiNW	
W10	Yes: Au		New	17-09-2012
W11	Yes: Cr/Au	Sputter-Lesker	New Mask	24-01-2013
W12	Yes: Cr/Au	Sputter-Lesker	New Mask	24-01-2013
W13	Yes: Cr/Au	Sputter-Lesker	New Mask	31-01-2013

C.3 Experimental protocols

C.3.1 Protocol: Grafting of 1,7-octadiyne to silicon surfaces using white light and hydride abstraction

All steps are carried out under a fume hood and wearing double nitrile gloves when handling HF solutions. The second pair of gloves is immediately discarded after the etching procedure as a precaution in case of any invisible spillage of HF. Each silicon surface was scratched to create a rough surface area with different crystal directions.

1. Rinse chip in ethanol(EtOH)
2. Place the chip in an eppendorf tube containing EtOH
3. Use a tweezer to transfer the chip to a tube containing 5 % HF (Highly toxic! Be careful when handling!)
4. Let the chip react with the acid for 20 s
5. Transfer the chip back to the tube containing EtOH using a tweezer
6. Let the chip stay there for 1 min
7. In the meantime prepare a tube containing the mixture of 1,7-octadiyne (concentrations: 0 M, 10 mM, 100 mM, 1 M and 3 M) and 5 mM Ph3C-BF4 (dissolved in EtOH). Usually 500 μL solution is sufficient to cover the chip.
8. Transfer the chip from the EtOH containing tube to the tube containing the mixture.
9. Incubate in strong light from a 60 W light bulb for 30 min.
10. Rinse with EtOH and store in EtOH at 4 °C until further functionalization.

C.3.2 Protocol: Labeling of the alkyne terminated surface with Alexa Fluor 594-azide

Materials:

- Phosphate buffered saline (PBS, pH 7.4)
- 1 mM stock solution of Alexa Fluor 594-azide
- 40mM$CuSO_4$ in MilliQ water
- 400 mM NaAscorbate in MilliQ water
- eppendorf tubes

Procedure:

1. Prepare 500 μL 'click'-solution for each surface as follows (2 μM Alexa Fluor 594-azide):
   - 462.5 μL PBS
   - 2.5 μL 40mM$CuSO_4$
   - 1 μL 1 mM Alexa 594-azide
   - at last add 25 μL 400 mM NaAscorbate)
2. Add 500 μL solution to a 1 mL eppendorf tube and insert the alkyne-modified silicon chip.
3. Incubate in the dark for 15 minutes.
4. Wash each surface 3 times with PBS.
5. Move the chips into a tube containing PBS for storage.

C.3.3 Protocol: Investigating the effect of 1,7-octadiyne grafting on the electrical properties of polysilicon nanoribbons

C.3.4 Protocol: Flowcell investigation of HF etching on polysilicon nanoribbons

A microfluidic flowcell device made of PMMA was with internal connection channels was used. It contained a single flowcell channel made from PDMS as interface between the nanoribbon chip and external tubing. A syringe pump (Chemyx Inc. N3000) was used to drive the liquid, which was loaded into a length of tubing separated by air bubbles and injected sequentially at a flow rate of 0.5 μL/min. To test the approximate time it takes for a specified volume of liquid or air to reach and cross the flowcell chamber, a test run with MilliQ water was done first.

Testrun

The syringe was filled with MilliQ water and the tubing was loaded with the reagents in reverse order using withdraw mode.

Medium	Volume [μL]	Injected at [s]	Passing time [s]
1 air	start	-	
2 water	2	67	299
3 air	2	366	177
4 water	2	543	319
5 air	2	862	149
6 water	2	1011	294
7 air	2	1305	158

The test run resulted in approximated passing times for 2 μL volume for air of 160 s and for water of 300 s.

Experimental run

The sensor chips used for the experiment were W11D13 and W11E14 and W12E12 and W12E13. The syringe was filled with MilliQ water and the tubing was loaded with the reagents in reverse order using withdraw mode. 1 μL of 1 % HF solution was used, separated by air bubbles from droplets of MilliQ water before and after. After filling of the tubing, the syringe pump was run forward at 0.5 $\mu L/min$ while the conductance of the nanoribbon was monitored using the setup described in 8.1.2 and an applied voltage of 50 mV at 1 Hz. The microfluidic flow was closely observed during the process to pinpoint the movement of the air bubbles through the system. The injection points of the liquids into the flowcell chamber are marked in the graphs accordingly. The outlet of the device was connected to a collection tube that was disposed of in the fume hood/chemical waste. After operation, the tubing was discarded and the device and chip thoroughly rinsed with MilliQ water in the fume hood to remove any traces of HF from the system.

C.3.5 Protocol: Surface functionalization with (3-aminopropyl)triethoxysilane

Materials:

- Glass desiccator dedicated to APTES functionalization
- Hot plate
- 50 μL and 200 μL Hamilton syringes dedicated to DIPEA / APTES
- Oxygen plasma chamber (Milling Lab)
- 3-Aminopropyltriethoxysilane (Sigma, 440140-100ML)
- N,N-Diisopropylethylamine (Sigma, 496219-100ML)

- Chloroform to clean syringes (fume hood)
- absolute Ethanol (>99
- petri dishes, glass slides, eppendorf tubes

Procedure:

1. (Ideally, surfaces should be cleaned in Piranha solution for 15 min at 105°C, for this refer to the Piranha cleaning protocol, but this can't be done with the SiNW chips.)
2. Before functionalization the chips should be cleaned thoroughly in absolute Ethanol and dried in a flow of nitrogen.
3. Place a hotplate in the fumehood, set at 60°C (place temperature sensors on plate, make sure it reads the temperature!).
4. Place dedicated glass desiccator on top. Nitrogen and vacuum lines should be connected via a T-junction so you can switch between the two.
5. Chips are placed on a microscope slide, facing upwards, and treated with oxygen plasma for 2 minutes (in the Milling lab at maximal power, 0.5 mbar oxygen)
6. After treatment, place chips immediately into 99
7. Break off two caps from eppendorf tubes and place into desiccator.
8. Clean Hamilton syringes with Chloroform, take 200 μL APTES and place into one of the caps
9. Do the same with the 50 μL Hünig's base (N,N-Diisopropylethylamine) using the other syringe
10. Clean both syringes thoroughly with Chloroform again.
11. Place chips to be functionalized on a microscope slide and place it into the desiccator next to the caps, keep a low flow of nitrogen.
12. Make sure the nitrogen valve is closed. Open vacuum line to evacuate desiccator for 3-5 minutes.
13. Close vacuum line and open nitrogen valve to flush the desiccator.
14. Repeat at least 3 times then keep a low overpressure of nitrogen (so that the top moves easily but doesn't fall off, can be fixed in place with tape).
15. Keep in desiccator for 1h.
16. Turn up the hotplate to 110°C and bake for another 7 min.
17. Store in desiccator under vacuum until further use.

C.3.6 Protocol: Flowcell protein immobilization on NH2-terminated surface using Glutaraldehyde

Materials:

- Phosphate buffered saline (PBS, pH 7.4)
- 100 μL aliquot of 25 % glutaraldehyde
- stock solution of 1 M sodium cyanoborohydride in 1 M NaOH
- Gold nanoparticles with conjugated anti-mouse IgG (AuNP-aIgG) (abcam)
- 4-chip flowcell with 2 channels

Procedure:

1. Prepare the solutions:
   (a) Prepare 2.5 % glutaraldehyde solution in MilliQ by adding 850 μL MilliQ to an aliquot and transfer 95 μL to a separate tube. Prepare a tube of only MilliQ water for the negative ctrl.
   (b) Add 5 μL 1 M sodium cyanoborohydride solution to the 95 μL Glutaraldehyde solution, resulting in a concentration of 50 μm.
   (c) AuNP-aIgG solution: prepare a 25 times dilution using 4 μL of μL NP stock solution and 91 μL PBS at pH 7.4.
   (d) Add 5 μL 1 M sodium cyanoborohydride solution to the 95 μL NP solution, resulting in a concentration of 50 μm.
   (e) For the blocking solution, add 50 μL of 1 M Tris HCl to 950 μL PBS for a final concentration of 50 mM.
   (f) Prepare a tube with MilliQ water and one with PBS for the washing steps.
2. Line up solutions in open Eppendorf tubes according to the order below for loading. One line for the samples and one for the controls.
3. Load the protocol steps into two labeled lengths of tubing by withdrawing with a syringe pump and two identical syringes.
   (a) Load by withdrawal at 30 $^{\mu L}/_{min}$ starting with the first step of the protocol according to the table below.
   (b) Switch the tubing ends around before staring the procedure (to avoid contact of tubing with subsequent steps)
4. Run protocol with syringe pump at 1 $^{\mu L}/_{min}$ through the two separate flow paths of the flow cell with 2 samples each

5. Store at +4C until further use.

Reagent (sample)	Reagent (neg. control)	Incubation time at 1 μL/min	Volume	Loading at 30 μL/min
1 Glutaraldehyde	MilliQ	30 min	30 μL	1 min + 5 s air
2 MilliQ	MilliQ	5 min	5 μL	10 s + 5 s air
3 AuNP-aIgG	AuNP-aIgG	30 min	30 μL	1 min + 5 s air
4 PBS	PBS	5 min	5 μL	10 s + 5 s air
5 TrisHCl	TrisHCl	30 min	30 μL	1 min + 5 s air
6 PBS	PBS	5 min	5 μL	10 s + 5 s air

C.3.7 Protocol: Protein immobilization on NH2-terminated surface using Glutaraldehyde

Materials:

- Phosphate buffered saline (PBS, pH 7.4)
- 100 μL aliquot of 25
- stock solution of 1 M sodium cyanoborohydride in 1 M NaOH
- receptor protein (antibody) in a concentration of XX mg/mL
- small petri dishes
- parafilm

Procedure:

1. Take a tube with 100 μL 25 % glutaraldehyde solution out of the freezer (alternatively take the bottle out of the freezer and prepare 100 μL aliquots).
2. Prepare 2.5 % glutaraldehyde solution in 1xPBS by adding 900 μL PBS to an aliquot.
3. Add 50 μL 1 M sodium cyanoborohydride solution per 1 mL protein solution, resulting in a concentration of 50 μM.
4. Cover the bottom of a petri dish in parafilm and place a 25 μL droplet of Glutaraldehyde solution for each chip on the surface.
5. Place chips upside down onto the droplets and incubate for 2 h at room temperature.
6. Wash twice by placing chips in small petri dish and covering with MilliQ water (min 3 mL). Put on shaker at low speed, so that the liquid swirls around in the petri dish, for 5 min each.

7. Prepare protein solution: for a concentration of XX μg/ml, add XX μL protein stock solution to PBS buffer at pH 7.4.

8. In the fume hood, add 50 μL 1 M sodium cyanoborohydride solution per 1 mL protein solution, resulting in a concentration of 50 μM.

9. Prepare a petri dish with parafilm as above and place a droplet of protein solution for each chip. Place chip upside down in droplet and incubate for 2 h at room temperature (4 h or overnight, agitated, in original protocol, Pierce).

10. Wash twice in PBS as above. After the second wash, place 3 mL PBS in the petri dish

11. For blocking, add 150 μL of 1 M Tris HCl to 3 mL PBS and incubate on shaker for 30 min (final concentration of TrisHCL 50 mM)

12. Wash again in PBS.

13. Store at +4C until further use.

C.3.8 Protocol: Azide labelling of protein

Materials:

- Phosphate buffered saline (PBS, pH 7.4)
- 100 mM NHS-Azide
- 1M TrisHCl, pH 8.0
- protein stock solution
- desalting column pre-loaded with PBS (0.5 mL Zeba^{TM}Spin Desalting Column)

Procedure:

1. Combine 20 uL protein stock solution with 1,2 uL NHS-Azide (100 mM) and 100 uL PBS.

2. Incubate 1 hr at room temperature.

3. Add 10 uL 1M TRIS pH 8.0 to quench.

4. Incubate 10 min.

5. Desalt the solution using a spin desalting column pre-loaded with PBS.

6. Store Protein-Azide at -20 in small aliquots.

C.3.9 Protocol: Preparation of Alkyne-terminated sensor surfaces

Materials:

- neat 1,7-Octadiyne (careful, strong smell, only open in fume hood)
- absolute ethanol >99 %
- 1 % HF (careful, toxic!)
- light bulb

Procedure:

1. Place chips in a tube holder under the fume hood.
2. Prepare for each chip a fresh tube with Ethanol and a tube containing 500 μL of reagent A
3. Take a tube of 1 % HF solution out of the fridge (Caution! Very Toxic! Wear chemical gloves)
4. For each chip (this step should take around 1 min):
   (a) With tweezers, take chip out of the Ethanol and place in HF. Let it react for 20 s.
   (b) Rinse chip thoroughly with Milli-Q water. Discard water into drain in the fume hood and flush with more water.
   (c) Replace chip into the Ethanol tube, close it and gently mix the liquid for washing.
   (d) Place chip into the reagent A containing tube and close it.
   (e) Discard the washing tubes. The HF is reused and returned to the fridge afterwards.
5. Take the tubes in the holder out of the fume hood and place under strong light. Incubate like this for 3 h. *This is done by placing all chips into the outermost position of the holder and turning the NWs toward the outside, so the light can reach it.*
6. Place the holder back into the fume hood and prepare again 3 tubes containing Ethanol for each chip.
7. Take chips out of the reagent and place in Ethanol, wash as above and repeat.
8. Dry the chips under air flow and keep in a fresh tube until further use.
9. Discard the washing and reagent tubes.

C.3.10 Protocol: Preparation of surfaces terminated by *t*Boc-protected amino groups

Materials:

- neat 10-N-Boc-amino-dec-1-ene
- absolute ethanol (96 %)
- 1 % HF
- petri dish with nitrogen flow
- microscope slides and coverslips
- light bulb

Procedure:

1. Place chips in a tube holder under the fume hood.
2. Use the petri dish with attached tube: Place a microscope slide in the bottom and close the lid. Turn on the nitrogen flow (at a very low flow rate, just to create a nitrogen atmosphere in the petri dish).
3. Prepare for each chip two fresh tubes with 1 mL 96 % ethanol.
4. Take a tube of 1 % HF solution out of the fridge (Caution! Toxic!)
5. For each chip (this step should take around 1 min per chip):
   (a) With tweezers, take chip out of the ethanol and place in HF. Let it react for 15 s.
   (b) Replace chip into the Ethanol tube, close it and gently mix the liquid for washing.
   (c) Repeat this twice with the two fresh tubes of ethanol. Keep chip in the last tube.
   (d) Discard the washing tubes. The HF is reused and returned to the fridge afterwards.
6. Dry the chips in the nitrogen chamber like this: Carefully open the petri dish so you can place the chips on the microscope slide (side-by-side) and replace the lid. Leave chips there for as long as it takes for the ethanol to evaporate.
7. Open the petri dish as much as necessary: Take 5 μL of the neat alkyne and cover the wires on each chip with a droplet. Cover with a wide coverslip (the alkyne will spread and cover the whole chip). Replace the lid.
8. Take the light bulb into the fume hood (place it in a convenient way so that it can not fall over) and direct it toward the petri dish so all the chips are in full light.
9. Keep chips incubated in light over night.

10. Next morning: Prepare a container with 70 % ethanol to clean the microscope slide and cover slip. Prepare three tubes with 96 % ethanol per nanowire chip and place in tube holder.

11. Turn off nitrogen flow. Open the petri dish. Remove the cover slip and place into washing container.

12. Place each chip into a washing tube. Close the lid and mix gently to wash.

13. Repeat twice.

14. Place microscope slide into washing container.

15. Take the tubes in the holder out of the fume hood.

C.3.11 Protocol: Protein immobilization on alkyne-terminated surfaces using CuAAC

Materials:

- Phosphate buffered saline (PBS, pH 7.4)
- 40 mM $CuSO_4$
- 50 μg/mL azide conjugated protein
- 400 mM Sodium ascorbate
- Pipetting frame

Procedure:

1. Prepare reagent mixture: 176 μL PBS, 10 μL $CuSO_4$ and 2 μL azide-protein
2. Place chips in pipetting frame (4 chips max)
3. Wash each frame with EtOH and MilliQ water by filling container and mixing with a pipette. Remove liquid from a corner.
4. Add 10 μL sodium ascorbate to the reagent mixture and use immediately. Add 50 μL into each container on top of the chips. Close the lids
5. Incubate in the dark for 15 minutes.
6. Remove the reagent and wash with PBS 3 times.
7. Remove the chips from the pipetting frame and store in PBS until use.

C.3.12 Protocol: Protein immobilization on COOH-terminated surfaces using EDC/NHS

Materials:

- 0.1M MES buffer (pH 6): (100 mL) 1.95g 2-(N-morpholino)ethanesulfonic acid (MES), 100 mL MilliQ water
- 50 mM NHS in 0.1M MES buffer: (50 mL) 0.288g N-Hydroxysuccinimide (NHS), 50 mL MES buffer
- 100 mM EDC in MES buffer: (56 μL) 1 μL 1-Ethyl-3-(3-dimethylaminopropyl)carbodiimide (EDC) (stored in freezer), 55 μL MES buffer
- Phosphate buffered saline (PBS, pH 7.4)
- 3 mg/mL Mouse Immunoglobulin Stock solution
- small petri dishes
- parafilm
- shaker

Procedure:

1. Prepare MES buffer with 5 mM NHS (pH 6) by mixing the pure buffer and buffer with 50 mM NHS 10:1.
2. Move to the fume hood to add EDC.
3. Add 20 μL 100 mM EDC solution per 1 mL buffer to obtain a final concentration of 2mM.
4. Mix carefully and use the activation buffer directly and incubate the carboxylated surfaces for 15 minutes in a small petri dish or individual Eppendorf tubes with on the shaker.
5. In the meantime prepare the antibody solution: add 1 μL IgG Stock solution per 150 μL PBS (makes a final concentration of 20 $\mu g/mL$ IgG in the functionalization solution).
6. Prepare a petri dish with parafilm and place a 25 μL droplet on it for each surface.
7. Thoroughly rinse the surfaces in PBS (it is important that the pH is over 7, to enable the aminocoupling reaction) to remove the active compounds from the now NHS ester terminated surface.
8. Immediately place the surfaces upside down onto the protein solution droplets and incubate at room temperature for 2h (alternatively in the fridge at 4°C overnight).
9. Store at +4°C until further use.

C.3.13 Protocol: Protein immobilization on NH2-terminated surfaces after Boc-deprotection using EDC/NHS

Materials:

- 50 mL beaker
- hotplate
- 0.1M MES buffer (pH 6): (100 mL) 1.95g 2-(N-morpholino)ethanesulfonic acid (MES), 100 mL MilliQ water
- 50 mM NHS in 0.1M MES buffer: (50 mL) 0.288g N-Hydroxysuccinimide (NHS), 50 mL MES buffer
- 100 mM EDC in MES buffer: (56 μL) 1 μL 1-Ethyl-3-(3-dimethylaminopropyl)carbodiimide (EDC) (stored in freezer), 55μL MES buffer
- Phosphate buffered saline (PBS, pH 7.4)
- 3 $^{mg}/_{mL}$ Mouse Immunoglobulin Stock solution
- small petri dishes
- parafilm
- shaker

Procedure:

1. In a small beaker, bring MilliQ water to a boil on a hot plate.
2. To remove the protective group from the amine (BOC group): Place chips to be functionalized into the bottom of the beaker in the boiling water and boil for 5 minutes.
3. Prepare MES buffer with 5 mM NHS by mixing the pure buffer and buffer with 50 mM NHS 10:1 (you need 44 μL per chip).
4. Add 0.5 μL IgG Stock soltuion per 44 μL buffer solution (makes a final concentration of 0.03 $^{mg}/_{mL}$ IgG in the functionalization solution.
5. Move to the fume hood to add EDC.
6. For a final concenctration of 2 mM, you need to prepare a higher concentration of EDC in MES buffer first. For this, use 1 μL EDC (in the freezer, middle drawer, red box, top right corner), and 55 μL MES buffer. This gives a 100 mM solution of which you can use 1 μL per 50 μL functionalization solution.
7. Mix carefully and use directly. EDC is very reactive and will inactivate the reactive groups over time.

8. For each chip (in the pipetting frame, 50 μL is sufficient):
9. Wash twice in MES buffer by filling the container and carefully mixing with the pipette. Remove liquid from a corner.
10. Fill container with the functionalization solution and incubate in the dark for 3 hours.
11. Remove the functionalization solution and was with MES buffer twice.
12. Wash twice in PBS and the chips into a tube containing PBS
13. Store at +4C until further use.

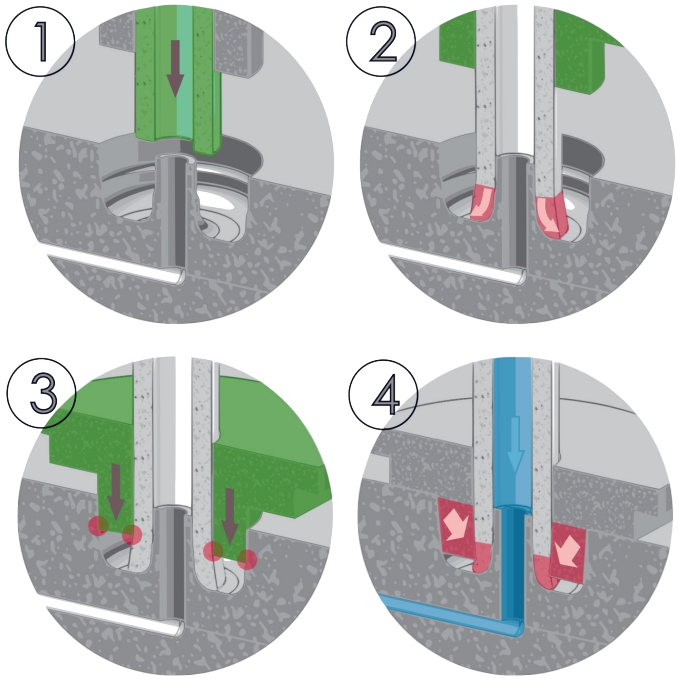

Published by:
DTU Nanotech
Department of Micro- and Nanotechnology
Technical University of Denmark
Ørsteds Plads, building 345C
DK-2800 Kgs. Lyngby